Springer ThesesRecognizing Outstanding Ph.D. Research

Joseph Grange

First Measurement of the Muon Anti-Neutrino Charged Current Quasielastic Double-Differential Cross Section



Springer Theses Recognizing Outstanding Ph.D. Research

More information about this series at http://www.springer.com/series/8790

Aims and Scope

The series "Springer Theses" brings together a selection of the very best Ph.D. theses from around the world and across the physical sciences. Nominated and endorsed by two recognized specialists, each published volume has been selected for its scientific excellence and the high impact of its contents for the pertinent field of research. For greater accessibility to non-specialists, the published versions include an extended introduction, as well as a foreword by the student's supervisor explaining the special relevance of the work for the field. As a whole, the series will provide a valuable resource both for newcomers to the research fields described, and for other scientists seeking detailed background information on special questions. Finally, it provides an accredited documentation of the valuable contributions made by today's younger generation of scientists.

Theses are accepted into the series by invited nomination only and must fulfill all of the following criteria

- They must be written in good English.
- The topic should fall within the confines of Chemistry, Physics, Earth Sciences, Engineering and related interdisciplinary fields such as Materials, Nanoscience, Chemical Engineering, Complex Systems and Biophysics.
- The work reported in the thesis must represent a significant scientific advance.
- If the thesis includes previously published material, permission to reproduce this must be gained from the respective copyright holder.
- They must have been examined and passed during the 12 months prior to nomination.
- Each thesis should include a foreword by the supervisor outlining the significance of its content.
- The theses should have a clearly defined structure including an introduction accessible to scientists not expert in that particular field.

Joseph Grange

First Measurement of the Muon Anti-Neutrino Charged Current Quasielastic Double-Differential Cross Section

Doctoral Thesis accepted by University of Florida, USA



Author Joseph Grange Argonne National Laboratory Lemont, IL, USA Supervisor Heather Ray Department of Physics University of Florida Gainesville, FL, USA

ISSN 2190-5053 ISSN 2190-5061 (electronic)
ISBN 978-3-319-09572-1 ISBN 978-3-319-09573-8 (eBook)
DOI 10.1007/978-3-319-09573-8
Springer Cham Heidelberg New York Dordrecht London

Library of Congress Control Number: 2014949352

© Springer International Publishing Switzerland 2015

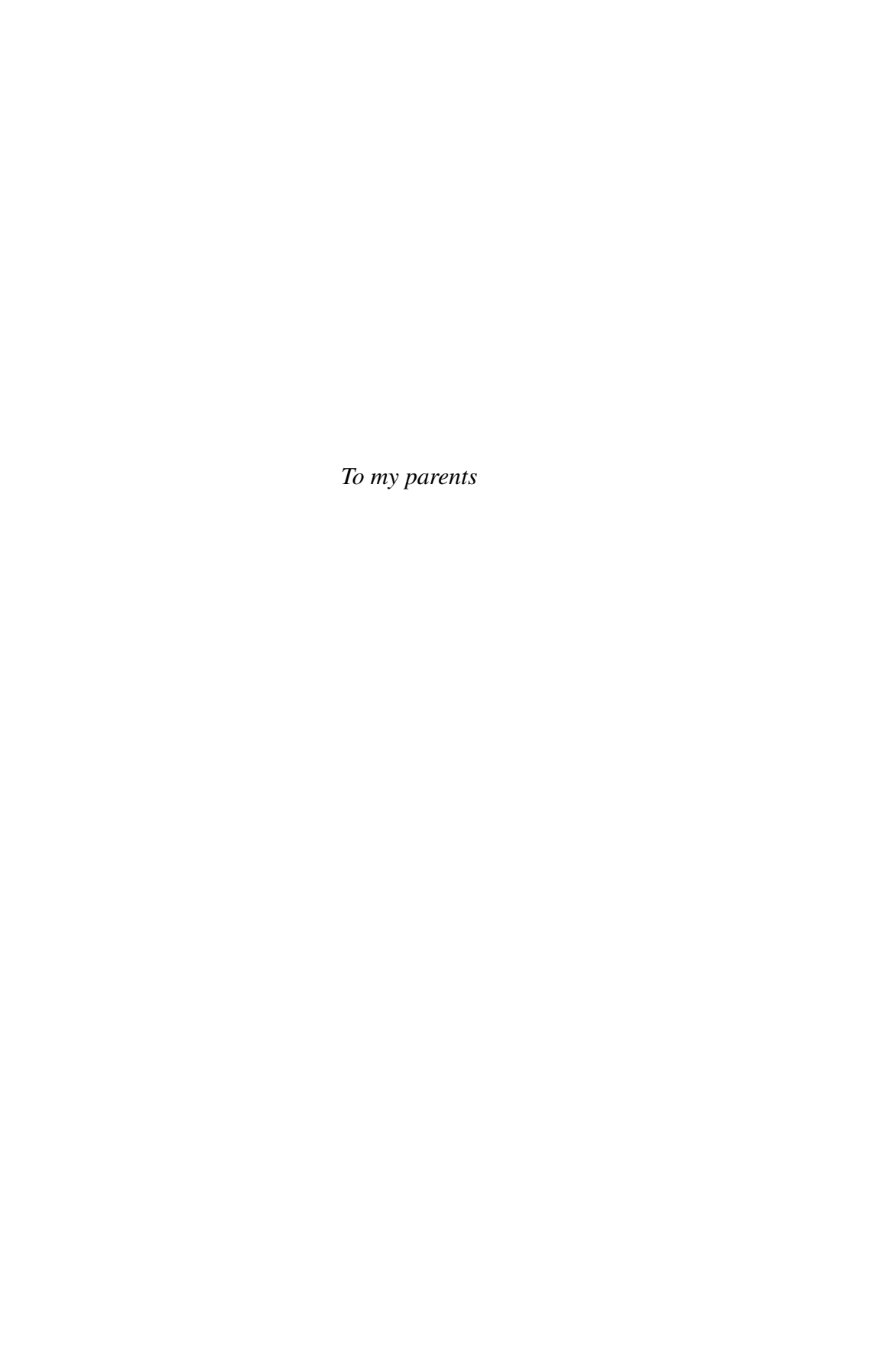
This work is subject to copyright. All rights are reserved by the Publisher, whether the whole or part of the material is concerned, specifically the rights of translation, reprinting, reuse of illustrations, recitation, broadcasting, reproduction on microfilms or in any other physical way, and transmission or information storage and retrieval, electronic adaptation, computer software, or by similar or dissimilar methodology now known or hereafter developed. Exempted from this legal reservation are brief excerpts in connection with reviews or scholarly analysis or material supplied specifically for the purpose of being entered and executed on a computer system, for exclusive use by the purchaser of the work. Duplication of this publication or parts thereof is permitted only under the provisions of the Copyright Law of the Publisher's location, in its current version, and permission for use must always be obtained from Springer. Permissions for use may be obtained through RightsLink at the Copyright Clearance Center. Violations are liable to prosecution under the respective Copyright Law.

The use of general descriptive names, registered names, trademarks, service marks, etc. in this publication does not imply, even in the absence of a specific statement, that such names are exempt from the relevant protective laws and regulations and therefore free for general use.

While the advice and information in this book are believed to be true and accurate at the date of publication, neither the authors nor the editors nor the publisher can accept any legal responsibility for any errors or omissions that may be made. The publisher makes no warranty, express or implied, with respect to the material contained herein.

Printed on acid-free paper

Springer is part of Springer Science+Business Media (www.springer.com)



Acknowledgements

So many folks had a hand in guiding my progress that it would be disingenuous to attempt a complete list here. But I certainly could not have accomplished what I did without the guidance, insight, and contagious enthusiasm of my advisor Heather Ray and those at Fermilab most influential to my analysis: Sam Zeller, Teppei Katori, Richard Imlay, and Chris Polly. I am so lucky to call you my mentors, and I hope to live up to your expectations in my postgraduate work.

Supervisor's Foreword

by Professor Heather Ray

When the neutrino was first proposed by Wolfgang Pauli in 1930, he uttered the dire prediction, "I have done a terrible thing. I have postulated a particle that cannot be detected; it is something no theorist should ever do." Thankfully Pauli was pessimistic when predicting we could never detect such a particle. The first observation of a neutrino occurred in 1956, and since that time the study of the neutrino has grown into one of the major thrusts of the worldwide experimental particle physics program.

However, after almost 70 years of experimental observation, the neutrino remains an enigma. Basic properties such as the absolute mass of the neutrino, how the neutrino acquires mass, and which neutrino is heaviest are poorly constrained. Other questions about the fundamental nature of the particle—if the neutrino and antineutrino are the same particle, and if neutrinos interact with matter in a way that is different from anti-neutrinos—remain entirely unanswered.

In addition, basic measurements of the rate with which neutrinos interact with matter, more precisely the interaction cross sections, have been similarly limited and subject to doubt both experimentally and theoretically. This imprecision has caused considerable difficulty, as cross-section rates are a critical lynchpin to any search for physics involving neutrino interactions. The mid-2000s through today has ushered in an era of high-precision cross sections, focusing on interaction rates of neutrinos and anti-neutrinos in a variety of physics channels and on nuclear targets of various size.

MiniBooNE is a neutrino oscillation experiment that was designed first and fore-most to search for oscillations of muon neutrinos and anti-neutrinos into electron neutrinos and anti-neutrinos. The copious amount of interactions in MiniBooNE's data set has allowed us to also lead the way on many of these cross-section fronts, producing several world's first and world's best results.

Prior to the release of MiniBooNE data, neutrino cross-section results were published in ways that made it difficult to compare between experiments, or to compare the experimental data with theory. For years, neutrino cross-section

measurements had disagreed with our theoretical models. Reporting cross sections in terms of measurable quantities has facilitated the comparison with theories, to elucidate discrepancies between data and theory.

As we began filling in the suite of cross-section measurements separated by physics channel, neutrino energy, and detector material, it became apparent there was a gap in our measurements: muon anti-neutrino cross sections below 1 GeV on any material. This dissertation presents the world's first measurement of the muon anti-neutrino charged current quasi-elastic double-differential cross section, a measurement that optimizes MiniBooNE's unique detector, the large statistics collected, and the critical energy range of the anti-neutrino exposure.

There are many reasons why this result is unique and significant in it's own right. This is the complementary measurement to the MiniBooNE muon neutrino charged current quasi-elastic double-differential cross section, and ratios of the two results can probe potential differences between neutrinos and anti-neutrinos.

Along the way of extracting this result, subtle and challenging background processes had to be carefully and thoroughly addressed. The production of an anti-neutrino beam at an accelerator naturally yields a rather large intrinsic contamination of their neutrino counterparts. In detectors with a magnetic field it is easy to separate the two contributions based on electric charge identification. The spherically symmetric MiniBooNE detector does not allow for such a luxury. This thesis presents three novel and complementary techniques that were used to measure the neutrino contamination present in the anti-neutrino data. This represents the first constraints on the neutrino contribution to an accelerator-produced anti-neutrino beam in a non-magnetized environment. The techniques described here may be of great use to current and future neutrino experiments that also operate without a magnetic field.

Finally, and perhaps most importantly, these results will undoubtedly help the next generation long-baseline accelerator-based neutrino experiments by providing key constraints on signal and background processes. Analyses of these precious future samples aim to discover the ordering of the neutrino masses and a process that may eventually explain the origin and existence of our universe.

Author's Foreword

Like most fields, the fundamental understanding of the basic building blocks of our universe has made tremendous progress in the last century. Theoretical visionaries like Albert Einstein, Neils Bohr, and Richard Feynmann paired with the litany of revolutions in experimental equipment and techniques produced and subsequently confirmed many surprises regarding the nature of our most fundamental constituents. In the mid-1970s these efforts culminated in a theory so seminal it has been classified as a proper noun: the Standard Model of particle physics. This description unites three of the four fundamental forces: electromagnetism, the strong force, and the weak force. This theory has been incredibly successful at describing not only the data that provided so many surprises in the preceding decades, but even today almost all results from modern particle physics experiments are consistent with their prediction from the Standard Model to high accuracy. But we know this description is at least incomplete. It fails to describe the force most intuitive to us in our day-to-day lives; general relativity or, more commonly, gravity. The history of physics is riddled with examples of finding deeper laws to describe seemingly distinct phenomena, and we insist this also be the case with the fundamental forces of nature. Therefore the main thrust of particle physics today is to continually probe the Standard Model by searching for any cracks that may be present so that we might some day arrive at a deeper and ultimately a fundamental understanding of the most basic participants present in the universe and their interactions.

The phenomenon of neutrino oscillations is one of the few concrete observations in particle physics not predicted by the Standard Model. Though it can be accommodated rather simply within the framework of the Standard Model, the root cause is entirely unknown and it is possible that uncovering the origins of oscillatory behavior could be part of pushing the field forward into a new era of discovery.

The dissertation presented here is directly related to the measurement of neutrino oscillations. To measure neutrino oscillations, one must always have a control sample with which to study the unoscillated neutrinos. In a broad and somewhat unfairly pejorative sense, that is what is accomplished here. I mention a few times in this text that the results presented here may aid the discovery of the mechanism

xii Author's Foreword

that led to structure in the universe and hence our existence. An overview of how this might come to fruition is worth mentioning up front.

It is commonly known that when matter and antimatter collide, they annihilate with each other and the objects convert into another form of energy. We also have an enormous body of evidence that our universe was initiated by a cataclysmic event called the big bang, where matter and antimatter particles would have been created in equal amounts. A natural question is why, then, when we look at the universe 14 billion years later, do we only see matter around us, and we only sparingly watch the antimatter counterparts wink in and out of existence? From our current understanding, we would predict that our present-day universe would be a hot soup of constantly annihilating matter and antimatter pairs, precluding the natural beauty and structure observed. We do not yet understand the connection between the big bang and our matter-dominated universe, and neutrinos currently offer the best chance at an explanation.

It is certain that the results of the present text will help the next generation of neutrino experiments, where a primary goal will be to search for the oscillation parameter δ . A nonzero value of this parameter causes extremely subtle differences in the way neutrinos oscillate compared to their antimatter counterpart antineutrinos. The search for this effect will take monstrously large detectors observing a highpowered neutrino beam from almost 1,000 miles away over a decade or more, the start of which is planned for the early-to-mid 2020s. Though these differences would be miniscule, it could be that such a subtlety combined with the enormous number of neutrinos and antineutrinos produced and interacting during the big bang period may have been enough to tip the scales in favor of producing the matter-dominated world we find ourselves in. Such an exciting prospect should be tempered, however: a definitive nonzero measurement of δ would be insufficient to explain the observed matter-antimatter asymmetry. The current best guess at the generation mechanism arising from neutrino oscillations involves the existence of at least an additional, never before seen and much heavier neutrino state. Therefore, in an extremely optimistic scenario, the measurement of neutrino and antineutrino cross sections described in the present work will provide important constraints on the data samples used to discover the δ ingredient used to ultimately determine the mechanism responsible for galaxy and planet formations by eliminating the natural abundance of antimatter.

To any early career academic readers of this text, I'd like to point out a few references that helped me along the way. For forming a solid basis on the current and historical landscape of experimental techniques as well as an understanding of the science behind how and why our tools work, please see **Leo, William R.** *Techniques for Nuclear and Particle Physics Experiments: A How-to Approach.* **Berlin: Springer-Verlag, 1987.** Even in the modern information age, I've found that quite often lessons learned in the past are lost in the face of pervasive experimental tunnel vision. The reference above gives a nice overview of what we can and cannot do in the lab and what could be possible should some limitations be mitigated (as they commonly are) in the future.

Author's Foreword xiii

A mild surprise I had coming into the field of particle physics was the amount of knowledge and agility required to deal with statistics. An excellent and canonical text appropriate for both introductory and reference purposes is the aptly named Lyons, Louis. Statistics for Nuclear and Particle Physicists. Cambridge: Cambridge UP, 1986. I came across a bigger surprise by learning empirically how valuable strong and crisp writing and language skills are in the hard sciences. From writing concise and informative correspondence with colleagues to preparing presentations, research papers, or grant applications, many researchers end up spending much more time communicating their work than you might think. For improvements in this area I'd like to refer the reader to Gibaldi, Joseph. MLA Handbook for Writers of Research Papers. New York: Modern Language Association of America, 2009. While all the aforementioned texts (along with many others) can be very helpful in cultivating the skills of early career scientists, I defer to and strongly agree with the wisdom of Professor Halzen, a theoretical physicist and also experimental powerhouse with the University of Wisconsin-Madison behind the revolutionary neutrino experiment IceCube: "I always advise my students 'don't read too many books - do things!' ".1

¹http://www.jotdown.es/2014/05/francis-halzen-i-always-advise-to-my-students-dont-read-too-many-books-do-things/.

Contents

1	Intr	oduction	
2	Neu	trino Overview	
	2.1	Discovery	
	2.2	Interaction and Propagation States	
	2.3	Flavors of Neutrinos	
	2.4	Chirality	
	2.5	Magnetic Moment	
	2.6	Absolute Mass	
	2.7	Neutrino Sources	
	Refe	erences	1
3	Neu	trino Oscillations	1
	3.1	Formalism	1
	0.12	3.1.1 Three-Neutrino Mixing	1
		3.1.2 Two-Neutrino Mixing	1
	3.2	Experimental Evidence for Neutrino Oscillations	1
		3.2.1 Solar Oscillations.	1
		3.2.2 Atmospheric Oscillations	1
		3.2.3 θ_{13} and δ Oscillations	2
		3.2.4 Hints for $\Delta m^2 \sim 1 \text{eV}^2$	2
	3.3	Summary and Outstanding Questions	2
	Refe	erences	2
4	Non	trino Interactions in MiniBooNE	2
•	4.1	Overview	2
	4.2	CCQE	3
	4.3	$CC\pi$	3
	4.4	Nuclear Effects.	3
		4.4.1 Nuclear Modeling	3
		4.4.2 Final-State Interactions.	3
	Refe	erences	3

xvi Contents

The	MiniB	ooNE Experiment
5.1		riew
5.2	The B	ooster Neutrino Beamline
	5.2.1	The Primary Proton Beam
	5.2.2	Beryllium Target and Magnetic Focusing Horn
	5.2.3	Meson Decay Region
	5.2.4	Neutrino Flux Calculation
5.3		tor
	5.3.1	Physical Layout
	5.3.2	Mineral Oil and Its Properties
	5.3.3	Photomultiplier Tubes
	5.3.4	Calibration Systems
	5.3.5	Analysis Tools
Ref	erences.	
Intr	oductio	on to the Cross-Section Measurement
6.1	Overv	riew
6.2	Event	Selection
Refe	erence	
Rac	koronn	d Measurements and Constraints
7.1	_	urements of the ν_{μ} Background
	7.1.1	Motivation
	7.1.2	General Strategy
	7.1.3	ν_{μ} Flux Measurement Using $CC\pi^+$ Events
	7.1.4	ν_{μ} Flux Measurement Using μ^{-} Nuclear Capture
	7.1.5	ν_{μ} Flux Measurement Using the $\cos \theta_{\mu}$ Distribution
	7.1.6	Summary of ν_{μ} Flux Measurements
7.2		$_{\mu}$ CC π^- Background
7.3		ther Backgrounds
7.4		ground Constraint Summary
Refe	_	
ī. (CCOE	Cross-Section Measurement
8.1		Stability
8.2		CQE Simulation
8.3		-Section Calculation
5.5	8.3.1	Unsmearing to True Quantities
	8.3.2	Efficiency Correction
	8.3.3	Flux and Interaction Targets
	8.3.4	Statistical Uncertainty
8.4		matic Uncertainty
0.7	8.4.1	Background Uncertainties
	8.4.2	Signal Errors
	8.4.3	Uncertainty Summary for $\bar{\nu}_{\mu}$ CCQE on Mineral Oil
	8.4.4	Uncertainty Summary for $\bar{\nu}_{\mu}$ CCQE on Carbon
	U. T.T	

Contents xvii

	8.5	Results	-
		8.5.1 Results Incident on Mineral Oil	129
		8.5.2 Results Incident on Carbon	132
	Refe	erences	141
9	Con	nbined ν_{μ} and $\bar{\nu}_{\mu}$ CCQE Measurements	143
	9.1	Correlated Measurements	143
	9.2	Combined ν_{μ} and $\bar{\nu}_{\mu}$ CCQE Measurements	144
		erences	
10	Con	clusion	151
	Refe	erence	152
Bio	grapl	nical Sketch	153

List of Figures

Fig. 2.1	The detection scheme for the first conclusive	
	demonstration of the existence of the neutrino. Image from [7]	5
Fig. 2.2	Results from a combined analysis of precision	
	measurements of the Z^0 width. The number of	
	light, active neutrino species is determined to be	
	2.9840 ± 0.0082 , consistent with direct observations of	
	the ν_e , ν_μ , and ν_τ neutrinos. Figure from [13]	7
Fig. 2.3	Summary of the various prolific neutrino sources in the	
	universe. The cross section for $\bar{\nu}_e + e^- \rightarrow \bar{\nu}_e + e^-$	
	is shown for comparison. Reprinted with permission	
	from J.A. Formaggio and G.P. Zeller [30]. Copyright	
	2012 by the American Physical Society. The following	
	statement applies to all APS-copyrighted material	
	throughout this text: Readers may view, browse, and/or	
	download material for temporary copying purposes	
	only, provided these uses are for noncommercial	
	personal purposes. Except as provided by law, this	
	material may not be further reproduced, distributed,	
	transmitted, modified, adapted, performed, displayed,	
	published, or sold in whole or part, without prior	
	written permission from the American Physical Society	10
Fig. 3.1	Solar ν_{μ} and ν_{τ} flux versus ν_{e} flux observed by the	
	SNO detector. The Standard Solar Model (SSM)	
	expectation is shown by the band between the dashed	
	lines and shows good agreement with the best-fit of the	
	SNO data, represented by the solid point. Surrounding	
	the best fit mark are 68 %, 95 % and 99 % C.L.	
	contours. Reprinted with permission from B. Aharmim	

xx List of Figures

Fig. 3.2	KamLAND $\bar{\nu}_e$ disappearance results. The ratio shown is the observed data relative to the no-oscillation	
	hypothesis, and the distribution clearly favors the sinusoidal form of neutrino oscillation over	
	alternatives. Reprinted with permission from T. Araki	
		19
Ei ~ 2.2	et al. [8]. Copyright 2005 by the American Physical Society	19
Fig. 3.3	Results from a fit to the KamLAND and solar neutrino	
	data to the oscillation parameters $\Delta m_{\rm solar}^2$ and $\theta_{\rm solar}$.	20
Ei ~ 2.4	Figure taken from [8] Data from the Super-Kamiokande experiment clearly	20
Fig. 3.4		
	showing an L/E dependence of the observed v_{μ} flux	
	relative to the prediction assuming no oscillations.	
	Reprinted with permission from Y. Ashie et al. [11].	21
E: 2.5	Copyright 2004 by the American Physical Society	21
Fig. 3.5	Summary of oscillation fits to data sensitive to	
	$\Delta m^2 \sim 10^{-3} \mathrm{eV}^2$. Reprinted with permission from	
	P. Adamson et al. [13]. Copyright 2008 by the	2.1
F: 0.6	American Physical Society	21
Fig. 3.6	Observed \bar{v}_e flux at the various Daya Bay experimental	
	halls (EH) as a function of distance from the $\bar{\nu}_e$ source	
	relative to the prediction assuming no oscillations. The	
	inset shows the compatibility of the data for various	
	values of $\sin^2 2\theta_{13}$, clearly ruling out $\theta_{13} = 0$ at greater	
	than 5σ C.L. Reprinted with permission from F.P. An	
	et al. [20]. Copyright 2014 by the American Physical Society	22
Fig. 3.7	Constraints on δ for various assumptions on the sign of	
	Δm^2 and the value of θ_{23} from the MINOS experiment.	
	It will be shown that the θ_{23} is nearly identical to θ_{atm} .	
	Reprinted with permission from P. Adamson et al. [15].	
	Copyright 2013 by the American Physical Society	23
Fig. 3.8	Results of a two-neutrino oscillation fit to the combined	
	v_e and \bar{v}_e appearance data from MiniBooNE. Also	
	shown are the LNSD allowed regions and limits from	
	the KARMEN experiment [24]. Figure taken from [3]	24
Fig. 3.9	The two possible neutrino mass orderings, shown with	
	their approximate couplings to the flavor states	26
Fig. 4.1	Comparison of expectations and experimental data	
118	across v_{μ} (top) and \bar{v}_{μ} (bottom) CC interactions. The	
	"QE" and "RES" labels here are referred to as CCQE	
	and $CC\pi$ interactions in the text. Figure from [30]	30
Fig. 4.2	Decomposition of the differential CCQE cross section	50
115. 7.2	for 700 MeV ν_{μ} 's. The ordinate axis is proportional to	
	$d\sigma/dO^2$. Figure from [9]	33

List of Figures xxi

Fig. 4.3	Comparison of the NUANCE prediction for π^+ absorption (top) and charge-exchange ($bottom$) to relevant data [42]. Figure from [19]	37
Fig. 5.1	Cartoon of the Fermilab pre-accelerator stage. Figure taken from [4]	40
Fig. 5.2	Injection diagram for H^- ions onto the Booster orbit as bare protons. Figure taken from [5]	41
Fig. 5.3	Timing structure of the BNB proton spills through the arrival time of neutrino events at MiniBooNE. The represented data is the neutrino-mode CCQE sample, and a time-of-flight correction based on the observed interaction vertex along the beam direction has been applied. The ~500 ns offset between the arrival and	
Fig. 5.4	recorded times is due to an offset in the timing instruments The BNB beryllium target. Shown is an expanded view of the segmented target (<i>top</i>) and its place inside the	42
	magnetic focusing horn (<i>bottom</i>). The proton beam strikes the target from the <i>left</i>	43
Fig. 5.5	A comparison of the azimuthal component of the magnetic field relative to the input current between data (in <i>points</i>) and the expectation (<i>solid curve</i>) of 1/r dependence. The <i>vertical line</i> identifies the inside edge	
Fig. 5.6	of the outer conductor. Figure taken from [6]	43
Eig 57	incoming proton beam (right). Figure taken from [7]	45
Fig. 5.7	Double-differential cross section $d^2\sigma/d\rho_\pi d\Omega_\pi$ for $p + \mathrm{Be} \to \pi^- + X$ in units of mb/(GeV sr). The angular axes have units of radians, and the momentum projections are in units of GeV. The blue curve is the Sanford–Wang parametrization based on the red HARP data points, and the black histogram with uncertainties is the spline interpolation. Figure taken from [13]	46
Fig. 5.8	Fluka [19] calculations of the tertiary π^+ yield from reinteractions in a graphite target. Given as a function of incident proton beam momentum p_0 , the π^+ fraction is given for the indicated thresholds on the longitudinal component of the π^+ momentum (<i>left</i>), and also for targets of 0.5, 1.0, and 2.0 interaction lengths (<i>right</i>). The primary proton beam at the BNB has momentum	-10
	8.9 GeV/c. Figure taken from [20]	47

xxii List of Figures

Fig. 5.9	The MiniBooNE flux prediction for (a) neutrino mode	40
E'. 5.10	and (b) antineutrino mode. Data taken from [1]	48
Fig. 5.10	Overview of the MiniBooNE detector housing. Image taken from [21]	49
Fig. 5.11	On the <i>left</i> , cutaway drawing of the MiniBooNE	7)
11g. 3.11	detector showing PMTs dispersed in the inner and	
	outer regions. The optical barrier separating the outer	
	veto region (painted <i>white</i>) from the inner signal region	
	(painted <i>black</i>) is shown on the <i>right</i>	50
Fig. 5.12	Photon extinction rate spectrum in the MiniBooNE	50
11g. 3.12	oil. As indicated, the <i>solid curves</i> correspond to	
	measurements, while the <i>dashed lines</i> are based on an	
	extrapolation of these data and are tuned to various in	
	situ calibration data samples. Figure taken from [2]	51
Fig. 5.13	Quantum efficiency for the newer MiniBooNE PMTs.	51
11g. 3.13	Figure taken from [25]	52
Fig. 5.14	Schematic of the laser calibration system. Image taken from [2]	52
Fig. 5.15	Cartoon of the muon calibration system. (left) and the	32
11g. 3.13	relationship between muon energy and range in data	
	and simulation subsequent to calibrations (<i>right</i>). Only	
	one of the seven scintillator cubes are shown in the <i>left</i>	
	figure, and the image is taken from [2]	54
Fig. 5.16	Typical PMT hit (ordinate axis) and timing signature	54
115. 5.10	of a $\bar{\nu}_{\mu}$ CCQE event. The prompt μ^{+} arrives in time	
	with the BNB spill (from 4,600–6,200 ns relative to	
	the beginning of the DAQ clock) with 100's of MeV	
	in kinetic energy, while the Michel is observed a	
	time characteristic of the muon lifetime later with an	
	energetic endpoint of \sim 53 MeV. Their signatures are	
	easily separated with the subevent definition	55
Fig. 5.17	Typical PMT hit topology and timing for muon (<i>left</i>)	
8	and electron (<i>right</i>) candidate events in MiniBooNE	
	data. PMT charge is correlated to the size of the	
	displayed hits, while timing is given by the color	
	spectrum, where <i>blue</i> hits arrived earliest and <i>red</i> hits	
	arrived last	56
Fig. 5.18	Kinetic energy and angular resolution of the	
U	MiniBooNE reconstruction to electrons, muons, and	
	neutral pions. Figure from [28]	57
Dia 61		
Fig. 6.1	Veto hits for early neutrino-mode data and MC for the	
	first two subevents. Points are data, the <i>dotted (dashed)</i>	
	blue (red) histogram is v_{μ} CCQE (all non- v_{μ} CCQE)	
	and the <i>solid line</i> is total MC. All distributions are	
	normalized to unit area. Cosmic rays are not simulated,	
	and this is the origin of the shape discrepancy between data and MC in the first subeyent. Figure from [1]	60
	uata and IVIC III the first subevent. Figure Ifolii [1]	OU

List of Figures xxiii

Fig. 6.2	Selection requirements 3–6. Descriptions are given in the text, and distributions are normalized to flux. With the exception of the subevent figure, all distributions	<i>C</i> 1
Fig. 6.3	have every cut applied except the one indicated in the figure T_{μ} dependent range cut for different channels and samples, as labeled. Events are plotted on a logarithmic scale	61
Fig. 6.4	An arbitrary t-channel exchange	64
Fig. 6.5	The four variables cross sections will be reported in.	
	Distributions are normalized to flux	66
Fig. 7.1	Predicted angular distributions of pions with respect	
	to the incident proton beam (θ_{π}) producing ν_{μ} and	
	$\bar{\nu}_{\mu}$ in neutrino (<i>left</i>) and antineutrino (<i>right</i>) modes.	
	Only pions leading to ν_{μ} and $\bar{\nu}_{\mu}$ events in the detector	
	are shown, and all distributions are normalized to	
	10.1×10^{20} protons on target. Arrows indicate the	
	region where HARP data [8] are available	68
Fig. 7.2	Generated ν_{μ} energy distributions accepted into	
Ü	the neutrino and antineutrino CCQE samples. The	
	substantial overlap indicates the v_{μ} 's background to the	
	$\bar{\nu}_{\mu}$ CCQE sample are kinematically covered by the ν_{μ}	
	cross sections observed in the neutrino-mode data	70
Fig. 7.3	The ν_{μ} CC π^{+} total cross section. <i>Black points</i> with	
	green error bands are MiniBooNE data, and red is the	
	MC expectation. Figure reproduced from [1]	73
Fig. 7.4	The $CC\pi^+$ fractional uncertainty conversion	73
Fig. 7.5	Summary of the normalization correction to the	
	v_{μ} CCQE cross section in the antineutrino-mode	
	simulation. The ratio of the data to the <i>red</i> MC	
	histogram is applied bin-by-bin to the simulated ν_{μ}	
	CCQE events. Also visible is the effect of low-precision	
	sampling with the NUANCE generator at high energies.	
	This is discussed further in Sect. 8.2	78
Fig. 7.6	The log-likelihood μ/e particle-ID variable in	
	the single-subevent sample. All other selection	
	requirements have been applied. The simulation is	
	normalized to flux, and errors shown on data are	
	statistical only	79
Fig. 7.7	Q_{OE}^2 for the single-subevent (top) and two-subevent	
-	(bottom) samples. All other selection cuts have	
	been applied. Events with $Q^2 > 0.2 \text{GeV}^2$ are	
	selected to reject some NC events, particularly in the	
	single-subevent sample. Distributions are normalized to flux	80

xxiv List of Figures

Fig. 7.8	Predicted muon endpoint radius for the single-subevent	
	(top left), two-subevent (top right) samples and the	
	ratio single/two subevents (bottom). All other selection	
	cuts have been applied. Data-MC discrepancy is only	
	present at high radius, presumably due to difficulties in	
	modeling Michel detection close to the optical barrier.	
	The peak above 500 cm in the single-subevent and the	
	ratio distribution is due to the lower Michel detection	
	efficiency in this region. There are zero events in the	
	first bin of the single-subevent data. Distributions are	
	relatively normalized to data	81
Fig. 7.9	Difference between average hit times for the	
J	Michel-like subevent and the muon-like subevent in	
	antineutrino mode. The distributions deviate from an	
	exponential form at low timing differences due to	
	the temporal definition of a subevent. Simulation is	
	relatively normalized to data	82
Fig. 7.10	Tank hit distributions for the second subevent in	
J	antineutrino mode. Simulation is normalized to data	82
Fig. 7.11	Tank hit distributions for the second subevent in	
	neutrino mode. Events from μ^- capture are expected to	
	only contribute in the lowest bins, and the consistency	
	between data and simulation gives confidence that	
	the μ^- capture model is adequate. MC is relatively	
	normalized to data	85
Fig. 7.12	Early separation between the two subevents in neutrino	
	mode. No significant shape difference is observed	
	between the four chronologically sequential groups of	
	data. Distributions are scaled to unit area	86
Fig. 7.13	The $\cos \theta_{\mu}$ distribution of the CCQE sample by	
	neutrino type before fitting. The nominal MC	
	prediction is normalized to flux, and notations used in	
	the legend are used in the execution of the fit	90
Fig. 7.14	Michel distance versus the range slope as described in	
	the text. Distributions are absolutely normalized	92
Fig. 7.15	Central-value (CV) $\cos \theta_{\mu}$ prediction versus 100	
=	distributions created by cross section throws for	
	right-sign (RS) $\bar{\nu}_{\mu}$ and wrong-sign (WS) ν_{μ} events	94

List of Figures xxv

Fig. 7.16	Correlation matrix for ν_{μ} and $\bar{\nu}_{\mu}$ events in the $\cos \theta_{\mu}$	
	distribution. From <i>left</i> to <i>right</i> and <i>bottom</i> to <i>top</i> , the	
	domain is $[-1,1]$ for the RS and WS distributions.	
	The block-diagonals give bin correlation information	
	between the v_{μ} events (top right) and \bar{v}_{μ} (bottom	
	<i>left</i>) events, while the off-diagonals contain the ν_{μ} - $\bar{\nu}_{\mu}$	
	correlations. All bins are positively correlated to each	
	other due to the dominant cross-section uncertainties,	
	many of which affect the generation of ν_{μ} and $\bar{\nu}_{\mu}$	
	events in the same way	95
Fig. 7.17	Results of the muon angular fits to the CCQE data.	
Ü	Shown are (a) the fits and (b) fractional differences	
	(data – simulation)/simulation for both the unmodified	
	prediction and the best fit. Along with an inclusive	
	sample, three reconstructed energy bins are considered.	
	The before-fit simulation is absolutely normalized to	
	5.66×10^{20} protons on target. As indicated, only events	
	with $\cos \theta_{\mu} < 0.91$ participate in the fit	98
Fig. 7.18	Summary of the results from three techniques used	
Ü	to measure the ν_{μ} flux in the antineutrino-mode	
	beam. Measurements performed in exclusive regions	
	of reconstructed energy are placed here at the mean	
	of their associated distribution of generated energy.	
	Shown as a <i>dotted line</i> at unity, the measurements are	
	made relative to an extrapolation of HARP data into a	
	region where no relevant hadroproduction data exists	100
Fig. 7.19	Summary of the MiniBooNE $CC\pi^+$ analysis for the	
C	background measurement to the ν_{μ} CCQE sample.	
	Shown is (a) the neutrino-mode CCQE sample and (b)	
	the $CC\pi^+$ sample before the application of constraints	
	and parameter fits. The <i>dashed line</i> in (b) shows the	
	ratio of prediction to data in the $CC\pi^+$ sample, and	
	its value is given by the right ordinate axis. This	
	measurement is used to indirectly constrain the rate and	
	kinematics of the $CC\pi^-$ contribution to the $\bar{\nu}_{\mu}$ CCQE	
	sample. Figure taken from [4]	102
Fig. 7.20	Comparison of the nominal Rein-Sehgal model to	
	a more modern model that also describes world	
	pion-production data more accurately	103
	· • · • · •	

xxvi List of Figures

Fig. 7.21	Three calculations for the $CC\pi^-$ background contribution to the $\bar{\nu}_{\mu}$ CCQE sample as a function of $\cos \theta_{\mu}$. The "central value" distribution corresponds to	
	the nominal Rein-Sehgal prediction for $CC\pi^-$ events	
	in MiniBooNE constrained by the observed kinematics	
	in the neutrino-mode ν_{μ} CC π^{+} sample. This agrees	
	well with a more recent calculation ("Berger-Sehgal	
	extended model") that is based on an improved version	
	of the Rein-Sehgal model. For comparison, the nominal	
	Rein-Sehgal prediction for $CC\pi^-$ events is also shown.	
	Distributions are normalized to flux	103
Fig. 8.1	Kolmogorov-Smirnoff test for different antineutrino	
	run periods. Each data point is the result of the K-S test	
	of that run against the sum of the other subsamples.	
	The data are consistent with a uniform distribution	
	between null and unity. Important to note is that E_v^{QE}	
	and Q_{OE}^2 are derived quantities from T_{μ} and $\cos \theta_{\mu}$, so	
	these tests are not independent	110
Fig. 8.2	Reconstructed antineutrino data for various run periods.	
	Good agreement within statistical errors indicate stable	
	running. Included here in "jul07" and not in the main	
	analysis is the small absorber down sample	111
Fig. 8.3	Normalization stability over various run periods.	
	Included uncertainties are statistics and a 2 % error on	
	delivered POT	111
Fig. 8.4	Comparison between generator-level total cross section	
	for bound signal events to the unfolded MC. The files	
	input to the MC distribution were generated with	
	$\kappa = 1.022$, and the failed attempt to recover $\kappa = 1.007$	
	through traditional reweighting is clear at lower	
	energies, while the flux sampling issue dominates the	
	discrepancy at high energy	112
Fig. 8.5	Weights as a function of muon kinematics applied to	
	MC to recover $\kappa = 1.007$. As expected, the weights are	
	strongest in regions of forward-going, low-energy muons	113
Fig. 8.6	Summary of the high energy rate correction for $\bar{\nu}_{\mu}$	
	CCQE interactions on hydrogen	113
Fig. 8.7	Comparison of NUANCE-generated single pion cross	
	sections to the unfolded MC. Unlike in the CCQE	
	interactions, the high energy flux sampling problem is	
	small enough to ignore here	114

List of Figures xxvii

Fig. 8.8	Fractional differences between truth and reconstructed quantities in the four relevant variables. As in all distributions peaked near null, the average fractional difference in Q_{QE}^2 is higher than it would be otherwise	115
Fig. 8.9	The matrix \check{U} connecting the true and reconstructed quantities for the four variables of interest. For the two-dimensional distribution, in principle \check{U} is four dimensional and only its diagonal entries are shown here	117
Fig. 8.10	Comparison of before and after the unsmearing procedure for signal events. The two-dimensional ratio includes a requirement that there be at least 10 events in each bin of both the reconstructed and unsmeared distributions	118
Fig. 8.11	Comparison of the two unsmearing methods studied in this section	119
Fig. 8.12	Detection efficiency for each cut in the relevant distributions. Only the total efficiency is shown for two-dimensional muon kinematics.	
Fig. 8.13	Predicted outgoing phase space for π^- before horn focusing. Only π^- 's focused by the horn and that subsequently lead to an interaction in the detector are shown. As printed on the figure, roughly 90% of the	121
Fig. 8.14	flux is covered by the HARP π^- cross-section data	122
Fig. 8.15	10.1×10^{20} POT	
Fig. 8.16	sum of the error sources shown	128
Fig. 8.17	including the hydrogen content as signal	129
Fig. 8.18	the quadrature sum of the error sources shown	131
Fig. 8.19	$\cos \theta_{\mu}$ and the double-differential cross sections	132
Fig. 8.20	hydrogen component <i>not</i> subtracted	133
	(1.000) for $M_A^C = 1.35$ (1.02) GeV and in both cases $M_A^H = 1.02$ GeV	134

xxviii List of Figures

Fig. 8.21	r: =	
	shape uncertainty compared to central value MC	
	with the hydrogen component <i>not</i> subtracted. For	
	the differential cross sections, MC is scaled to the	
	integrated cross section from data $(\int \frac{d\sigma}{dX} dX)$, while for	
	the total cross section MC is scaled to data based on the	
	discrepancy in the bin at the interaction peak (0.65–0.7 GeV)	135
Fig. 8.22	Extracted $\bar{\nu}_{\mu}$ CCQE cross sections with total	
118. 0.22	uncertainty compared to central value MC with the	
	hydrogen component subtracted	136
Fig. 8.23		150
11g. 0.23	carbon with total uncertainty	137
Fig. 8.24	Extracted $\bar{\nu}_{\mu}$ CCQE cross sections with total and shape	137
11g. 0.24	F:	
	uncertainty compared to central value MC with the	
	hydrogen component <i>subtracted</i> . For the differential	
	cross sections, MC is scaled to the integrated cross	
	section from data $(\int \frac{d\sigma}{dX} dX)$, while for the total cross	
	section MC is scaled to data based on the discrepancy	120
	in the bin at the interaction peak (0.65–0.7 GeV)	138
Fig. 8.25	Shape comparison for hydrogen-subtracted data and	
	the RFG under various parameter choices. The shape of	
	central value MC with $M_A = 1.35 \text{GeV}$ and $\kappa = 1.007$	
	agrees with data remarkably well. In particular, the	
	mild change in κ (1.000 \rightarrow 1.007) determined from	
	the ν_{μ} CCQE analysis seems to be preferred by the	
	data. Also printed on the figure is the scale for each	
	prediction to match the data in normalization	139
Fig. 8.26	Comparison between MiniBooNE and NOMAD ν_{μ}	
	and $\bar{\nu}_{\mu}$ data, as well as some predictions from the RFG.	
	Tension exists across both ν_{μ} and $\bar{\nu}_{\mu}$ data from the two	
	experiments under the assumptions of CCQE with the	
	RFG. NOMAD data from [32]	140
Fig. 8.27	Total cross section per nucleon for $\bar{\nu}_{\mu}$ CCQE data with	
	the hydrogen content removed compared to various predictions	140
Fig. 8.28	Total cross section per nucleon for ν_{μ} and $\bar{\nu}_{\mu}$ CCQE	
Ü	data compared to various predictions. The "RFG"	
	distribution assumes $M_A = 1.35 \text{GeV}$ and $\kappa = 1.007$.	
	Total uncertainty is shown with both MiniBooNE data sets	141
T. 0.4	•	
Fig. 9.1	Recovered ν_{μ} (left half of each distribution) and	
	$\bar{\nu}_{\mu}$ (right half of each distribution) CCQE cross	
	sections for the correlation analysis. Each bin in the	
	$E_{\nu}^{QE,RFG}$ distribution (<i>left</i>) is $\in \{0.4, 2.0\}$ GeV and	
	is identical to the bins delimited in Fig. 8.27, while	
	the Q_{QE}^2 distribution (<i>right</i>) is $\in \{0.0, 2.0\}$ GeV ² and	
	corresponds to the binning in Fig. 8.25	146

List of Figures xxix

Fig. 9.2	Correlation matrices for the various ν_{μ} and $\bar{\nu}_{\mu}$ cross	
	section results. To highlight the important information,	
	only the $\rho_{\nu,\bar{\nu}}$ coefficients are shown for each bin in the	
	$\frac{d^2\sigma}{dT_{\mu}d\cos\theta_{\mu}}$ distribution (bottom). The analogous entries	
	correspond to the on-diagonal coefficients of the ν_{μ} - $\bar{\nu}_{\mu}$	
	off-diagonal blocks in the $\sigma(E_{\nu}^{QE,RFG})$ (top left) and	
	$d\sigma/dQ_{OE}^2$ (top right) matrices	147
Fig. 9.3	Correlation coefficients by uncertainty type for the	
	various distributions. As expected, the correlations are	
	mostly positive between the ν_{μ} and $\bar{\nu}_{\mu}$ CCQE measurements	148
Fig. 9.4	Difference measurements of the ν_{μ} and $\bar{\nu}_{\mu}$ CCQE cross	
	sections compared to various predictions. The "RFG"	
	curve in the <i>top left figure</i> assumes $M_A = 1.35 \text{GeV}$	
	and $\kappa = 1.007$. The "uncorrelated uncertainty", found	
	by setting $\rho_{\nu,\bar{\nu}} = 0$ in the uncertainty determination, is	
	included to appreciate the level of sensitivity gained by	
	using the correlation information	149
Fig. 9.5	Ratio measurements of the ν_{μ} and $\bar{\nu}_{\mu}$ CCQE cross	
	sections compared to various predictions. The "RFG"	
	curve in the <i>top left figure</i> assumes $M_A = 1.35 \text{GeV}$	
	and $\kappa = 1.007$. The "uncorrelated uncertainty", found	
	by setting $\rho_{\nu,\bar{\nu}} = 0$ in the uncertainty determination, is	
	included to appreciate the level of sensitivity gained by	
	using the correlation information	150

List of Tables

Table 5.1	Momentum threshold for production of Čerenkov radiation for four important particle types in mineral	
	oil compared to water	50
Table 6.1	Purity and detection efficiency for the sample	
	described in this section	63
Table 6.2	Predicted composition of the sample described in this section	63
Table 7.1	Summary of data periods used in the analyses of	
	$CC\pi^+$ events and the $\cos \theta_{\mu}$ distribution (Sect. 7.1.5)	72
Table 7.2	Summary of selection cuts in the $CC\pi^+$ sample	74
Table 7.3	Summary of the $CC\pi^+$ sample in antineutrino mode,	
	including the nucleon-level composition	75
Table 7.4	Antineutrino-mode $CC1\pi^+$ sample details and ν_{μ}	
	flux component measurement	76
Table 7.5	Antineutrino-mode purity in % for all ν_{μ} and $\bar{\nu}_{\mu}$	
	charged-current events in the one- and two-subevent samples	79
Table 7.6	Summary of predicted nucleon-level interactions in	
	the antineutrino-mode subevent samples	83
Table 7.7	A brief description of the neutrino-mode subevent	
	samples for the same selection described in the	
	previous section	84
Table 7.8	Calibration summary for Michel detection	
	inefficiency (δ) and the rate of effective μ^- nuclear	
	capture (β)	84
Table 7.9	1SE and 2SE event details in four sequential and	
	roughly equally sized neutrino-mode data groups	85
Table 7.10	Results for scale factors relative to the expectation	
	for the ν_{μ} and $\bar{\nu}_{\mu}$ charged-current content of the	
	antineutrino-mode data	87

xxxii List of Tables

Uncertainty summary for the μ^- capture-based	
measurement of the ν_{μ} flux	88
Summary of measurements for the ν_{μ} flux scale α_{ν}	
and the $\bar{\nu}_{\mu}$ rate scale $\alpha_{\bar{\nu}}$	89
Summary of systematic error contribution to the scale	
parameter α_{ν} in the inclusive energy fit	96
Summary of cross-section errors used in this analysis	97
Fit results in three energy bins and an inclusive sample	97
Fractional composition of the antineutrino-mode	
CCQE sample before and after angular fits	97
Summary of background constraints and uncertainties	
in the $\bar{\nu}_{\mu}$ CCQE sample	105
Summary of data groups input to the stability tests	110
	130
Normalization errors for each cross section and each	
as background	130
	measurement of the ν_{μ} flux

Abstract of Dissertation Presented to the Graduate School of the University of Florida in Partial Fulfillment of the Requirements for the Degree of Doctor of Philosophy

First Measurement of the Muon Anti-neutrino Charged Current Quasielastic Double-Differential Cross Section

By

Joseph M. Grange

May 2013

Chair: Heather Ray Major: Physics

Abstract This dissertation presents the first measurement of the muon antineutrino charged current quasi-elastic double-differential cross section. These data significantly extend the knowledge of neutrino and anti-neutrino interactions in the GeV range, a region that has recently come under scrutiny due to a number of conflicting experimental results. To maximize the precision of this measurement, three novel techniques were employed to measure the neutrino background component of the data set. Representing the first measurements of the neutrino contribution to an accelerator-based anti-neutrino beam in the absence of a magnetic field, the successful execution of these techniques carries implications for current and future neutrino experiments.

Finally, combined measurements of these antineutrino and the previously published neutrino cross-section data using the same apparatus maximize the extracted information from these results by exploiting correlated systematic uncertainties. The results of this analysis will help to understand signal and background processes in present and future long-baseline neutrino experiments, the principal goal of which is to measure the ordering of the neutrino masses and a process that may ultimately explain the origin of our matter-dominated universe.

Chapter 1 Introduction

The work presented here represents a major step forward in experimentally understanding the behavior of muon neutrinos and antineutrinos. Apart from providing a world's-first measurement of these interactions in a mostly-unexplored energy region, these data advance the neutrino community's preparedness to search for an asymmetry between matter and anti-matter that may well provide the physical mechanism for the existence of our universe.

The details of these measurements are preceded by brief summaries of the history of the neutrino (Chap. 2), the phenomenon of neutrino oscillations (Chap. 3), and a description of their interactions (Chap. 4). Details of the experimental setup for the measurements are given in Chap. 5. Chapter 6 introduces the muon antineutrino cross-section measurement and motivates the need for dedicated, in situ background constraints. The world's first measurements of the neutrino component of an antineutrino beam using a non-magnetized detector, as well as other crucial background constraints, are presented in Chap. 7. The muon antineutrino cross-section measurement is given in Chap. 8. By exploiting correlated systematic uncertainties, combined measurements of the muon neutrino and antineutrino cross sections described in Chap. 9 maximize the precision of the extracted information from both results. Finally, the results are summarized in Chap. 10.

1

Chapter 2 Neutrino Overview

This chapter touches on the various milestone measurements in the history of the neutrino and outlines many of their basic properties. As perhaps the most important development in its young history, a more complete development and review of neutrino oscillations is saved for Chap. 3.

2.1 Discovery

At the beginning of the twentieth century, much of the physics community were content to believe the universe was fundamentally composed of electrons, photons and, in the literal sense, atoms. An example of historically bad advice given by an advisor to their student came when the supervisor of Max Planck suggested that "in this field, almost everything is already discovered, and all that remains is to fill a few unimportant holes" [1]. Planck went on to revolutionize the field with his description of quantum mechanics and ultimately helped expose human knowledge to a litany of new particles and phenomena.

And so, like many of the particles discovered in the twentieth century, the neutrino came as a surprise. The first hints came through observations of so-called β decay in the 1920s, where a neutron inside a nucleus spontaneously decays. Though the picture of the proton and neutron structure of the nucleus was not yet clear, by energy and spin conservation the decay was believed to be a two-body process:

$$n \to p + e^-, E_e = \frac{m_n^2 + m_e^2 - m_p^2}{2m_n},$$
 (2.1)

where E_e is the energy of the ejected electron in the rest frame of the neutron and m_n, m_p , and m_e are the neutron, proton, and electron masses, respectively. As the

4 2 Neutrino Overview

neutrons housed in nuclei are on average at rest, the observed electron spectrum ought to be nearly monoenergetic. Multiple experiments using a variety of β -decay sources conclusively rejected this hypothesis [2].

Of the many alternate explanations for the observed electron spectrum, Wolfgang Pauli proposed in 1931 the ultimately proven hypothesis: the products of β decay include a third, electrically neutral particle of mass far less than the electron and whose interactions are rare enough to have escaped direct detection. The β decay reaction is now described as:

$$n \to p + e^- + \nu, E_e \in \left\{ m_e, \frac{m_n^2 + m_e^2 - \left(m_p^2 + m_\nu^2\right)}{2m_n} \right\},$$
 (2.2)

where the presence of the neutrino kinematically allows the electron to have a continuous energy spectrum. Regarding the proposed feeble interaction rate of the neutrino, Pauli famously quipped "I have done a terrible thing. I have postulated a particle that cannot be detected" [3].

Fortunately, it took only a few decades for experimental technology and techniques to reach the level of precision necessary to directly observe the neutrino. If Pauli's interpretation of the β decay spectrum and Enrico Fermi's extended description of the particle [4, 5] were correct, two prolific sources of neutrinos in the 1950s were available in atomic explosions and nuclear reactors. One of the early plans to detect the neutrino involved a retrospectively comical proposal to detonate a dedicated atomic bomb while a neutrino detector was simultaneously dropped down a nearby mineshaft [6]. They eventually proceeded with a more pacific design, aiming to observe neutrinos produced in a nuclear reactor.

If Eq. (2.2) is the correct description of β decay, the inverted process induced by a neutrino should also be allowed: $v + p \rightarrow n + e^+$. In a tank of liquid scintillator doped with cadmium, the positron produced in this inverted β decay reaction will annihilate with an in-medium electron, producing two prompt gamma rays emitted in opposing directions ($e^+ + e^- \rightarrow 2\gamma$, $\theta_{\gamma\gamma} = \pi$). The neutron has a large probability for being captured on the cadmium nuclei, and the characteristic de-excitation photons following this process provides a clean neutron signature. The detection schematic is shown in Fig. 2.1. Photomultiplier tubes collect the photons from the annihilation and capture reactions, and data from a detector using these principles yielded the first definitive detection of the neutrino in 1956 [8].

2.2 Interaction and Propagation States

Any intelligent discussion of the nature of the neutrino must be built on an understanding of its peculiarly misaligned interaction and propagation eigenstates. Generically, an eigenstate is a vector returned by the action of a particular operator. Neutrinos only interact through the weak force, so the eigenstates available upon

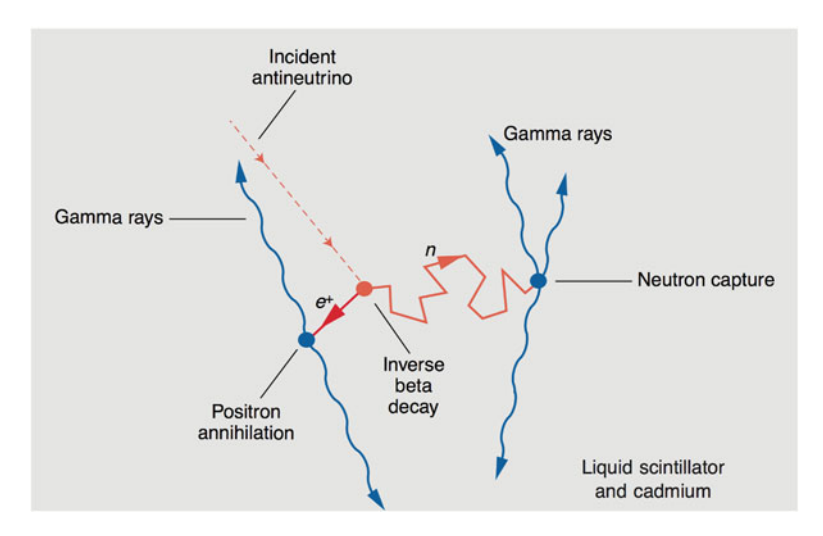


Fig. 2.1 The detection scheme for the first conclusive demonstration of the existence of the neutrino. Image from [7]

action with the weak operator (or, more intuitively, upon an interaction with a W or Z boson) are the weakly-participating leptonic "flavors" e, μ , and τ . The other eigenstate that governs the behavior of the neutrino is its Hamiltonian state. This describes the physical propagation of the neutrino in time with a definite value of mass. Throughout this work, the interaction eigenstate is often referred to as the weak, or flavor, state, just as the Hamiltonian state is equated with the propagation, or mass, eigenstate.

For most fundamental particles, their interaction and Hamiltonian eigenstates are indistinguishable. However, nothing demands this be the case, and a divergence between the states has been observed in two sectors: quarks and neutrinos. A helpful way to describe the relationship between the flavor and Hamiltonian eigenstates is a unitary mixing matrix U that connects the arbitrary flavor state $|\psi_{\alpha}\rangle$ to the mass states $|\psi_{k}\rangle$: $|\psi_{\alpha}\rangle = \sum_{\alpha} U_{\alpha k}^{*} |\psi_{k}\rangle$. Precision measurements of a variety of baryonic weak interactions yield the following approximate relationship between the quark Hamiltonian and flavor states [9]:

$$\begin{pmatrix} \psi_{d'} \\ \psi_{s'} \\ \psi_{b'} \end{pmatrix} = \begin{pmatrix} 0.974 \ 0.225 \ 0.003 \\ 0.225 \ 0.973 \ 0.041 \\ 0.009 \ 0.040 \ 0.999 \end{pmatrix} \begin{pmatrix} \psi_d \\ \psi_s \\ \psi_b \end{pmatrix}, \tag{2.3}$$

where d', s', and b' refer to the quarks of flavor down, strange, and bottom, respectively, and the convention of using d, s, and b for the Hamiltonian states is used. Note that, due to the unitary nature of U, this description of the mixing in terms of the down-type quarks instead of the up-type quarks is arbitrary.

6 2 Neutrino Overview

The same relationship for neutrino mixing, the formalism for which and whose measurements are described in Chap. 3, is given by:

$$\begin{pmatrix} \psi_e \\ \psi_\mu \\ \psi_\tau \end{pmatrix} = \begin{pmatrix} 0.822 & 0.547 & -0.150 \\ -0.356 & 0.704 & 0.614 \\ 0.442 & -0.452 & 0.774 \end{pmatrix} \begin{pmatrix} \psi_1 \\ \psi_2 \\ \psi_3 \end{pmatrix}, \tag{2.4}$$

where the values shown assume the mass hierarchy to be normal and the CP-violating phase δ to be zero (see Chap. 3 for details of both quantities). Equations (2.3) and (2.4) clearly show the flavor and mass eigenstates to be distinct for neutrinos and quarks, but also that the details of this mixing differ greatly between the two species. The origin of these mixing parameters is not understood, and is one of the outstanding issues preventing a fundamental understanding of the weak interaction.

2.3 Flavors of Neutrinos

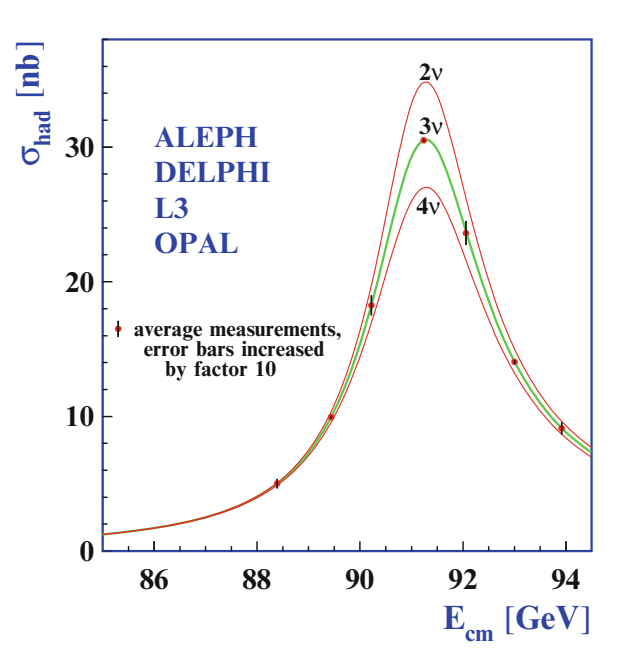
We now know that the creation or annihilation of a charged lepton (e, μ, τ) must also involve either its own charged antiparticle or a neutrino (or antineutrino) of the same flavor $(\nu_e, \nu_\mu, \nu_\tau)$. This certainly did not need to be the case, and the prediction of this lepton conservation symmetry in the Standard Model (SM) did not arrive until decades after the discovery of the neutrino.

Following the discovery of the neutrino, many experiments contributed to the quickly-growing body of knowledge regarding its properties. Likely the most significant in this period, both in terms of the engineering that would become the future of the field and the milestone it represented in the emerging picture of the neutrino, came from the first observation of neutrinos from an accelerator-based beam [10]. The experiments, led by L. Lederman, observed an off-axis flux of neutrinos dominantly created from π^+ decay, the reaction of which was known to proceed via $\pi^+ \to \mu^+ + \nu$. However, unlike in the first observation of the neutrino using a nuclear reactor source, the charged particles that emerged in the detector were negatively charged muons, not positrons. This was particularly compelling because it could have been the case that muons were not created in reactor neutrino interactions simply because their production would not be energetically allowed: the energy of the source ($<10 \,\text{MeV}$) is much less than the muon mass ($\sim105 \,\text{MeV}$). That no positrons or electrons were observed in the accelerator-based experiment conclusively demonstrated the reactor neutrinos to be distinct from those created in π^+ decays. Through the development of the SM, these soon became to be known as electron and muon flavored neutrinos v_e and v_u .

With the discovery of the τ particle in 1975 [11], a third fundamental neutrino was presumed to accompany it. However, the large mass of the τ ($m_{\tau} \sim 1.8 \, \text{GeV}$) and its rapid decay (with a lifetime of $\mathcal{O}\left(10^{-13}\right)$ s) with a number of both hadronic

2.4 Chirality 7

Fig. 2.2 Results from a combined analysis of precision measurements of the Z^0 width. The number of light, active neutrino species is determined to be 2.9840 ± 0.0082 , consistent with direct observations of the ν_e , ν_μ , and ν_τ neutrinos. Figure from [13]



and leptonic modes available made the direct observation of the ν_{τ} particularly challenging. It wasn't until the year 2000 that the particle was experimentally confirmed, when a team observed four candidate ν_{τ} events on a calculated background of 0.34 from an accelerator-based beam of $\sim\!100\,\text{GeV}~\nu_{\tau}$'s [12]. Since then, not more than twenty total ν_{τ} events have been observed, making it one of the least experimentally-probed SM members.

Finally, consistent with the direct observations discussed in this section, precision measurements of the Z^0 boson width has definitively concluded that there exist exactly three neutrino flavors with effective mass less than half the Z^0 mass and whom also participate in the weak interaction [13]. Figure 2.2 presents the measurement of the Z^0 width.

2.4 Chirality

In the same year the neutrino was discovered, another paramount experimental result revealed an unexpected aspect of the weak interaction. Using a magnetic field to polarize the spin of a collection of unstable 60 Co atoms, the observed direction of the emitted electron in the β -decay reaction was nearly always opposite to the direction of the aligned spin of the parent nuclei [14]. The nearly-perfect anti-correlation between the nuclei spins and the electron direction indicated that the mirror-symmetry of parity is violated in weak interactions. It had been suggested previously that the parity symmetry in the weak interaction need not be strictly

8 2 Neutrino Overview

conserved [15], but the experimental evidence concluded that parity violation was *maximal*. The implication for the behavior of observable neutrinos was clear: to balance the spin and momentum of the reaction, the observed kinematics of the electron dictate that it must be accompanied by an antineutrino with a definite alignment between its momentum and spin vectors. These data were ambiguous between the two vectors being aligned or anti-aligned for the neutrino, but a few years later a clever technique was executed to measure this correlation: observations of the polarization of de-excitation photons following orbital electron capture on nuclei determined the spin and momentum vectors for the neutrino to be anti-aligned [16]. The inner product between a particle's spin and momentum at any instant is known as it's helicity, and the natural preference for helicity values (if any) is the more fundamental quantity of chirality. Thus, using the mechanical analogy of ordinary screws, the chirality of leptons in the weak interaction is left-handed, while (via the CPT theorem) anti-leptons are right-handed.

One of the direct consequences of neutrino oscillations is the implication of non-zero neutrino mass. With non-zero neutrino mass, it is in principle possible to boost to a frame with velocity v such that $v_v < v < c$, in which a neutrino (antineutrino) would have positive (negative) helicity.

Worth noting, the correlation between chirality and helicity is perfect for massless particles and decreases sharply for those of non-zero mass, and so the production of positive helicity e^- is much more allowed relative the emission of negative-helicity antineutrinos. A consequence of this suppression that is crucial to the experimental neutrino program is that the electronic decay of pions $(\pi \to e + \nu_e)$ relative to the muonic decay $(\pi \to \mu + \nu_\mu)$ is suppressed by approximately $(m_e/m_\mu)^2 \left(\frac{m_\pi^2 - m_e^2}{m_\pi^2 - m_\mu^2}\right)^2 \sim 1.2 \times 10^{-4}$. This allows for high-purity sources of ν_μ and $\bar{\nu}_\mu$ from the decay of pions in accelerator environments, and the control of the beam energy and propagation distance afforded by these artificial sources has made this the standard for probing neutrino oscillation physics.

2.5 Magnetic Moment

Non-zero neutrino mass allows for the possibility of a magnetic moment. Though electrically neutral, electromagnetic properties of neutrinos may be accessed through magnetic couplings with photons in loop diagrams. Much like neutrino mass, the magnetic moment would be a property intrinsic to the Hamiltonian eigenstate, and therefore observations of magnetic moments through weak interactions probe superpositions of the true quantities. This relationship can be described as [17]:

$$\mu_{\alpha}^{2} = \sum_{i} \left| \sum_{k} U_{\alpha k} e^{-iE_{k}L} \mu_{jk} \right|^{2},$$
(2.5)

2.7 Neutrino Sources 9

where j and k index the Hamiltonian eigenstates, U connects the Hamiltonian eigenstates to the flavor state α , E and L are the energy and travel distance of the neutrino, respectively, and μ_{jk} describes the coupling of the mass eigenstates to the electromagnetic field.

As a calculable SM process, the neutrino-electron elastic scattering channel $\nu_{\alpha} + e \rightarrow \nu_{\alpha} + e$ is typically used to search for the neutrino's magnetic moment. Evidence of an electromagnetic coupling between the neutrino and electron would present itself as events in excess of the predicted cross section or a distortion in the recoiling electron spectrum.

Many searches for the neutrino magnetic moment have been executed using astrophysical data [18–20] and more direct observations of neutrinos from solar [21], accelerator [22], reactor [23], and supernova [24] sources. The current best limit on the effective magnetic moment for any neutrino species comes from observations of reactor $\bar{\nu}_e$'s, where it was found $\mu_{\bar{\nu}_e} < 7.4 \times 10^{-11} \,\mu_B$, where $\mu_B = e/2m_e$ (using natural units) is the Bohr magneton, at 90 % confidence level (C.L.) [25].

2.6 Absolute Mass

From neutrino oscillation observations, the mass of at least two of the neutrino states is known to be non-zero, but the sensitivity of various experimental tests have not yet reached the level of precision required to measure their values. Also known from neutrino oscillations, the most massive state is greater or equal to $\sqrt{\Delta m_{32}^2} \sim 0.05 \, \text{eV}$. Meanwhile, observations of cosmological radiation set an upper limit on the sum of active neutrino masses of $\sum m_{\nu} < 0.2$ –0.4 eV at 95 % C.L., where the limit depends on assumptions used to analyze the Lyman- α data [26]. One of the current prospects in probing lower mass regions involves the very interaction that led to the neutrino's discovery: β decay. As suggested by Eq. (2.2), the endpoint of the β decay spectrum is sensitive to the mass of the $\bar{\nu}_e$. This measurement would give the effective mass of the $\bar{\nu}_e$, which is a superposition of the true mass states according to their coupling with the electron-flavor neutrino. Currently the best limit based on observations of the endpoint of the β decay spectrum is $m_{\nu_e} < 2.3 \, \text{eV}$ (95 % C.L.) [27], while the next-generation experiments aim to achieve sub-eV precision [28, 29].

2.7 Neutrino Sources

Though the neutrino remains rather poorly understood, many natural and artificial sources spanning an immense energy range are available to continue to probe its nature. Figure 2.3 shows the various neutrino sources and their approximate spectral contributions.

10 2 Neutrino Overview

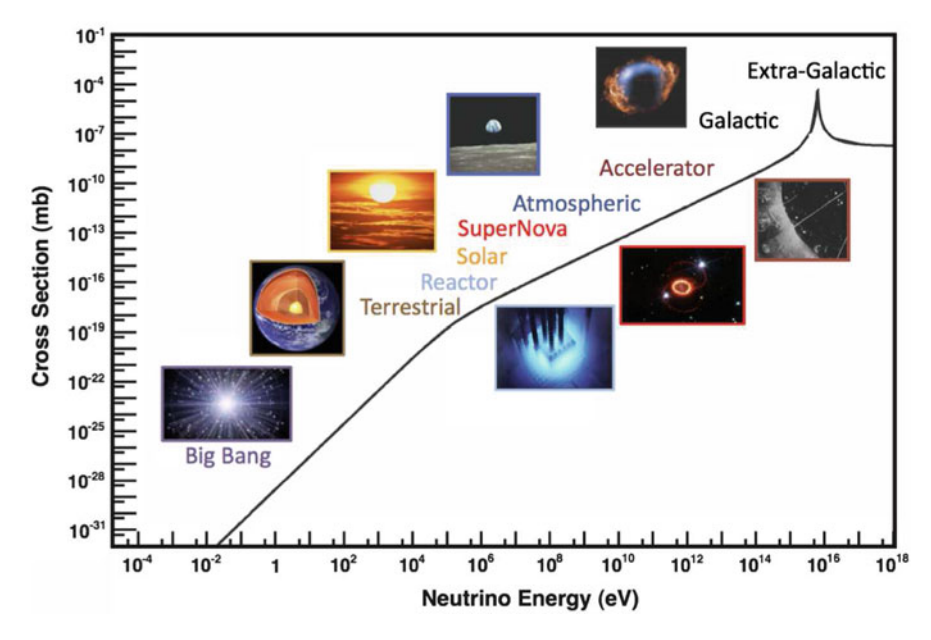


Fig. 2.3 Summary of the various prolific neutrino sources in the universe. The cross section for $\bar{\nu}_e + e^- \rightarrow \bar{\nu}_e + e^-$ is shown for comparison. Reprinted with permission from J.A. Formaggio and G.P. Zeller [30]. Copyright 2012 by the American Physical Society. The following statement applies to all APS-copyrighted material throughout this text: Readers may view, browse, and/or download material for temporary copying purposes only, provided these uses are for noncommercial personal purposes. Except as provided by law, this material may not be further reproduced, distributed, transmitted, modified, adapted, performed, displayed, published, or sold in whole or part, without prior written permission from the American Physical Society

Generally, technology for direct neutrino detection is most effective for neutrinos of energy $\sim 10^6 - 10^{11}$ eV. While we have learned a great deal from observations of this energy range, Fig. 2.3 suggests there are many opportunities to expand this knowledge using freely available neutrinos. It may be possible to learn more not only about the neutrino, but there may be rich physics in their production mechanisms as well.

As an example, a preliminary analysis of two neutrino events of energy $> 10^{12} \, \text{eV}$ was recently reported [31]. These neutrinos have the highest energy ever recorded, and their origin is not clear [32, 33]. At the low end of the spectrum, neutrino remnants from the Big Bang are predicted to *still* permeate the universe at a density of $\sim 100 \, \text{cm}^{-3}$. Figure 2.3 shows the cross section for these neutrinos are many orders of magnitude below the currently-accessible range; however, if these neutrinos could be observed, it would be a fantastic addition to the body of evidence for the birth of our universe.

References 11

References

1. A. Lightman, *The Discoveries: Great Breakthroughs in Twentieth-Century Science, Including the Original Papers* (Alfred A. Knopf, Toronto, 2005), p. 8

- 2. C.D. Ellis, W.A. Wooster, The continuous spectrum of β -rays. Nature **119**, 563 (1927)
- C. Sutton, Spaceship Neutrino (Cambridge University Press, Cambridge, 1992) (As quoted by F. Reines in the Foreword)
- 4. E. Fermi, Versuch einer theorie der β -strahlen. Z. Phys. **88**, 161 (1934)
- 5. E. Fermi, tentativo di una teoria dei raggi β . Nuovo Cimento 11, 1 (1934)
- F. Reines, C. Cowan, The Reines-Cowan experiments: detecting the poltergeist. Los Alamos Sci. 25, 3 (1997)
- 7. N.G. Cooper, Celebrating the neutrino Los Alamos Sci. **25**, 1 (1997)
- 8. C.L. Cowan, Jr. et al., Detection of the free neutrino: a confirmation. Science 124, 103 (1956)
- K. Nakamura et al., Review of particles physics: the CKM quark-mixing matrix. J. Phys. G37, 75021 (2010)
- G. Danby et al., Observation of high-energy neutrino reactions and the existence of two kinds of neutrinos. Phys. Rev. Lett. 9, 36 (1962)
- 11. M.L. Perl et al., Evidence for anomalous lepton production in e⁺ e⁻ annihilation. Phys. Rev. Lett. **35**, 1489 (1975)
- 12. K. Kodama et al. [DONUT Collaboration], Observation of tau neutrino interactions. Phys. Lett. **B504**, 218 (2001)
- 13. [ADELPH et al. Collaborations], Precision electroweak measurements on the z resonance. Phys. Rept. **427**, 257 (2006).
- C.S. Wu et al., Experimental Test of parity conservation in beta decay. Phys. Rev. 105, 1413 (1957)
- T.D. Lee, C.N. Yang, Question of parity conservation in weak interactions. Phys. Rev. 104, 254 (1956)
- 16. M. Goldhaber, L. Grodzins, A.W. Sunyar, Helicity of neutrinos. Phys. Rev. 109, 1015 (1958)
- 17. J.F. Beacom, P. Vogel, Phys. Rev. Lett. 83, 5222 (1999)
- S. Dodelson, G. Gyuk, M.S. Turner, Primordial nucleosynthesis with a decaying tau neutrino. Phys. Rev. D49, 5068 (1994)
- G.G. Raffelt, New bound on neutrino dipole moments from globular-cluster stars. Phys. Rev. Lett. 64, 2856 (1990)
- 20. J.M. Lattimer, J. Cooperstein, Phys. Rev. Lett. 61, 23 (1988)
- D.W. Liu et al. [Super-Kamiokande Collaboration], Limits on the neutrino magnetic moment using 1496 days of super-kamiokande-i solar neutrino data. Phys. Rev. Lett. 93, 021802 (2004)
- L.B. Auerbach et al., Measurement of electron-neutrino electron elastic scattering. Phys. Rev. D63, 112001 (2001)
- 23. F. Reines, H.S. Gurr, H. W. Sobel, Detection of $\bar{\nu}_e$ -e scattering. Phys. Rev. Lett. 37, 315 (1976)
- 24. R. Barbieri, R.N. Mohapatra, Limit on the magnetic moment of the neutrino from supernova 1987A observations. Phys. Rev. Lett. **61**, 27 (1988)
- H.T. Wong et al., Search of neutrino magnetic moments with a high-purity germanium detector at the kuo-sheng nuclear power station. Phys. Rev. D75, 012001 (2007)
- 26. A. Goobar et al., The neutrino mass bound from WMAP 3 year data, the baryon acoustic peak, the SNLS supernovae and the Lyman-α forest. JCAP **06**, 019 (2006)
- 27. C. Kraus et al. [Mainz Collaboration], Eur. Phys. J. C40, 447 (2005)
- 28. L. Bornschein et al. [KATRIN Collaboration], Nucl. Phys. A752, 14 (2005)
- 29. S. Kraft-Bermuth et al. [MARE Collaboration], J. Phys. Conf. Ser. 136, 042055 (2008)
- J.A. Formaggio, G.P. Zeller, From eV to EeV: Neutrino cross sections across energy scales. Rev. Mod. Phys. 84, 1307 (2012)

12 2 Neutrino Overview

31. A. Ishihara [for the IceCube Collaboration], Ice cube: ultra high energy neutrinos. A presentation at the Neutrino 2012 conference, Kyoto, 2012. http://neu2012.kek.jp/index.html

- 32. I. Cholis, D. Hooper, On the origin of icecube's pev neutrinos. arXiv:1211.1974
- V. Barger, J. Learned, S. Pakvasa, IceCube PeV cascade events initiated by electronantineutrinos at glashow resonance. arXiv:1207.4571

Chapter 3 Neutrino Oscillations

The phenomenon of neutrino oscillations and its immediate consequence of non-zero neutrino mass is one of the very few particle physics results not predicted by the SM. This chapter describes the discovery of this process, the state of knowledge as of today, and it's phenomenological implications.

3.1 Formalism

Central to any discussion of neutrino oscillations is the divergence between its interaction and Hamiltonian eigenstates, an introduction to which is given in Sect. 2.2. The state of the neutrino accessible by experiments is the interaction eigenstate, which is typically determined by the flavor of charged lepton produced as a result of charged current (CC) interactions $(v_l + X \rightarrow l + X', l = e, \mu, \tau)$. If the mechanism through which the neutrino is created is known precisely, then the weak eigenstate at the time of creation is also known. To characterize neutrino oscillations we must dynamically describe the connection between creation and detection. Since the neutrino propagates in its Hamiltonian eigenstate, we begin there. The neutrino with mass eigenstate i will evolve in time according to the time-dependent Schröedinger equation:

$$i\frac{\partial}{\partial t}|\psi_{i}(t)\rangle = \hat{H}|\psi_{i}(t)\rangle = \sqrt{\left(p_{i}^{2} + m_{i}^{2}\right)}|\psi_{i}(t)\rangle = p_{i}\sqrt{1 + \frac{m_{i}^{2}}{p_{i}^{2}}}|\psi_{i}(t)\rangle$$

$$\approx \left(E + \frac{m_{i}^{2}}{2E}\right)|\psi_{i}(t)\rangle \tag{3.1}$$

where natural units of $\hbar = c = 1$ are used, p is the neutrino momentum and m its mass. The neutrino is assumed to travel through free space, and as its mass is much smaller than its momentum for all practical applications, terms of order two

and higher in (m_i^2/p_i^2) in the expansion are ignored. This also implies the neutrino energy $E \approx p_i$ for each mass state *i*. A solution to this first-order differential equation is immediately apparent:

$$|\psi_i(t)\rangle = e^{-i\left(E + m_i^2/2E\right)t} |\psi_i(0)\rangle. \tag{3.2}$$

This form is particularly convenient because the only time a neutrino's propagation eigenstate corresponds exactly to a single flavor eigenstate occurs in coincidence with its creation. Choosing t=0 as the time of a weak interaction to create a neutrino of flavor eigenstate α , the propagation state i can be written as:

$$|\psi_i(0)\rangle = |\psi_\alpha\rangle = \sum_k U_{\alpha k}^* |\psi_k\rangle$$
 (3.3)

where the arbitrary unitary matrix U describes the coupling between the propagation and interaction eigenstates. If the propagation and interaction eigenstates were identically equal, U would simply be the identity matrix and neutrinos would not oscillate. Substituting Eq. (3.3) into Eq. (3.2) and again exploiting the assumption of negligible neutrino mass compared to its energy so that $t \approx L$, where L is the distance propagated in time t, we find the probability density of a neutrino created in weak eigenstate α after traveling a distance L to be:

$$|\psi_{\alpha}(t=L)\rangle = \sum_{\beta} \left(\sum_{k} U_{\alpha k}^{*} e^{-i\left(E + m_{i}^{2}/2E\right)L} |\psi_{k}\rangle U_{\beta k} \right) |\psi_{\beta}\rangle, \qquad (3.4)$$

where β also indexes the weak eigenstates. Now we can write the probability for a neutrino created in weak eigenstate α to be detected in state β as a function of only its energy and the distance traversed:

$$P\left(\psi_{\alpha} \to \psi_{\beta}\right) = \left|\left\langle\psi_{\beta} \middle| \psi_{\alpha}(L)\right\rangle\right|^{2} = \left|\sum_{k} U_{\alpha k}^{*} U_{\beta k} e^{-i\left(E + m_{i}^{2}/2E\right)L}\right|^{2}$$

$$= \sum_{k j} U_{\alpha k}^{*} U_{\beta k} U_{\alpha j} U_{\beta j}^{*} \exp\left(-i\frac{\Delta m_{k j}^{2} L}{2E}\right)$$

$$= \delta_{\alpha \beta} - 4 \sum_{k > j} \operatorname{Re}\left[U_{\alpha k}^{*} U_{\alpha j} U_{\beta k} U_{\beta j}^{*}\right] \sin^{2}\left(\frac{\Delta m_{k j}^{2} L}{4E}\right)$$

$$+2 \sum_{k > j} \operatorname{Im}\left[U_{\alpha k}^{*} U_{\alpha j} U_{\beta k} U_{\beta j}^{*}\right] \sin\left(\frac{\Delta m_{k j}^{2} L}{2E}\right) \tag{3.5}$$

3.1 Formalism 15

where $\Delta m_{kj}^2 \equiv m_k^2 - m_j^2$ is referred to as the "mass splitting" between the Hamiltonian eigenstates ψ_k and ψ_j , and the unitary nature of the matrix U is used in the last step.

Equation (3.5) is valid for any number of neutrino species; in the next two sections we consider the case of three and two species. Three neutrino species is consistent with direct observations of neutrino flavors (Sect. 2.3), and the study of two species is particularly instructive to understand oscillatory behavior and also gives an excellent approximation for most experimental probes of the phenomenon.

3.1.1 Three-Neutrino Mixing

With three observed flavors of neutrinos ($\psi_{\alpha} = \psi_{e}, \psi_{\mu}, \psi_{\tau}$), it is natural to assume there also exist three Hamiltonian eigenstates ($\psi_{i} = \psi_{1}, \psi_{2}, \psi_{3}$). This is analogous to the observed mixing in the quark sector. Though many parametrizations of the mixing matrix U are possible, the canonical choice follows the form of the quark-mixing matrix. Under this choice it is referred to as the Pontecorvo-Maki-Nakagawa-Sakata (PMNS) matrix. Using the PMNS matrix, the flavor states are related to the Hamiltonian states by:

$$\begin{pmatrix} \psi_e \\ \psi_\mu \\ \psi_\tau \end{pmatrix} = \begin{pmatrix} c_{12}c_{13} & s_{12}c_{13} & s_{13}e^{-i\delta} \\ -s_{12}c_{23} - c_{12}s_{23}s_{13}e^{i\delta} & c_{12}c_{23} - s_{12}s_{23}s_{13}e^{i\delta} & s_{23}c_{13} \\ s_{12}s_{23} - c_{12}c_{23}s_{13}e^{i\delta} & -c_{12}s_{23} - s_{12}c_{23}s_{13}e^{i\delta} & c_{23}c_{13} \end{pmatrix} \begin{pmatrix} \psi_1 \\ \psi_2 \\ \psi_3 \end{pmatrix}, \quad (3.6)$$

where $c_{ij} \equiv \cos\left(\theta_{ij}\right)$ and $s_{ij} \equiv \sin\left(\theta_{ij}\right)$ are trigonometric functions of the amplitude for mixing between the Hamiltonian eigenstates i and j, and δ is an arbitrary phase that allows for neutrinos to oscillate differently than antineutrinos [1]. Under the assumptions of $m_3 > m_1$ and $\delta = 0$, the values of the PMNS matrix are given in Eq. (2.4). An advantage of the U^{PMNS} matrix is that it may be factored to isolate the effects of each mixing angle θ_{ij} :

$$U^{\text{PMNS}} = \begin{pmatrix} 1 & 0 & 0 \\ 0 & \cos(\theta_{23}) & \sin(\theta_{23}) \\ 0 - \sin(\theta_{23}) & \cos(\theta_{23}) \end{pmatrix} \times \begin{pmatrix} \cos(\theta_{13}) & 0 & \sin(\theta_{13})e^{-i\delta} \\ 0 & 1 & 0 \\ -\sin(\theta_{13})e^{i\delta} & 0 & \cos(\theta_{13}) \end{pmatrix} \times \begin{pmatrix} \cos(\theta_{12}) & \sin(\theta_{12}) & 0 \\ -\sin(\theta_{12}) & \cos(\theta_{12}) & 0 \\ 0 & 0 & 1 \end{pmatrix}.$$
(3.7)

As will be described further, most experimental data are consistent with the existence of exactly three Hamiltonian eigenstates and three weakly-interacting neutrinos whose effective mass state lies well below the Z^0 boson mass of \sim 91 GeV. Under these conditions, the PMNS matrix fully describes the phenomenon of

neutrino oscillations. However, some experimental evidence supports the existence of additional Hamiltonian eigenstates. The strongest hints come from the LSND [2] and MiniBooNE [3] experiments. If these signals are confirmed, the PMNS matrix would have to be significantly extended to accommodate the additional degrees of freedom [4]. Data from these experiments and their implications are further discussed in Sect. 3.2.4.

3.1.2 Two-Neutrino Mixing

In the case of only two neutrino flavor (α, β) and Hamiltonian (1, 2) eigenstates, the matrix U can be expressed in terms of a single mixing angle θ :

$$\begin{pmatrix} \psi_{\alpha} \\ \psi_{\beta} \end{pmatrix} = \begin{pmatrix} \cos\theta & \sin\theta \\ -\sin\theta & \cos\theta \end{pmatrix} \begin{pmatrix} \psi_{1} \\ \psi_{2} \end{pmatrix}, \tag{3.8}$$

With this simplified mixing matrix, the arbitrary oscillation probability (Eq. (3.5)) reduces to:

$$P\left(\psi_{\alpha} \to \psi_{\beta}\right) = \delta_{\alpha\beta} - \sin^2 2\theta \, \sin^2 \left(1.267 \frac{\Delta m^2 L}{E}\right),\tag{3.9}$$

where the units of $\Delta m^2 = m_1^2 - m_2^2$, L and E are eV², km, and GeV, respectively, and the factor of 1.267 incorporates numerical constants including the factors of \hbar and c ignored previously. Even a cursory examination of Eq. (3.9) shows how the oscillation parameters Δm^2 and θ affect the experimental signature L and E: the amplitude of the oscillation probability is proportional to θ , while Δm^2 sets the frequency for oscillation as a function of the ratio L/E.

The consequences of Eq. (3.9) are worth a few more remarks:

- for a given mixing amplitude θ , the oscillation probability is maximized for $L/E \sim (\Delta m^2)^{-1}$. This informs experimentalists how to choose the parameters L and E to gain sensitivity to a certain region of mass splitting Δm^2 . It follows that if the employed L and E are such that $\Delta m^2 L/E \ll 1$, the effect of Δm^2 on observables will be minimal.
- as $\sin^2\theta$ is an even function in its argument, neutrino oscillations are only sensitive to the absolute value of Δm^2 —that is, the more massive state between the two participating Hamiltonian eigenstates cannot be determined from oscillation observations alone.
- if $\Delta m^2 = 0$, $P(\psi_{\alpha} \to \psi_{\beta}) = \delta_{\alpha\beta}$ and neutrinos do not oscillate. This would imply the Hamiltonian eigenstates probed have the same mass, whether zero or non-zero.

• if $\theta = 0$, again $P(\psi_{\alpha} \to \psi_{\beta}) = \delta_{\alpha\beta}$ and neutrinos do not oscillate. This would imply U reduces to the identity matrix and the neutrino interaction and Hamiltonian eigenstates are identically equal.

It follows from the last two observations that an immediate consequence of the confirmation of neutrino oscillations is that there exist at least as many neutrino Hamiltonian states with non-zero mass as the observed number of mass splittings Δm^2 , and the weak and Hamiltonian eigenstates mix. Though the above conditions are most readily recognized with the neutrino oscillation probability under the assumption of only two participating species, they apply equally to the arbitrary case of Eq. (3.5).

As mentioned previously, neutrino oscillations were not predicted in the SM and so the scales of Δm^2 values were completely unconstrained. Fortunately, nature has provided us with two sources of organic neutrinos whose energy E and distance from creation to Earthly detection L is such that their ratio L/E probes two independent neutrino mass splittings. Experiments using artificial neutrino sources such as accelerator-based beams and neutrinos emitted from nuclear reactors have confirmed and refined measurements of these oscillation parameters. Neutrinos from nuclear reactors have very recently also provided measurements of the mixing angle θ_{13} . The experimental evidence for each follows.

3.2 Experimental Evidence for Neutrino Oscillations

Assuming three Hamiltonian eigenstates $(\psi_1, \psi_2, \text{ and } \psi_3)$ and three flavor eigenstates $(\psi_e, \psi_\mu \text{ and } \psi_\tau)$, there exist two independent mass splittings Δm_{12}^2 and Δm_{23}^2 (since $|\Delta m_{13}^2| = |\Delta m_{12}^2 \pm \Delta m_{23}^2|$) that mix with the weak eigenstates through three independent mixing angles and one CP-violating phase. The following presents their current measurements or constraints.

3.2.1 Solar Oscillations

Often referred to colloquially as solar neutrino oscillations, the first experimental hints of any oscillation signature were caused by the Δm_{12}^2 mass splitting and were observed in 1968 [5]. These hints remained a puzzle for more than three decades, when the SNO collaboration [6] provided observations of the entire flux of neutrinos created in solar processes having transmuted into a different flavor composition from creation to detection.

Solar neutrinos are dominantly produced as ν_e 's in the nuclear fusion reaction $p+p \rightarrow {}^2{\rm H} + e^+ + \nu_e$. Because of the low energy of these neutrinos (<10 MeV), only electrons are energetically allowed to be produced in CC interactions. Therefore, if solar neutrinos were oscillating into the ν_μ and ν_τ weak eigenstates,

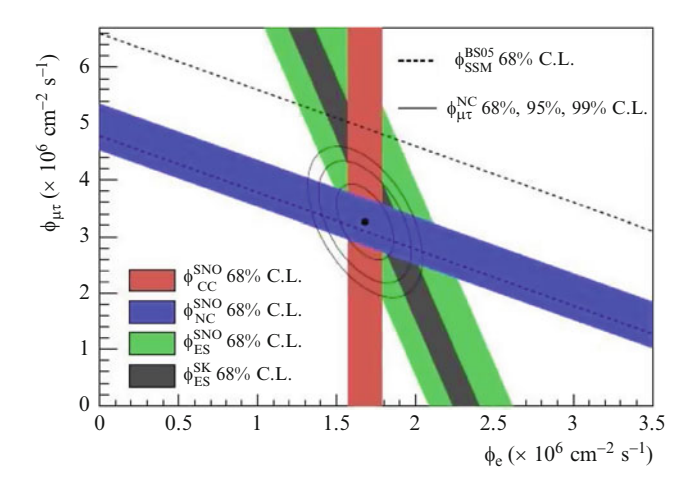


Fig. 3.1 Solar ν_{μ} and ν_{τ} flux versus ν_{e} flux observed by the SNO detector. The Standard Solar Model (SSM) expectation is shown by the band between the dashed lines and shows good agreement with the best-fit of the SNO data, represented by the solid point. Surrounding the best fit mark are 68 %, 95 % and 99 % C.L. contours. Reprinted with permission from B. Aharmim et al. [6]. Copyright 2005 by the American Physical Society

their entire flux as seen on Earth could only be observed using neutral current (NC) interactions. SNO used the novel idea of employing heavy water (2H_2O) as the detection medium to exploit neutron capture on deuterium and observe both NC and CC events:

$$\nu_e + {}^2\text{H} \to p + p + e^-$$
 (CC) (3.10)

$$\nu_{\alpha} + {}^{2}\text{H} \rightarrow p + n + \nu_{\alpha}$$
 (NC)

$$\hookrightarrow +^2 H \to ^3 H + \gamma \tag{3.11}$$

$$\nu_{\alpha} + e^{-} \rightarrow \nu_{\alpha} + \mathbf{e}^{-} \tag{ES}$$

where the particles observed to determine the reaction are in bold. The analysis of these three reactions is summarized in Fig. 3.1. A global fit to these data show they are compatible with $\nu_e \to \nu_\mu, \nu_\tau$ oscillations with parameters $\Delta m_{\rm solar}^2 \sim 10^{-4}~{\rm eV}^2$ and $\theta_{\rm solar} \sim 34^\circ$ [7].

The KamLAND experiment provided an invaluable confirmation of the $(\Delta m_{12}^2, \theta_{12})$ values reported by SNO using an artificial neutrino source [8]. Perhaps more compelling than the confirmation of the oscillation parameters, their data provided the first clear observation of the sinusoidal nature of neutrino oscillations as a function of L/E.

Observing a flux of $\bar{\nu}_e$ from 53 nuclear power reactors in Japan, KamLAND measured the probability for $\bar{\nu}_e$ disappearance using the inverse β decay reaction $\bar{\nu}_e + p \rightarrow e^+ + n$. The strong correlation between the positron and the incident

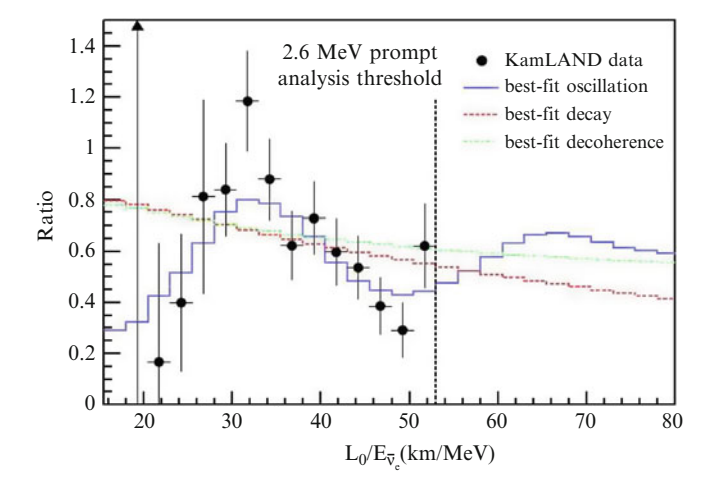


Fig. 3.2 KamLAND $\bar{\nu}_e$ disappearance results. The ratio shown is the observed data relative to the no-oscillation hypothesis, and the distribution clearly favors the sinusoidal form of neutrino oscillation over alternatives. Reprinted with permission from T. Araki et al. [8]. Copyright 2005 by the American Physical Society

antineutrino energy and direction allowed for a measurement of the oscillation probability with the ratio L/E, clearly supporting the trigonometric form of Eq. (3.9). This is shown in Fig. 3.2, and the results of a fit for the oscillation parameters including these and the SNO data are presented in Fig. 3.3. Consistency in the observed oscillatory behavior between the $\bar{\nu}_e$'s at KamLAND and the solar ν_e 's observed at SNO supports the CPT theorem. The fit finds $\Delta m_{\rm solar}^2 = 7.9_{-0.5}^{+0.6} \times 10^{-5}$ eV² and $\theta_{\rm solar} = 32.3_{-2.4}^{+3.0}$ ° [8]. A update to this analysis using additional data from both experiments yields the most sensitive measurements of the solar oscillation parameters to date: $\Delta m_{\rm solar}^2 = 7.59_{-0.21}^{+0.20} \times 10^{-5}$ eV² and $\theta_{\rm solar} = 34.06_{-0.84}^{+1.16}$ ° [9].

Notice we are being careful to refer to these oscillation parameters as "solar" instead of as the mixing between two mass eigenstates. In principle, every observed oscillation is affected by all oscillation modes, and so a single set of observed oscillation parameters are highly degenerate in interpretations of the mass splittings and mixing angles chosen by nature. However, we will see in the following sections that the confirmed mass splittings are sufficiently separated to eventually refer to these solar parameters as the mixing between only two Hamiltonian states to excellent approximation.

3.2.2 Atmospheric Oscillations

Cosmically-produced high energy protons, electrons and stable nuclei collide with Earth's upper atmosphere and produce a flux of neutrinos through pion and muon

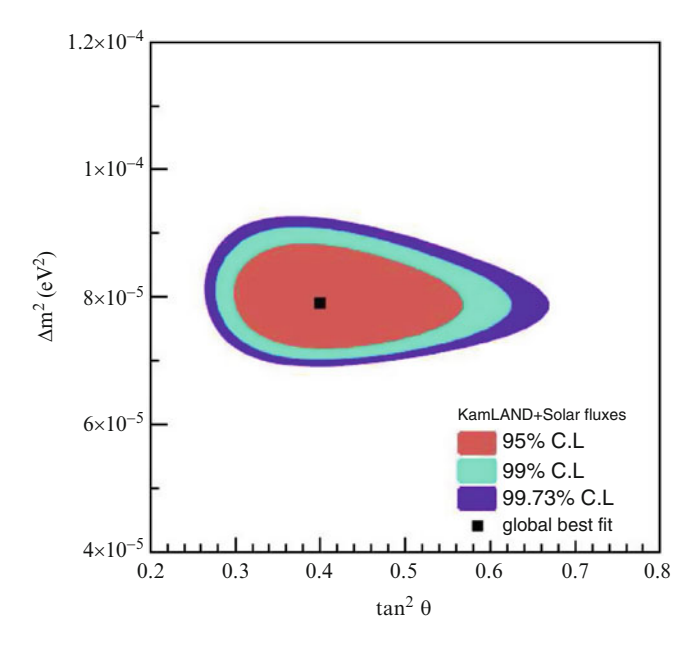


Fig. 3.3 Results from a fit to the KamLAND and solar neutrino data to the oscillation parameters $\Delta m_{\rm solar}^2$ and $\theta_{\rm solar}$. Figure taken from [8]

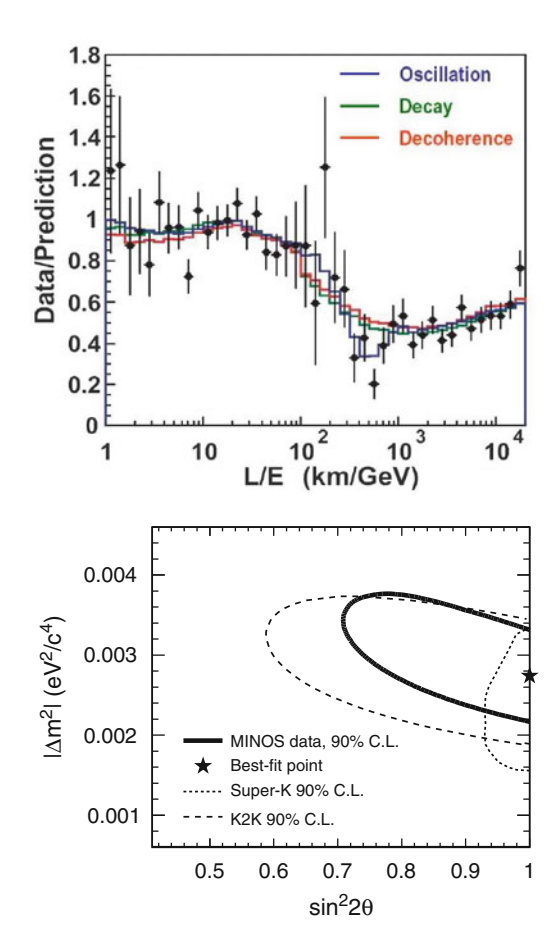
decay sufficiently intense to be studied on Earth. The Kamiokande detector in Japan [10] was originally designed to search for proton decay, but the secondary physics goal of atmospheric neutrino studies proved much more interesting. As in the puzzle of solar neutrino flux discussed in the previous section, expectations of the neutrino content were not met: the observed ratio ν_{μ}/ν_{e} was significantly lower than predicted [10]. Super-Kamiokande succeeded Kamiokande and featured upgrades that allowed for CC measurements of ν_{μ} and ν_{e} interactions as a function of neutrino travel distance. Knowledge of the neutrino propagation length was possible through the strong correlation between the direction of the observed charged lepton in CC interactions and the origin of the incident neutrino.

The ratio of observed ν_{μ} CC events relative to the no-oscillation hypothesis from Super-Kamiokande detector as a function of L/E is shown in Fig. 3.4. A fit to the two-neutrino oscillation hypothesis using these data yields $1.9 \times 10^{-3} < \Delta m_{\rm atm}^2 < 3.0 \times 10^{-3}$ and $\sin^2 2\theta_{\rm atm} > 0.90$ at 90% C.L [11].

Independent confirmation of these oscillation parameters come from the K2K [12] and MINOS [13] experiments, by observing fluxes of accelerator-based neutrino beams at multiple positions along the line of neutrino travel. Motivated by the Super-Kamiokande observations, the neutrino beam energies and detector positions were chosen such that L and E were distinct between the two experiments but the ratio L/E for both K2K and MINOS afforded sensitivity to $\Delta m^2 \sim 10^{-3}\,\mathrm{eV}^2$. With such control over the oscillation region explored by

Fig. 3.4 Data from the Super-Kamiokande experiment clearly showing an L/E dependence of the observed ν_{μ} flux relative to the prediction assuming no oscillations. Reprinted with permission from Y. Ashie et al. [11]. Copyright 2004 by the American Physical Society

Fig. 3.5 Summary of oscillation fits to data sensitive to $\Delta m^2 \sim 10^{-3} \text{ eV}^2$. Reprinted with permission from P. Adamson et al. [13]. Copyright 2008 by the American Physical Society



this experimental setup, this method for searching for neutrino oscillations has since become the community standard. Both experiments observed deficits in the observed flux of ν_{μ} consistent with $\Delta m^2 \sim 10^{-3} \, \mathrm{eV^2}$, and the C.L. regions from K2K, MINOS, and Super-Kamiokande are shown in Fig. 3.5. A more recent fit to world data sensitive to this mass splitting gives $|\Delta m_{\mathrm{atm}}^2| = 2.43_{-0.10}^{+0.06} \times 10^{-3} \, \mathrm{eV^2}$ and $\sin^2\theta_{\mathrm{atm}} = 0.386_{-0.014}^{+0.024} \, [14]$.

3.2.3 θ_{13} and δ Oscillations

As mentioned previously, the magnitude of the mass splitting Δm_{13}^2 is constrained by $|\Delta m_{13}^2| = |\Delta m_{12}^2 \pm \Delta m_{23}^2|$, where the states either add or subtract depending on the unknown mass hierarchy (discussed in Sect. 3.3). Considering the separation in the values $\Delta m_{\rm sol}^2 \sim 10^{-5}\,{\rm eV}^2$ and $\Delta m_{\rm atm}^2 \sim 10^{-3}\,{\rm eV}^2$, $|\Delta m_{13}^2| \sim \Delta m_{\rm atm}^2$ to

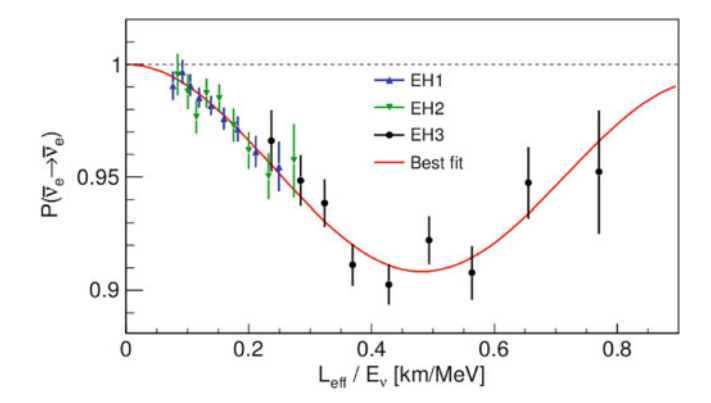


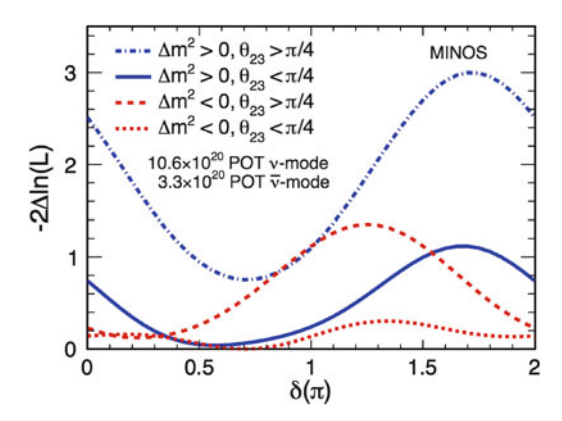
Fig. 3.6 Observed $\bar{\nu}_e$ flux at the various Daya Bay experimental halls (EH) as a function of distance from the $\bar{\nu}_e$ source relative to the prediction assuming no oscillations. The inset shows the compatibility of the data for various values of $\sin^2 2\theta_{13}$, clearly ruling out $\theta_{13} = 0$ at greater than 5σ C.L. Reprinted with permission from F.P. An et al. [20]. Copyright 2014 by the American Physical Society

good approximation. However, the mixing angle between the (1,3) Hamiltonian eigenstates is unconstrained by the other oscillation parameters and must be independently determined.

The θ_{13} mixing angle is the most recently measured and confirmed oscillation parameter, its measurement coming last mostly because its diminutive size leads to more subtle effects compared to the other mixing amplitudes. While the accelerator-based experiments MINOS [15] and T2K [16] provided indications that its value is non-zero through $\nu_{\mu} \rightarrow \nu_{e}$ conversions, it was observations of reactor $\bar{\nu}_{e}$ disappearance with the Daya Bay [17] and Reno [18] experiments that provided the first measurements of θ_{13} . The Daya Bay experiment uses an impressive number of nearly-identical detectors to measure the reactor $\bar{\nu}_{e}$ flux at a variety of distances, and as shown in Fig. 3.6, clearly observes $\bar{\nu}_{e}$ disappearance. This measurement is the most precise to date and finds $\sin^{2} 2\theta_{13} = 0.089 \pm 0.011$ [19].

The neutrino transitions affected by δ and the sign of Δm_{13}^2 are most readily experimentally accessible through a comparison of $P\left(\nu_{\mu} \to \nu_{e}\right)$ with $P\left(\bar{\nu}_{\mu} \to \bar{\nu}_{e}\right)$. These probabilities cannot be reasonably approximated by the two-neutrino case, as all three mixing angles and mass splittings contribute significantly to the process [21]. Though this indicates Eq. (3.9) is less helpful here, the experimental sensitivity to these transitions are still governed principally by the appropriate ratio of L/E, and in this case is $\mathcal{O}\left(\frac{10\text{m}}{10^{3}\text{eV}}\right)$. To allow for reasonable production phase-space for the observation of the muon in ν_{μ} CC interactions, E must be $\mathcal{O}(1\text{ GeV})$, setting L of $\mathcal{O}(10^{9}\text{ m})$. This distance is roughly an order of magnitude longer than any previous observations of artificial sources. As the neutrino flux is roughly proportional to $1/L^2$ at large distances from the source, it will be enormously challenging to achieve the beam power and detection precision required to probe values of δ .

Fig. 3.7 Constraints on δ for various assumptions on the sign of Δm^2 and the value of θ_{23} from the MINOS experiment. It will be shown that the θ_{23} is nearly identical to θ_{atm} . Reprinted with permission from P. Adamson et al. [15]. Copyright 2013 by the American Physical Society



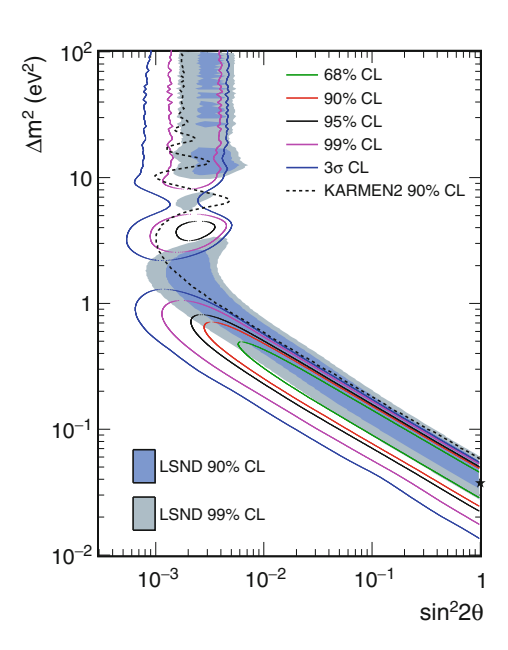
Currently the only constraints on δ come from the MINOS [15] experiment, and are shown in Fig. 3.7. It can be seen that no value of δ for either sign of Δm_{13}^2 (referred to in the figure simply as Δm^2) is strongly preferred over others.

The determination of the sign of Δm_{13}^2 and precision measurements of δ is currently at the forefront of today's experimental neutrino program, and may dominate the high-energy physics landscape in the US for decades. Current experiments NOvA [22] and T2K, and later LBNE [23], will lead the search by comparing $P(\nu_{\mu} \rightarrow \nu_{e})$ with $P(\bar{\nu}_{\mu} \rightarrow \bar{\nu}_{e})$ using few-GeV beams of ν_{μ} and $\bar{\nu}_{\mu}$. One of the challenges that must be met before a clean measurement of δ is possible is a high-precision understanding of the fundamental contributing ν_{μ} and $\bar{\nu}_{\mu}$ interactions at this energy range. The work presented in this dissertation provides a first measurement of $\bar{\nu}_{\mu}$ cross sections below 1 GeV and thus significantly advances the community's preparedness to search for CP violation with neutrinos.

3.2.4 Hints for $\Delta m^2 \sim 1 eV^2$

One of the major outstanding questions in neutrino physics is the existence of another mass splitting in the range of $\Delta m^2 \sim 1\,\mathrm{eV}^2$. As with the other mixing parameters, this hypothesis is entirely experimentally-driven. The first indication came from the LSND experiment, where an excess of $\bar{\nu}_e$ events were observed from a stopped-pion $\bar{\nu}_\mu$ source [2]. As with the accelerator-based confirmations of the solar mixing described in Sect. 3.2.1, the MiniBooNE experiment was designed to provide an independent check of this splitting by probing the same ratio L/E while L and E were themselves distinct from the values used at LSND. An indication of both $\nu_\mu \to \nu_e$ and $\bar{\nu}_\mu \to \bar{\nu}_e$ oscillations were observed in the MiniBooNE data as well [3], however neither of the signals from the two experiments exclude the no-oscillation hypothesis at greater than 4σ . The allowed $(\Delta m^2, \theta)$ regions from both experiments are shown in Fig. 3.8.

Fig. 3.8 Results of a two-neutrino oscillation fit to the combined v_e and \bar{v}_e appearance data from MiniBooNE. Also shown are the LNSD allowed regions and limits from the KARMEN experiment [24]. Figure taken from [3]



Less significant signals indicating $\Delta m^2 \sim 1 \,\mathrm{eV^2}$ come from cosmological observations [25], radioactive source experiments [26], and from reactor antineutrino data [27]. Particularly in light of the implications of such a mass splitting as discussed in the next section, this signal must be rigorously tested in the near future. Proposed experiments to do so include OscSNS [28], nuSTORM [29], and a search using decay-at-rest kaons [30].

3.3 Summary and Outstanding Questions

Noting that the Δm^2 scales discussed in the previous section differ by orders of magnitude, we can drop their conservative solar and atmospheric labels and refer to them as the genuine splitting between neutrino Hamiltonian eigenstates to excellent approximation.¹ Under the suspicion of symmetry between the ordering of the neutrino mass states and that of the other leptons, we refer to the smaller mass splitting as Δm_{12}^2 and the larger splitting as Δm_{23}^2 . The confirmed values for the neutrino mixing parameters are:

¹Note also this is also true if there exists a mass splitting near 1 eV².

$$\Delta m_{12}^2 = -7.59_{-0.21}^{+0.20} \times 10^{-5} \text{ eV}^2 \quad \theta_{12} = 34.06_{-0.84}^{+1.16} \circ \left| \Delta m_{32}^2 \right| = 2.43_{-0.10}^{+0.06} \times 10^{-3} \text{ eV}^2 \sin^2 \theta_{23} = 0.386_{-0.014}^{+0.024} \Delta m_{13}^2 \sim \Delta m_{32}^2 \qquad \theta_{13} = 9.0_{-0.5}^{+0.4} \circ$$
(3.13)

With two independent mass splittings, as least two neutrino mass eigenstates must be non-zero. One of the most important questions about the nature of the neutrino concerns how these masses may be integrated into the SM. This issue is fundamentally tied to whether the neutrino is its own anti-particle, indicating a Majorana nature; if the neutrino and antineutrino are distinct, neutrinos are Dirac particles. For Dirac particles the extension of neutrino mass into the SM is quite simple in that, like other massive particles, the masses are generated by the Higgs field and both left- and right-handed neutrinos and antineutrinos exist. Neutrinos with opposing chirality to the observed states are then not experimentally accessible not because of the nature of the neutrino, but because they only interact through the maximally parity-violating weak interaction.

A popular model of the alternative of Majorana neutrinos is equally viable and offers an explanation of the diminutive scale of the neutrino mass compared to the other fermions. In this model the masses of the light and active neutrinos are accompanied by some number of possibly non-weakly interacting neutrinos N such that the product of the two neutrino family masses are related to the scale of the quark q or charged lepton l families: $m_v m_N \sim m_{q,l}^2$ [31]. In this way, the large mass of the N neutrino provides a counter-balance for the observed neutrinos to be arbitrarily light, and this model is therefore referred to as the See-Saw mechanism.

Currently, the best experimental probe to determine whether the neutrino is Majorana or Dirac involves the neutrino-less double-beta decay reaction $(n + n \rightarrow p + p + e^- + e^-)$. The decay would involve the emission of an $\bar{\nu}_e$ at one vertex of ordinary β decay and it's immediate absorption at a second β decay vertex playing the role of ν_e . Consequently, this process is allowed for Majorana neutrinos but is forbidden if neutrinos are Dirac particles. One experiment has claimed to have observed evidence of this process [32], but this remains unconfirmed.

Another currently-degenerate fundamental property related to the neutrino mass is their hierarchical ordering. From the Mikheyev-Smirnov-Wolfenstein (MSW) effect in solar oscillations, it is known that $m_2 > m_1$, while the ordinal label between the third mass state and the others is arbitrary. As shown in Sect. 3.1, observations of splittings sensitive to only two mass eigenstates reveal only the absolute value of the splitting, and the current neutrino oscillation data are degenerate between the smaller mass splitting separating the two lightest states and the same splitting separating the most massive states. Figure 3.9 pictorially shows this degeneracy in the mass hierarchy along with the approximate mixing amplitudes between each flavor and mass state. As mentioned in Sect. 3.2.3, the mass ordering will be addressed in the current and next round of experiments simultaneously searching for the CP-violating phase δ .

It can be seen in Eq. (3.7) that the CP-violating phase δ is inextricably tied to the mixing angle θ_{13} and therefore the sign of Δm_{13}^2 . The observation of a non-zero

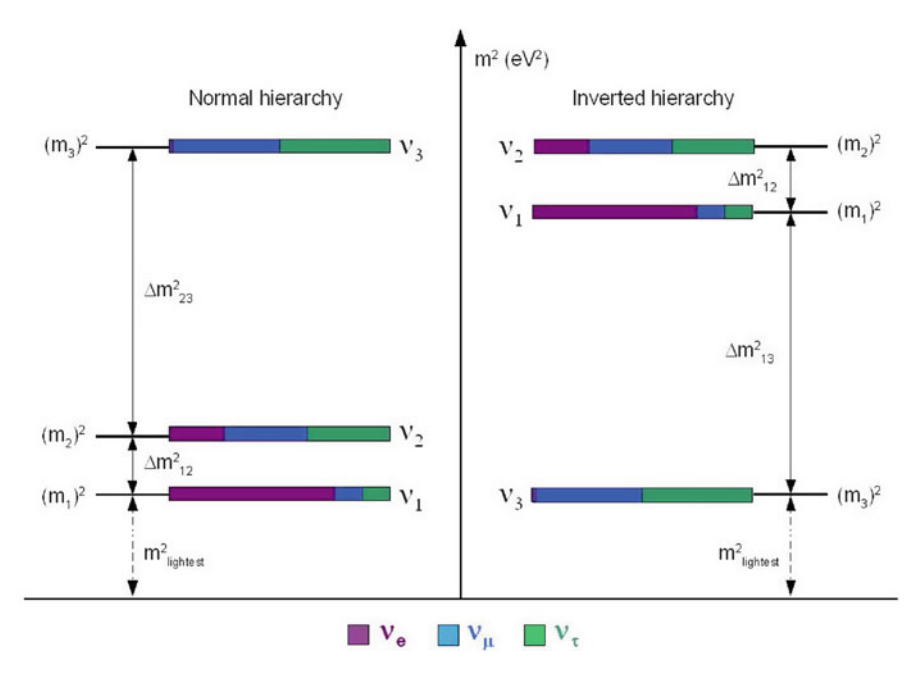


Fig. 3.9 The two possible neutrino mass orderings, shown with their approximate couplings to the flavor states

value for θ_{13} offers the opportunity to search for CP-violation in the lepton sector, which is currently one of the best hypotheses for explaining the baryon asymmetry in the universe [33]. It is worth noting that a sufficiently large value of δ must be accompanied by at least one more species of neutrino, much more massive than the known types, to explain the observed baryon asymmetry. Nevertheless, as the observed CP-violation in the quark sector is far too meager to account for the evolution of our matter-dominated universe [9], searches for the origin of the asymmetry using neutrinos are well-motivated and compelling.

Finally, if confirmed, the experimental hints of another mass splitting presented in Sect. 3.2.4 would imply a fourth neutrino mass state, with a fundamentally different coupling to the weak interaction. If there exists a mass splitting near $1 \, \text{eV}^2$, from the precision constraint of the Z^0 width (shown in Fig. 2.2), it must not directly couple to the weak interaction. From the disconnect between its mass and the interaction states, this hypothesized extra neutrino is known as sterile. Furthermore, arguments based on symmetry between neutrinos and the other fermions would suggest these ought to exist in sets of three, if any, and analyses to global data do mildly prefer the addition of more than a single sterile mass state [4]. This would introduce a litany of extra degrees of freedom in neutrinos oscillations in the form of mass splittings and mixing angles, the signals from which are almost entirely degenerate in current experiments.

References 27

It is clear by now a quantum mechanical process not predicted by the standard model is real and may be a consequence of some deeper laws of physics we do not yet appreciate. Though there are many unknowns in neutrino physics that will presumably lead to a more fundamental understanding of the weak interaction and how it fits into nature, the concrete observation of neutrino oscillations reveal two pieces of information crucial to this quest: that the neutrino mass is non-zero, and that lepton number is not a strictly conserved quantity.

As a final note, it was entirely fortuitous that the community realized the phenomenon of neutrino oscillations. If the nature of oscillations were such that solar and atmospheric neutrinos were unaffected, our ignorance of this process would have persisted for at least many more decades. Therefore, though it appears the community may fully populate the PMNS matrix (Eq. 3.6) with precision measurements in the coming decades, it seems unlikely that this will complete our fundamental understanding of neutrino oscillations.

References

- 1. F. Englert, R. Brout, Phys. Rev. Lett. 13, 321 (1964)
- 2. A. Aguilar et al. [LSND Collaboration], Evidence for neutrino oscillations from the observation of $\bar{\nu}_e$ appearance in a $\bar{\nu}_\mu$ beam. Phys. Rev. D **64**, 112007 (2001). arXiv:0104049
- 3. A. Aguilar et al. [MiniBooNE Collaboration], An improved search for $\bar{\nu}_{\mu} \to \bar{\nu}_{e}$ oscillations in the MiniBooNE experiment. arXiv:1303.2588
- J.M. Conrad et al., Sterile neutrino fits to short baseline neutrino oscillation measurements. arXiv:1207.4765.
- R.J. Davis, D.S. Harmer, K.C. Hoffman, Search for neutrinos from the sun. Phys. Rev. Lett. 20, 1205 (1968)
- 6. B. Aharmim et al. [SNO Collaboration], Electron energy spectra, fluxes, and day-night asymmetries of B-8 solar neutrinos from the 391-day salt phase SNO data set. Phys. Rev. C 72, 055502 (2005). arXiv:nucl-ex/0502021
- M.C. Gonzalez-Garcia, M. Maltoni, Phenomenology of massive neutrinos. arXiv:hep-ph/0704. 1800v2.
- T. Araki et al. [KamLAND Collaboration], Measurement of neutrino oscillation with Kam-LAND: Evidence of spectral distortion. Phys. Rev. Lett. 94, 081801 (2005). arXiv:hep-ex/ 0406035
- 9. B. Aharmim et al. [SNO Collaboration], Low energy threshold analysis of the phase I and phase II data sets of the Sudbury Neutrino Observatory. Phys. Rev. C81, 055504 (2010)
- Y. Fukuda et al. [Kamiokande Collaboration], Atmospheric muon-neutrino / electron-neutrino ratio in the multi-GeV energy range. Phys. Lett. B335, 237 (1994)
- 11. Y. Ashie et al. [Super-Kamiokande Collaboration], Evidence for an oscillatory signature in atmospheric neutrino oscillations. Phys. Rev. Lett. 93, 101801 (2004). arXiv:hep-ex/0404034
- E. Aliu et al. [K2K Collaboration], Evidence for muon neutrino oscillation in an acceleratorbased experiment. Phys. Rev. Lett. 94, 081802 (2005). arXiv:hep-ex/0411038
- P. Adamson et al. [MINOS Collaboration], Study of muon neutrino disappearance using the Fermilab Main Injector neutrino beam. Phys. Rev. D77, 072002 (2008)
- G.L. Fogli et al., Global analysis of neutrino masses, mixings and phases: entering the era of leptonic CP violation searches. Phys. Rev. D 86, 013012 (2012). arXiv:hep-ex/1205.5254
- 15. P. Adamson et al. [MINOS Collaboration], Electron neutrino and antineutrino appearance in the full MINOS data sample. Phys. Rev. Lett. **110**, 171801 (2013)

16. K. Abe et al. [T2K Collaboration], Indication of electron neutrino appearance from an accelerator-produced off-axis muon neutrino beam. Phys. Rev. Lett. **107**, 041801 (2011)

- 17. F.P. An et al. [Daya Bay Collaboration], Phys. Rev. Lett. **108**, 171803 (2012)
- 18. J.K. Ahn et al. [Reno Collaboration], Phys. Rev. Lett. **108**, 191802 (2012)
- 19. F.P. An et al. [Daya Bay Collaboration], Improved measurement of electron antineutrino disappearance at Daya Bay. Chin. Phys. C37, 011001 (2013). arXiv:hep-ex/1210.6327
- 20. F.P. An et al. [Daya Bay Collaboration], Spectral measurement of electron antineutrino oscillation amplitude and frequency at Daya Bay. Phys. Rev. Lett. **112**, 061801 (2014)
- M.C. Gonzalez-Garcia, M. Maltoni, Phenomenology with massive neutrinos. Phys. Rept. 460, 1 (2008)
- D.S. Ayres et al. [NOvA Collaboration], The NOvA Technical Design Report. FERMILAB-DESIGN-2007-01
- V. Barger et al. [LBNE Collaboration], Report of the us long baseline neutrino experiment study. arXiv:0705.4396
- 24. B. Armbruster et al. [KARMEN Collaboration], Phys. Rev. **D65**, 112001 (2002)
- 25. J. Hamann et al., Cosmology favoring extra radiation and sub-eV mass sterile neutrinos as an option. Phys. Rev. Lett. **105**, 181301 (2010)
- C. Giunti, M. Laveder, Short-baseline electron neutrino disappearance, tritium beta decay and neutrinoless Double-Beta Decay. Phys. Rev. D82, 053005 (2010)
- G. Mention et al., The reactor antineutrino anomaly. Phys. Rev. D83, 073006 (2011). arXiv: 1101.2755
- 28. H. Ray for the OscSNS Collaboration. arXiv:0810.3175
- P. Kyberd et al. [nuSTORM Collaboration], nuSTORM: Neutrinos from STORed muons. arXiv:1206.0294
- 30. J. Spitz, Sterile neutrino search with kaon decay at rest. Phys. Rev. **D85**, 093020 (2012)
- 31. M. Gell-Mann, P. Ramond, R. Slansky, PRINT-80-0576-CERN (1980)
- H.V. Klapdor-Kleingrothaus et al. [The Heidelberg-Moscow Collaboration], Evidence for neutrinoless double beta decay. Mod. Phys. Lett. A16, 2409 (2001)
- 33. S. Davidson, E. Nardi, Y. Nir, Phys. Rep. 466, 105 (2008)

Chapter 4 Neutrino Interactions in MiniBooNE

4.1 Overview

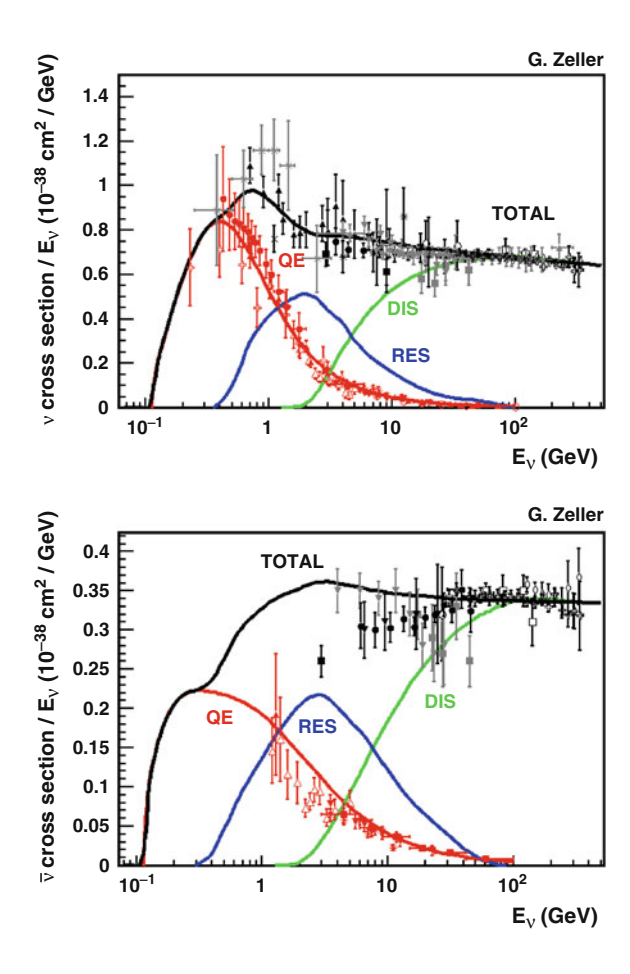
MiniBooNE uses the NUANCE neutrino event generator [1] to predict and simulate neutrino interactions in the detector. NUANCE includes a comprehensive cross-section model which considers known interactions in the neutrino energy range from $\sim\!100\,\text{MeV}$ to 1 TeV. Ninety-nine reactions are modeled separately and combined with nuclear models describing bound nucleon states and final-state interactions to predict event rates and kinematics.

Figure 4.1 shows the expectation and experimental data for ν_{μ} and $\bar{\nu}_{\mu}$ CC interactions across a wide range of energies. As the MiniBooNE fluxes of ν_{μ} and $\bar{\nu}_{\mu}$ are peaked near 700 MeV (Fig. 5.9), the charged-current quasi-elastic (CCQE) and charged-current single pion (CC π) interactions are the most abundant interactions in the MiniBooNE data sets. For this reason, in this chapter we concentrate on the expectations and experimental evidence associated with these processes.

A wealth of information is summarized in Fig. 4.1, and it is important to point out the overall structure of the cross sections and the features most relevant to the measurements executed in this dissertation. When the neutrino energy is large enough to resolve individual quarks, the CC cross section is approximately linear with energy. This behavior is a confirmation of the quark parton model [2], where higher energy probes gain sensitivity to more scattering interactions through the quark sea. This approximation, of course, breaks down at lower energies where elastic interactions are dominant.

Experimentally, Fig. 4.1 shows that these interactions at lower energies feature total error on the order of tens of percent. This is mostly due to experimental difficulties in separating the various contributing processes, a challenge that is unique to the various detector technologies and usually includes dependence on assumptions about the contributing signal and background processes. Finally, the antineutrino cross sections are experimentally known less accurately compared to

Fig. 4.1 Comparison of expectations and experimental data across v_{μ} (top) and \bar{v}_{μ} (bottom) CC interactions. The "QE" and "RES" labels here are referred to as CCQE and CC π interactions in the text. Figure from [30]



the analogous neutrino processes, and in particular there are no antineutrino CC cross-section measurements below 1 GeV. The lower precision and more sparse antineutrino data is due in general to a number of effects, most notably relatively larger backgrounds and low statistics. The measurements in this dissertation break significant ground on both experimental challenges: Chap. 7 presents a first demonstration of a set of techniques to statistically measure a background typical of artificial beams of antineutrinos, and Chap. 8 presents an analysis of antineutrino interactions with more than an order of magnitude of higher statistics compared to all other previously-published antineutrino cross-section measurements *combined*. In addition, the average antineutrino energy for these measurements is 650 MeV, and so these data are sensitive to an almost entirely unprobed energy region.

4.2 CCQE 31

4.2 CCQE

The CCQE process $(v_l + n \rightarrow l^- + p)$ for neutrinos, and $\bar{v}_l + p \rightarrow l^+ + n$ for antineutrinos) is the most abundant interaction at the MiniBooNE energy range, accounting for ~40% of interactions in the detector. It is typically used as the signal process in neutrino oscillation measurements due to its simple multiplicity, and also the ability to reconstruct the incident neutrino energy, under a few important assumptions, based solely on observations of the charged lepton (Chap. 6). Typically credited to Llewellyn-Smith [3], the differential cross section for this process assuming the exchange of a single W boson as a function of the momentum transfer O^2 is:

$$\frac{d\sigma}{dQ^2} = \frac{M^2 G_F^2 |V_{ud}|^2}{8\pi E_v^2} \left[A\left(Q^2\right) \pm B\left(Q^2\right) \times \left(\frac{s-u}{M^2}\right) + C\left(Q^2\right) \times \left(\frac{s-u}{M^2}\right)^2 \right],\tag{4.1}$$

where the positive (negative) sign refers to neutrino (antineutrino) scattering, G_F is the Fermi coupling constant, V_{ud} is the Cabbibo coupling between down and up quarks, m is the mass of the charged lepton, M the mass of the target nucleon, and s, u are the usual Mandelstam variables. For a derivation of this expression, see [4]. Note the terms are organized in powers of $\frac{s-u}{M^2} = \frac{4ME_v-Q^2-m}{M^2}$ and the interference between the axial and vector currents that governs the difference in scattering amplitudes between neutrinos and antineutrinos is entirely contained in the $B(Q^2)$ term. This interference is a consequence of the V-A nature of the weak interaction. The auxiliary functions $A(Q^2)$, $B(Q^2)$, $C(Q^2)$ are parameterized in terms of vector, axial and pseudoscalar form factors:

$$A(Q^{2}) = \frac{(m^{2} + Q^{2})}{M^{2}} [(1+\tau) F_{A}^{2} - (1-\tau) F_{1}^{2} + \tau (1-\tau) F_{2}^{2} + 4\tau F_{1} F_{2}$$
$$-\frac{m^{2}}{4M^{2}} (F_{1} + F_{2})^{2} + (F_{A} + 2F_{P})^{2} - 4F_{P}^{2} (1+\tau)]$$
(4.2)

$$B(Q^{2}) = \frac{Q^{2}}{M^{2}} F_{A}(F_{1} + F_{2})$$
(4.3)

$$C(Q^2) = \frac{1}{4} (F_A^2 + F_1^2 + \tau F_2^2),$$
 (4.4)

where $\tau = \frac{Q^2}{4M^2}$, F_1 and F_2 are vector form factors, F_A is the axial form factor, and F_P is the pseudoscalar form factor. The vector form factors are:

$$F_{1} = \frac{1 + \tau \left(1 + \mu_{p} - \mu_{n}\right)}{\left(1 + \tau\right) \left(1 + \frac{Q^{2}}{m_{V}^{2}}\right)^{2}}$$
(4.5)

$$F_2 = \frac{\mu_p - \mu_n}{(1+\tau)\left(1 + \frac{Q^2}{m_V^2}\right)^2},\tag{4.6}$$

where μ_P (μ_n) = 2.793 (-1.913) × μ_N is the proton (neutron) anomalous magnetic moment [5], and m_V is the empirically-determined "vector mass". Using the conserved vector current (CVC) hypothesis, the results of the plentiful and high-quality elastic electron scattering ($e^- + N \rightarrow e^- + N$) data can be used to constrain these form factors. The dipole forms of Eqs. (4.5) and (4.6) are adequately described with a vector mass of $m_V^2 = 0.71 \text{ GeV}^2$, but recent fits to these data show a clear preference for a non-dipole form [6].

The pseudoscalar form factor is given by:

$$F_P = \frac{2M^2}{m_\pi^2 + O^2} F_A,\tag{4.7}$$

where m_{π} is the pion mass. Notice the contribution of F_P to the CCQE cross section is suppressed by $\frac{m^2}{M^2}$, and so its effect relative to the other terms is small.

Finally, and most importantly for the measurements of this dissertation, the axial form factor is:

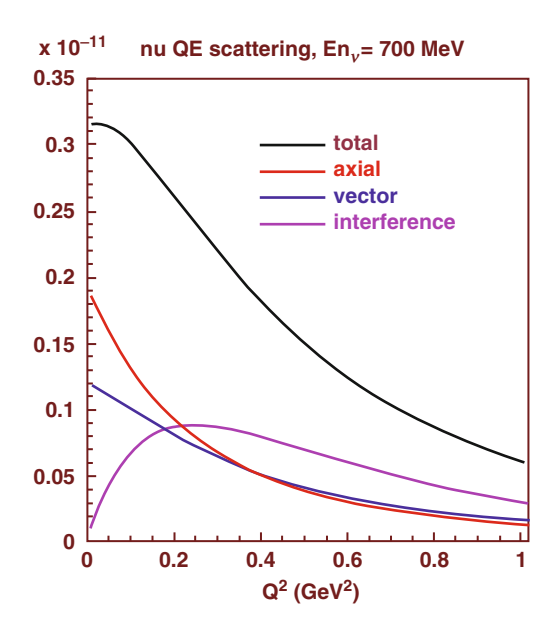
$$F_A = \frac{g_A}{\left(1 + \frac{Q^2}{M_A^2}\right)^2},\tag{4.8}$$

where g_A and M_A are empirical inputs, and the dipole form is again assumed. Like the vector form factors taken from electron-scattering data, g_A is also constrained by external information: β decay measurements give $g_A = F_A(Q^2 = 0) = -1.267 \pm 0.002$ [7]. This leaves the axial mass M_A as the only free parameter in the CCQE cross section. For decades, this parameter was measured with observations of both the total observed CCQE cross section and its shape as a function of the momentum transfer. A combined analysis of the world data through the twentieth century yields $M_A = 1.026 \pm 0.021$ GeV [8]. Important to point out, most of these measurements were performed with bubble-chamber detectors housing mostly hydrogen and deuterium media. More recent results from experiments employing larger nuclei in order to more easily gain the statistics needed for oscillation experiments have found tension with these data, and as a result the model for nuclear effects typically used by experiment has come under scrutiny. Further discussion of this model and its implications is found in Sect. 4.4.

As a final remark, the interference term proportional to $B(Q^2)$ in Eq. (4.2) gives rise to stark kinematic differences in the behavior of neutrinos compared to antineutrinos in CCQE interactions. In Fig. 4.2, the differential cross section for ν_{μ} CCQE scattering is separated into terms arising from the vector and axial currents, as well as the interference between the two. As the interference term is constructive for neutrino scattering and destructive for antineutrinos, is clear that the divergence of their amplitudes grows with momentum transfer. Momentum transfer

 $4.3 \quad CC\pi$

Fig. 4.2 Decomposition of the differential CCQE cross section for 700 MeV ν_{μ} 's. The ordinate axis is proportional to $d\sigma/dQ^2$. Figure from [9]



of the interaction is closely related to the production angle of the charged lepton relative to the neutrino direction, and this difference is exploited in Sect. 7.1.5 to measure the ν_{μ} and $\bar{\nu}_{\mu}$ content of the MiniBooNE antineutrino-mode data.

4.3 CCπ

Neutrinos with energy \sim 400 MeV and above can produce pions through the excitation and subsequent decay of baryonic resonances. Resonances of Delta (Δ) particles are most important for the neutrinos observed by MiniBooNE, and their decays are dominated by $\Delta \to N\pi$ [7]. The formalism to describe these interactions is taken from the Rein-Sehgal model [10], where the relativistic harmonic oscillator quark model is assumed [11] and the pion angular distribution due to the spin structure of the resonances is considered. Eighteen resonances are modeled, though the Δ (1232) is dominant in the energy range spanned by MiniBooNE. Multi-pion production mechanisms are also modeled, though their contribution is predicted to be small.

As the primary interaction for the CC π processes ($v_l + N \rightarrow l + \Delta$) is closely related to CCQE interactions, the formalism also includes a single tunable axial mass parameter $M_A^{1\pi}$. The axial masses in the resonance channels are set simultaneously to reproduce inclusive non-MiniBooNE charged-current data [12]. The extracted values are $M_A^{1\pi} = 1.10 \pm 0.27$ GeV and $M_A^{\text{multi}-\pi} = 1.30 \pm 0.52$ GeV (multi-pion production).

Various levels of discrepancy between this model and the MiniBooNE single π production results spanning normalization differences of up to 60% have been observed [13–15], and these differences continue to persist in more modern single- π production calculations [16]. For these reasons, whenever possible, the various MiniBooNE cross-section and oscillations measurements rely on direct constraints from the various MiniBooNE single- π production samples.

4.4 Nuclear Effects

4.4.1 Nuclear Modeling

The MiniBooNE detector is filled with mineral oil, and as a hydrocarbon material, the bare neutrino-nucleon interaction amplitudes must be combined with effects arising from the nuclear environment for interactions with material bound in carbon. MiniBooNE uses the Relativistic Fermi Gas (RFG) model [17] to describe this connection. Broadly, it combines the free-nucleon cross sections with a potential well in the form of binding energy as well as Pauli blocking to restrict the available kinematics of struck nucleons. The binding energy E_B increases the threshold for the reaction to occur, while the effects of Pauli blocking are more subtle.

The phenomenon of Pauli blocking arises from the exclusion principle, which dictates that no two fermions may share the identical set of quantum eigenstates. The RFG model simulates bound nucleons as a "gas" of particles, with a uniform momentum distribution from the lowest state up to an empirically-determined maximum k_F . These modifications to the CCQE amplitudes are implemented by integrating, with respect to the initial nucleon momentum \vec{k} , the free-nucleon cross sections scaled by a factor proportional to:

$$\Theta(k_F - |\vec{k}|) \ \Theta(|\vec{k} + \vec{q}| - k_F) \ \delta(E_{\vec{k}} - E_{\vec{k} + \vec{q}} - E_B + \omega),$$
 (4.9)

where $\omega=E_{\nu}-E_{l}$ is the energy transfer, $\vec{q}=\vec{p}_{\nu}-\vec{p}_{l}$ is the three-momentum transfer, and $E_{\vec{k}}$ and $E_{\vec{k}+\vec{q}}$ are the energies of the initial and struck nucleon, respectively. The first term requires the nucleon participating in the interaction to have momentum below k_{F} , the second enforces Pauli blocking, and the third assures energy conservation. The second term is appropriate only to nuclear transitions involving $n\leftrightarrow p$ so that the struck nucleon is required to be above the Fermi momentum of the *other*, fully-populated nucleon Fermi sea. In the case of carbon-12, where Z=N=6, a single momentum k_{F} specifies the maximum of both the proton and neutron Fermi levels.

The energy of the lowest-allowed struck nucleon momentum state is closely related to low values of the squared momentum transfer distribution $Q^2 \equiv -q^2$, where q^2 here is the four-momentum transfer. This region in the MiniBooNE ν_{μ}

4.4 Nuclear Effects 35

CCQE data was insufficiently described by this RFG model [18], and even after a more rigorous evaluation of the backgrounds it was found that a mild scaling (" κ ") of this energy level:

$$E_{\text{low}} = \kappa \left(\sqrt{k_F^2 + M^2} - \omega + E_B \right) \tag{4.10}$$

was preferred by the data at the level of a \sim 1 % modification to E_{low} [19].

The values for the binding energy and Fermi momentum of carbon are informed by electron scattering data. Described in [20], the peak of quasielastic electron-scattering $(e^- + N \rightarrow e^- + N)$ data is well-described by a Fermi gas model and $E_B(p_F) = 25$ (221) MeV, where natural units are used.

The Fermi momentum $p_F = 221$ MeV is directly implemented into the RFG. However, for CCQE scattering where $n \leftrightarrow p$, the binding energy must be modified from the determination from electron scattering data, where the initial and outgoing nucleons are of the same type. Additional coulomb repulsion for $n \to p$ transitions (appropriate to ν_{μ} CCQE interactions) adds to the effective binding energy of the system. The asymmetry term in the semi-empirical mass formula [21] estimates this adds 9 MeV to the energy for this transition, resulting in an effective binding energy of 34 MeV for ν_{μ} CCQE interactions on carbon-12.

Particularly in the context of this dissertation, it is important to note the RFG assumes all nucleons behave entirely independently of one another. Recent deviations from RFG expectations in the measurements of the CCQE interaction with relatively heavy nuclear targets have cast suspicion on this assumption. While measurements of M_A using mostly light nuclear material (discussed in Sect. 4.2) agree fairly well, data from experiments using relatively heavy nuclei and higher-precision detectors have extracted values of M_A systematically higher than 1.026 GeV [19, 22–24]. Adding complexity, the modern heavy nuclear target experiment NOMAD has measured values of M_A consistent with the light-target analyses [25], while preliminary shape results from the MINER ν A experiment seem to also favor $M_A \sim 1$ GeV [26].

An essential first step to understanding this apparent discrepancy is to recognize the particulars of the model dependence introduced by comparing values of M_A between the many experiments. Important experimental differences that may contribute to the discrepancy include disparate neutrino spectra, different neutrino detection technologies and the size of the nuclear media employed. Among the liberties taken to compare M_A values across these scattering experiments include the dipole form of F_A , various expectations of hadronic activity consistent with single-nucleon ejection and the previously-mentioned independent nucleon assumption implicit in both the formalism and in the inference of the Q^2 distribution. A possible reconciliation between the data sets has been proposed by offering a mechanism resulting in intra-nuclear correlations of greater strength than previously expected [27–35]. Such a mechanism is consistent with electron scattering data [36, 37]. If this process is confirmed for weak interactions via neutrino scattering, its detailed understanding will significantly expand knowledge of intra-nuclear

behavior, and some neutrino oscillation results may need to be revisited [38,39]. The best chance to definitively resolve this crucial ambiguity lies in the community's ability and willingness to produce and compare model-independent information in both the leptonic and hadronic interaction sectors between experimental data and theoretical calculations. The results of this dissertation offer a first look at antineutrino CCQE interactions below 1 GeV and thus significantly expand the body of experimental data contributing to this picture. In recognizing the possible deficiencies of the RFG, the main result of this work is the double-differential CCQE cross section $\left(\frac{d^2\sigma}{dT_\mu d\cos\theta_\mu}\right)$ on mineral oil, where no assumptions about the underlying process are necessary.

4.4.2 Final-State Interactions

An important connection between fundamental neutrino-nucleus interactions and what is observed in the detector are the possible strong interactions between the struck baryon and its nuclear environment.

For neutrino interactions with a nucleon bound in carbon, NUANCE propagates the outgoing hadrons including nucleons, mesons and baryonic resonances, and simulates their re-interaction as they exit the nucleus. The initial interaction model employs the impulse approximation which assumes an instantaneous exchange with independent nucleons. Subsequent to the initial neutrino interaction, particles produced inside the nucleus are propagated step-wise in 0.3 fm increments until they emerge from the ~2.5 fm radius sphere. Intermittently, the probability for hadronic re-interaction is calculated using a radially-dependent nucleon density distribution [40] along with external $\pi - N$, N - N cross-section measurements [41]. For Δ re-interactions ($\Delta + N \rightarrow N + N$), an energy-independent probability of 20 % (10 %) is taken for $\Delta^+ + N$, $\Delta^0 + N$ ($\Delta^{++} + N$, $\Delta^- + N$) based on K2K data [12] and is assigned 100 % uncertainty.

Out of all hadronic reinteraction processes, pion absorption $(\pi^{\pm} + X \to X')$ and charge exchange $(\pi^{\pm} + X \leftrightarrow \pi^0 + X')$ are the most relevant in predicting the composition of the samples studied in the analyses of this dissertation. Shown in Fig. 4.3, intranuclear fractional uncertainties on pion absorption (charge-exchange) are set to 25 % (30 %) based on comparisons between external data [42] and the NUANCE prediction.

References 37

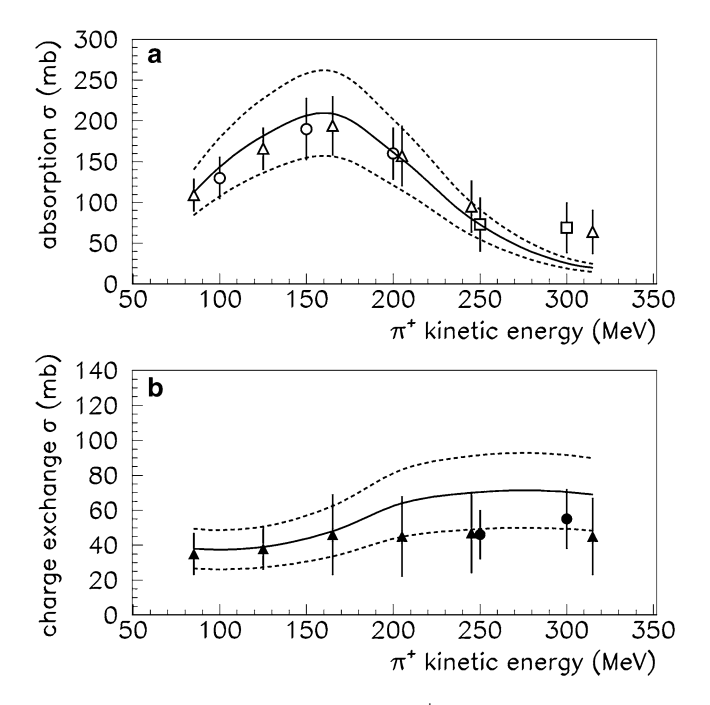


Fig. 4.3 Comparison of the NUANCE prediction for π^+ absorption (*top*) and charge-exchange (*bottom*) to relevant data [42]. Figure from [19]

References

- 1. D. Casper, Nucl. Phys. Proc. Suppl. 112, 161 (2002)
- 2. R. Feynman, Very high-energy collisions of hadrons. Phys. Rev. Lett. 23, 1415 (1969)
- 3. C.H. Llwellyn-Smith, Phys. Rep. 3, 261 (1972)
- 4. T. Katori, Ph.D. thesis, Indiana University, 2008
- 5. W.-M. Yao et al., J. Phys. G33, 1 (2006)
- H. Budd, A. Bodek, J. Arrington, Modeling quasi-elastic form factors for electron and neutrino scattering. arXiv:hepex/0308005
- 7. C. Amsler et al. (Particle Data Group), Phys. Lett. 667B, 1 (2008)
- 8. V. Bernard et al., J. Phys. G28, R1 (2002)
- 9. G.P. Zeller, private communication
- 10. D. Rein, L.M. Sehgal, Ann. Phys. 133, 79 (1981)
- 11. R.P. Feynman, M. Kislinger, F. Ravndal, Phys. Rev. **D3**, 2706 (1971)
- 12. D. Casper, private communication
- 13. A.A. Aguilar-Arevalo et al. [MiniBooNE Collaboration], Phys. Rev. D83, 052007 (2011)
- 14. A.A. Aguilar-Arevalo et al. [MiniBooNE Collaboration], Phys. Rev. D81, 013005 (2010)
- 15. A.A. Aguilar-Arevalo et al. [MiniBooNE Collaboration], Phys. Rev. **D83**, 052009 (2011)
- 16. O. Lalakulich, U. Mosel, Pion production in the MiniBooNE experiment. arXiv:1210.4717
- R.A. Smith, E.J. Moniz, Nucl. Phys. B43, 605 (1972); erratum: R.A. Smith, E.J. Moniz, Nucl. Phys. B101, 547 (1975)
- A.A. Aguilar-Arevalo [MiniBooNE Collaboration], Measurement of muon neutrino quasielastic scattering on carbon. Phys. Rev. Lett. 100, 032301 (2008)

- 19. A.A. Aguilar-Arevalo et al. [MiniBooNE Collaboration], Phys. Rev. D81, 092005 (2010)
- E.J. Moniz et al., Nuclear fermi momenta from quasielastic electron scattering. Phys. Rev. Lett. 26, 445 (1971)
- 21. C.F. Weizäcker et al., On the theory of nuclear masses. J. Phys. 96, 431 (1935)
- 22. R. Gran et al., Phys. Rev. D74, 052002 (2006)
- 23. M. Dorman for the MINOS collaboration, AIP Conf. Proc. 1189, 133 (2009)
- 24. J.L. Alcaraz-Aunion, J. Walding, AIP Conf. Proc. 1189, 145 (2009)
- 25. K.S. Kuzmin, V.V. Lyubushkin, V.A. Naumov, Eur. Phys. J. C 54, 517 (2008); V.V. Lyubushkin et al. [NOMAD Collaboration]. arXiv:0812.4543 [hep-ex]
- 26. K. McFarland for the MINER vA Collaboration, AIP Conf. Proc. 1405, 95 (2011)
- M. Martini et al., A unified approach for nucleon knock-out, coherent and incoherent pion production in neutrino interactions with nuclei. Phys. Rev. C80, 065501 (2009). arXiv:0910. 2622
- M. Martini et al., Neutrino and antineutrino quasielastic interactions with nuclei. Phys. Rev. C81, 045502 (2010)
- M. Martini et al., Quasielastic and multinucleon excitations in antineutrino-nucleus interactions. arXiv:1303.7199
- J. Nieves et al., Inclusive charged-current neutrino-nucleus reactions. Phys. Rev. C83,045501 (2011). arXiv:1102.2777
- J. Nieves et al., Two particle-hole excitations in charged current quasielastic antineutrinonucleus scattering. arXiv:1302.0703
- 32. J. Amaro et al., Relativistic analyses of quasielastic neutrino cross sections at MiniBooNE kinematics. Phys. Rev. **D84**, 033004 (2011). arXiv:1104.5446
- J. Amaro et al., Meson-exchange currents and quasielastic antineutrino cross sections in the SuperScaling Approximation. arXiv:1112.2123
- 34. A. Meucci, C. Giusti, Phys. Rev. **D85**, 093002 (2012)
- 35. A. Bodek et al., Eur. Phys. J. C71, 1726 (2011)
- 36. W.M. Alberico et al., Phys. Rev. C38, 1801 (1988)
- 37. T.W. Donnelly, I. Sick, Phys. Rev. C60, 065502 (1999)
- 38. M. Martini et al., arXiv:1202.4745 [hep-ph]
- 39. O. Lalakulich, U. Mosel, Phys. Rev. C86, 054606 (2012).
- 40. W. Reuter et al., Phys. Rev. C 26, 806 (1982)
- V. Flaminino et al., CERN-HERA-83-01 (1983); CERN-HERA-83-02 (1983); CERN-HERA-84-01 (1984)
- D. Ashery et al., Phys. Rev. C23, 2173 (1981); M.K. Jones et al., Phys. Rev. C48, 2800 (1993);
 R.D. Ransome et al., Phys. Rev. C45, R509 (1992)

Chapter 5 The MiniBooNE Experiment

5.1 Overview

The MiniBooNE experiment was designed to optimize the search for the appearance of ν_e events in a beam of ν_μ . Accordingly, many design choices were made and auxiliary systems implemented to maximize detection efficiency for ν_μ and ν_e CC events sensitive to mass splittings of $\Delta m^2 \sim 1\,\mathrm{eV}^2$ while maintaining discrimination power between the two neutrino species. This chapter describes the physical layout of the experiment and the detector subsystems most crucial to the measurement of muon kinematics. An expanded description of the beamline and neutrino flux calculation can be found in [1], while the overall design and performance of the detector is discussed in more detail in [2].

5.2 The Booster Neutrino Beamline

The Booster Neutrino Beamline (BNB) collides 8.9 GeV/c momentum protons onto a beryllium target, and a magnetic horn is used to sign-select and focus the secondary meson beam in the direction of the detector. Depending on the polarity of the magnetic field, the selected meson decay modes yield an enhanced ν_{μ} or $\bar{\nu}_{\mu}$ beam. This section steps through the important instruments in this process, finally arriving at the calculation of the neutrino flux observed by the detector.

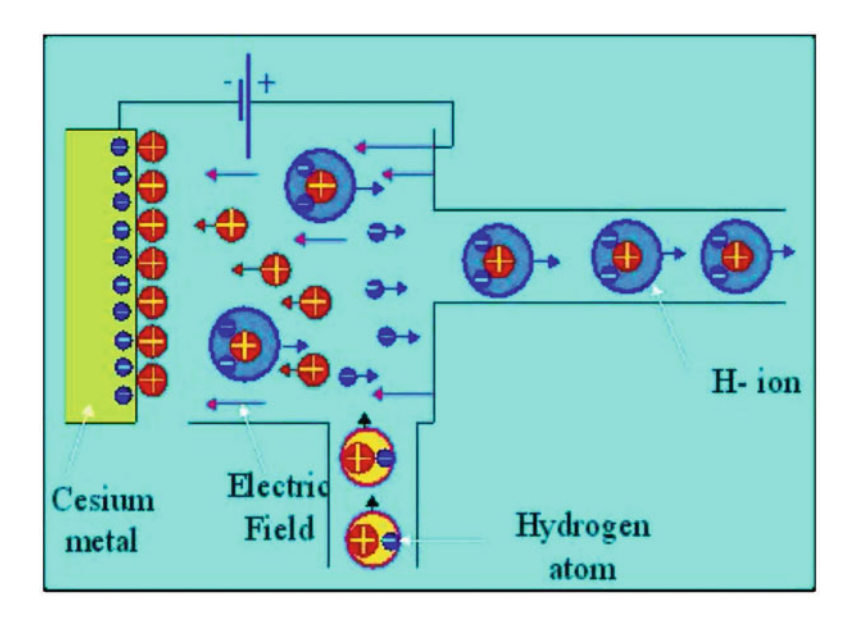


Fig. 5.1 Cartoon of the Fermilab pre-accelerator stage. Figure taken from [4]

5.2.1 The Primary Proton Beam

The Fermilab accelerator chain begins with a bottle of hydrogen gas and a voltage multiplier system first demonstrated in 1913 [3]. This Cockroft–Walton system generates a large DC voltage from a small AC input with a ladder network of capacitors and diodes. At each successive stage, the charge on each capacitor is doubled by simultaneously collecting charge stored in the previous capacitor and the AC input.

The Fermilab Cockroft-Walton machine applies a voltage difference of $750\,\mathrm{kV}$ across an ionization chamber, the negative potential side of which is coated with cesium metal, and the other wall is partially open in the direction of the Fermilab linear accelerator (linac). Hydrogen atoms that drift into this chamber will ionize, and the bare protons will collide with the cesium metal. Cesium has a relatively low work function, and some of these collisions result in the transfer of two valence electrons to the proton, forming an H^- ion. These 750 keV kinetic energy negatively-charged atoms drift to the wall of positive potential, and may pass through the opening and continue to the next accelerator stage. A cartoon of this process is shown in Fig. 5.1.

The H^- atoms then enter the linac, where an alternately polarized electric field accelerates the ions between gaps of Faraday cage drift tubes. Beam bunches are formed with pulses roughly 5 ns apart, and the 130 m long linac terminates with H^- batches of 400 MeV kinetic energy.

As shown in Fig. 5.2, these bunches are injected into the Booster synchrotron via a system featuring a stripping foil placed between a series of dipole magnets

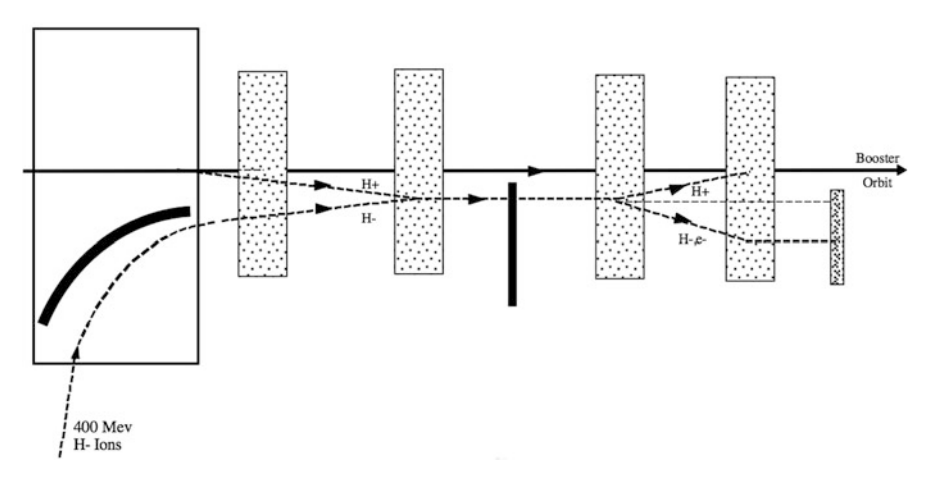


Fig. 5.2 Injection diagram for H^- ions onto the Booster orbit as bare protons. Figure taken from [5]

in a "dogleg" configuration. The foil strips the H^- ions of their electrons, and the subsequent magnets steer the bare protons onto the Booster orbit. The dogleg dipole magnet configuration has the effect of a focusing and defocusing (FODO) quadrupole system, where the injected H^- atoms and the Booster protons converge to a single beam.

To avoid unnecessary beam divergences in the Booster, the dogleg dipoles are only pulsed when beam is injected from the linac. The Booster synchrotron accelerates the 400 MeV kinetic energy protons up to 8 GeV through 17 radio-frequency (RF) stages and is kept on-orbit by 24 periods of FOFDOOD cells. This acceleration takes roughly 33 ms and 20,000 turns around the 150 m diameter ring. The harmonic number of the Booster is 84, though typically three buckets are not used. These 81 bunches, each separated by \sim 19 ns, of 8 GeV kinetic energy protons are extracted from the Booster in a 1.6 μs spill. Shown in Fig. 5.3, this structure is clearly visible in the arrival of neutrino events at the MiniBooNE detector. These spills typically contain 5 \times 10 12 protons and are delivered to the MiniBooNE target and horn system at a maximum rate of 5 Hz. Full details of the Booster synchrotron is available in [5].

5.2.2 Beryllium Target and Magnetic Focusing Horn

The next stage in the BNB converts the proton spill into a focused beam of mesons. The proton beam strikes a 71.1 cm long target, composed of seven 10.2 cm long and 0.5 cm radius cylindrical beryllium slugs.

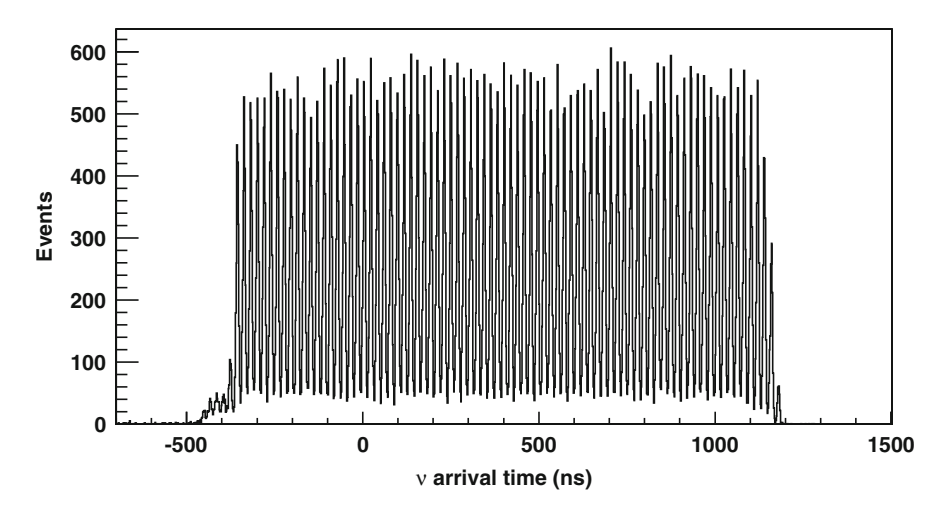


Fig. 5.3 Timing structure of the BNB proton spills through the arrival time of neutrino events at MiniBooNE. The represented data is the neutrino-mode CCQE sample, and a time-of-flight correction based on the observed interaction vertex along the beam direction has been applied. The \sim 500 ns offset between the arrival and recorded times is due to an offset in the timing instruments

The proton-beryllium interactions deposit $\sim\!600\,\mathrm{W}$ under normal running conditions, and so an air-cooling system is implemented to reduce radiation damage to the system and the surrounding environment. The beryllium target is separated from its housing using three supporting "fins", also made of beryllium, and allows for air to be circulated along its entire length. The air flow rate is $\sim\!8\times10^{-3}\,\mathrm{m}^3/\mathrm{s}$ and, due to a heat exchanger system, flows continuously during normal running conditions. Engineering designs for the beryllium target and its installation inside the magnetic horn are shown in Fig. 5.4.

The proton-beryllium interactions create a spray of secondary particles, including many neutrino-parent mesons. A set of connected inner and outer conductors form a horn system, and an electric current of $\pm 174\,\mathrm{kA}$ pulsed through these conductors in time with the BNB proton spill creates a toroidal magnetic field as shown in Fig. 5.5. This field simultaneously focuses particles with positive or negative charge, while defocusing the other. In this way, the polarity of this system defines the running mode - focusing positively-charged mesons yields an enhanced ν_{μ} beam (dominantly via $\pi^+ \to \mu^+ \nu_{\mu}$) while selecting negative mesons creates a $\bar{\nu}_{\mu}$ -enhanced beam (via $\pi^- \to \mu^- \bar{\nu}_{\mu}$).

The magnetic horn simultaneously controls the neutrino composition of the BNB beam and substantially increases the neutrino flux. In neutrino-mode running, the horn increases the observed rate of neutrino interactions by roughly a factor of six. As with the beryllium targets, the magnetic horn must also be cooled to protect against radiation damage. A closed water system keeps the system exceptionally stable. The first BNB horn pulsed 96 million times before failing due to corrosion,

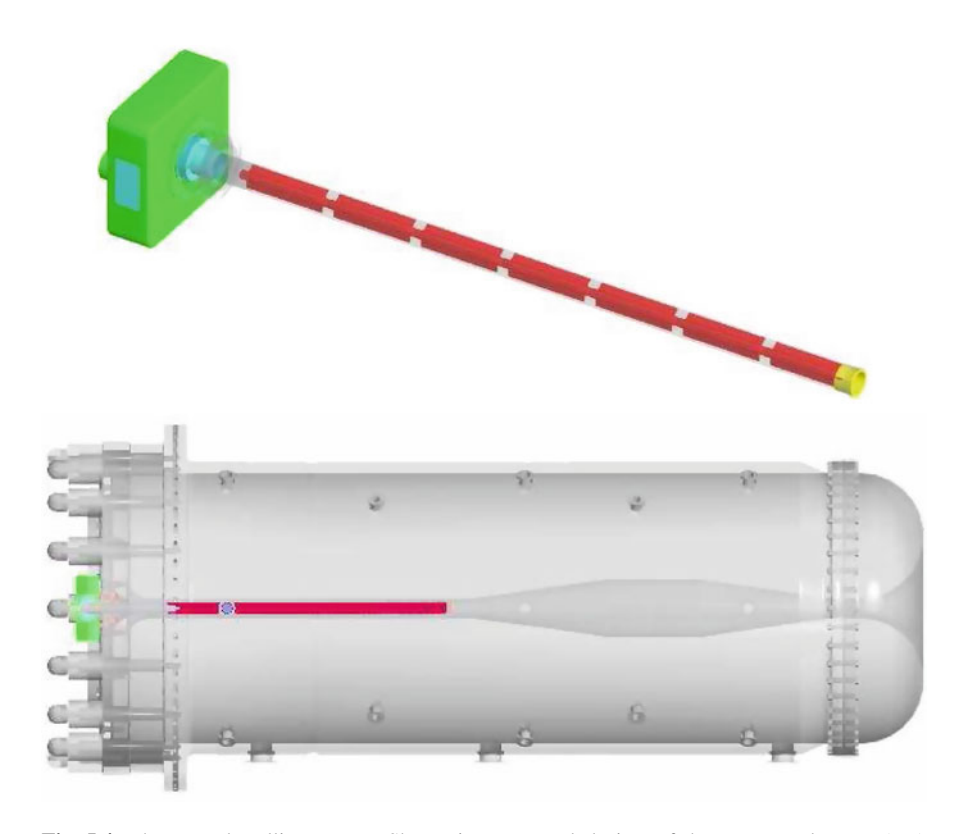
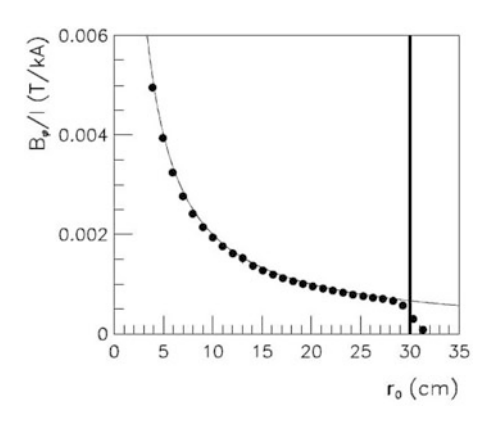


Fig. 5.4 The BNB beryllium target. Shown is an expanded view of the segmented target (*top*) and its place inside the magnetic focusing horn (*bottom*). The proton beam strikes the target from the *left*

Fig. 5.5 A comparison of the azimuthal component of the magnetic field relative to the input current between data (in *points*) and the expectation (*solid curve*) of 1/r dependence. The *vertical line* identifies the inside edge of the outer conductor. Figure taken from [6]



while the second horn is still operational and has been pulsed a world's record 397 million times as of March 2013.

5.2.3 Meson Decay Region

The mesons accepted into the neutrino beam are collimated immediately downstream through a 60 cm opening in a concrete slab and subsequently enter a 50 m long, air-filled decay volume. The mesons decay in flight to produce charged leptons and neutrinos, or are absorbed by a concrete wall at the end of the decay volume. Protons that do not strike the beryllium target may interact with the air molecules in the decay region before terminating at the beam dump. These interactions may also produce mesons boosted towards the detector, and these processes contribute $\sim 5\,\%$ of the neutrino flux at MiniBooNE.

Ten 25-ton steel absorber beams are housed above the middle of the decay region, and could be deployed in the hall to systematically alter the normalization and energy spectrum of the neutrino beam. Specifically, the shortened decay region would remove higher-energy neutrinos, including an appreciable amount of the intrinsic ν_e and $\bar{\nu}_e$ from the $\pi^{\pm} \to \mu^{\pm}$ decay chain. Meanwhile, the overall ν_{μ} and $\bar{\nu}_{\mu}$ flux would be reduced by roughly 10% per deployed absorbed. So far, these absorbers have not been intentionally deployed; however, in an early period of antineutrino-mode running, one and then another absorber fell into the beamline. A total of 5.69 (6.12) \times 10¹⁹ POT was collected in antineutrino-mode with one (two) absorbers present in the decay hall. Details of the systematic effects caused by these blocks was implemented into simulation, and consistency between the observed and predicted rate and kinematics suggest the modeling is adequate. As the MiniBooNE $\bar{\nu}_{\mu} \rightarrow \bar{\nu}_{e}$ oscillation search is limited by statistics to date [3], these data are included in the oscillation analysis, as is the case with an early determination of the v_{μ} contribution to the antineutrino-mode beam presented in Sect. 7.1.5. However, the double-differential cross section $\frac{d^2\sigma}{dT_\mu d\cos\theta_\mu}$ for $\bar{\nu}_\mu$ CCQE interactions is limited by statistics only in small regions of the distribution tails, and so these absorber-down data are not used in the main result of this dissertation.

5.2.4 Neutrino Flux Calculation

The most important piece of an absolute neutrino flux calculation is the production of the neutrino and antineutrino parent π^+ and π^- created in proton-beryllium interactions at the target. It is common to rely on a combination of hadroproduction models and data-based extrapolations to meet this goal. However, Fig. 5.6 shows modern models [8–11] for primary hadroproduction ($p+Be \to \pi^\pm + X$) at 8.9 GeV proton beam momentum dramatically disagree.

Clearly, precision neutrino and antineutrino cross section measurements cannot be made with information from hadroproduction models alone. A much more clean and direct method for constraining the neutrino flux was fortunately available to MiniBooNE: the HARP hadroproduction experiment at CERN collected dedicated data using the same proton momentum and target material as in the BNB.

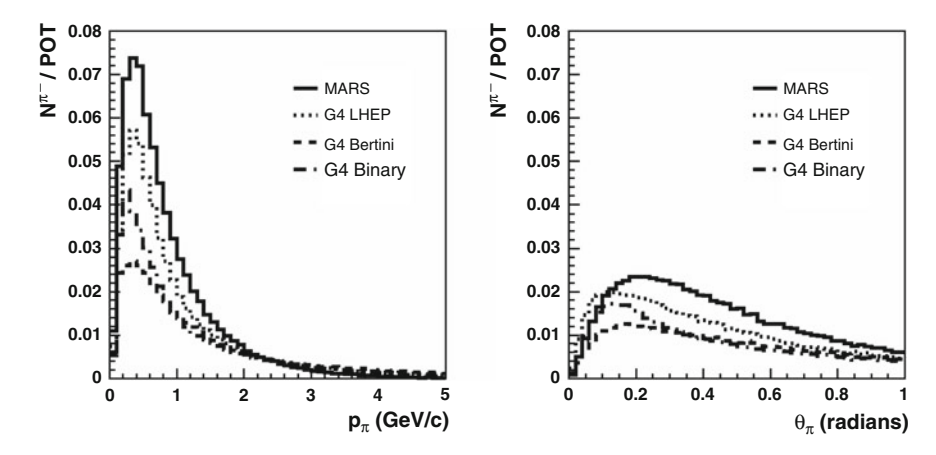


Fig. 5.6 Production of primary π^- per POT for 8.9 GeV momentum protons incident on beryllium for various hadroproduction models as a function of π^- momentum (*left*) and opening angle with respect to the incoming proton beam (*right*). Figure taken from [7]

Double-differential cross sections in terms of pion kinematics was measured for both π^+ [12] and π^- [7], allowing for a minimally model-dependent determination of primary π production at the BNB for both the neutrino-mode and antineutrino mode run configurations.

However, even with dedicated data appropriate to the experimental setup of MiniBooNE, there remain small regions of phase space relevant to the antineutrinomode beam not covered by the HARP measurements. As will be expanded and directly addressed in Chap. 7, of particular importance to this work is the production of very forward pions with respect to the direction of the incoming proton beam. In the HARP experiment, this same angular region suffers from re-interactions in the target and a severe proton background, preventing a clean measurement of the pion production cross section. For these reasons, pion cross sections in the θ_{π} < 30 mrad region, where θ_{π} is the angle the outgoing pion makes with respect to incoming protons, are not covered by the HARP data. Instead, the nominal primary π production cross section for this region in the MiniBooNE flux calculation is extrapolated from the existing HARP data using a Sanford-Wang [14] parameterization. More suitable for extrapolating uncertainties, errors on primary π production come from the piecewise polynomial spline interpolation [15]. This extrapolation is only one of many possible choices, and is therefore subject to large uncertainties. Figure 5.7 shows the HARP data, the Sanford-Wang parametrization, and the production uncertainty from the spline procedure for primary π^- production.

The HARP data was taken on a thin version (5% proton interaction length) of the full-sized (170%) MiniBooNE beryllium target, and so these data do not include possible hadronic re-interactions inside the target. The total cross section for these secondary interactions are calculated with the Glauber model [16], and this calculation is verified with comparisons to data wherever possible. Based on

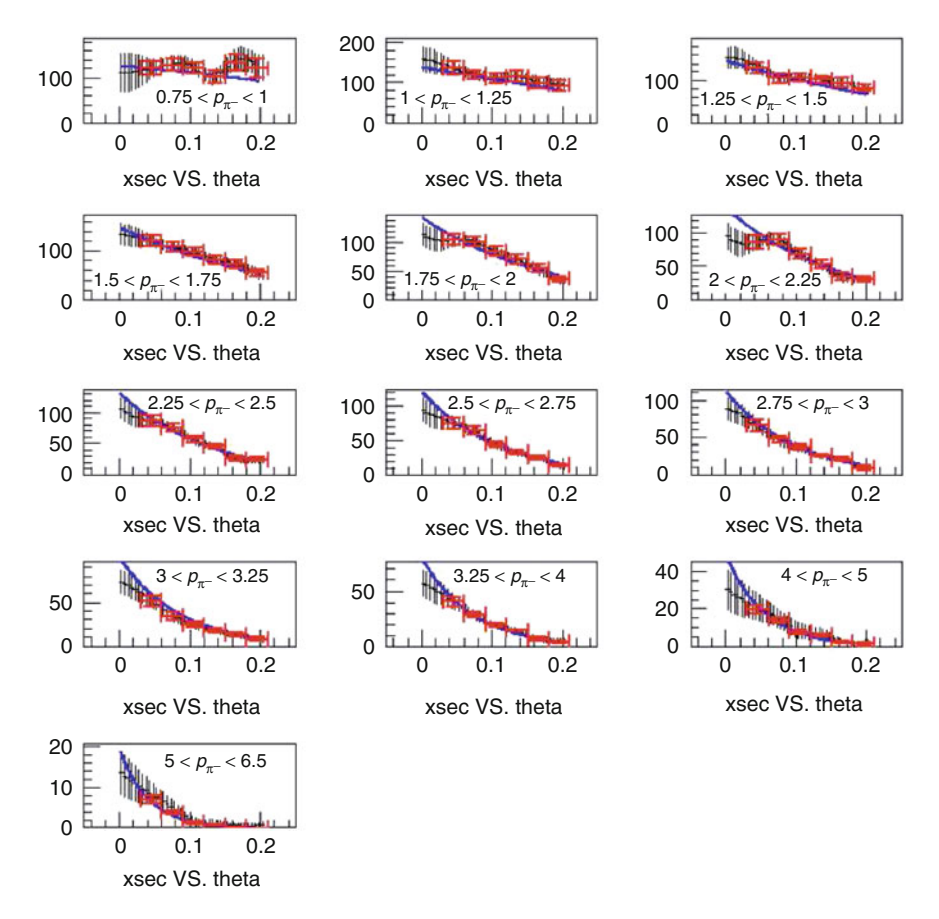


Fig. 5.7 Double-differential cross section $d^2\sigma/dp_\pi d\Omega_\pi$ for $p + Be \to \pi^- + X$ in units of mb/(GeV sr). The angular axes have units of radians, and the momentum projections are in units of GeV. The blue curve is the Sanford–Wang parametrization based on the red HARP data points, and the black histogram with uncertainties is the spline interpolation. Figure taken from [13]

the agreement between this model and the available data, uncertainties on the most important processes contributing pions to the beam are set around $20\,\%$ and higher [1, 17]. Fortunately, while some details of this calculation are model-dependent, Fig. 5.8 shows the overall contribution of these processes to the overall neutrino flux is rather mild, at the level of $\sim 10\,\%$. Moreover, the same figure also suggests the contribution from tertiary pions present in the long MiniBooNE target but not in the thin target data from HARP is small. Therefore, with the exception of the very forward-going angular region, the HARP data allows for a minimally model-dependent determination of the production of neutrino and antineutrino parent pions at the BNB.

A GEANT4-based package [18] is used to calculate the neutrino flux observed at MiniBooNE. The simulation takes as input the previously-described meson production and considers the beamline geometry, proton travel to the target, p-Be

5.3 Detector 47

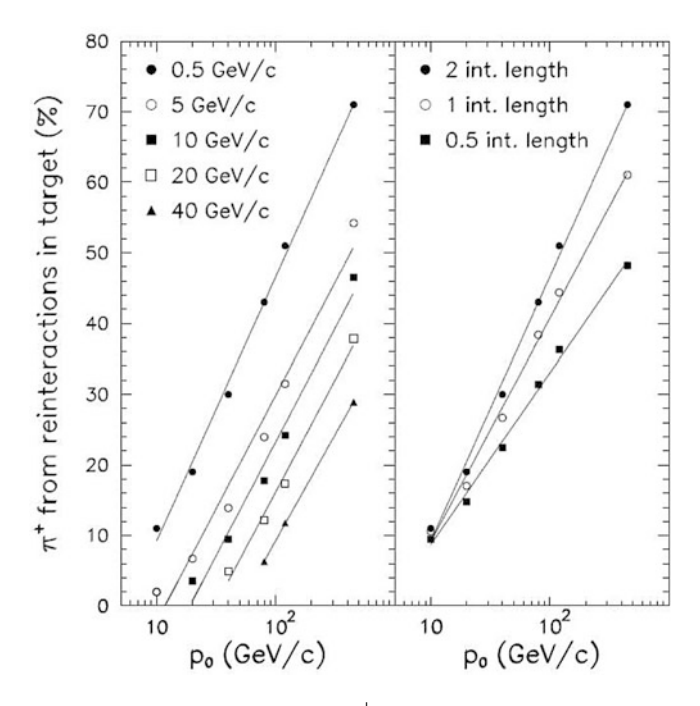


Fig. 5.8 Fluka [19] calculations of the tertiary π^+ yield from reinteractions in a graphite target. Given as a function of incident proton beam momentum p_0 , the π^+ fraction is given for the indicated thresholds on the longitudinal component of the π^+ momentum (left), and also for targets of 0.5, 1.0, and 2.0 interaction lengths (right). The primary proton beam at the BNB has momentum 8.9 GeV/c. Figure taken from [20]

interactions in the target, magnetic horn focusing, particle propagation, meson decay, and finally neutrino and antineutrino transport to the detector. For both neutrino and antineutrino mode run configurations, the uncertainty on pion production and the set of all other beamline uncertainties contribute roughly equally to the $\sim 9\,\%$ total uncertainty on the absolute flux prediction for the selected neutrino species. Figure 5.9 shows the predicted flux of ν_{μ} , $\bar{\nu}_{\mu}$, ν_{e} , and $\bar{\nu}_{e}$ observed by the MiniBooNE detector for both neutrino and antineutrino run modes.

5.3 Detector

5.3.1 Physical Layout

Shown schematically in Fig. 5.10, the detector is a 12.2 m diameter sphere housed in a 13.7 m underground cylindrical vault such that the top of the tank sits roughly at ground level. The detector shape was motivated by maximizing the volume to

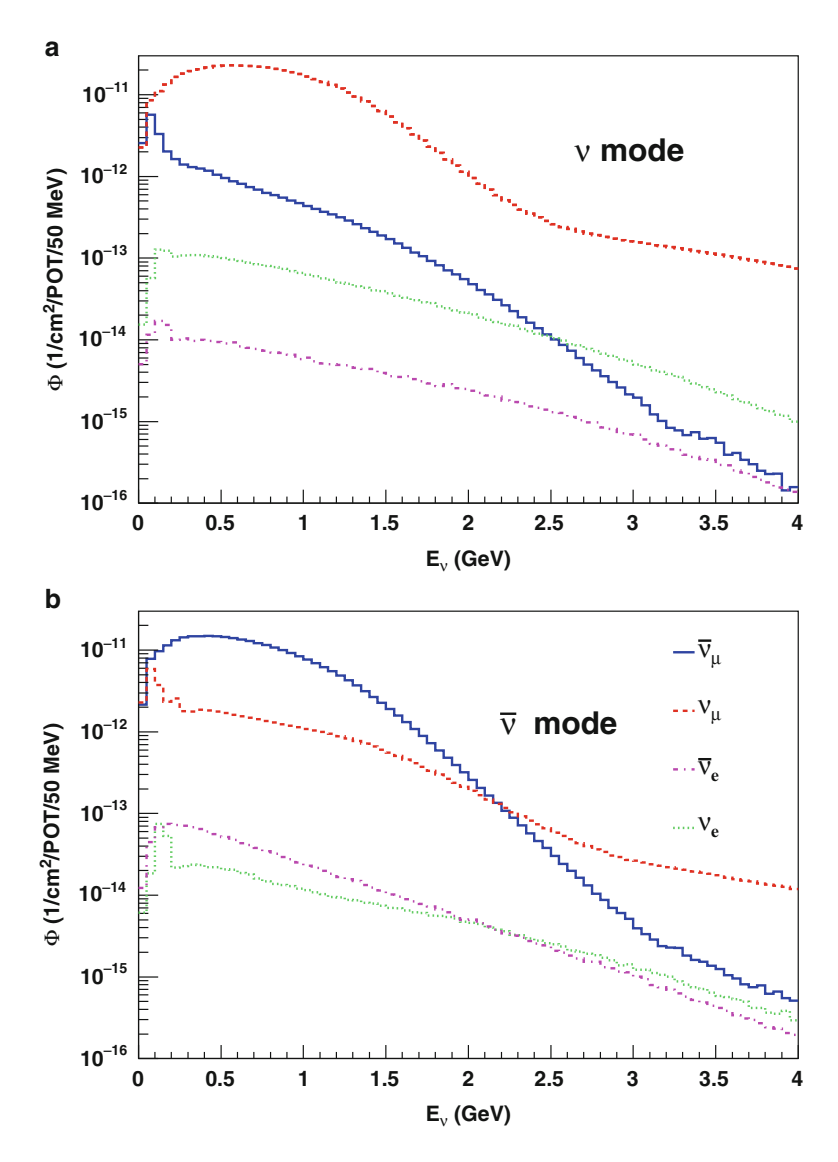


Fig. 5.9 The MiniBooNE flux prediction for (a) neutrino mode and (b) antineutrino mode. Data taken from [1]

surface area ratio, affording greater photocathode coverage for the same number of PMTs. The simple spherical geometry also allows for globally symmetric reconstruction algorithms and thus equal sensitivity to particle kinematics across all scattering angles. An earth overburden of ~ 3 m reduces the rate of cosmic-ray muons entering the detector to ~ 10 kHz. Between the detector and the overburden is

5.3 Detector 49

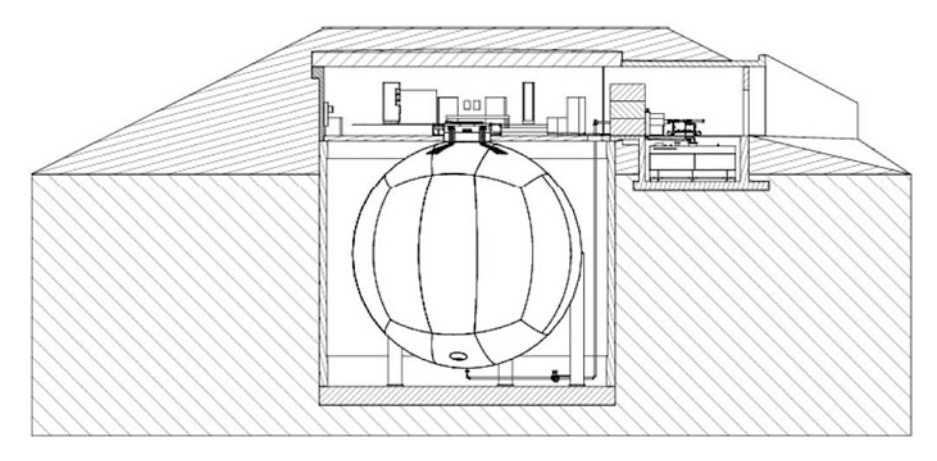


Fig. 5.10 Overview of the MiniBooNE detector housing. Image taken from [21]

an access room housing the main electronics, including the muon calibration system crucial to the measurement of this dissertation discussed in Sect. 5.3.4.

The tank is filled with 818 tons of undoped mineral oil, optically segregated into an inner signal region of radius 575 m and an outer veto shell of 35 cm thickness. Light produced in the detector is collected by 1,520 8-inch Hamamatsu photomultiplier tubes (PMTs), 1,280 of which face into the signal region (11.3 % coverage) while 240 are inside the outer shell. Figure 5.11 shows a cartoon of the MiniBooNE detector partially cut away to show the inner components as well as a photo of the optical barrier separating the two regions. Low activity in the veto region is required in physics analyses to ensure containment of charged particles produced by beam-induced neutrinos while also eliminating contamination from charged particles entering the tank. To encourage photon rescattering and thus maximize detection efficiency for charged particles traversing the veto region, the surfaces are painted white. In contrast, to improve the kinematical resolution of signal events, photon rescattering is minimized with a black surface for the inner region.

5.3.2 Mineral Oil and Its Properties

A common choice for the detection medium in Čerenkov-based experiments is water. In the case of MiniBooNE, mineral oil was selected over water for a variety of reasons:

 the increased index of refraction yields a lower momentum threshold on Čerenkov light production for all particles, globally improving detection efficiency

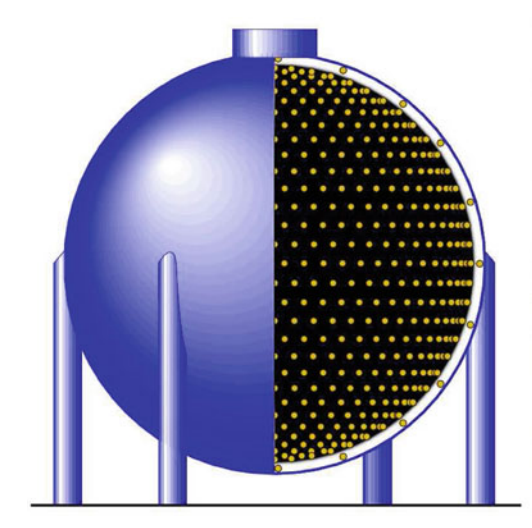




Fig. 5.11 On the *left*, cutaway drawing of the MiniBooNE detector showing PMTs dispersed in the inner and outer regions. The optical barrier separating the outer veto region (painted *white*) from the inner signal region (painted *black*) is shown on the *right*

Table 5.1 Momentum threshold for production of Čerenkov radiation for four important particle types in mineral oil compared to water

	Čerenkov threshold		
Particle	Mineral oil, $n = 1.47$	Water, $n = 1.33$	
Electron	0.7 MeV/c	0.8 MeV/c	
Muon	144 MeV/c	160 MeV/c	
Pion	190 MeV/c	212 MeV/c	
Proton	1280 MeV/c	1423 MeV/c	

- nuclear capture of stopped μ^- is $\sim 8\,\%$ in mineral oil, compared to $\sim\!20\,\%$ in water. This allows a cleaner tagging of ν_μ CC events, again improving detection efficiency while simultaneously reducing its background contribution to the ν_e CC sample.
- by exploiting PMT activity timing information, the lowered speed of light in the medium improves interaction vertex resolutions

Kept at ~ 20 ° C, the mineral oil has a density of 0.845 g/cm³ and an index of refraction of 1.47. Under these conditions, charged particles with velocity $\beta > 0.68$ produce Čerenkov radiation. The momentum thresholds for production of Čerenkov radiation for relevant particle species in mineral oil and water are compared in Table 5.1.

The above benefits come at the cost of significantly more complex mechanisms for light production and propagation through the detector. Due to impurities in the oil, molecular excitations produce delayed photons with an isotropic direction and of longer wavelength than the absorbed particle. These are known as fluorophores, or fluors, and four distinct modes were observed in table-top measurements of the MiniBooNE oil [2]. The measured and extrapolated extinction rates of these fluors are shown in Fig. 5.12.

5.3 Detector 51

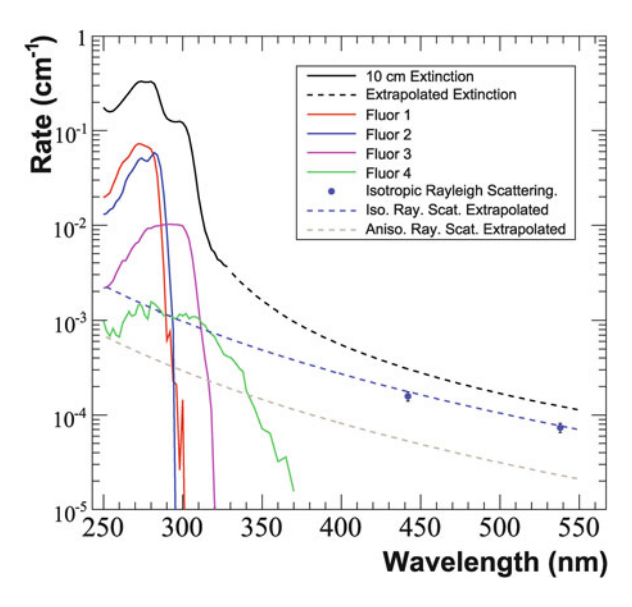


Fig. 5.12 Photon extinction rate spectrum in the MiniBooNE oil. As indicated, the *solid curves* correspond to measurements, while the *dashed lines* are based on an extrapolation of these data and are tuned to various in situ calibration data samples. Figure taken from [2]

The presence of fluors obfuscate the topology of the Čerenkov signature and bias the correlation between the collected Čerenkov light and the true energy of the particle. Fortunately, calibration samples and systems discussed in the next section exist to measure these biases so that their effect on most analyses (including the topic of this dissertation) are minimal. Though the fluors complicate the understanding of the detector, without their presence scintillation-based measurements such as the neutral current elastic cross sections [22, 23] would not be possible.

5.3.3 Photomultiplier Tubes

Of the 1,520 PMTs, 1,198 are nine-stage and have been repurposed following their use in the LSND experiment, while the remainder are ten-stage tubes purchased for MiniBooNE. Tests for charge and time resolution, the voltage level required to meet the desired gain, and the dark current were performed for all PMTs installed into MiniBooNE. The newer tubes feature average timing (charge at one photoelectron) resolution of \sim 1.1 ns (40%), while the older tubes resolve the same quantities at \sim 1.7 ns (130%) [24]. The average dark current for the new (old) tubes was found to be 1.0 (1.4) kHz at their operating voltage. Due to their superior performance, the newer PMTs are distributed uniformly in the signal region, while the LSND tubes with higher amounts of dark noise are used in the veto region. The quantum efficiency for the new PMTs is given in Fig. 5.13.

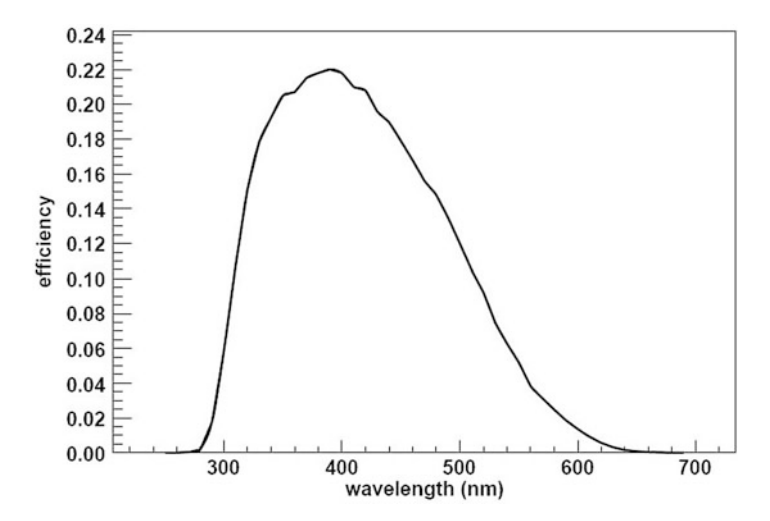


Fig. 5.13 Quantum efficiency for the newer MiniBooNE PMTs. Figure taken from [25]

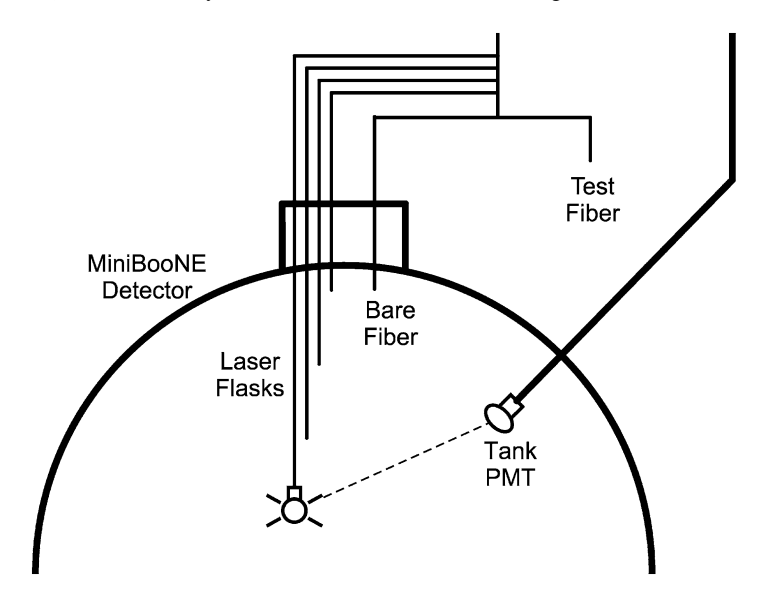


Fig. 5.14 Schematic of the laser calibration system. Image taken from [2]

5.3.4 Calibration Systems

In situ measurements of the PMT performance and the oil attenuation length over the lifetime of the experiment is afforded by a pulsed laser calibration system, shown schematically in Fig. 5.14. Four laser dispersion flasks and a single bare optical fiber are distributed throughout the detector and are pulsed at 3.33 Hz during normal data

5.3 Detector 53

taking. Given the peak efficiency for the MiniBooNE PMTs at ~400 nm, these lasers are pulsed at 397 nm and signals from the dispersion flasks illuminate all PMTs with roughly equal intensities. Interpretations of the signals from the dispersion flasks are somewhat degenerate between effects arising from degrading oil properties and changing PMT performance. This degeneracy is partially broken by the signal from the bare optical fiber, which illuminates a small circle of PMTs near the bottom of the detector and is used to more directly study any evolution of the oil properties.

The most important aspects of the PMT performance probed at 3.33 Hz under normal running conditions (though the system is vetoed in case of coincidence with a beam spill from the BNB) by the laser calibration system are PMT time offsets and gain calibrations. Time offsets due to differing transit times for each readout system are obtained by a simple comparison of the observed laser signal arrival time to the known laser pulse, while also considering travel time for the laser light. The gain of individual PMTs can vary in subtle but important ways, and these effects are calibrated by normalizing the response of each PMT to a single value, based on the input intensity of the laser light. The calibrated time offsets are critical to the detector's ability to separate the Čerenkov signatures from different particles, most notably those connected by decay processes, while the gain corrections allow for precise measurements of particle energy uniform in production position and direction.

Even more crucial to the study of $\bar{\nu}_{\mu}$ CCQE interactions, cosmic-ray muons and a dedicated calibration system allow the muon reconstruction algorithm to be verified against data. The detector response to muons is independently measured by observation of the energy and direction of cosmic-ray muons up to 800 MeV. A scintillator hodoscope directly above the detector and seven scintillator cubes at various depths within the detector are used to track these particles. Figure 5.15 shows the layout of this system in the MiniBooNE detector.

Each cube is connected by an optical fiber to a PMT for readout. The direction of cosmic-ray muons are measured in the hodoscope, and they may be identified as stopping in one of the scintillation cubes by the observation of a decay electron produced inside the cube. With knowledge of the cube's position and the muon's incident position and angle, it's energy can be calculated based on how much oil it crossed and the Bethe-Block formula for energy loss. In this way, the muon reconstruction algorithm can be verified against data for a variety of muon energies. After all calibration studies, the energy (angle) resolution for muons improves from 12 % (5.4 deg) at 100 MeV to 3.4 % (1.0 deg) at 800 MeV. More details of this reconstruction are given in the next section.

5.3.5 Analysis Tools

This section describes the connection between the PMT signals and the analysis of $\bar{\nu}_{\mu}$ CCQE interactions.

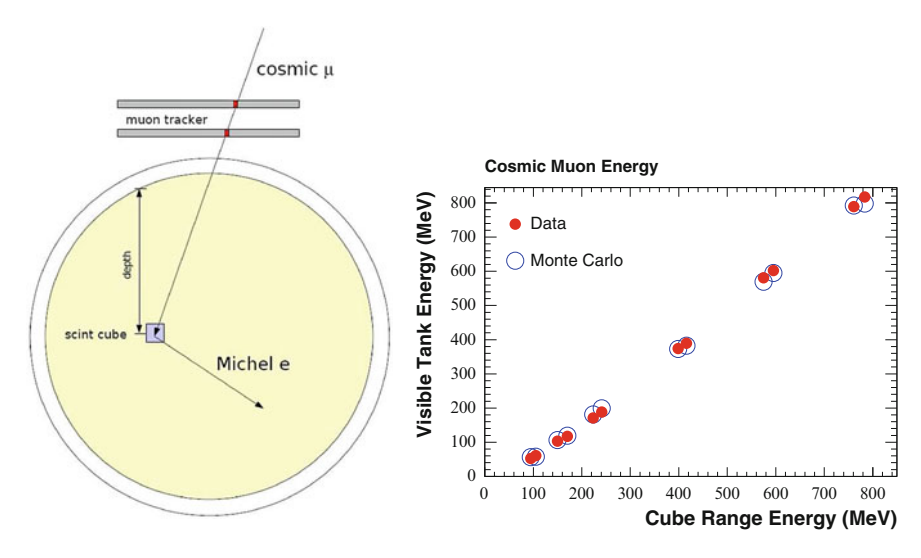


Fig. 5.15 Cartoon of the muon calibration system (*left*) and the relationship between muon energy and range in data and simulation subsequent to calibrations (*right*). Only one of the seven scintillator cubes are shown in the *left figure*, and the image is taken from [2]

A total of 16 triggers may activate the data acquisition (DAQ) system for a total rate of ${\sim}26\,\text{Hz}$ under normal running conditions, and are used a variety of calibration purposes and physics analyses [26,27]. Up to 5 Hz are due to the primary BNB trigger, and in this case the DAQ records PMT charge and time information from all 1,520 phototubes for a total of 19.2 μs beginning ${\sim}5\,\mu s$ before the 1.6 μs long proton spill. Cosmic-ray muons stopped in the signal region prior to the start of the DAQ window may decay in time with the BNB spill, so PMT activity 5 μs before proton delivery is monitored and used to minimize this contamination. Activity is recorded subsequent to the beam window for more than 10 μs to observe electrons from the at-rest decay of muons (hereafter referred to as "Michel" electrons) produced either directly or indirectly through the primary neutrino interaction.

The PMT timing information is used to associate clusters of activity with the signature of a single particle using PMT "hits"; temporal groups of hits form "subevents". A PMT pulse passing the discriminator threshold of $\sim\!\!0.1$ photoelectrons is defined as a hit, and forms the basic unit of the observed signal intensity. A group of PMT activity with at least 10 hits within a 200 ns window and individual hit times less than 10 ns apart, while allowing for at most two spacings of 10–20 ns, defines a subevent. These subevents separate particles whose transit emits significant amounts of Čerenkov light with high efficiency, and so are primarily used isolate the signatures and topologies of muons and electrons. Interactions of $\bar{\nu}_{\mu}$ CCQE typically yield two subevents, the first from the prompt μ^+ , and the second from its decay positron. Figure 5.16 shows the timing and PMT hit signature of a typical $\bar{\nu}_{\mu}$ CCQE event.

5.3 Detector 55

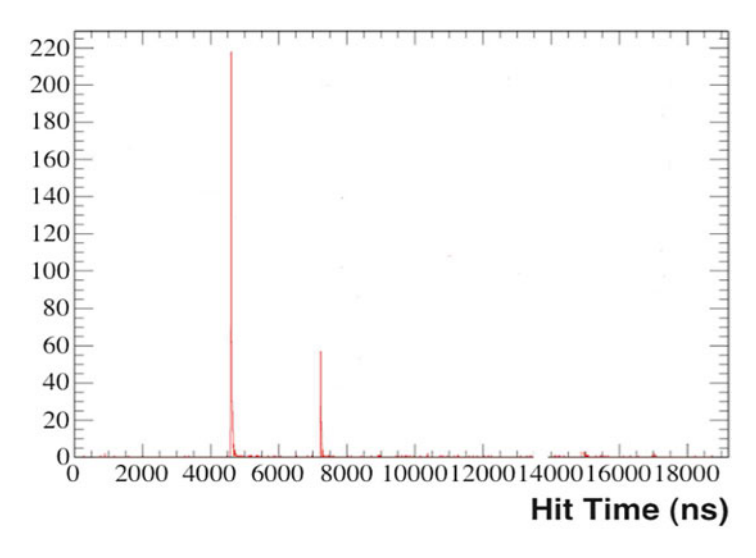


Fig. 5.16 Typical PMT hit (ordinate axis) and timing signature of a $\bar{\nu}_{\mu}$ CCQE event. The prompt μ^+ arrives in time with the BNB spill (from 4,600–6,200 ns relative to the beginning of the DAQ clock) with 100's of MeV in kinetic energy, while the Michel is observed a time characteristic of the muon lifetime later with an energetic endpoint of \sim 53 MeV. Their signatures are easily separated with the subevent definition

The pattern, timing, and total charge of prompt Čerenkov radiation collected by the PMTs in the first subevent are used to identify muon kinematics, the quantity most important to the main result of this dissertation. A likelihood function is compared to the topology and timing of the observed PMT hits:

$$\mathcal{L}(\mathbf{x}) = \prod_{\text{unhit PMTs } i} (1 - P(i \text{ hit}; \mathbf{x})) \times \prod_{\text{hit PMTs } i} P(i \text{ hit}; \mathbf{x}) f_q(q_i; \mathbf{x}) f_t(t_i; \mathbf{x}), \quad (5.1)$$

where $P(i \text{ hit}; \mathbf{x})$ is the probability for PMT i to register a hit given the muon vertex and kinematic vector \mathbf{x} , and $f_q(f_t)$ is a probability distribution function (PDF) for the hit to return the measured charge (time) $q_i(t_i)$. As the energy range of particles observed by MiniBooNE is sensitive to the mass difference between muons and electrons, an electron's path of travel in the MiniBooNE detector is more likely to be deflected compared to a muon's via the Bremstrahlung and multiple scattering processes. Electrons may also create electromagnetic showers, and this leads to distinct Čerenkov topologies and therefore different f_q and f_t PDFs for the two charged leptons. Figure 5.17 compares typical electron and muon timing and charge signatures in MiniBooNE.

The vector \mathbf{x} is composed of the particle's time, energy and position at creation, as well as its momentum projections along the azimuthal and polar angles in spherical coordinates. The negative logarithm of the likelihood function in Eq. (5.1) simultaneously varies these seven parameters while comparing to the observed

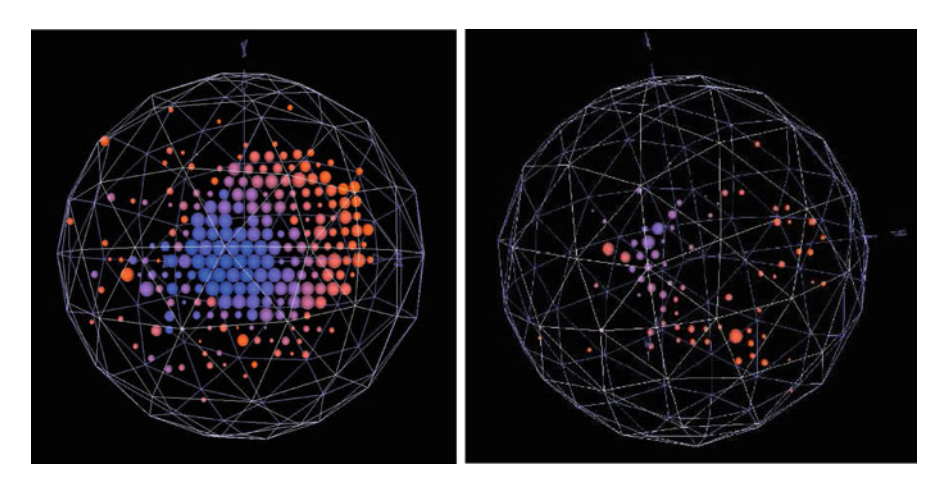


Fig. 5.17 Typical PMT hit topology and timing for muon (*left*) and electron (*right*) candidate events in MiniBooNE data. PMT charge is correlated to the size of the displayed hits, while timing is given by the color spectrum, where *blue* hits arrived earliest and *red* hits arrived last

PMT hits. The parameters from the maximized likelihood function yield the reconstructed lepton kinematics. A two-track version of this reconstruction was also developed to identify π^0 candidate events, and the angular and energy resolutions of this reconstruction to all three particle species, operating Eq. (5.1) under the appropriate hypothesis, are given in Fig. 5.18. Further details on this reconstruction can be found in [28].

The direct and high-resolution observation of muon properties using this reconstruction further motivates the choice of emphasizing the $\bar{\nu}_{\mu}$ CCQE cross section as a function of muon kinematics as the main result of this work, while the statistics of the data set also yield unprecedented sensitivity to the behavior of the μ^+ in $\bar{\nu}_{\mu}$ CCQE interactions.

References

- A.A. Aguilar-Arevalo et al. [MiniBooNE Collaboration], The neutrino flux prediction at MiniBooNE. Phys. Rev. D79, 072002 (2009)
- A.A. Aguilar-Arevalo et al. [MiniBooNE Collaboration], Nucl. Instrum. Methods A599, 28 (2009)
- H. Greinacher, The ionometer and its application to the measurement of radium and Röntgen rays. Physikal. Zeitsch. 15, 410 (1914)
- 4. See http://nagysandor.eu/AsimovTeka/tevatron_hu/multiturn.html (2000)
- B. Worthel et al. Booster Rookie Book (1980). http://www-bdnew.fnal.gov/operations/rookie_books/Booster_V4.1.pdf
- M. Sorel, Search for sterile neutrinos using the MiniBooNE beam. Ph.D. thesis, Columbia University, 2005

References 57

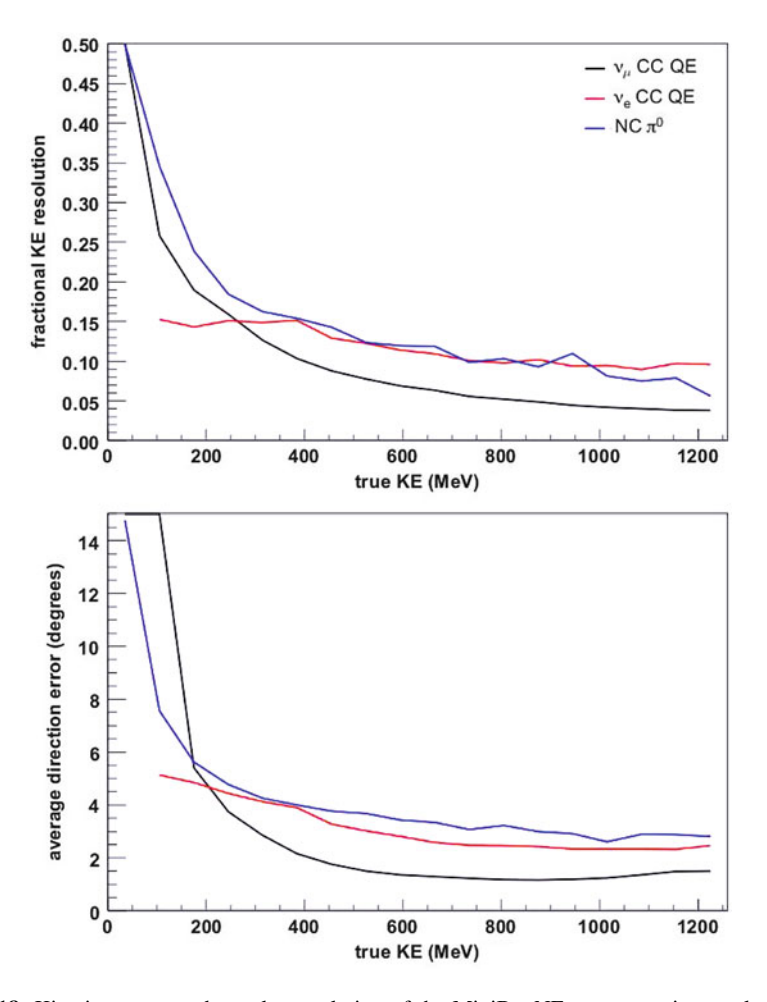


Fig. 5.18 Kinetic energy and angular resolution of the MiniBooNE reconstruction to electrons, muons, and neutral pions. Figure from [28]

- 7. D. Schmitz, A measurement of hadron production cross-sections for the simulation of accelerator neutrino beams and a search for muon neutrino to electron neutrino oscillations in the $\Delta m^2 \sim 1 \, \text{eV}^2$ region. PhD Thesis, Columbia University (2008)
- 8. N.V. Mokhov, S.I. Striganov, MARS15 overview. AIP Conf. Proc. 896, 50 (2007)
- 9. See http://geant4.web.cern.ch/geant4/UserDocumentation/UsersGuides/PhysicsReferenceManual/html/node110.html (2003)
- A. Heikkinen, N. Stepanov, J.P. Wellisch, Bertini intra-nuclear cascade implementation in Geant4. arXiv:nucl-th/0306008
- G. Folger, V.N. Ivanchenko, J.P. Wellisch, The binary cascade model. Eur. Phys. J. A21, 407 (2004)
- 12. M.G. Catanesi et al. [HARP Collaboration], Eur. Phys. J. C52, 29 (2007)
- 13. S. Brice, MiniBooNE Note 257 (2008)
- 14. J.R. Sanford, C.L. Wang, Brookhaven National Laboratory Note 11299 (1967)

- 15. The CERN Program Library (CERNLIB) (2009), see cernlib.web.cern.ch/cernlib
- R.J. Glauber, in *Lectures in Theoretical Physics*, ed. by W.E. Britten et al. vol. 1 (Interscience, New York, 1959)
- 17. M. Wilking, Measurement of neutrino induced, charged current, charged pion production. PhD Thesis, University of Colorado (2009)
- 18. S. Agostinelli et al. Nucl. Instrum. Methods A506, 250 (2003)
- 19. G. Collazuol et al. Nucl. Instrum. Methods **449**, 609 (2000)
- 20. S. Kopp, Accelerator neutrino beams. Phys. Report. 439, 101 (2007). arXiv:0609129
- I. Stancu et al. The MiniBooNE Detector Technical Design Report (2001). http://www-boone. fnal.gov/about_boone/
- A.A. Aguilar-Arevalo et al. [MiniBooNE Collaboration], Measurement of the neutrino neutralcurrent elastic differential cross section. Phys. Rev. D82, 092005 (2010)
- 23. A.A. Aguilar-Arevalo et al. [MiniBooNE Collaboration], Neutrino and antineutrino cross sections at MiniBooNE. AIP Conf. Proc. 1382, 271 (2011)
- S. Brice et al., Photomultiplier tubes in the MiniBooNE experiment. Nucl. Instrum. Methods A562, 97 (2006)
- 25. R.B. Patterson, A search for muon neutrino to electron neutrino oscillations at $\Delta m^2 > 0.1 \text{ eV}^2$. PhD Thesis, Princeton University (2009)
- A.A. Aguilar-Arevalo et al. [MiniBooNE Collaboration], A search for core-collapse supernovae using the MiniBooNE neutrino detector. Phys. Rev. D81, 032001 (2010)
- 27. A.A. Aguilar-Arevalo et al. [MiniBooNE Collaboration], First measurement of ν_{μ} and ν_{e} events in an off-axis horn-focused neutrino beam. Phys. Rev. Lett. **102**, 211801 (2009)
- R.B. Patterson et al. The extended-track event reconstruction for MiniBooNE. Nucl. Instrum. Methods A608, 206 (2009)

Chapter 6

Introduction to the Cross-Section Measurement

6.1 Overview

This dissertation describes the first measurement of the muon antineutrino CCQE cross section with $\langle E_{\bar{\nu}} \rangle < 1$ GeV. Before exploring the details, it is helpful to first describe the overall strategy and identify the areas of the calculation deserving of the most attention.

Generically, for one to measure a differential cross section in the distribution X, given a data set d, total background b, using a detector housing a number of interaction targets N with detection efficiency ϵ and a total $\bar{\nu}_{\mu}$ exposure Φ , the formula is rather simple:

$$\frac{d\sigma}{dX_i} = \frac{\sum_j U_{ij} \left(d_j - b_j \right)}{\Delta X_i \, \epsilon_i \, \Phi \, N},\tag{6.1}$$

where i indexes the region of measurement in the absence of detector effects, ΔX_i is the width of this region, j labels the same region as observed by the detector, and the matrix U_{ij} connects the two. The other cross-section configurations measured in this work are simple extensions of Eq. (6.1) and will be discussed later. Before we proceed with a cross-section calculation, an analysis sample must be identified. In describing this in the next section, it will become clear that a major complication of this analysis is the presence of large and nominally uncertain backgrounds.

6.2 Event Selection

Optimizing the sample to study a particular type of interaction always involves a balance between retaining as many high-quality signal events as possible while

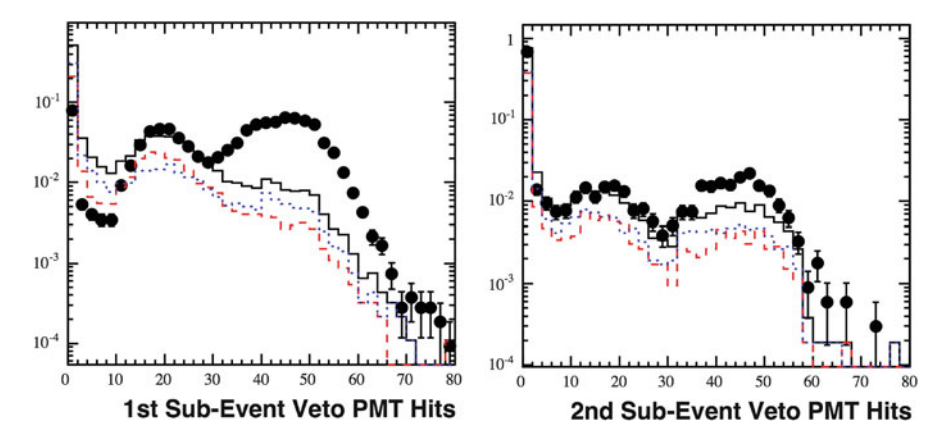


Fig. 6.1 Veto hits for early neutrino-mode data and MC for the first two subevents. Points are data, the *dotted* (*dashed*) *blue* (*red*) histogram is ν_{μ} CCQE (all non- ν_{μ} CCQE) and the *solid line* is total MC. All distributions are normalized to unit area. Cosmic rays are not simulated, and this is the origin of the shape discrepancy between data and MC in the first subevent. Figure from [1]

minimizing the contamination from background interactions. The selection and its efficacy for the antineutrino-mode CCQE sample follows:

- 1. Veto hits < 6, all subevents
- 2. First subevent in beam window: 4,000 < T(ns) < 7,000, where T is the average PMT hit time
- 3. Two subevents
- 4. Reconstructed vertex < 500 cm from tank center, first subevent
- 5. $T_{\mu} > 200 \,\text{MeV}$ (kinetic energy of first subevent)
- 6. $ln(\mu/e) > 0.0$, first subevent
- 7. Distance between 1st and 2nd subevent vertices > $500 \,\mathrm{cm/GeV} \times T_{\mu}$ $100 \,\mathrm{cm}$
- 8. Distance between 1st and 2nd subevent vertices > 100 cm

Cut 1 simultaneously rejects incoming charged particles and enforces containment of charged particles created in the tank. The upper bound on the acceptable number of veto hits is motivated in Fig. 6.1, where six veto hits accepts low-level PMT noise but rejects most exiting and entering activity. Cut 2 requires the first subevent be in time with the proton beam spill.

To motivate and isolate the effects of selections 3–8, the distribution under examination is presented with all other requirements applied. To avoid placing requirements on subevents that may not exist, the subevent distribution is the lone exception.

Figure 6.2 shows the impact of cuts 3–6. Cut 3 simultaneously ensures there are no final-state pions and the event is consistent with the production of a contained muon. The selection of the sample represented in the subevent figure is cuts 1 and 2, where the veto hit requirement is applied to each subevent present. The large excess in the single subevent bin is dominated by Michel electrons produced in time with

6.2 Event Selection 61

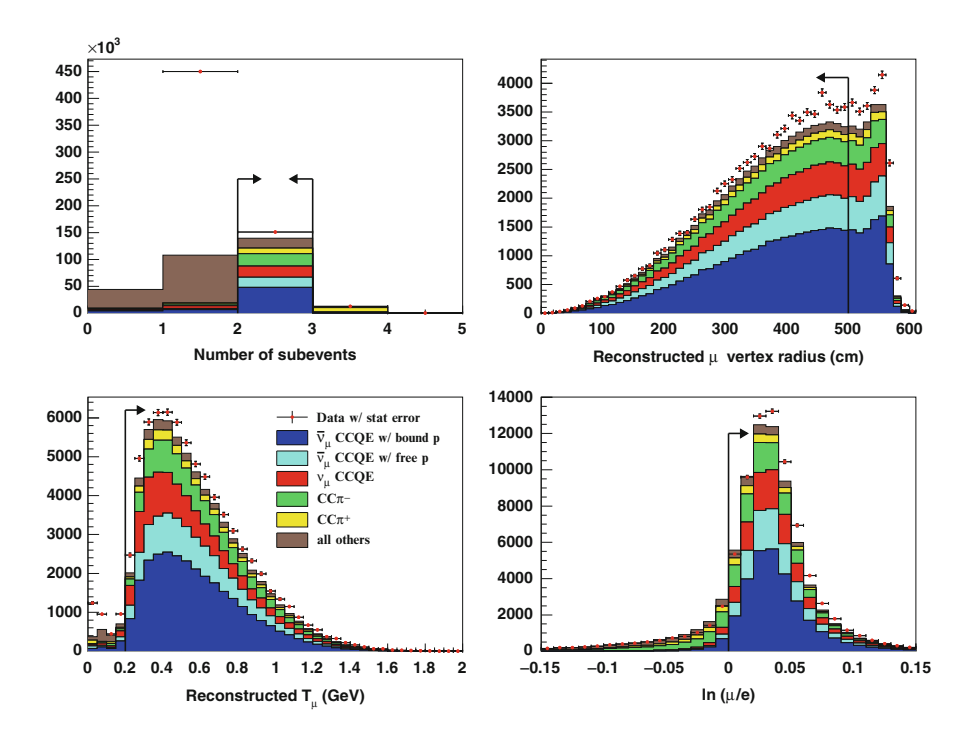


Fig. 6.2 Selection requirements 3–6. Descriptions are given in the text, and distributions are normalized to flux. With the exception of the subevent figure, all distributions have every cut applied except the one indicated in the figure

the beam from cosmic-ray muons, which are not simulated, entering prior to the start of the DAQ window. Cut 4 avoids a class of events that may be reconstructed poorly due to greater sensitivity to PMT coverage. The spike at high radius is due to the relatively dense material in the optical barrier. The requirement of cut 5 also improves reconstruction reliability while avoiding a double-coincidence of the kind of Michel electrons mentioned earlier. Cut 6 enhances the purity of the sample by rejecting many $CC\pi$ events where the pion is energetic enough to produce some Čerenkov light and cause the muon ring to receive a more electron-like score. The $ln(\mu/e)$ variable is found by comparing the muon-like to the electron-like score of the reconstruction described in Sect. 5.3.5.

Cut 7 enhances the sample purity by requiring the distance between the vertices of the two subevents be consistent with the production and subsequent decay of a minimum ionizing particle (MIP). Cut 8 further reduces the small neutral current π background. Cuts 7 and 8 are shown in Fig. 6.3.

Stepwise purity and detection efficiency for the resultant sample is presented in Table 6.1, where values are given for both bound (from the carbon contribution to mineral oil) and free (from the hydrogen content) $\bar{\nu}_{\mu}$ CCQE scattering. A breakdown of the predicted sample composition is given in Table 6.2.

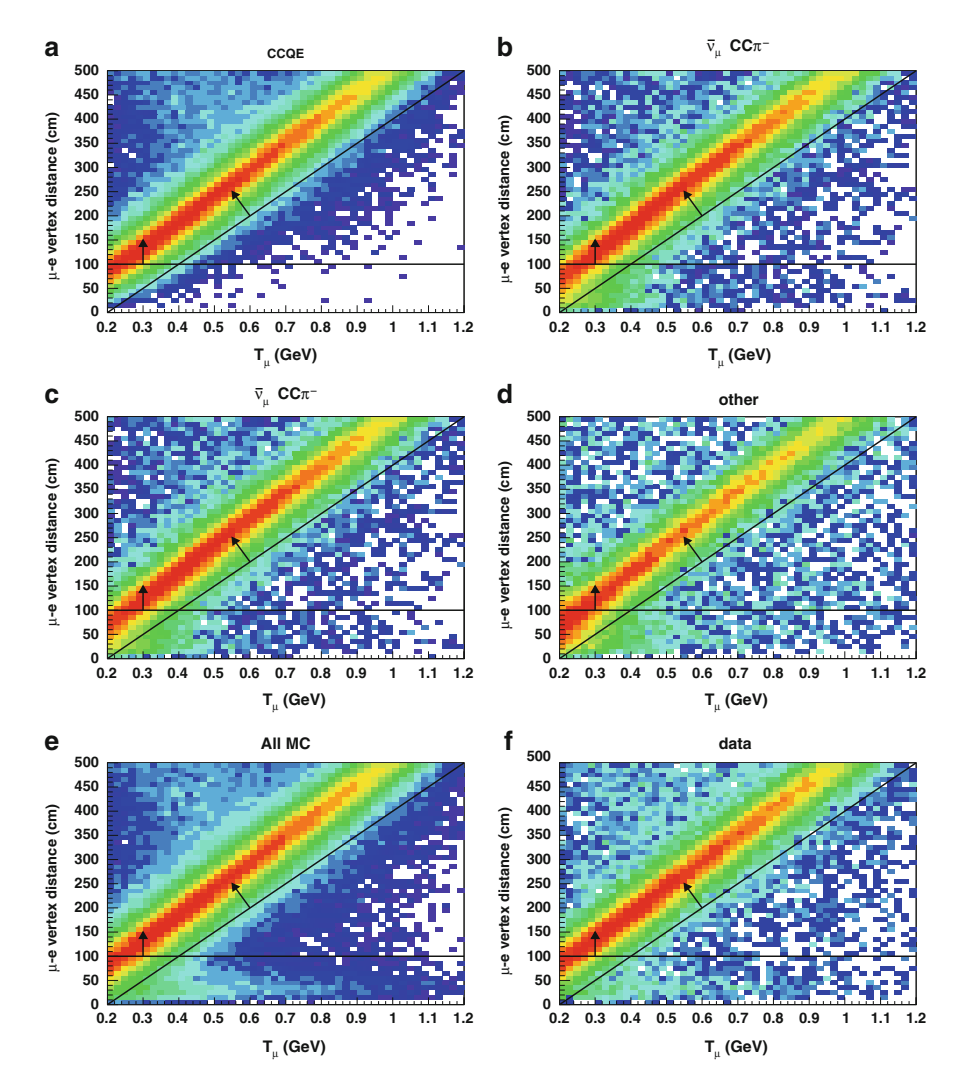


Fig. 6.3 T_{μ} dependent range cut for different channels and samples, as labeled. Events are plotted on a logarithmic scale

From these data we will extract three main cross sections: as a function of neutrino energy, with respect to Q_{QE}^2 (reconstructed four-momentum transfer under the assumption of CCQE interactions), and the minimally model-dependent double-differential cross section as a function of μ kinematics. Reconstructing the incident neutrino energy and the squared four momentum transfer on an event-by-event basis is possible only by assuming the observed interaction is $\bar{\nu}_{\mu}$ CCQE on carbon, and also that it occurs on a single independent nucleon at rest. To begin these

6.2 Event Selection 63

	Purity (%)		Efficiency (%)			
Cut description	¹² C	H ₂	Total	¹² C	H ₂	Total
No cuts	22.6	9.0	32.3	100	100	100
Veto hits < 6, all subevents	19.5	7.7	27.6	50.9	50.4	50.8
First subevent in beam window	19.6	7.7	27.7	50.5	49.9	50.3
$T_{\mu} > 200 \text{MeV}$	25.9	10.1	36.9	44.3	43.4	44.0
Two subevents	33.8	13.2	48.4	39.1	38.3	38.8
Reconstructed radius within 500 cm	34.4	13.5	49.2	32.8	32.1	32.6
μ -e dist. > 500 cm/GeV × T_{μ} - 100 cm μ -e dist. > 100 cm	38.2	15.0	54.3	30.8	30.3	30.6
$\ln\left(\mu/e\right) > 0$	43.2	17.1	61.0	29.6	29.3	29.5

Table 6.1 Purity and detection efficiency for the sample described in this section

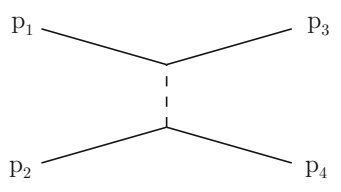
Signal $\bar{\nu}_{\mu}$ CCQE interactions are presented in their bound ("¹²C") and free ("H₂") components and also as the sum. A pre-cut of generated vertex radius < 550 cm for the primary subevent has been applied, and these estimates reflect the measurements and constraints described in Chap. 7

Table 6.2 Predicted composition of the sample described in this section

$\begin{array}{llllllllllllllllllllllllllllllllllll$		
Energy-integrated $\bar{\nu}_{\mu}$ flux 2.93 × 10 ¹¹ $\bar{\nu}_{\mu}$ / cm ² $\bar{\nu}_{\mu}$ CCQE candidate events 71176 $\bar{\nu}_{\mu}$ CCQE efficiency ($R < 550$ cm) 29.5% Interaction Contribution (%) $\bar{\nu}_{\mu} + p$ (bnd) $\rightarrow \mu^{+} + n$ 43.2 $\bar{\nu}_{\mu} + p$ (free) $\rightarrow \mu^{+} + n$ 17.1 $\nu_{\mu} + n \rightarrow \mu^{-} + p$ 16.6 $\bar{\nu}_{\mu} + n \rightarrow \mu^{+} + n + \pi^{-}$ 7.9 $\bar{\nu}_{\mu} + A \rightarrow \mu^{+} + A + \pi^{-}$ 3.3 $\nu_{\mu} + p \rightarrow \mu^{-} + p + \pi^{+}$ 3.1 $\nu_{\mu} + p \rightarrow \mu^{-} + p + \pi^{-}$ 2.5	Integrated POT	10.1×10^{20}
$\begin{array}{ll} \overline{v}_{\mu} \text{ CCQE candidate events} & 71176 \\ \hline v_{\mu} \text{ CCQE efficiency } (R < 550 \text{ cm}) & 29.5 \% \\ \hline \textit{Interaction} & \textit{Contribution } (\%) \\ \hline v_{\mu} + p \text{ (bnd)} \rightarrow \mu^{+} + n & 43.2 \\ \hline v_{\mu} + p \text{ (free)} \rightarrow \mu^{+} + n & 17.1 \\ \hline v_{\mu} + n \rightarrow \mu^{-} + p & 16.6 \\ \hline v_{\mu} + n \rightarrow \mu^{+} + n + \pi^{-} & 7.9 \\ \hline v_{\mu} + A \rightarrow \mu^{+} + A + \pi^{-} & 3.3 \\ \hline v_{\mu} + p \rightarrow \mu^{-} + p + \pi^{+} & 3.1 \\ \hline v_{\mu} + p \rightarrow \mu^{+} + p + \pi^{-} & 2.5 \\ \hline \end{array}$	Mean $\bar{\nu}_{\mu}$ energy	665 MeV
$\begin{array}{lll} & \bar{\nu}_{\mu} \text{ CCQE efficiency } (R < 550 \text{ cm}) & 29.5 \% \\ \hline \textit{Interaction} & \textit{Contribution } (\%) \\ & \bar{\nu}_{\mu} + p \text{ (bnd)} \rightarrow \mu^{+} + n & 43.2 \\ & \bar{\nu}_{\mu} + p \text{ (free)} \rightarrow \mu^{+} + n & 17.1 \\ & \nu_{\mu} + n \rightarrow \mu^{-} + p & 16.6 \\ & \bar{\nu}_{\mu} + n \rightarrow \mu^{+} + n + \pi^{-} & 7.9 \\ & \bar{\nu}_{\mu} + A \rightarrow \mu^{+} + A + \pi^{-} & 3.3 \\ & \nu_{\mu} + p \rightarrow \mu^{-} + p + \pi^{+} & 3.1 \\ & \bar{\nu}_{\mu} + p \rightarrow \mu^{+} + p + \pi^{-} & 2.5 \\ \hline \end{array}$	Energy-integrated $\bar{\nu}_{\mu}$ flux	$2.93 \times 10^{11} \ \bar{\nu}_{\mu} \ / \ \text{cm}^2$
Interaction Contribution (%) $\bar{v}_{\mu} + p \text{ (bnd)} \rightarrow \mu^{+} + n$ 43.2 $\bar{v}_{\mu} + p \text{ (free)} \rightarrow \mu^{+} + n$ 17.1 $v_{\mu} + n \rightarrow \mu^{-} + p$ 16.6 $\bar{v}_{\mu} + n \rightarrow \mu^{+} + n + \pi^{-}$ 7.9 $\bar{v}_{\mu} + A \rightarrow \mu^{+} + A + \pi^{-}$ 3.3 $v_{\mu} + p \rightarrow \mu^{-} + p + \pi^{+}$ 3.1 $\bar{v}_{\mu} + p \rightarrow \mu^{+} + p + \pi^{-}$ 2.5	$\bar{\nu}_{\mu}$ CCQE candidate events	71176
$\begin{array}{cccccccccccccccccccccccccccccccccccc$	$\bar{\nu}_{\mu}$ CCQE efficiency ($R < 550 \text{ cm}$)	29.5 %
$ \frac{\overline{v}_{\mu} + p \text{ (free)} \to \mu^{+} + n}{v_{\mu} + n \to \mu^{-} + p} \qquad 17.1 $ $ \frac{\overline{v}_{\mu} + n \to \mu^{-} + p}{\overline{v}_{\mu} + n \to \mu^{+} + n + \pi^{-}} \qquad 7.9 $ $ \frac{\overline{v}_{\mu} + A \to \mu^{+} + A + \pi^{-}}{v_{\mu} + p \to \mu^{-} + p + \pi^{+}} \qquad 3.3 $ $ \frac{v_{\mu} + p \to \mu^{-} + p + \pi^{+}}{\overline{v}_{\mu} + p \to \mu^{+} + p + \pi^{-}} \qquad 2.5 $	Interaction	Contribution (%)
$\begin{array}{cccccccccccccccccccccccccccccccccccc$	$\bar{\nu}_{\mu} + p \text{ (bnd)} \rightarrow \mu^{+} + n$	43.2
	$\bar{\nu}_{\mu} + p \text{ (free)} \rightarrow \mu^{+} + n$	17.1
	$\nu_{\mu} + n \to \mu^{-} + p$	16.6
$v_{\mu} + p \to \mu^{-} + p + \pi^{+}$ 3.1 $\bar{v}_{\mu} + p \to \mu^{+} + p + \pi^{-}$ 2.5	$\bar{\nu}_{\mu} + n \rightarrow \mu^{+} + n + \pi^{-}$	7.9
$\overline{v}_{\mu} + p \rightarrow \mu^{+} + p + \pi^{-} \qquad 2.5$	$\bar{\nu}_{\mu} + A \rightarrow \mu^{+} + A + \pi^{-}$	3.3
	$\nu_{\mu} + p \to \mu^{-} + p + \pi^{+}$	3.1
	$\bar{\nu}_{\mu} + p \rightarrow \mu^{+} + p + \pi^{-}$	2.5
$\bar{\nu}_{\mu} + p \rightarrow \mu^{+} + \Lambda^{0}$	$\bar{\nu}_{\mu} + p \rightarrow \mu^{+} + \Lambda^{0}$	
$\bar{\nu}_{\mu} + n \to \mu^{+} + \Sigma^{-} \tag{2.0}$		2.0
$\bar{\nu}_{\mu} + p \rightarrow \mu^{+} + \Sigma^{0}$	$\bar{\nu}_{\mu} + p \rightarrow \mu^{+} + \Sigma^{0}$	
$\bar{\nu}_{\mu} + p \to \mu^{+} + n + \pi^{0}$ 2.0	$\bar{\nu}_{\mu} + p \rightarrow \mu^{+} + n + \pi^{0}$	2.0
$\nu_{\mu} + n \to \mu^{-} + n + \pi^{+}$ 0.7	$\nu_{\mu} + n \rightarrow \mu^{-} + n + \pi^{+}$	0.7
$\nu_{\mu} + n \to \mu^{-} + p + \pi^{0}$ 0.8	$\nu_{\mu} + n \rightarrow \mu^{-} + p + \pi^{0}$	0.8
$\nu_{\mu} + A \to \mu^{-} + A + \pi^{+}$ 0.2	$\nu_{\mu} + A \rightarrow \mu^{-} + A + \pi^{+}$	0.2
All other 0.5	All other	0.5

These estimates reflect the measurements and constraints described in the following chapters

Fig. 6.4 An arbitrary t-channel exchange



calculations, we start with an arbitrary t-channel exchange between two particles $1+2 \rightarrow 3+4$ shown in Fig. 6.4. The momentum transfer q^2 in this interaction is given by:

$$q^2 = (p_1 - p_3)^2 = (p_2 - p_4)^2,$$
 (6.2)

where p is the particle's four-momentum. Using the notation of four-vectors and focusing on the momentum transfer between the 1 and 3 particles,

$$q^{2} = (E_{1} - E_{3}, \vec{p}_{1} - \vec{p}_{3}) = (E_{1} - E_{3})^{2} - |\vec{p}_{1} - \vec{p}_{3}|^{2}$$

$$= E_{1}^{2} + E_{3}^{2} - 2E_{1}E_{3} - (|\vec{p}_{1}|^{2} + |\vec{p}_{3}|^{2} - 2|\vec{p}_{1}||\vec{p}_{3}|\cos\theta_{1-3}), \quad (6.3)$$

 \vec{p} is the three-momentum vector, and θ_{1-3} is the scattering angle of particle 3 with respect to the direction of particle 1. In the case of a neutrino for particle 1, $|\vec{p}_1| = E_1$ to excellent approximation. For a ν_μ or $\bar{\nu}_\mu$ CC interaction, particle 3 is a muon, and

$$Q^{2} = -q^{2} = 2E_{\nu}^{QE}(E_{\mu} - |\vec{p}_{\mu}|\cos\theta_{\nu-\mu}) - m_{\mu}^{2}, \tag{6.4}$$

where, for convenience, Q^2 is defined to be a positive quantity. The form of Eq. (6.4) is particularly useful for accelerator-based neutrino measurements, as the scattering angle $\theta_{\nu-\mu}$ is simply the observed angle of the muon relative to the beam direction, hereafter simply referred to as θ_{μ} . However, these neutrino sources typically feature a broad range of neutrino energies, and so additional information is needed to find Q^2 . To reconstruct the incident neutrino energy, we employ the same assumptions as before and also introduce an at-rest proton target and an outgoing neutron in the hadronic vertex, appropriate to $\bar{\nu}_{\mu}$ CCQE. Note that the kinematic assumption on the proton is wildly inaccurate; however, as the momentum distribution about any spatial direction must be centered around zero, with enough statistics the bias

6.2 Event Selection 65

is small and acceptable. Neglecting the small binding energy for interactions with bound nucleons, four-momentum conservation gives

$$(E_{\nu}^{QE} + m_p, \vec{p}_{\nu}) = (E_{\mu} + E_n, \vec{p}_{\mu} + \vec{p}_n). \tag{6.5}$$

Note the neutrino energy is labeled to explicitly recognize its assumption of a CCQE interaction. Eliminating the neutron kinematics and again neglecting the neutrino mass gives:

$$m_p^2 + E_\mu^2 + 2(m_p E_\nu^{QE} - E_\mu E_\nu^{QE} - m_p E_\mu) = m_n^2 + |\vec{p}_\mu|^2 - 2E_\nu^{QE} |\vec{p}_\mu| \cos\theta_\mu.$$
 (6.6)

Rearranging Eq. (6.6) yields a determination of the neutrino energy solely in terms of muon kinematics:

$$E_{\nu}^{QE} = \frac{m_n^2 - m_p^2 - m_{\mu}^2 - 2m_p E_{\mu}}{2\left(m_p - E_{\mu} + |\vec{p}_{\mu}|\cos\theta_{\mu}\right)}.$$
 (6.7)

We can use this quantity in finding the four-momentum transfer, carrying over the "QE" label to again recognize the propagated CCQE assumption:

$$Q_{OE}^{2} = 2E_{\nu}^{QE} \left(E_{\mu} - p_{\mu} \cos \theta_{\mu} \right) - m_{\mu}^{2}. \tag{6.8}$$

As many theoretical groups predict a sizable contribution from an unexpected background to the MiniBooNE CCQE sample (Sect. 4.4.1), the assumption of CCQE interactions embedded in E_{ν}^{QE} and Q_{QE}^2 is particularly troubling. This is the primary motivation for highlighting the double-differential cross section $\frac{d^2\sigma}{dT_{\mu}d\cos\theta_{\mu}}$ as the main result of this work. Nevertheless, producing cross sections in E_{ν}^{QE} and Q_{OE}^2 can be helpful to facilitate historical comparisons.

The full MiniBooNE $\bar{\nu}_{\mu}$ CCQE sample in E_{ν}^{QE} , Q_{QE}^{2} and the kinematics of the muon is shown in Fig. 6.5, as well as the two-dimensional muon kinematical ratio of data to the prediction.

Table 6.2 estimates the $\bar{\nu}_{\mu}$ CCQE sample features a purity of ~60 %. With a signal:background rate approaching 1:1, it is crucial to evaluate how well these backgrounds are understood before they can be reliably subtracted from the data to produce $\bar{\nu}_{\mu}$ CCQE cross sections. The next chapter is dedicated to the various measurements and constraints obtained for the dominant backgrounds.

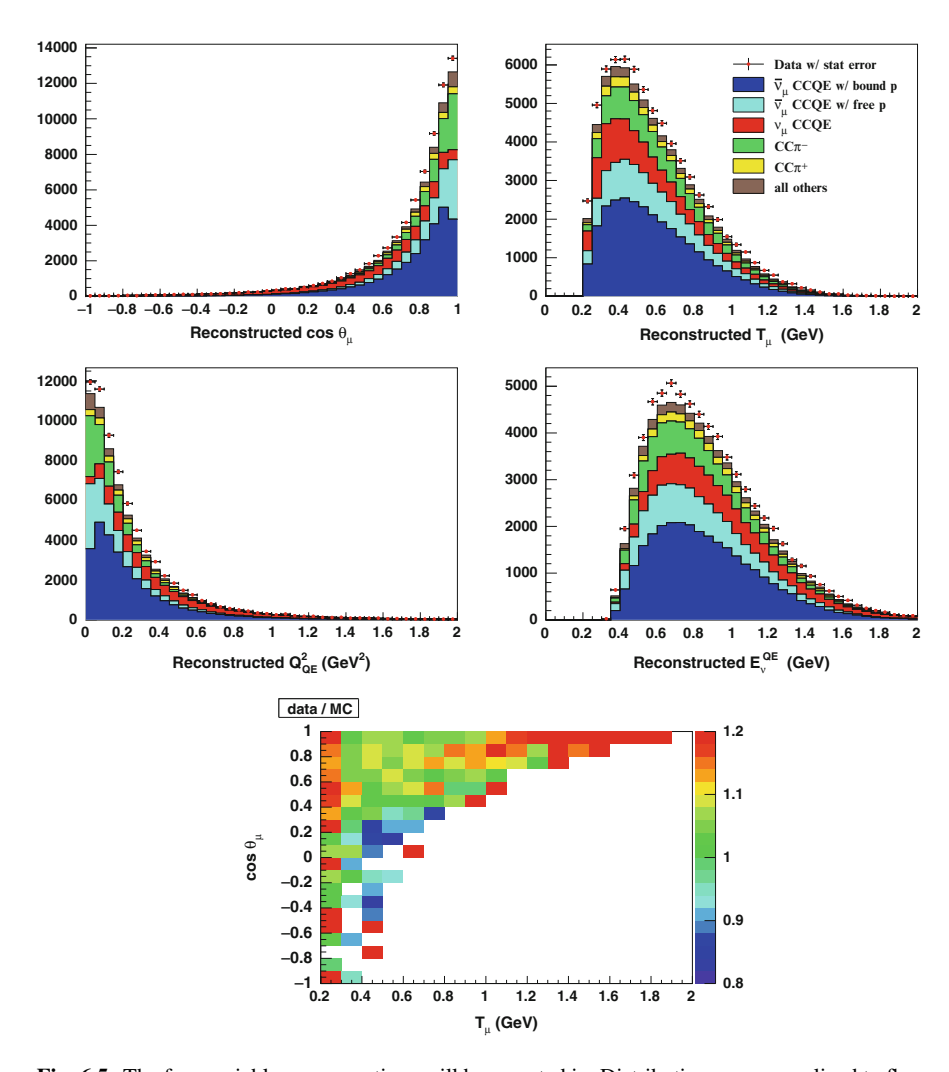


Fig. 6.5 The four variables cross sections will be reported in. Distributions are normalized to flux

Reference

1. J.R. Monroe, A combined ν_μ and ν_e oscillation search at MiniBooNE. Ph.D. thesis, Columbia University, 2006

Chapter 7 Background Measurements and Constraints

With backgrounds accounting for nearly half of the total sample studied, their precise contribution and kinematics must be rigorously verified before a reliable background subtraction can be made. This section presents various measurements and constraints on these processes. As ν_{μ} and $CC\pi^{-}$ interactions are dominant, particular attention is paid to understanding their contribution.

7.1 Measurements of the v_{μ} Background

7.1.1 Motivation

Interactions induced by ν_{μ} events form the largest single background to the $\bar{\nu}_{\mu}$ CCQE sample, accounting for ~20% of the selected events, and half of the total background. Given the high-quality pion production data from the HARP experiment and the litany of ν_{μ} cross-section measurements from the MiniBooNE neutrino-mode data [1–7], one might assume the ν_{μ} contribution to the antineutrino-mode data is well-constrained. However, as Fig. 7.1 shows, the majority of the ν_{μ} events contributing to the antineutrino-mode data are produced in a kinematic region of the parent π^+ that is not constrained by the HARP data. The particulars of Fig. 7.1 warrant a few more remarks:

- both parent pion distributions leading to the "wrong-sign" contribution (neutrinos in antineutrino mode and vice versa) peak at the lowest opening angles. This shows how these events contribute to the beam: their transverse momentum is insufficient to be significantly altered by the magnetic field, and so their path is much less deflected compared to pions created at larger θ_{π} .
- the antineutrino contribution to the neutrino-mode data is minuscule in comparison to the converse. This is due to a convolution of flux and cross-section

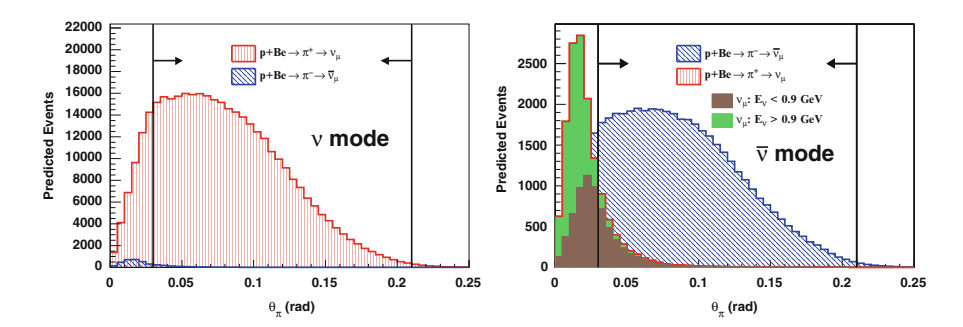


Fig. 7.1 Predicted angular distributions of pions with respect to the incident proton beam (θ_{π}) producing ν_{μ} and $\bar{\nu}_{\mu}$ in neutrino (*left*) and antineutrino (*right*) modes. Only pions leading to ν_{μ} and $\bar{\nu}_{\mu}$ events in the detector are shown, and all distributions are normalized to 10.1×10^{20} protons on target. *Arrows* indicate the region where HARP data [8] are available

effects that simultaneously serve to enhance the neutrino component while the antineutrino contribution is suppressed: the leading-particle effect at the beryllium target (the p + Be initial state has a net positive charge) naturally leads to the creation of roughly twice as many π^+ as π^- , and neutrino cross sections are typically around three times as large as antineutrino cross sections around 1 GeV.

- the above observation explains why this is a complication unique to antineutrino mode: the wrong-sign component in neutrino-mode data is small enough so that even for large fractional uncertainty on this background, the resultant error on the ν_{μ} cross-section measurements are negligible compared to other systematic uncertainties.
- as seen in the antineutrino-mode distribution, high-energy ν_{μ} 's are strongly correlated with the decay of π^+ created at very small opening angles. This indicates their flux is more poorly constrained by the HARP data compared to lower-energy ν_{μ} 's. So, not only is the overall ν_{μ} flux in antineutrino mode highly uncertain, the accuracy of the extrapolated ν_{μ} flux prediction may be a function of neutrino energy.

The above observations motivate dedicated studies of the ν_{μ} contribution to the antineutrino-mode beam, and in as many exclusive regions of neutrino energy as is allowed by statistics to examine the flux spectrum.

Many other experiments deal with this background in a much more direct way: they employ a magnetic field to determine the sign of the outgoing lepton. This provides $\nu/\bar{\nu}$ discrimination for CC interactions on an event-by-event basis. Modern examples of magnetized neutrino oscillation experiments include MINOS [9], NOMAD [10], and the T2K near detector [11].

The analyses in this section provide a first demonstration that, in the absence of a magnetic field, ν_{μ} and $\bar{\nu}_{\mu}$ content of any mixed neutrino flux can be modestly separated using statistical methods. These methods could also aid current and future neutrino experiments that will test for CP violation in the lepton sector using large

unmagnetized detectors. This includes experiments such as NO ν A [12], the T2K far detector, LBNE [13], LAGUNA [14], and Hyper-K [15]. Also, it has been argued that the separation of charged-current neutrino and antineutrino events afforded by these kinds of analyses may be sufficient to meet the lofty physics goals of neutrino factories [16]. Finally, the MINER ν A [17] neutrino cross-section experiment could gain crucial kinematic and statistical sensitivity by using these kinds of techniques to analyze CC events not accepted into their magnetized muon calorimeter.

The following sections present the first measurement of the ν_{μ} component of an antineutrino-mode beam observed by a non-magnetized detector. Three statistical techniques are used to constrain this ν_{μ} background to a sub-dominant uncertainty in the extraction of the $\bar{\nu}_{\mu}$ CCQE cross sections. These analyses are published in [18] and [19].

7.1.2 General Strategy

To statistically measure the wrong-sign background, we must exploit asymmetries in the way neutrinos, antineutrinos, and their byproducts interact in the detector. Analyzing the various samples gives a direct handle on their contribution to the data, which is the only knowledge necessary for performing the background subtraction. However, with the valuable cross-section data from MiniBooNE's neutrino-mode run, we can extract information about the ν_{μ} flux as well, which can be used to test the accuracy of the extrapolation of the HARP data (described in Sect. 5.2.4) into the low-angle region. The ν_{μ} channels contributing to the physics samples we will analyze are dominated by CCQE and $CC\pi^+$ interactions, and results from their cross-section analyses in the neutrino-mode data [1, 4] are applied to the antineutrino-mode simulation. With accurate cross sections implemented into the Monte Carlo (MC) simulation, differences of the observed rates and the expectation from simulation reflect the accuracy of the model-dependent ν_{μ} flux prediction.

The relevance of the measured ν_{μ} cross sections to the antineutrino-mode beam depends on the relative overlap in the ν_{μ} spectra between the two running modes. As the ν_{μ} π^+ -parent particles are sign-selected in neutrino mode and feature a focusing peak, while their acceptance in antineutrino mode is mostly due to low-angle and high energy production, it is reasonable to expect the relative ν_{μ} spectra to be drastically different. Figure 5.9 shows this to be the case, where the *produced* ν_{μ} flux spectrum in antineutrino mode is significantly harder compared to the ν_{μ} 's in neutrino-mode running. If the antineutrino-mode data were sensitive to the details of the differing spectra, this would indicate the relevance of the observed ν_{μ} cross sections is only marginal, and interpretations of these analyses as flux measurements would be inaccurate. Fortunately, Fig. 7.2 shows that the *accepted* spectrum of ν_{μ} 's in the CCQE samples across both run modes is very similar. This is mostly due to the rejection of high-energy ν_{μ} 's via the muon containment requirement. The large overlap between these spectra allows the observed ν_{μ}

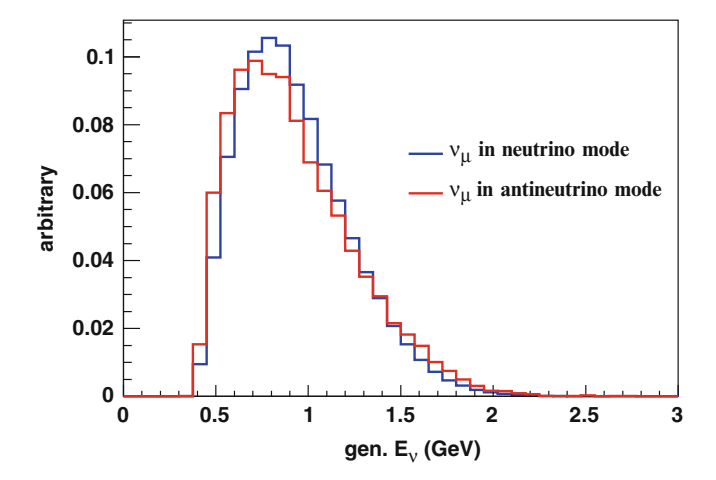


Fig. 7.2 Generated ν_{μ} energy distributions accepted into the neutrino and antineutrino CCQE samples. The substantial overlap indicates the ν_{μ} 's background to the $\bar{\nu}_{\mu}$ CCQE sample are kinematically covered by the ν_{μ} cross sections observed in the neutrino-mode data

interactions in the antineutrino-mode beam to be tightly constrained by the neutrinomode measurements.

In principle, the extracted flux information from these analyses could be used to re-analyze the neutrino-mode data with much stronger constraints on the low-angle region of the ν_{μ} flux prediction. Figure 7.1 shows this region contributes roughly 10% of the ν_{μ} flux in neutrino-mode running. Notice that, due to the small overlap between the parent π^+ phase space across the two running modes, some circularity would be present in such an analysis. Nonetheless, this last advantage exposes a unique feature of this technique: it will be shown that the ν_{μ} flux measurement in antineutrino mode is dominated by uncertainties on the MiniBooNE ν_{μ} cross-section measurements, which are in turn dominated by the π^+ HARP errors through the ν_{μ} flux uncertainty. So the techniques presented here effectively constrain regions of hadroproduction phase-space not covered by the HARP data to the level of precision of the regions that are covered.

A final advantage of determining a flux with this strategy is the cancellation of systematic uncertainties that affect the ν_{μ} processes in the same way across both run mode configurations. These fully-correlated errors are mostly detector-related; in particular, a unique feature of this measurement of the ν_{μ} flux is its independence of many final-state interaction processes.

7.1.3 v_{μ} Flux Measurement Using $CC\pi^+$ Events

The first and most direct measurement of the ν_{μ} background is a simple rate analysis of the three subevent sample. In the neutrino-mode data, this sample is dominated

by $CC\pi^+$ production, mostly through the $\Delta(1232)$ resonance. The three subevents arise from the prompt μ^- and two decay electrons, one each from the μ^- and π^+ :

1:
$$\nu_{\mu} + p(n) \rightarrow \mu^{-} + p(n) + \pi^{+}$$

$$\hookrightarrow \mu^{+} + \nu_{\mu}$$
2/3: $\hookrightarrow e^{-} + \bar{\nu}_{e} + \nu_{\mu}$

$$\hookrightarrow e^{+} + \nu_{e} + \bar{\nu}_{\mu}.$$
(7.1)

The mono-energetic μ^+ from decay-at-rest π^+ is below Čerenkov threshold, and regardless the quick decay of the π^+ would make the μ^+ not separable from the prompt μ^- using timing alone. Also, due to the fast decay of the π^+ , it is effectively random which decay electron yields the second or third subevent. Few other processes in the MiniBooNE detector yield this signal, and the neutrino-mode $CC\pi^+$ sample has a purity of $\sim 90\%$ [1].

From simple electric charge and lepton number conservation, the analogous charged-current single pion mechanism induced by antineutrinos yields a π^- . As stopped- π^- experiences nuclear capture on 12 C at nearly 100% [20], its decay is not observed and therefore it mostly yields two subevents:

1:
$$\bar{\nu}_{\mu} + p(n) \rightarrow \mu^{+} + p(n) + \pi^{-}$$

$$\pi^{-} + {}^{12}C \rightarrow X \qquad (7.2)$$
2: $\hookrightarrow e^{+} + \nu_{e} + \bar{\nu}_{\mu}$

where the remnants of π^- nuclear capture X typically do not yield observable light in the detector. While the π^- nuclear capture mechanism vacates $CC\pi^-$ events from the three subevent sample and so allows for the present measurement of the ν_μ flux, one can readily recognize the sample $CC\pi^-$ events do populate is the main study of this dissertation, that of $\bar{\nu}_\mu$ CCQE. This background is addressed in Sect. 7.2.

Some $CC\pi^-$ events do yield a third subevent, mostly when the π^- decays in flight. Even with this additional background, the simple requirements outlined in the next section give a high-purity sample of ν_μ $CC\pi^+$ events with which we can use to make a powerful measurement of the ν_μ flux in the antineutrino-mode beam.

At the time of the analysis of $CC\pi^+$ events, only a subset of the full 1.0×10^{20} POT taken in antineutrino mode was available. Since fewer data were available at this time, some less reliable runs were used in which absorber blocks accidentally fell into the decay tunnel at the BNB (described in Sect. 5.2.3). These blocks preferentially absorb high-energy π 's and μ 's, reducing the contribution of high-energy ν_{μ} and $\bar{\nu}_{\mu}$ to the beam. Since this measurement is not limited by statistics, the analysis was not updated as more POT became available. This is also the case for the analysis of the $\cos\theta_{\mu}$ distribution (Sect. 7.1.5). Table 7.1 shows the contribution of these absorber-down runs to the total amount analyzed.

Table 7.1 Summary of data periods used in the analyses of $CC\pi^+$ events and the $\cos \theta_\mu$ distribution (Sect. 7.1.5)

Period	POT (e20)
0 absorbers	4.480
1 absorber	0.569
2 absorbers	0.612
Total	5.661

Implementation of the ν_{μ} CC π^+ Cross Section

An important distinction in this analysis is the definition of $CC\pi^+$ events treated as signal. To avoid dependence on final-state interactions, the MiniBooNE neutrino-mode ν_μ $CC\pi^+$ cross section was reported as an observable quantity: specifically, the final state studied consisted of one μ^- , one π^+ , and any number of nucleons [1]. This final state was *not* corrected for final-state interactions. Some of the more important implications are that some amount of nucleon-level $CC\pi^0$ $(\nu_\mu + N \to \mu^- + \pi^0 + N')$ contribute to this sample, while some $CC\pi^+$ events are not present due to the pion charge-exchange $(\pi^\pm + X \leftrightarrow \pi^0 + X')$ and absorption $(\pi^\pm + X \to X')$ processes. While this introduces a level of ambiguity in interpretations between the nucleon-level $CC\pi^+$ process and final-state interactions, it is an experimentally clean signature and may be used to rigorously test the $CC\pi^+$ process when final-state interactions are better understood. As we use this neutrino-mode $CC\pi^+$ result in this work, observable $CC\pi^+$ events are also treated as signal here.

A number of single and double-differential MiniBooNE ν_{μ} CC π^+ cross sections are published in kinematics of the μ^- and π^+ . However, since the present study is a simple rate measurement, it is sufficient to simply implement the total cross section as a function of neutrino energy. Figure 7.3 compares the data to the simulation expectation.

Functionally, the ν_{μ} CC π^+ cross section data is implemented into this analysis through correcting the antineutrino-mode expectation of observable CC π^+ . The ratio data/MC is measured in regions of generated neutrino energy, according to the bin delimitations. Note this is only possible because the exact set of underlying physics parameters, most importantly the single-pion axial masses and the final-state interaction model, are *identical* between the neutrino-mode simulation used to calculate the expectation shown in Fig. 7.3 and the MC used in the present antineutrino-mode analysis. With the observed ν_{μ} CC π^+ cross-section data implemented in this analysis, the rate measurement presented in this section is also a measurement of the ν_{μ} flux contribution to the antineutrino-mode beam.

As will be shown, the uncertainty on this measurement is dominated by error on the ν_{μ} CC π^{+} cross section. To convert the uncertainty from the original measurement to the binning optimized for this analysis, a polynomial of order 4 is fit to the fractional CC π^{+} systematic uncertainty, and the values of this function evaluated in the center for the bins chosen in this analysis are taken as the CC π^{+}

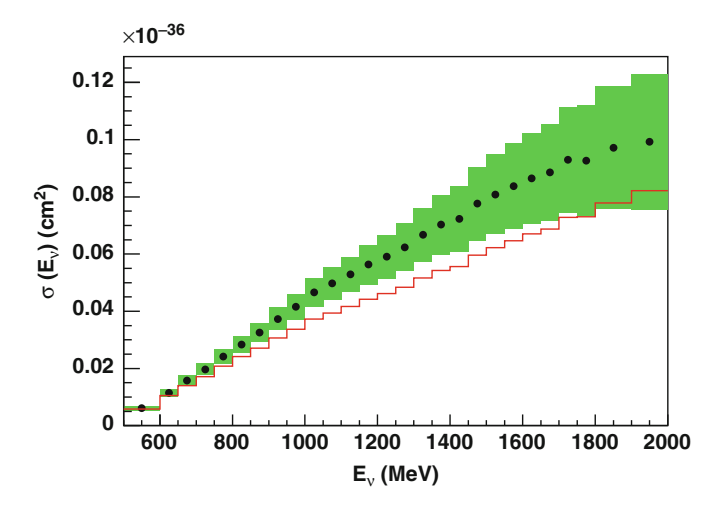


Fig. 7.3 The ν_{μ} CC π^+ total cross section. *Black points* with *green* error bands are MiniBooNE data, and *red* is the MC expectation. Figure reproduced from [1]

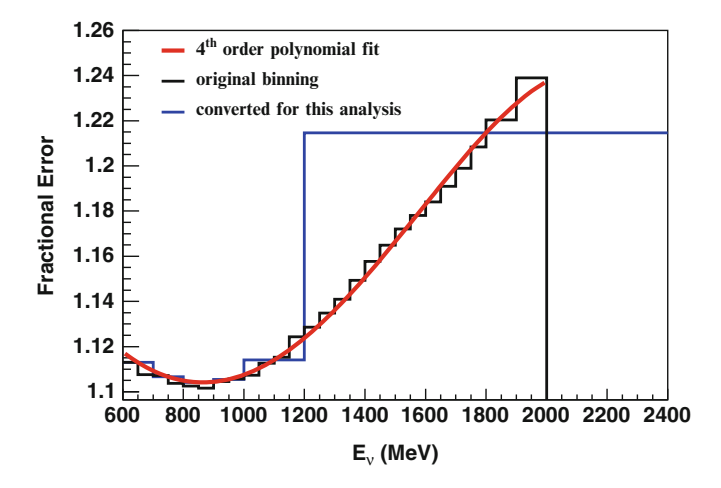


Fig. 7.4 The $CC\pi^+$ fractional uncertainty conversion

uncertainty. Figure 7.4 shows the polynomial function and the two fractional error distributions.

The largest contribution to the uncertainty on the $CC\pi^+$ cross section comes from the neutrino-mode flux uncertainty, which is the only systematic error associated with the cross-section measurement that is also independent of the measurement made here. Because the other $CC\pi^+$ uncertainties are treated as uncorrelated between the neutrino-mode and the antineutrino-mode data, a partial cancellation of errors is ignored in the present ν_μ flux measurement.

The Selected Sample

As mentioned in the previous section, the main requirement to select a $CC\pi^+$ sample is the observation of three subevents. The full selection set is:

- 1. Three subevents
- 2. First subevent in beam window: 4000 < T(ns) < 7000, where T is the average PMT hit time
- 3. All subevents: reconstructed vertex < 500 cm from tank center
- 4. 1st subevent: tank hits > 200
- 5. 2nd and 3rd subevents: tank hits < 200
- 6. All subevents: veto hits < 6
- 7. Distance between calculated end of first subevent and nearest decay electron vertex < 150 cm

Cut 1 requires the event be consistent with the production of three leptons above Čerenkov threshold, and cut 2 assures it be associated with the proton beam spill. Cuts 3 and 4 enhance the reliability of the reconstruction used, and cut 5 requires the final two subevents be consistent with a Michel electron, whose energetic endpoint of \sim 53 MeV leads to roughly 175 tank hits. Cut 6 ensures the leptons be contained and that no charged particles entered the detector. Finally, cut 7 enforces spatial correlation between one of the Michel electrons and the end of the calculated muon path. As mentioned previously, due to the fast decay of the π^+ , timing alone cannot determine the origin of the decay electrons. Using this selection, Table 7.2 presents the detection efficiency and purity for $CC\pi^+$ events, and Table 7.3 summarizes the sample composition.

Table 7.2 Summary of selection cuts in the $CC\pi^+$ sample

Cut #	Description	Efficiency (%)	Purity (%)
0	No cuts	100	10
1	Three subevents	30	29
2	First subevent in event time window	28	34
	4000 <t(ns) 7000<="" <="" td=""><td></td><td></td></t(ns)>		
3	All subevents: reconstructed	23	36
	vertex < 500 cm from tank center		
4	First subevent: tank hits > 200	22	39
5	second and third subevents: tank hits < 200	19	65
6	All subevents: veto hits < 6	16	78
7	Distance between reconstructed		
	end of first subevent and nearest	12	82
	Michel electron vertex < 150 cm		

Purity and efficiency numbers are sequential and are calculated for the "observable $CC\pi^+$ " event signature: 1 μ^- , 1 π^+

Table 7.3 Summary of the $CC\pi^+$ sample in antineutrino mode, including the nucleon-level composition

Integrated POT	5.66×10^{20}
$CC\pi^+$ candidate events	3,268
Observable $CC\pi^+$ efficiency ($R < 550 \text{ cm}$)	12.0 %
Interaction	Contribution (%)
$\nu_{\mu} N \rightarrow \mu^{-} \pi^{+} N \text{ (resonant)}$	64
$\nu_{\mu} A \to \mu^{-} \pi^{+} A \text{ (coherent)}$	7
$\bar{\nu}_{\mu} N \rightarrow \mu^{+} \pi^{-} N' \text{ (resonant)}$	6
$v_{\mu} n \rightarrow \mu^{-} p$	6
$v_{\mu} n \to \mu^- \pi^0 p$	2
$\bar{\nu}_{\mu} p \rightarrow \mu^{+} \pi^{0} n$	1
Other (mostly DIS)	14
"Observable $CC\pi^+$ " $(1 \mu^-, 1 \pi^+)$	82

ν_{μ} Flux Measurement Using CC π^+

The purity of the $CC\pi^+$ sample is sufficiently high to perform a simple background-subtracted rate measurement to test the ν_μ flux. With the notation A for data, B for the expected $\bar{\nu}_\mu$ contributions, C for signal $CC\pi^+$, and D for non- $CC\pi^+$ ν_μ events, we calculate the flux measurement α_ν as

$$\alpha_{\nu} = \frac{A - B}{C + D}.\tag{7.3}$$

The assigned uncertainties on these quantities are as follows:

- A: statistical uncertainty on the data. Following gaussian statistics, the uncertainty is taken as \sqrt{N} , where N is the number of observed events.
- B: $\bar{\nu}_{\mu}$ background. This accounts for 14 % of the sample, mostly $\bar{\nu}_{\mu}$ deep inelastic scattering (DIS) and $CC\pi^-$ events in which the π^- decayed in flight. An overall uncertainty of 30 % is assigned.
- C: signal observable $CC\pi^+$. Per Fig. 7.3, fractional uncertainty on this process varies with neutrino energy and is at a minimum of $\sim 10\%$ around $800 \,\text{MeV}$.
- D: non-signal ν_{μ} events. This accounts for 6% of the sample, and is dominated by ν_{μ} DIS. An overall uncertainty of 30% is assigned.

These fractional uncertainties are propagated onto the ν_{μ} flux measurement α_{ν} with a simple quadrature sum of the uncorrelated uncertainties due to the processes A, B, C and D:

$$\frac{\delta \alpha_{\nu}}{\alpha_{\nu}} = \sqrt{\left(\frac{\delta A}{A}\right)^2 + \left(\frac{\delta B}{B}\right)^2 + \left(\frac{\delta C}{C}\right)^2 + \left(\frac{\delta D}{D}\right)^2} \tag{7.4}$$

$$= \frac{1}{C+D} \sqrt{(\delta A)^2 + (\delta B)^2 + \left(\frac{A-B}{C+D}\right)^2 [(\delta C)^2 + (\delta D)^2]}$$
 (7.5)

To test the accuracy of the simulated flux spectrum, the ν_{μ} flux measurement is performed in exclusive regions of reconstructed energy E_{ν}^{Δ} , where E_{ν}^{Δ} follows the derivation of Eq. (6.7) appropriate to $CC\pi^+$ events:

$$E_{\nu}^{\Delta} = \frac{m_{\Delta}^2 - m_p^2 - m_{\mu}^2 - 2m_p E_{\mu}}{2(m_p - E_{\mu} + |\vec{p}_{\mu}| \cos \theta_{\mu})}.$$
 (7.6)

This reconstruction assumes a quasi-elastic interaction $\nu_{\mu} + N \rightarrow \Delta + N$ for all events. While this is a model-dependent valuation of the neutrino energy, separating the sample into exclusive regions of E_{ν}^{Δ} nevertheless affords statistical sensitivity to the accuracy of the simulated flux spectrum. The ν_{μ} flux measurement in the antineutrino-mode beam using $CC\pi^+$ events is summarized in Table 7.4.

7.1.4 v_{μ} Flux Measurement Using μ^{-} Nuclear Capture

Another opportunity to measure the ν_{μ} flux using nuclear capture is available through the μ^- . Any CC event from ν_{μ} and $\bar{\nu}_{\mu}$ will produce a muon, the μ^- 's of which will produce fewer Michel electrons due to \sim 8% nuclear capture on carbon [20]. An advantage of this analysis over the determination of the ν_{μ} flux in antineutrino mode using the CC π^+ sample is the natural sensitivity to lower ν_{μ} energies. The dominant mechanism for CC π^+ production involves the $\Delta(1232)$

component m	easurement				
E_{ν}^{Δ} range	Mean gen.	Events	Expected	i	ν_{μ} Flux
(MeV)	E _v (MeV)	in data	ν_{μ}	$\bar{\nu}_{\mu}$	Scale α_{ν}
600–700	961	465	556	104	0.65 ± 0.10
700-800	1,072	643	666	118	0.79 ± 0.10
800–900	1,181	573	586	97	0.81 ± 0.10
900-1,000	1,285	495	474	78	0.88 ± 0.11

Table 7.4 Antineutrino-mode ${\rm CC1}\pi^+$ sample details and ν_μ flux component measurement

571

521

3,268

1,000-1,200

1,200-2,400

Inclusive

1,426

1,685

1,266

92

74

563

646

614

3,542

 0.74 ± 0.10

 0.73 ± 0.15

 0.76 ± 0.11

[&]quot;Mean Gen. E_{ν} " is the average generated neutrino energy in each reconstructed energy bin

resonance, and the examination of the ν_{μ} flux using these interactions tests ν_{μ} energies greater than 900 MeV. Fortunately, the present analysis can reach further down in neutrino energy to directly test the flux spectrum of the ν_{μ} 's that are background to the main analysis of $\bar{\nu}_{\mu}$ CCQE interactions.

A complication of this measurement is the substantial component of $\bar{\nu}_{\mu}$ CCQE events present in the analysis samples, and so it is critical to evaluate the bias caused by the assumptions used to predict their contribution. If this bias were significant and the measurement were used to subtract the ν_{μ} background from the data, the final $\bar{\nu}_{\mu}$ CCQE cross section would have an appreciable dependence on the CCQE interaction model. It will be shown that this is the case for the angular analysis of CCQE events presented in Sect. 7.1.5, and so its results are ignored in subtracting the ν_{μ} background from the $\bar{\nu}_{\mu}$ CCQE sample. Meanwhile, it will be shown that the bias caused by assumptions on the $\bar{\nu}_{\mu}$ CCQE cross section in the present μ^- capture analysis is small and negligible compared to other uncertainties.

Implementation of the ν_{μ} CC Cross Sections

The MiniBooNE ν_{μ} CCQE analysis found the shape of the kinematics in data to be described well by the RFG assuming a few empirical parameter adjustments: $M_A=1.35\pm0.17\,\mathrm{GeV}$ and $\kappa=1.007\pm0.012$ [4]. While the observed normalization is also consistent with this model within uncertainties, the data lies ~8% high. Therefore, to implement the ν_{μ} CCQE cross section into the present ν_{μ} flux measurement, the RFG model with $M_A=1.35\,\mathrm{GeV}$ and $\kappa=1.007$ is assumed by simulation and the mild normalization discrepancy is accounted for by reweighting events. The reweighting values are found by a generator-level comparison between the observed MiniBooNE ν_{μ} CCQE total cross section and the RFG with the previously-mentioned parameter adjustments. Figure 7.5 compares the unfolded MC distributions before and after the correction.

The $CC\pi^+$ interactions also contribute significantly to the selected μ^- capture samples. Their interaction rate and kinematics are implemented through the Q_{QE}^2 -based measurement in the neutrino-mode data [4]. This function and its origin are explained further in Sect. 7.2.

It will be shown that the ν_{μ} CCQE and CC π^+ interactions represent more than 94% of the ν_{μ} channels contributing to the μ^- capture samples. With both the kinematics and the normalization of these interactions implemented into the antineutrino-mode MC, the rate measurement of the ν_{μ} contribution to the μ^- capture analysis samples may be cleanly interpreted as measurement of the ν_{μ} flux component of the antineutrino-mode beam.

Muon Capture Model and Event Selection

In mineral oil, stopped μ^- are captured on carbon nuclei with a probability of 7.78 \pm 0.07 % [20]. For such capture events in MiniBooNE, typically little or no

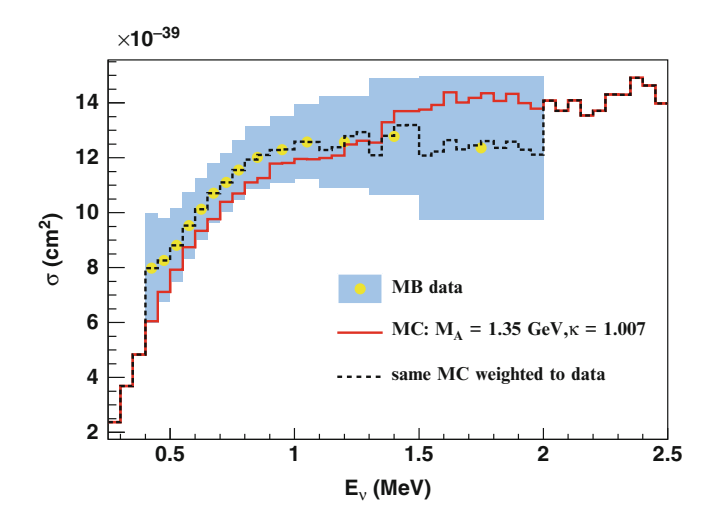


Fig. 7.5 Summary of the normalization correction to the ν_{μ} CCQE cross section in the antineutrino-mode simulation. The ratio of the data to the *red* MC histogram is applied bin-by-bin to the simulated ν_{μ} CCQE events. Also visible is the effect of low-precision sampling with the NUANCE generator at high energies. This is discussed further in Sect. 8.2

extra activity is observed in the detector. However, the low-energy neutron and photons from the primary capture reaction as well as de-excitations of the boron isotope may be energetic enough to produce a Michel-like event. The simulated production of these particles is based on the measurements of [21–26], and the model that propagates these particles and possible re-interactions through the MiniBooNE detector estimates 6.60% of μ^- capture events lead to activity similar to a low-energy Michel. Thus, the apparent μ^- nuclear capture probability in the detector is predicted to be $7.78\times(1-6.60\%)=7.26\pm0.20\%$, where the uncertainty is substantially increased to recognize the model dependence of the rate to regain Michel-like events following μ^- capture. This rate is partially constrained by the calibration procedure described in Sect. 7.1.4, and it will be shown that the assigned uncertainty on effective μ^- nuclear capture has a negligible impact on the final measurements.

Sensitivity to the μ^- content of the data is obtained by simultaneously analyzing two samples: those with only a muon candidate event, and events consistent with the observation of a muon and its decay electron. Therefore, this analysis takes as signal ν_μ and $\bar{\nu}_\mu$ CC events. Apart from the requirement of either one or two subevents, the event selection for this analysis closely follows that described in Sect. 6.2 with a few changes appropriate to different backgrounds and a higher sensitivity to Michel detection efficiency. Table 7.5 details the ν_μ and $\bar{\nu}_\mu$ charged-current purity of the two samples after each cut.

The primary samples of this analysis are separated by cut 1, where ν_{μ} CC events have an enhanced contribution in the single subevent sample due to μ^{-} capture.

		One subevent		Two st	ibevents
Cut #	Description	ν_{μ} CC	$\bar{\nu}_{\mu}$ CC	ν_{μ} CC	$\bar{\nu}_{\mu}$ CC
1	Subevent cut	18	33	26	57
2	Veto hits < 6 for all subevents	9	11	30	65
3	First subevent in beam window: $4000 < T(ns) < 7000$	9	11	29	65
4	Reconstructed vertex radius < 500 cm for first subevent	8	11	29	65
5	Kinetic energy > 200 MeV for the first subevent	20	27	29	68
6	μ/e log-likelihood ratio > 0.02 for first subevent	36	54	27	72
7	Predicted μ stopping radius < 500 cm	39	46	28	71
8	$Q_{OE}^2 > 0.2 \mathrm{GeV}^2$	57	36	43	56

Table 7.5 Antineutrino-mode purity in % for all ν_{μ} and $\bar{\nu}_{\mu}$ charged-current events in the one- and two-subevent samples

A pre-cut of generated radius < 550 cm is applied

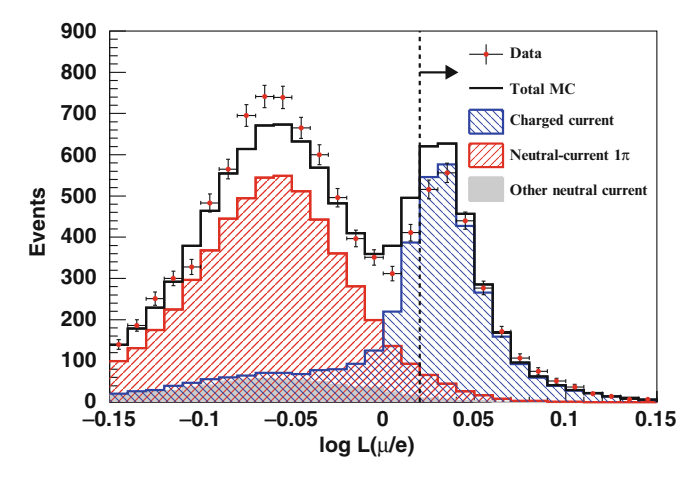


Fig. 7.6 The log-likelihood μ/e particle-ID variable in the single-subevent sample. All other selection requirements have been applied. The simulation is normalized to flux, and errors shown on data are statistical only

Cuts 2–5 are common to the analysis presented in the main body of this work and are motivated in Sect. 6.2. Cuts 6 and 8 reduce the NC background in the single-subevent sample. Figure 7.6 shows NC single π events are largely rejected by the requirement on the μ/e log-likelihood variable, while Fig. 7.7 shows cut 8 further reduces their contribution.

Cut 7 eliminates events in which the Michel electron is produced near the optical barrier, where modeling of the electron detection efficiency may be less reliable. In this region many more Michels are lost due to the minimum requirement of 10 PMT tank hits to form a subevent, while some are missed due to Michels entering the veto region. To explore these effects, we begin with a prediction of where the

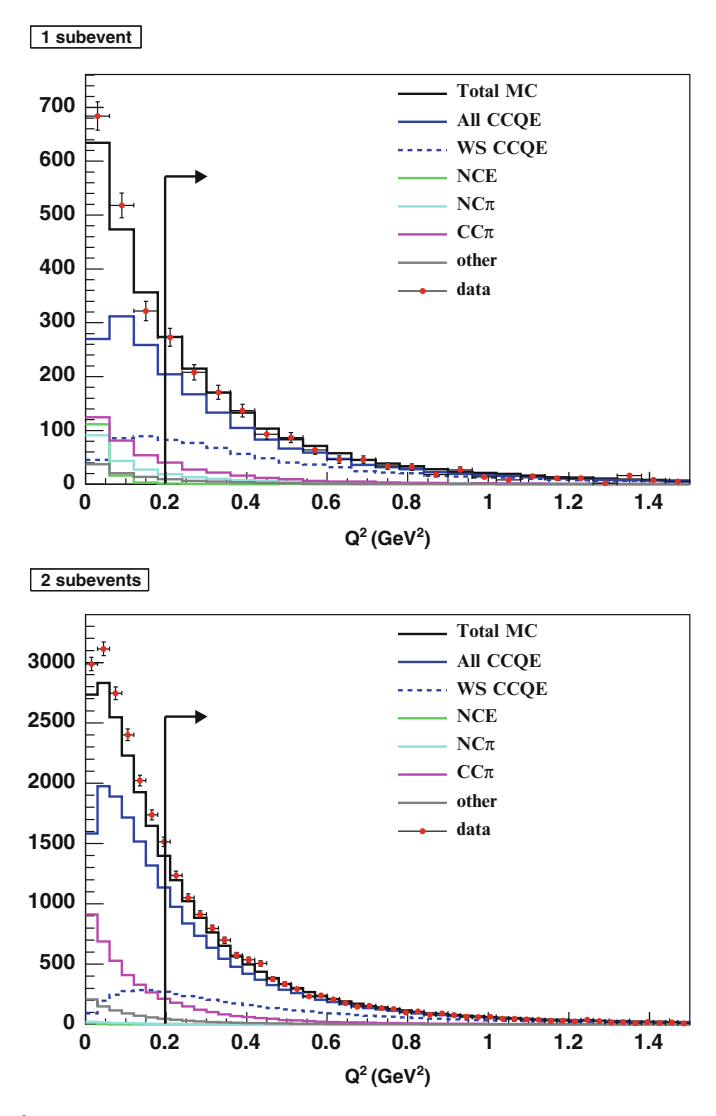


Fig. 7.7 Q_{QE}^2 for the single-subevent (top) and two-subevent (bottom) samples. All other selection cuts have been applied. Events with $Q^2 > 0.2 \, \text{GeV}^2$ are selected to reject some NC events, particularly in the single-subevent sample. Distributions are normalized to flux

Michel ought to be produced, assuming it is the decay product of the prompt muon. Calculating the stopping radius of the muon based on its observed vertex, direction and energy, we find:

$$\mu$$
 stopping radius = $\sqrt{(V_x + \overline{dE/dX}^{-1} \times T_\mu \times U_x)^2 + [\text{same for y and z directions}]}$, (7.7)

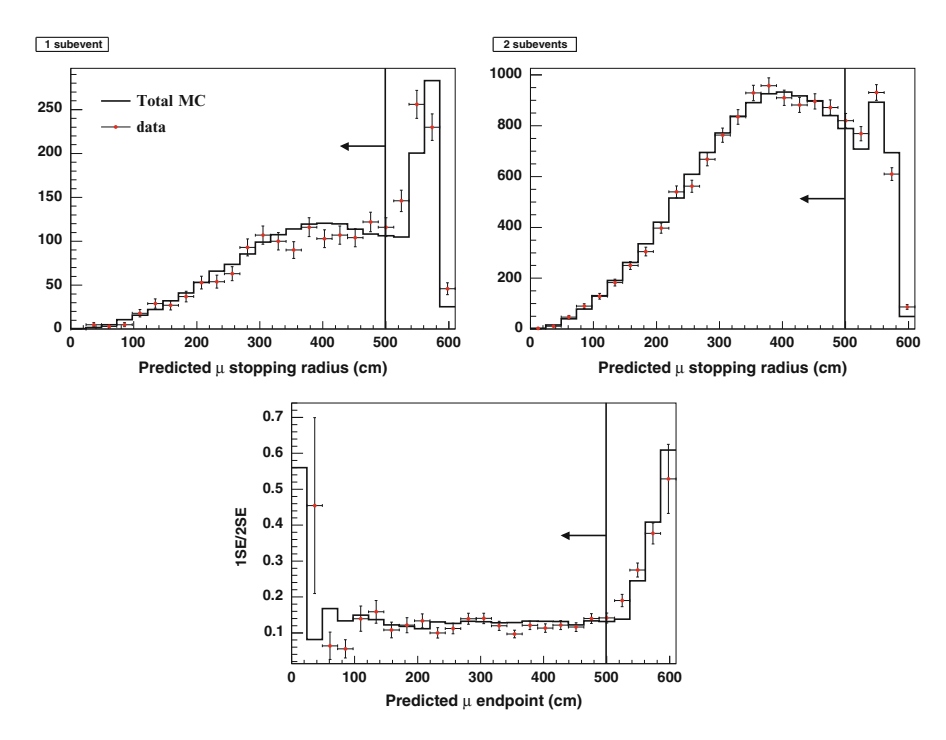


Fig. 7.8 Predicted muon endpoint radius for the single-subevent (*top left*), two-subevent (*top right*) samples and the ratio single/two subevents (*bottom*). All other selection cuts have been applied. Data-MC discrepancy is only present at high radius, presumably due to difficulties in modeling Michel detection close to the optical barrier. The peak above 500 cm in the single-subevent and the ratio distribution is due to the lower Michel detection efficiency in this region. There are zero events in the first bin of the single-subevent data. Distributions are relatively normalized to data

where V_x and U_x are the reconstructed muon vertex and direction in the x-direction respectively, and T_μ is the muon kinetic energy. $\overline{dE/dx}$ is the average energy deposited per unit of distance traveled for muons in mineral oil at MiniBooNE energies. Fitting dE/dX data for stopping power of mineral oil to a linear function finds $\overline{dE/dx} = 1.9 \, \text{MeV/cm}$.

Figure 7.8 shows adequate agreement between data and simulation at high radius in the 2SE sample, where a Michel is both produced and detected, while the agreement is worse in the single-subevent sample. Regardless, the ratio of single/two subevent events as a function of the muon endpoint presented in the same figure shows this ratio clearly increases with radius at large values and so is quite sensitive to the details of Michel detection near the optical barrier.

Away from this barrier, where Michel detection is not a function of position, most Michel electrons not detected are missed due to the timing cut used to separate subevents and not the requirement of at least ten tank PMT hits within the temporal window. Figure 7.9 shows the difference in the timing distributions for the 2SE

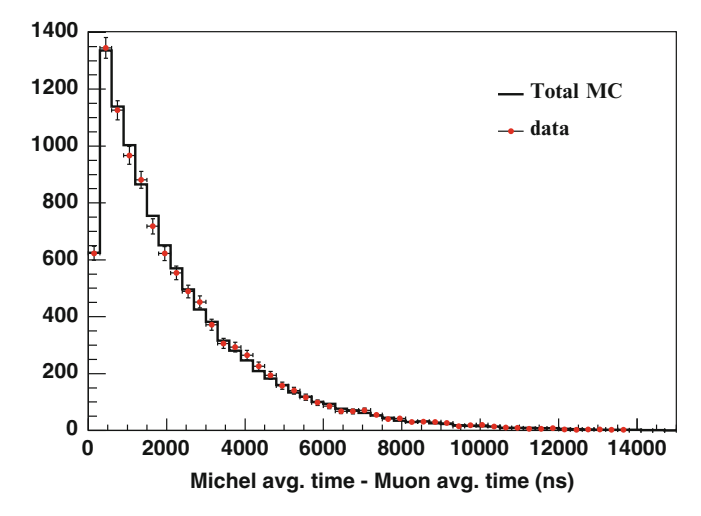


Fig. 7.9 Difference between average hit times for the Michel-like subevent and the muon-like subevent in antineutrino mode. The distributions deviate from an exponential form at low timing differences due to the temporal definition of a subevent. Simulation is relatively normalized to data

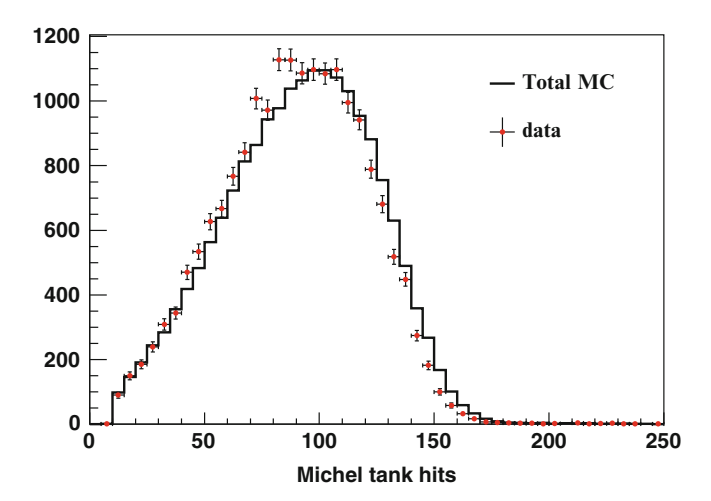


Fig. 7.10 Tank hit distributions for the second subevent in antineutrino mode. Simulation is normalized to data

sample, while Fig. 7.10 presents the tank hit distribution for the second subevent. Less than 0.5% of events are rejected by the 10 PMT hit requirement, while $\sim\!\!8\%$ of Michels are produced too close in time with the muon to be temporally separated.

Cut 7 also enhances ν_{μ} purity due to kinematic differences between ν_{μ} and $\bar{\nu}_{\mu}$ CCQE, where the more forward-going nature of the μ^{+} from $\bar{\nu}_{\mu}$ interactions preferentially stop at high radius in the downstream region of the detector.

	Contribution (9	%) to
Process	One subevent	Two subevents
$\bar{\nu}_{\mu} + p \rightarrow \mu^{+} + n$	31	49
$\nu_{\mu} + n \to \mu^{-} + p$	48	36
$\bar{\nu}_{\mu} + N \rightarrow \mu^{+} + N + \pi^{-}$	3	5
$\nu_{\mu} + N \rightarrow \mu^{-} + N + \pi^{+}$	7	7
$\nu_{\mu}(\bar{\nu}_{\mu}) + N \rightarrow \nu_{\mu}(\bar{\nu}_{\mu}) + N$	1	0
$\nu_{\mu}(\bar{\nu}_{\mu}) + N \rightarrow \nu_{\mu}(\bar{\nu}_{\mu}) + N + \pi^{0}$	3	0
$\nu_{\mu}(\bar{\nu}_{\mu}) + N \rightarrow \nu_{\mu}(\bar{\nu}_{\mu}) + N + \pi^{\pm}$	4	0
Other	3	3
All ν_{μ}	58	43
All $\bar{\nu}_{\mu}$	42	57

Table 7.6 Summary of predicted nucleon-level interactions in the antineutrino-mode subevent samples

The small contribution from neutral current processes are presented as the sum of the ν_{μ} and $\bar{\nu}_{\mu}$ interactions

With the full selection, nucleon-level interaction contributions to the subevent samples are given in Table 7.6.

Calibrations and Stability Checks Using the Neutrino-Mode Data

The success of this analysis is dependent upon being able to interpret differences between the one- and two-subevent antineutrino-mode data and MC samples as being due to the amount of ν_{μ} in the beam. In principle, any difference discovered between data and the simulation is ambiguous between the ν_{μ} content and inadequate modeling of the total migration rate between the subevent samples.

Fortunately, the neutrino-mode data offers an opportunity to calibrate the migration rate between the subevent samples for ν_{μ} CC events. Due to the convolution of flux and cross-section effects discussed in Sect. 7.1.1, the neutrino-mode subevent samples are dominantly due to CC ν_{μ} interactions. Table 7.7 shows the predicted neutrino species and interaction type contributions to the neutrino-mode subevent samples with the same selection described in the previous section. With a high-purity ν_{μ} CC sample, the accuracy of Michel detection and effective μ^- capture in simulation can be tested. For CC ν_{μ} events without final-state pions (" ν_{μ} CC"), the number of events in the neutrino-mode one-subevent ("1SE") and two-subevent ("2SE") samples are given by:

$$1SE^{\nu} = \nu_{\mu}CC \times (\delta + \beta(1 - \delta)) + N_1^{\nu}$$
(7.8)

$$2SE^{\nu} = \nu_{\mu}CC \times (1 - \delta - \beta(1 - \delta)) + N_2^{\nu}$$
 (7.9)

Table 7.7 A brief description of the neutrino-mode subevent samples for the same selection described in the previous section

Table 7.8 Calibration summary for Michel detection inefficiency (δ) and the rate of effective μ^- nuclear capture (β)

	Contribution (%) to		
Process	One subevent	Two subevents	
All ν_{μ} CC	95.4	99.0	
All $\bar{\nu}_{\mu}$	0.4	0.7	
All NC	4.3	0.3	

Process	Data	MC	Data/MC
δ	0.073	0.074	0.98
β	0.071	0.073	0.98

Note that both processes cannot be simultaneously constrained

where N_1^{ν} (N_2^{ν}) is the NC contribution to the 1SE (2SE) sample, δ is the Michel detection inefficiency and β is the effective μ^- capture rate described previously. The rate for Michel non-detection can be solved in terms of the effective μ^- capture rate and the small NC contribution:

$$\delta = \frac{\frac{1SE^{\nu} - N_{1}^{\nu}}{1SE^{\nu} + 2SE^{\nu} - (N_{1}^{\nu} + N_{2}^{\nu})} - \beta}{1 - \beta}$$
(7.10)

Noting the symmetry in Eqs. (7.8) and (7.9) between δ and β , Eq. (7.10) can also express the effective μ^- capture rate in terms of Michel detection with $\delta \leftrightarrow \beta$. Table 7.8 gives values of δ and β from simulation and data based on the observed or predicted event rates in the $1SE^{\nu}$ and $2SE^{\nu}$ samples.

As the ν_{μ} charged-current migration rate to the single-subevent sample is due to a convolution of Michel detection and effective μ^- capture, the processes cannot be simultaneously calibrated with the neutrino-mode data - that is, for example, the calibration of δ assumes the MC valuation of β is correct. Future experiments may be able to break this degeneracy by examining the low-energy region of the Michel spectrum across both neutrino and antineutrino modes, where the contribution from activity following μ^- capture is enhanced. In the case of MiniBooNE, the Michel spectrum in antineutrino-mode is given in Fig. 7.10, and the neutrino-mode analogue is shown in Fig. 7.11. While consistency in the low-energy region between data and simulation indicate the μ^- capture model is not grossly wrong, the statistics of the antineutrino sample prevent a rigorous test of the Michel-like contributions following μ^- capture.

As the calibration results shown in Table 7.8 are quite mild and within systematic uncertainties, this procedure gives confidence in the ability to unambiguously measure the ν_{μ} content of the antineutrino-mode data using μ^{-} capture.

The substantially higher event rate in neutrino-mode compared to antineutrino-mode also offers the opportunity for a robust stability check of the Michel detection efficiency. If there were some variation or degradation of the electronics during neutrino-mode running that would affect the detection of Michels, it should appear as differences in some suitable variables between temporal bins.

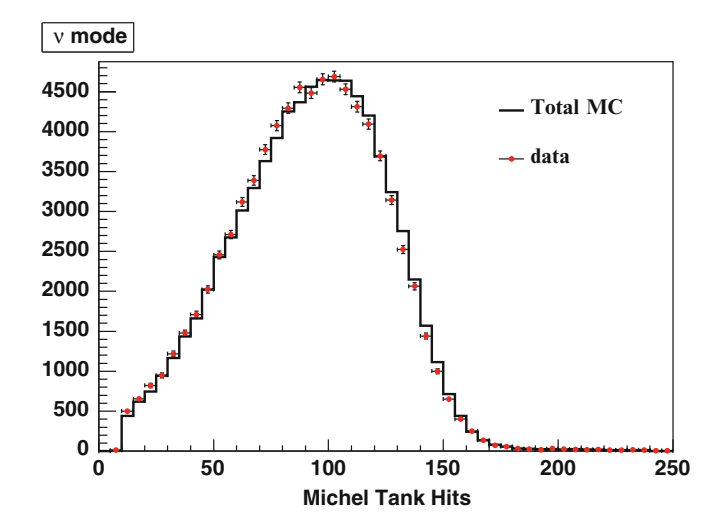


Fig. 7.11 Tank hit distributions for the second subevent in neutrino mode. Events from μ^- capture are expected to only contribute in the lowest bins, and the consistency between data and simulation gives confidence that the μ^- capture model is adequate. MC is relatively normalized to data

Table 7.9 1SE and 2SE event details in four sequential and roughly equally sized neutrino-mode data groups

Run numbers	1SE events	2SE events	1SE/2SE
3,539–7,999	3,658	21,318	0.172 ± 0.003
8,000-10,999	4,413	26,380	0.167 ± 0.003
11,000-11,999	2,355	13,933	0.169 ± 0.003
12,000–12,842,	3,112	18,576	0.168 ± 0.003
15,833-17,160	3,112	10,570	0.108 ± 0.003

The 1SE/2SE ratios are consistent within one standard deviation

The neutrino-mode data is separated into four chronologically sequential groups of data with roughly equal POT contributions. The first variable to look at is the ratio 1SE/2SE. Table 7.9 offers event counts in the 1 and 2SE samples and their ratio with statistical error for the four data groups. Within statistical uncertainty, the subevent ratios are consistent and we find no evidence of systematic variations affecting Michel detection.

A final check on Michel detection stability can be made by looking at the very early timing distribution of the 2SE sample. Figure 7.12 presents a 0–800 ns window of the average time separating the two subevents for the four sets of neutrino-mode data. No evidence of a time-dependent shift between the data runs is observed.

We conclude that in the sample most sensitive to any pathological evolution of Michel detection in time, none are observed. The statistics of the single-subevent sample in antineutrino mode prohibit the execution of the same tests using the primary analysis samples.

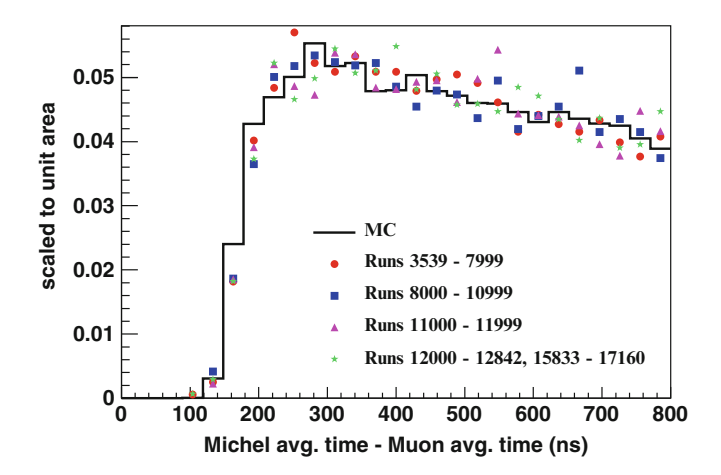


Fig. 7.12 Early separation between the two subevents in neutrino mode. No significant shape difference is observed between the four chronologically sequential groups of data. Distributions are scaled to unit area

ν_{μ} Flux Measurement Using μ^{-} Capture

The ν_{μ} flux in the antineutrino-mode beam is measured by adjusting the MC prediction of the ν_{μ} and $\bar{\nu}_{\mu}$ content to match the data in regions of reconstructed energy for the subevent samples. Following the conventions of Eqs. (7.8) and (7.9) and introducing $\bar{\nu}_{\mu}$ CC for the $\bar{\nu}_{\mu}$ charged-current content, the predicted ν_{μ} and $\bar{\nu}_{\mu}$ contributions to the subevent samples in antineutrino mode are defined as

$$\nu_{\text{MC}}^{\text{ISE}} = \nu_{\mu} \text{CC} \times (\delta + \beta(1 - \delta)) \tag{7.11}$$

$$\nu_{\text{MC}}^{\text{2SE}} = \nu_{\mu} \text{CC} \times (1 - \delta - \beta(1 - \delta)) \tag{7.12}$$

$$\bar{\nu}_{MC}^{1SE} = \bar{\nu}_{\mu} CC \times \delta \tag{7.13}$$

$$\bar{\nu}_{\text{MC}}^{\text{2SE}} = \bar{\nu}_{\mu} \text{CC} \times (1 - \delta) \tag{7.14}$$

Then the single- (" $1SE^{\bar{\nu}}$ ") and two-subevent (" $2SE^{\bar{\nu}}$ ") data samples in antineutrino mode are given by

$$1SE^{\bar{\nu}} = \alpha_{\nu} \times \nu_{MC}^{1SE} + \alpha_{\bar{\nu}} \times \bar{\nu}_{MC}^{1SE} + N_1^{\bar{\nu}}$$
(7.15)

$$2SE^{\bar{\nu}} = \alpha_{\nu} \times \nu_{MC}^{2SE} + \alpha_{\bar{\nu}} \times \bar{\nu}_{MC}^{2SE} + N_2^{\bar{\nu}}$$
 (7.16)

where α_{ν} and $\alpha_{\bar{\nu}}$ are scale factors for the ν_{μ} and $\bar{\nu}_{\mu}$ charged-current content, respectively, to be measured in this analysis. The NC content $(N_2^{\bar{\nu}} \text{ and } N_1^{\bar{\nu}})$ include contributions from both ν_{μ} and $\bar{\nu}_{\mu}$. Equations (7.15) and (7.16) can be solved for α_{ν} and $\alpha_{\bar{\nu}}$:

Table 7.10 Results for scale factors relative to the expectation for the v_{μ} and \bar{v}_{μ} charged-current content of the antineutrino-mode data

	Calibrated	E_{ν}^{QE} ra		
Parameter	process	< 0.9	≥ 0.9	All
α_{ν}	δ	0.78	0.79	0.78
	β	0.78	0.79	0.78
	Average	0.78	0.79	0.78
$\alpha_{\overline{\nu}}$	δ	1.16	1.15	1.16
	β	1.16	1.15	1.16
	Average	1.16	1.15	1.16

$$\alpha_{\nu} = \frac{(1SE^{\bar{\nu}} - N_1^{\bar{\nu}})\bar{\nu}_{MC}^{2SE} - (2SE^{\bar{\nu}} - N_2^{\bar{\nu}})\bar{\nu}_{MC}^{1SE}}{\bar{\nu}_{MC}^{2SE}\nu_{MC}^{1SE} - \bar{\nu}_{MC}^{1SE}\nu_{MC}^{2SE}}$$
(7.17)

$$\alpha_{\bar{\nu}} = \frac{(1SE^{\bar{\nu}} - N_1^{\bar{\nu}})\nu_{MC}^{2SE} - (2SE^{\bar{\nu}} - N_2^{\bar{\nu}})\nu_{MC}^{1SE}}{\nu_{MC}^{2SE}\bar{\nu}_{MC}^{1SE} - \nu_{MC}^{1SE}\bar{\nu}_{MC}^{2SE}}$$
(7.18)

To check the modeling of the ν_{μ} flux spectrum, this measurement is performed in three regions of reconstructed energy E_{ν}^{QE} (Eq. 6.7): above and below 900 MeV, and an inclusive energy sample.

As described in the previous section, the calibration from the neutrino-mode data is ambiguous between Michel detection and the effective μ^- capture model. As these effects change the expectations for $\bar{\nu}_{MC}^{1SE}$, $\bar{\nu}_{MC}^{2SE}$, ν_{MC}^{1SE} and ν_{MC}^{2SE} in different ways, the measurement of α_{ν} and $\alpha_{\bar{\nu}}$ is, in principle, sensitive to which rate is calibrated. In the absence of a compelling reason to choose one over the other, the final evaluations for α_{ν} and $\alpha_{\bar{\nu}}$ are taken to be the average of the two calculations assuming each rate is calibrated. A calibration uncertainty spanning the difference in the two measurements is added to the systematic errors discussed next. The central values for α_{ν} and $\alpha_{\bar{\nu}}$ are presented in Table 7.10.

Systematic Errors

Systematic uncertainties on α_{ν} and $\alpha_{\bar{\nu}}$ are evaluated by assigning relevant errors to the physics processes contributing to the subevent samples and observing how the measurement changes as the channels are varied within their uncertainty. These uncertainties are treated as uncorrelated, so the uncertainty on α_{ν} , for example, due to physics processes P_1, \dots, P_N is simply

$$\delta\alpha_{\nu}^{2} = \sum_{i=1}^{N} \left(\frac{\partial\alpha_{\nu}}{\partial P_{i}}\delta P_{i}\right)^{2} \tag{7.19}$$

Table 7.11 shows the errors assigned to the various contributing processes and their propagated uncertainty onto α_{ν} and $\alpha_{\bar{\nu}}$. The most important process for

flux
~
_
the
Ŧ
Ψ.
0
measurement
_
capture-based
L
π
the
or
Ŧ
summary s
Ē
Uncertain
_
Ξ
7.1
•
able
ğ
Table

Uncertainty	Frac.	Uncertainty of	Uncertainty contribution to α_{ν} Uncertainty contribution to $\alpha_{\bar{\nu}}$	α_{ν}	Uncertainty c	ontribution to	$lpha_{ar{ u}}$
source	error (%)	$E_{\nu}^{QE} < 0.9$	error (%) $\mid E_{\nu}^{QE} < 0.9 \mid E_{\nu}^{QE} \ge 0.9 \mid \mathrm{All} \mid E_{\nu}^{QE} < 0.9 \mid E_{\nu}^{QE} \ge 0.9 \mid$	All	$E_{\nu}^{QE} < 0.9$	$E_{\nu}^{QE} \ge 0.9$	All
$\nu_{\mu} + n \rightarrow \mu^{-} + p$	10	0.07	80.0	0.07	0.00	0.00	0.00
$\bar{\nu}_{\mu} + p \rightarrow \mu^+ + n$	20	0.04	0.02	0.03	0.20	0.20	0.21
$\nu_{\mu}(\bar{\nu}_{\mu}) + N \to \mu^{-}(\mu^{+}) + N + \pi^{+}(\pi^{-})$	20	0.04	0.05	0.04	0.02	0.02	0.01
$\nu_{\mu}(\bar{\nu}_{\mu}) + N \to \nu_{\mu}(\bar{\nu}_{\mu}) + N$	30	0.00	0.00	0.00	0.00	0.00	0.00
$\nu_{\mu}(\bar{\nu}_{\mu}) + N \rightarrow \nu_{\mu}(\bar{\nu}_{\mu}) + N + \pi^{0}$	25	0.02	0.01	0.01	0.01	0.01	0.01
$\nu_{\mu}(\bar{\nu}_{\mu}) + N \to \nu_{\mu}(\bar{\nu}_{\mu}) + N + \pi^{\pm}$	50	0.05	0.02	0.01	0.03	0.03	0.01
μ^- capture	2.8	0.00	0.00	0.00	0.00	0.00	0.00
$\bar{\nu}$ -mode statistics	ı	0.10	0.11	0.08	0.08	0.08	90.0
ν-mode statistics	ı	0.04	0.05	0.04	0.03	0.03	0.03
All		0.14	0.16	0.12	0.22	0.22	0.22

reconstructed neutrino energy studied. The regions of E_{ν}^{QE} are given in GeV. The statistics of the ν -mode data enter the uncertainty from the calibration procedure described in Sect. 7.1.4. Note the 20% uncertainty on the $\bar{\nu}_{\mu}$ CCQE process contributes an uncertainty 0.04 or less to the measurement of α_{ν} . This assures the ν_{μ} flux measurement is not biased by assumptions on $\bar{\nu}_{\mu}$ CCQE Included are the assumed error on physics processes and their contribution to the total error in α_{ν} and $\alpha_{\bar{\nu}}$ in the regions of

Table 7.12 Summary of measurements for the ν_{μ} flux scale α_{ν} and the $\bar{\nu}_{\mu}$ rate scale $\alpha_{\bar{\nu}}$

	E_{ν}^{QE} range (C	GeV)	
Parameter	< 0.9	≥ 0.9	All
α_{ν}	0.78 ± 0.14	0.79 ± 0.16	0.78 ± 0.12
$\alpha_{\overline{\nu}}$	1.16 ± 0.22	1.15 ± 0.22	1.16 ± 0.22

extracting the ν_{μ} flux measurement is the ν_{μ} CCQE interaction, and its cross section and assigned uncertainty reflect the measurement and accuracy of the MiniBooNE result [4]. The same is true for the ν_{μ} and $\bar{\nu}_{\mu}$ neutral-current single π^0 channels [27]; however the error is increased to recognize a possible rate difference in these interactions between the cross-section measurements and this analysis due to using the opposite side of the log-likelihood variable shown in Fig. 7.6. The ν_{μ} and $\bar{\nu}_{\mu}$ charged-current single charged π channels are adjusted to reflect the ν_{μ} measurement [4] and their uncertainty is increased to recognize the extrapolation to the $\bar{\nu}_{\mu}$ processes. Treating the uncertainties on the ν_{μ} processes constrained by MiniBooNE data as uncorrelated ignores a common dependence on the neutrino-mode flux uncertainties, and a small cancellation of errors that could be propagated onto α_{ν} and $\alpha_{\bar{\nu}}$ is ignored. The ν_{μ} neutral-current elastic process is also constrained by MiniBooNE data [28], while the neutral-current charged-pion production processes are completely unconstrained and so the assigned uncertainty is large. Preliminary results for the $\bar{\nu}_{\mu}$ CCQE process [29] informs the choice of a 20 % uncertainty relative to the RFG model with $M_A = 1.35$ GeV. With these systematic uncertainty assumptions, as seen in Table 7.11, the uncertainty on the main result of this work α_{ν} is dominated by statistics and the ν_{μ} CCQE cross section. As the ν_{μ} CCQE process is directly constrained by MiniBooNE data, the measurement of the ν_{μ} flux scale α_{ν} features negligible model dependence. Table 7.12 summarizes the measurements of α_{ν} and $\alpha_{\bar{\nu}}$.

As the cross sections for the dominant ν_{μ} processes have been applied to simulation, the deviation from unity for α_{ν} represents the accuracy of the ν_{μ} flux prediction in antineutrino mode. As the bulk of the $\bar{\nu}_{\mu}$ flux prediction is constrained by the HARP data, the $\alpha_{\bar{\nu}}$ scale factor is representative of the level of cross-section agreement between data and the RFG with $M_A=1.35\,\mathrm{GeV}$ for the $\bar{\nu}_{\mu}$ CCQE process.

7.1.5 v_{μ} Flux Measurement Using the $\cos \theta_{\mu}$ Distribution

Overview

The final constraint on ν_{μ} events comes from the observed muon angular distribution $\cos\theta_{\mu}$, where θ_{μ} is the muon scattering direction relative to the incoming neutrino beam. Due to the axial-vector interference term (Sect. 4.2), the contribution from $\bar{\nu}_{\mu}$ events to backward-scattering muons is predicted to be heavily suppressed.

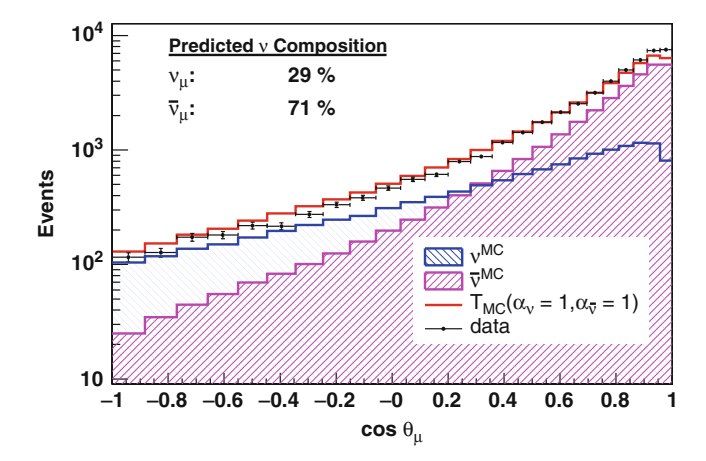


Fig. 7.13 The $\cos\theta_{\mu}$ distribution of the CCQE sample by neutrino type before fitting. The nominal MC prediction is normalized to flux, and notations used in the legend are used in the execution of the fit

Figure 7.13 compares the predicted v_{μ} and \bar{v}_{μ} contributions to the muon scattering angle with data.

This large asymmetry offers the opportunity to fit a combination of the ν_{μ} and $\bar{\nu}_{\mu}$ content to the observed data. However, this asymmetry is model-dependent, as the details of $\bar{\nu}_{\mu}$ CCQE scattering are not well known, and in fact the $\bar{\nu}_{\mu}$ processes contributing to the MiniBooNE CCQE sample may be much more isotropic than suggested by Fig. 7.13. Of course, detailed measurements of $\bar{\nu}_{\mu}$ CCQE scattering is the main focus of this dissertation. Therefore, any dependence of the background ν_{μ} estimation on assumptions of $\bar{\nu}_{\mu}$ CCQE must be strictly avoided. For this reason, the results of this analysis are not used to subtract the ν_{μ} background to the $\bar{\nu}_{\mu}$ CCQE sample. However, in the future, when the processes contributing to samples like these are better understood, this technique could prove to be powerful.

As mentioned in Sect. 7.1.3, the data used in this analysis does include the small absorber-down antineutrino-mode runs.

Sample Selection

The only difference between the CCQE sample selected here and that used in the main analysis of $\bar{\nu}_{\mu}$ CCQE interactions (detailed in Sect. 6.2) is the replacement of the μ range-based cut with the requirement that the reconstructed vertex of the second subevent be within a 100 cm radius of the predicted μ stopping point. The radius between the predicted muon μ stopping point and the Michel vertex is hereafter referred to as the "Michel distance."

To directly see the difference between these cuts, the slope of the range cut versus the Michel distance can be examined. The slope of the range cut is $\frac{Range+100\,\mathrm{cm}}{T_u}$

(cm/GeV), and 500 cm/GeV is the cut used in the neutrino CCQE analysis. The 500 cm/GeV cut is simply the inverse of the standard MIP energy loss 2 MeV/cm. The range cut slope versus Michel distance for is plotted for data, MC, and the significant interaction channels in Fig. 7.14. Note the effect of the 100 cm μ range cut (cut 8 in Sect. 6.2) is not included in this comparison. It can be seen that the μ range-based cut keeps more signal events while rejecting around the same amount of background. However, either choice of spatial correlation requirement between the muon and its decay electron result in mostly the same purity and efficiency for ν_{μ} and $\bar{\nu}_{\mu}$ events.

Measurement Execution

To measure the neutrino content using the muon angular distribution, the MC sample is separated into two $\cos\theta_{\mu}$ templates, one arising from all ν_{μ} interactions and the other from $\bar{\nu}_{\mu}$, regardless of interaction channel. A linear combination of these two templates is then formed,

$$T_{MC}(\alpha_{\nu}, \alpha_{\bar{\nu}}) \equiv \alpha_{\nu} \, \nu^{MC} + \alpha_{\bar{\nu}} \, \bar{\nu}^{MC} \tag{7.20}$$

where T_{MC} is the total predicted $\cos \theta_{\mu}$ distribution to be fit to data, α_{ν} and $\alpha_{\bar{\nu}}$ are neutrino and antineutrino rate scales, and ν^{MC} and $\bar{\nu}^{MC}$ are the MC neutrino and antineutrino scattering angular predictions, respectively.

Many backgrounds to the CCQE sample peak in the most forward scattering region of the $\cos\theta_{\mu}$ distribution. This includes pion production and hydrogen CCQE scattering—while the latter is technically not a background, the proper handling of the difference in nuclear effects between bound and free targets is not straightforward. Additionally, the forward scattering region is dominated by $\bar{\nu}_{\mu}$ interactions, while the present analysis is principally interested in ν_{μ} -dominated backwards scattering region. For these reasons, events with $\cos\theta_{\mu} > 0.91$ are not included in the fit to data, where θ_{μ} is the outgoing muon angle relative to the incoming neutrino beam.

Ignoring this forward-scattering region, the modified simulation sample in Eq. (7.20) is compared to data by forming a goodness-of-fit χ^2 test as a function of the rate scales:

$$\chi^{2}(\alpha_{\nu},\alpha_{\bar{\nu}}) = \sum_{i,j} \left(T_{MC}(\alpha_{\nu},\alpha_{\bar{\nu}})_{i} - d_{i} \right) M_{ij,\text{FIT}}^{-1} \left(T_{MC}(\alpha_{\nu},\alpha_{\bar{\nu}})_{j} - d_{j} \right). \tag{7.21}$$

where i and j label bins of $\cos \theta_{\mu}$, d is data and $M_{\rm FIT}$ is the covariance matrix described in the next section.

The linearity of this fit allows for an analytic solution. The scales α_{ν} and $\alpha_{\bar{\nu}}$ describe the data best when the χ^2 function in Eq. (7.21) is minimized simultaneously with respect to both parameters:

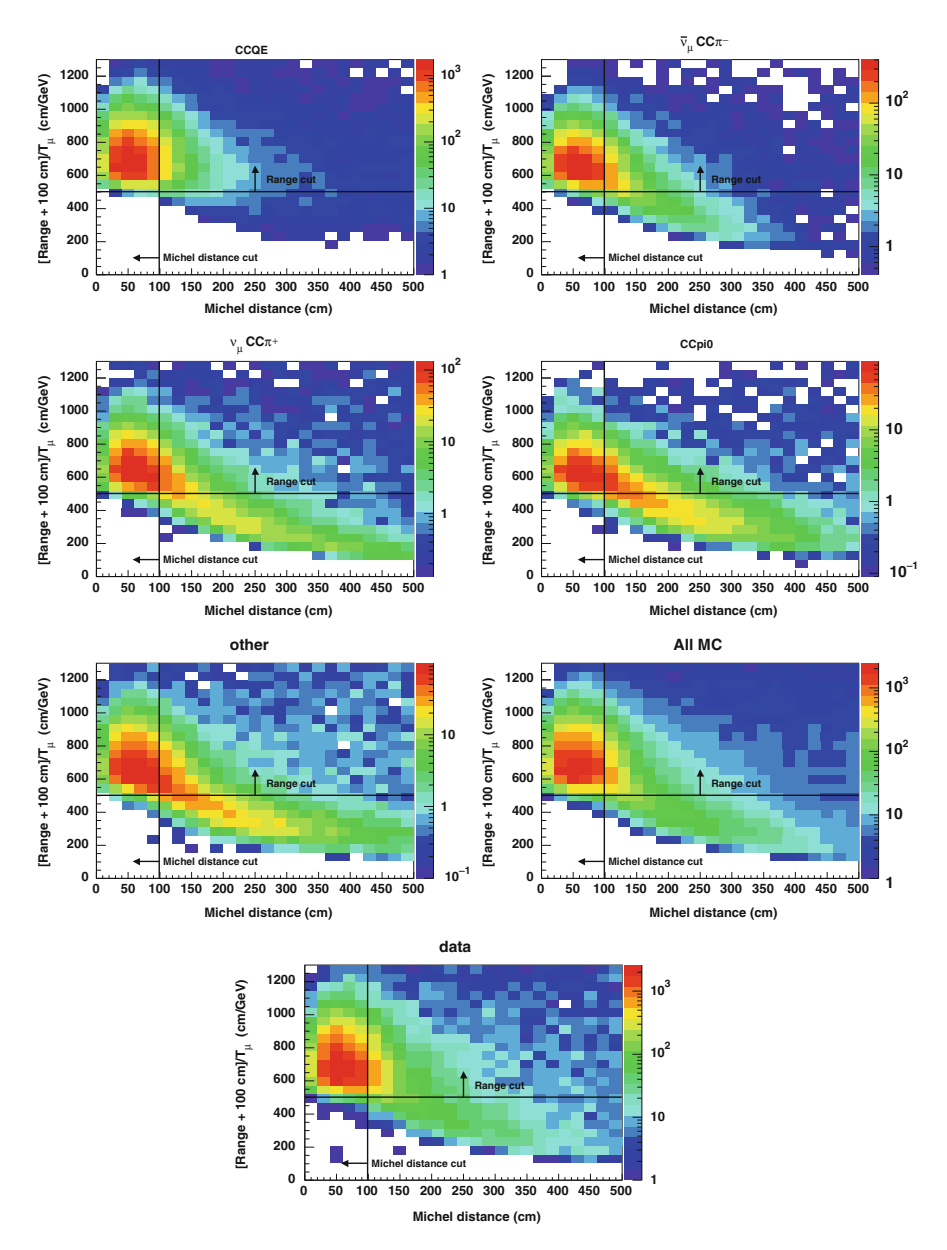


Fig. 7.14 Michel distance versus the range slope as described in the text. Distributions are absolutely normalized

$$\frac{\partial \chi^2}{\partial \alpha_{\nu}} = \frac{\partial \chi^2}{\partial \alpha_{\bar{\nu}}} = 0. \tag{7.22}$$

By exploiting the symmetric nature of the error matrix, we can simplify and arrive at a unique solution for the fit parameters α_{ν} and $\alpha_{\bar{\nu}}$ in terms of the data d and MC distributions of ν_{μ} (" ν^{MC} ") and $\bar{\nu}_{\mu}$ (" $\bar{\nu}^{MC}$ "):

$$\begin{bmatrix} \alpha_{\bar{\nu}}^{\text{BF}} \\ \alpha_{\nu}^{\text{BF}} \end{bmatrix} = \begin{bmatrix} \sum_{i,j} \bar{v}_{i}^{MC} \bar{v}_{j}^{MC} M_{ij,\text{FIT}}^{-1} \sum_{i,j} \bar{v}_{i}^{MC} v_{j}^{MC} M_{ij,\text{FIT}}^{-1} \\ \sum_{i,j} v_{i}^{MC} \bar{v}_{j}^{MC} M_{ij,\text{FIT}}^{-1} \sum_{i,j} v_{i}^{MC} v_{j}^{MC} M_{ij,\text{FIT}}^{-1} \end{bmatrix}^{-1} \begin{bmatrix} \sum_{i,j} \bar{v}_{i}^{MC} d_{j} M_{ij,\text{FIT}}^{-1} \\ \sum_{i,j} v_{i}^{MC} d_{j} M_{ij,\text{FIT}}^{-1} \end{bmatrix},$$
(7.23)

where α_{ν}^{BF} and $\alpha_{\bar{\nu}}^{BF}$ are the best-fit scales for the neutrino and antineutrino distributions, respectively. The uncertainty on α_{ν} and $\alpha_{\bar{\nu}}$ is determined by the projections of the χ^2 function (Eq. (7.21)) for each parameter while holding the other fixed at its best-fit value. The uncertainty on the parameters is:

$$\delta\alpha_{\nu} = \left| \alpha_{\nu}^{\text{BF}} - \alpha_{\nu} \left[\chi^{2}(\alpha_{\nu}^{\text{BF}}, \alpha_{\bar{\nu}}^{\text{BF}}) \pm \Delta \chi^{2} \right] \right| \tag{7.24}$$

$$\delta\alpha_{\bar{\nu}} = \left| \alpha_{\bar{\nu}}^{\text{BF}} - \alpha_{\bar{\nu}} \left[\chi^2(\alpha_{\nu}^{\text{BF}}, \alpha_{\bar{\nu}}^{\text{BF}}) \pm \Delta \chi^2 \right] \right|, \tag{7.25}$$

where $\Delta \chi^2$ for the 68 % C.L. in a two-parameter fit is 2.30 [30]. Note the uncertainties symmetric in the fit parameters assumed by Eqs. (7.24) and (7.25) are not general, and is the case here due to the linearity of the fit.

The Covariance Matrix

The covariance matrix is used to propagate correlated uncertainties on parameters and processes to the quantities reported in the analysis while accounting for correlations between ν_{μ} and $\bar{\nu}_{\mu}$ events. It is made by first forming weights corresponding to simulation excursions set by Gaussian variations of parameters within their associated error. The difference of these weighted events from the simulated central value forms the error matrix. Correlations between ν_{μ} and $\bar{\nu}_{\mu}$ are not considered in the generation of these excursions, and so must be explicitly addressed in this analysis.

The $\cos\theta_{\mu}$ correlations between ν_{μ} and $\bar{\nu}_{\mu}$ are treated by first expanding the distributions input to the covariance matrix to include both ν_{μ} and $\bar{\nu}_{\mu}$ $\cos\theta_{\mu}$ templates, side-by-side. An example of the central value distribution and 100 instances of cross section uncertainties related to the various contributing interactions is shown in Fig. 7.15.

Using these distributions, the covariance matrix is calculated as:

$$M_{ij} = \frac{1}{K} \sum_{s=1}^{K} (N_i^s - N_i^{CV}) \times (N_j^s - N_j^{CV}) = \rho_{ij} \sigma_i \sigma_j,$$
 (7.26)

where K simulation excursions are used (K = 100 in this analysis), N^s is the re-weighted number of entries corresponding to the s^{th} simulation set and N^{CV}

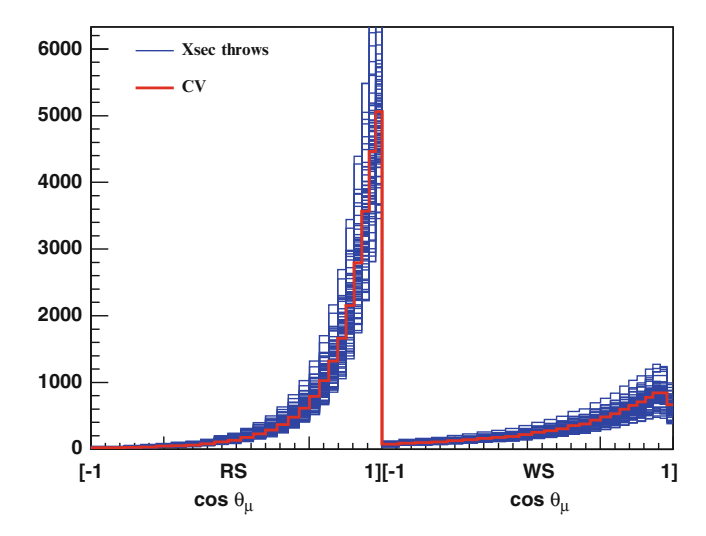


Fig. 7.15 Central-value (CV) $\cos\theta_{\mu}$ prediction versus 100 distributions created by cross section throws for right-sign (RS) $\bar{\nu}_{\mu}$ and wrong-sign (WS) ν_{μ} events

represents the simulation central value. The total uncertainty in each bin i is σ_i , and the correlation between bins i and j is given by ρ_{ij} . In this analysis, for uncertainties on processes with correlated errors, K=100 while K=1 is sufficient for uncorrelated errors. This technique is further described in [31]. Systematic uncertainties requiring correlated errors include the production of π^- in the proton beam target, the connection between π^- production and the focused $\bar{\nu}_{\mu}$ beam, optical transport in the detector, and final-state interactions.

With the ν_{μ} and $\bar{\nu}_{\mu}$ input distributions separated as in Fig. 7.15, this matrix contains ν_{μ} - and $\bar{\nu}_{\mu}$ -only covariance information on the block-diagonals, while the off-diagonal pieces contain the level of correlation between ν_{μ} and $\bar{\nu}_{\mu}$ events. A simple rearranging of Eq. (7.26) gives the correlation values:

$$\rho_{ij} = M_{ij}/(\sigma_i \sigma_j), \tag{7.27}$$

where the individual bin uncertainties σ_i are trivially found from $M_{ii} = \sigma_i^2$, since $\rho_{ii} = 1$. Figure 7.16 shows the level of correlation between all bins in the ν_{μ} and $\bar{\nu}_{\mu} \cos \theta_{\mu}$ distributions. It will be shown that the overall positive correlation is mostly due to the dominant uncertainties related to highly-correlated ν_{μ} and $\bar{\nu}_{\mu}$ cross sections.

To use the covariance matrix in the context of a fit, its size must first be reduced to the dimension of a single $\cos\theta_{\mu}$ distribution. Since the total sample T_{MC} in each bin i is a simple sum of ν_{μ} and $\bar{\nu}_{\mu}$ events,

$$T_{i,MC}(1,1) = v_i^{MC} + \bar{v}_i^{MC}$$
 (7.28)

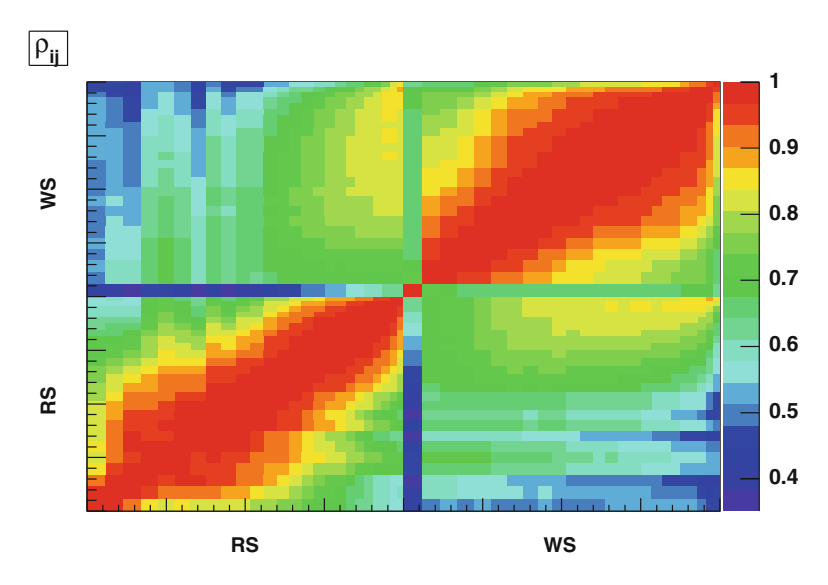


Fig. 7.16 Correlation matrix for ν_{μ} and $\bar{\nu}_{\mu}$ events in the $\cos\theta_{\mu}$ distribution. From *left* to *right* and *bottom* to *top*, the domain is [-1,1] for the RS and WS distributions. The block-diagonals give bin correlation information between the ν_{μ} events (*top right*) and $\bar{\nu}_{\mu}$ (*bottom left*) events, while the off-diagonals contain the ν_{μ} - $\bar{\nu}_{\mu}$ correlations. All bins are positively correlated to each other due to the dominant cross-section uncertainties, many of which affect the generation of ν_{μ} and $\bar{\nu}_{\mu}$ events in the same way

Using j for another arbitrary $\cos \theta_{\mu}$ bin, the covariance for this distribution is:

$$\sigma_{T_{i,MC}}\sigma_{T_{j,MC}}\rho_{\left(T_{i,MC}-T_{j,MC}\right)} = \sigma_{v_i^{MC}}\sigma_{v_j^{MC}}\rho_{\left(v_i^{MC}-v_j^{MC}\right)} + \sigma_{\bar{v}_i^{MC}}\sigma_{\bar{v}_j^{MC}}\rho_{\left(\bar{v}_i^{MC}-\bar{v}_j^{MC}\right)} + 2\sigma_{v_i^{MC}}\sigma_{\bar{v}_j^{MC}}\rho_{\left(v_i^{MC}-\bar{v}_j^{MC}\right)}$$

$$(7.29)$$

The terms on the right side of Eq. (7.29) can be recognized as entries of the full covariance matrix in Eq. (7.26). Finally, if the dimension of a single $\cos \theta_{\mu}$ distribution is N_d , the final error matrix to be used in this analysis is:

$$M_{i,j}^{\text{FIT}} = M_{i,j} + M_{i+N_d,j} + M_{i,j+N_d} + M_{i+N_d,j+N_d}, \tag{7.30}$$

where i and $j \in [0, N_d]$.

Results and Systematic Errors

As the present analysis directly measures the neutrino component in the antineutrino-mode beam, systematic errors relating to beam geometry and meson production at the target are not considered. The remaining systematic errors include

Table 7.13 Summary of systematic error contribution to the scale parameter α_{ν} in the inclusive energy fit

Source of error	Fractional uncertainty (%)
Statistical	8
Detector modeling	11
$CC\pi^+$ constraint	4
Cross section	26
Total fractional error	35

Individual error contributions are found for the ith systematic error by first repeating the fits with only independent systematics considered. The fractional error contributions are then found by $\sqrt{(\Delta\alpha_{\nu}/\alpha_{\nu})_{syst_{l}+stat}^{2}-(\Delta\alpha_{\nu}/\alpha_{\nu})_{stat}^{2}}, \text{ where } \Delta\alpha_{\nu}$ is the one-sigma error reported in Table 7.15. The statistical error is found by considering the second term only. This method does not account for small changes in the α_{ν} best fit parameter between the fits considering various errors, and so the individual fractional errors do not add in quadrature to produce the total fractional error reported in Table 7.15 and in the final column

those arising from detector modeling, the single pion production background, and the cross section parameters in the underlying CCQE model. Contributions propagated from these errors to the uncertainty on the parameter α_{ν} in the inclusive energy sample are given in Table 7.13.

Apart from final-state interaction uncertainties leading to errors on the cross section, the error on the $CC\pi^+$ background contributes to the systematic error through the error labeled " $CC\pi^+$ Constraint" in Table 7.13. This measurement uncertainty is based on a Q^2 -dependent shape-only scale factor to improve data-simulation agreement in the neutrino-mode $CC\pi^+$ sample [32]. The cross section (both CCQE and $CC\pi^+$) uncertainty is dominant in these fits and warrants further discussion. Table 7.14 offers a breakdown of cross section parameters and associated errors. The error on carbon M_A^C has been reduced from that reported in [4] to avoid double-counting MiniBooNE systematic errors applicable to both the measurement of M_A and the measurement reported here. The 26% uncertainty due to cross-section errors reported in Table 7.13 can be expanded as the quadrature sum of 16% from the 10% normalization errors on $\bar{\nu}_\mu$ and CCQE processes, 14% from the error on M_A and κ , and 15% from the remaining processes.

The fit is performed analytically in three bins of reconstructed energy and also in an inclusive energy sample. Results including statistical and systematic uncertainties are presented in Table 7.15, and the fits to data are shown in Fig. 7.17. As the main contributions to the dominant cross section systematic error apply to both ν_{μ} and $\bar{\nu}_{\mu}$ scattering, α_{ν} and $\alpha_{\bar{\nu}}$ are positively correlated as reported in Table 7.15. The adjusted contributions of ν_{μ} and $\bar{\nu}_{\mu}$ to the CCQE sample are compared to the prediction in Table 7.16.

Table 7.14 Summary of cross-section errors used in this analysis

Parameter	Value with error
M_A^C (carbon target)	$1.35 \pm 0.07 \text{GeV}$
M_A^H (hydrogen target)	$1.03 \pm 0.02 \text{GeV}$
К	1.007 ± 0.005
E_B	$34 \pm 9 \mathrm{MeV}$
Δs	0.0 ± 0.1
$M_A^{1\pi}$	$1.10 \pm 0.28 \text{ GeV}$
$M_A^{\text{multi}-\pi}$	$1.30 \pm 0.52 \text{GeV}$
p_F	$220 \pm 30 \mathrm{MeV}$
	Fractional
Process	uncertainty (%)
π^+ charge exchange	50
π^+ absorption	35
CCQE σ normalization	10
All $\bar{\nu}_{\mu} \sigma$ normalization	10
$\Delta + N \rightarrow N + N$	100

The bottom portion presents fractional uncertainties assigned to processes *in addition* to parameter errors. Errors given on pion absorption and charge exchange are relevant to pion propagation in the detector medium

Table 7.15 Fit results in three energy bins and an inclusive sample

$E_{\bar{\nu}}^{QE}$ range	Mean generated	Events			$\rho_{\alpha_{\nu}-\alpha_{\bar{\nu}}}$ fit	χ^2
(MeV)	E _ν (MeV)	in data	α_{ν} fit	$\alpha_{\bar{\nu}}$ fit	correlation	(DOF = 21)
<600	675	15,242	0.65 ± 0.22	0.98 ± 0.18	0.33	13
600–900	897	16,598	0.61 ± 0.20	1.05 ± 0.19	0.49	21
>900	1,277	15, 626	0.64 ± 0.20	1.18 ± 0.21	0.45	7
Inclusive	950	47,466	0.65 ± 0.23	1.00 ± 0.22	0.25	16

The results are consistent with an over-prediction of the ν_{μ} contamination of the MiniBooNE antineutrino-mode CCQE sample

Table 7.16 Fractional composition of the antineutrino-mode CCQE sample before and after angular fits

$E_{\bar{\nu}}^{QE}$ range	Befo	ore fit (%)	After fit	(%)
(MeV)	ν_{μ}	$\bar{ u}_{\mu}$	ν_{μ}	$ar{ u}_{\mu}$
<600	25	75	18 ± 6	82 ± 16
600-900	26	74	17 ± 6	83 ± 15
>900	35	65	23 ± 7	77 ± 15
Inclusive	29	71	21 ± 8	79 ± 18

The χ^2 value for the angular fit in the reconstructed energy range $E_{\nu}^{\rm QE} > 900\,{\rm MeV}$ is unusually low at $\chi^2=7$ for 21 degrees of freedom. This is likely to be simply due to chance, as the statistical error only fit agrees with the data exceptionally well within the error, returning $\chi^2=13$ for 21 degrees of freedom.

As the ν_{μ} angular template has been corrected for the observed cross section per [4], α_{ν} may be interpreted as a flux scale factor, and significant deviations

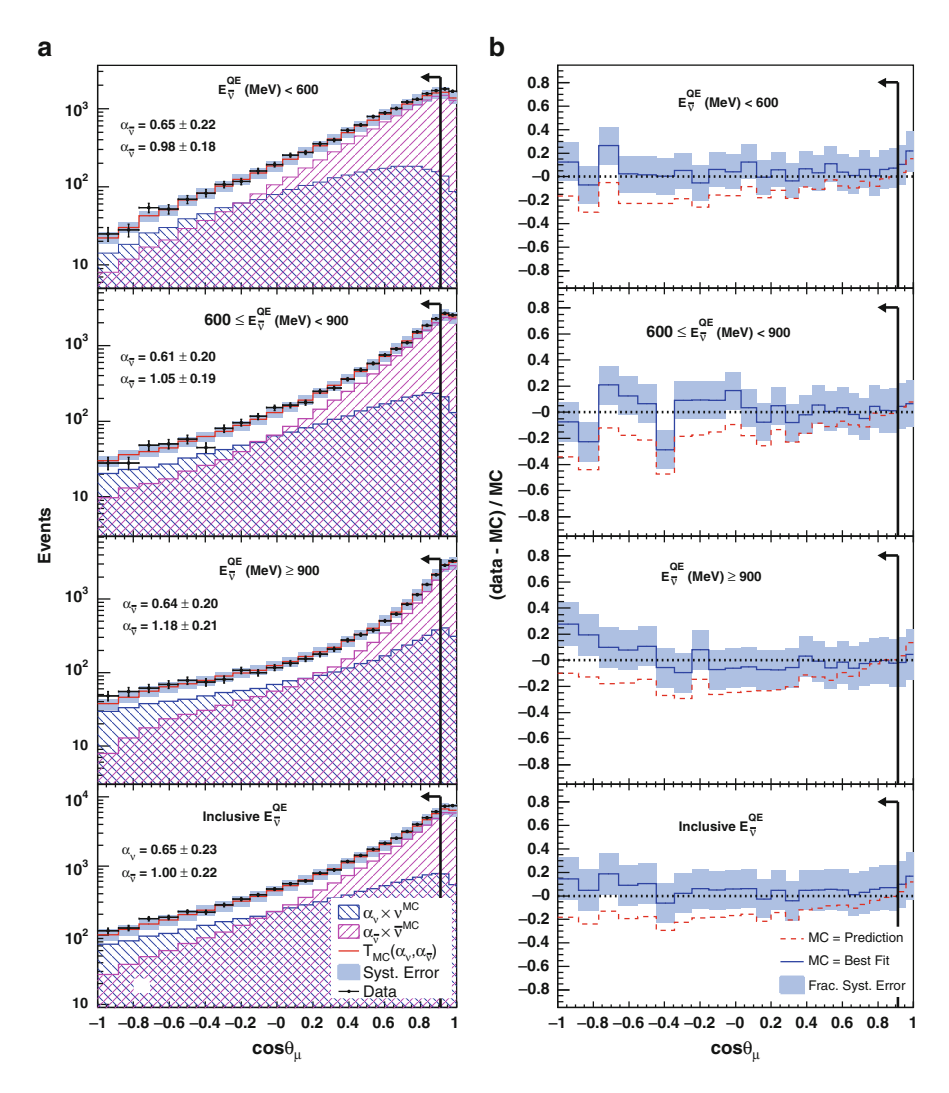


Fig. 7.17 Results of the muon angular fits to the CCQE data. Shown are (a) the fits and (b) fractional differences (data — simulation)/simulation for both the unmodified prediction and the best fit. Along with an inclusive sample, three reconstructed energy bins are considered. The before-fit simulation is absolutely normalized to 5.66×10^{20} protons on target. As indicated, only events with $\cos\theta_{\mu} < 0.91$ participate in the fit

from unity would imply a flux mismodeling. Consistent with the results reported in the previous sections using $CC\pi^+$ and μ^- capture events, fits in the antineutrinomode CCQE sample indicate the true neutrino flux to be somewhat lower than the simulation predicts. Over all reconstructed energies, the neutrino flux component of the antineutrino-mode beam should be scaled by 0.65 to match the observed data. Fits in individual reconstructed energy bins indicate that the neutrino flux

component shape is well-modeled. The rate scale $\alpha_{\bar{\nu}}$ is ambiguous in interpretation, as the cross section is yet unmeasured.

The results from this technique depend on knowing the angular distributions of neutrino and antineutrino CCQE interactions in the detector. While the procedure relies on exploiting the effect of the interference term in the CCQE cross section, the angular distributions may be somewhat altered by nuclear effects. In this analysis the measured angular distribution of neutrino interactions on carbon [4] is employed, but the measurement relies on the scattering model to predict antineutrino interactions. This model does not include two-body current effects which may be larger than previously expected [33–38] and may introduce additional neutrino and antineutrino angular differences. Despite this inherent model dependence, the results present a demonstration of a technique aimed at informing future experiments looking to separately constrain neutrino and antineutrino events in an unmagnetized environment. By that time, the effect of additional nuclear processes on the angular dependence of antineutrino CCQE scattering should be better known.

7.1.6 Summary of v_{μ} Flux Measurements

The results from Sects. 7.1.3–7.1.5 provide the first demonstration of a set of statistical techniques used to measure the ν_{μ} component of an antineutrino-mode beam. Their results are summarized in Fig. 7.18, where measurements performed in exclusive reconstructed neutrino energy bins are given as a function of the mean generated neutrino energy for that region.

Results from all three measurements indicate the normalization of the nominal ν_{μ} flux prediction using a Sanford-Wang-based [39] extrapolation of the HARP data (discussed in Sect. 5.2.4) requires a uniform reduction of 20–30 %. This indicates the simulated shape of the flux spectrum appears to be adequate. Interesting to note, given the results in Fig. 7.18 along with the comparison of two possible π^- extrapolations into the low-angle region shown in Fig. 5.7, the spline-based prediction appears to more accurately describe the data.

It is helpful to mention again that the analysis of the $\cos\theta_{\mu}$ distribution is somewhat dependent on the model for $\bar{\nu}_{\mu}$ CCQE interactions assumed by the simulation, and so its results are not used in the background subtraction of ν_{μ} events from the $\bar{\nu}_{\mu}$ CCQE sample. Conversely, it has been shown that the analyses based on CC π^+ and μ^- capture events are almost entirely free from model dependence. Moreover, that the analyzed samples are dominated by different physics processes indicates a level of independence between the two measurements. The results of these two analyses can therefore be used to find a combined measurement of the ν_{μ} flux in the antineutrino-mode beam featuring a reduced uncertainty compared to either measurement alone. For two measurements x_1 , x_2 , along with their associated uncertainties σ_1 , σ_2 and correlation ρ , the combined measurement and uncertainty can be expressed as [40]:

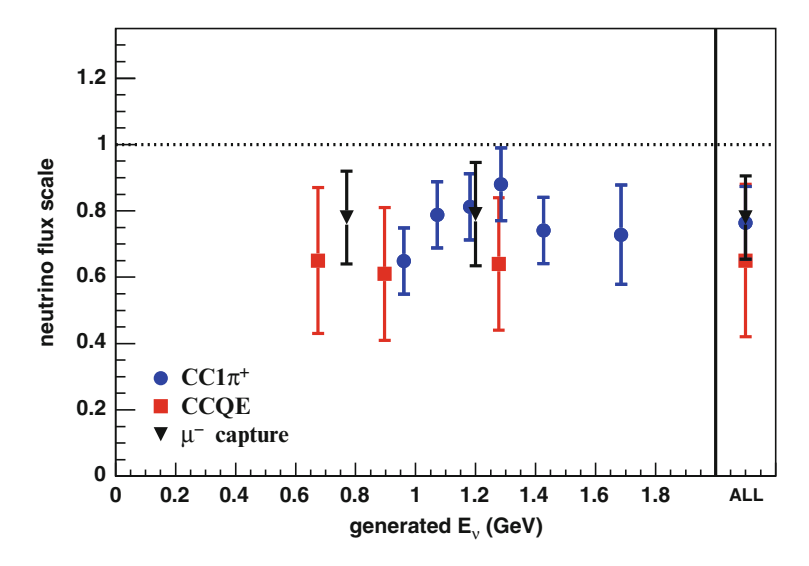


Fig. 7.18 Summary of the results from three techniques used to measure the ν_{μ} flux in the antineutrino-mode beam. Measurements performed in exclusive regions of reconstructed energy are placed here at the mean of their associated distribution of generated energy. Shown as a *dotted line* at unity, the measurements are made relative to an extrapolation of HARP data into a region where no relevant hadroproduction data exists

$$\langle x \rangle = x_1 + \frac{1 - a\rho}{1 - 2a\rho + a^2} (x_2 - x_1)$$
 (7.31)

$$\langle \sigma \rangle^2 = \frac{(1 - \rho^2) a^2 \sigma_1^2}{1 - 2a\rho + a^2}$$
 (7.32)

where $a = \sigma_2/\sigma_1$ and $\sigma_2 \ge \sigma_1$. Consistency of the μ^- capture and $CC\pi^+$ measurements across the observed energy range (Fig. 7.18) indicates the simulated v_{μ} flux shape to be well-modeled, and so a combined measurement applied universally to the ν_{μ} background events is adequate. The measurement from the μ^- capture measurement gives 0.78 \pm 0.12, while the CC π^+ measurement yields 0.76 ± 0.11 . The uncertainty in the μ^- capture measurement is in roughly equal parts due to statistics and the neutrino-mode flux errors, while the error in the $CC\pi^+$ measurement is dominated by the neutrino-mode flux uncertainty. Based on this, the correlation coefficient ρ is estimated to be 0.5. With these values implemented into Eqs. (7.31) and (7.32), the combined measurement of the ν_{μ} flux in the antineutrino-mode beam is 0.77 ± 0.10 relative to the extrapolated and highly-uncertain prediction. This will be the data-based constraint of the ν_{μ} uncertainty assumed in the background subtraction process in finding the $\bar{\nu}_{\mu}$ CCQE cross sections presented in Chap. 8. Notice the level of knowledge necessary for background subtraction is how many events are present in the analysis sample, which is directly measured through the μ^- capture-based measurement. Therefore, using the uncertainty on the v_{μ} flux results in a mild overestimate of the uncertainty of the ν_{μ} background.

7.2 The $\bar{\nu}_{\mu}$ CC π^- Background

While the high rate of stopped- π^- nuclear capture allows for the powerful measurement of the ν_μ flux using $CC\pi^+$ events presented in Sect. 7.1.3, $CC\pi^-$ events migrate into the $\bar{\nu}_\mu$ CCQE sample and form an irreducible background to the main analysis of this dissertation. Following the discussion of $\bar{\nu}_\mu$ CCQE selection efficacy given in Sect. 6.2, Table 6.2 reports that these $CC\pi^-$ events are predicted to account for $\sim\!15\,\%$ of the sample. Considering the level of agreement between various calculations and the experimental data for single-pion interactions discussed in Sect. 4.3, constraints and uncertainties for $CC\pi^-$ events are based entirely on direct comparisons with MiniBooNE data.

An indirect constraint of $CC\pi^-$ events is obtained through an extrapolation of a MiniBooNE $CC\pi^+$ -based measurement, and a discussion of the origin of this correction is warranted. As suggested in Sect. 7.1.3, single-pion events induced by ν_μ typically give rise to Michel electrons through the decay chain $\pi^+ \to \mu^+ \to e^+$ of stopped pions, which can be observed and used to reject these events. However, an appreciable number of π^+ are destroyed in flight through the nuclear absorption process $(\pi^+ + X \to X')$ and therefore formed a significant background to the neutrino-mode ν_μ CCQE sample. Measurements of $CC\pi^+$ events tagged through the observation of an additional Michel allowed a direct constraint of the rate and kinematics of the $CC\pi^+$ background to the ν_μ CCQE analysis.

Figure 7.19 shows the MiniBooNE neutrino-mode $CC\pi^+$ data, prediction, and the obtained constraint. To guarantee the selected sample probes the same kinematics of $CC\pi^+$ events that enter as backgrounds to the CCQE selection, sample formation was identical to that for CCQE described in Sect. 6.2, with the replacement of the two subevent requirement with three subevents. Along the same lines, the measurement is based on Q_{QE}^2 (Eq. (6.8) with $n\leftrightarrow p$, appropriate to ν_μ CCQE scattering), which assumes the underlying interaction to be CCQE. Clearly this assumption is incorrect for this physics sample, and so the comparison in Fig. 7.19 cannot be rigorously used to identify the level of agreement between data and the underlying model for $CC\pi^+$ interactions. However, obtaining the constraint in this variable does allow its direct application to $CC\pi^+$ events background to the ν_μ CCQE sample.

Due to π^- nuclear capture, using an analogous procedure to measure the rate and kinematics of $CC\pi^-$ events is not possible. In the absence of such a measurement, the constraint obtained in neutrino mode for ν_μ $CC\pi^+$ is applied to the $CC\pi^-$ Rein-Sehgal prediction. This assumes the underlying effects observed in the MiniBooNE $CC\pi^+$ data not predicted by the Rein-Sehgal model are identical for the $CC\pi^-$ process. In the absence of additional information, a large extrapolation uncertainty would be warranted.

Fortunately, a more modern external calculation with success in describing world single-pion production data is available to use in predicting the contribution of $CC\pi^-$ events to the $\bar{\nu}_{\mu}$ CCQE sample [41]. This alternate model is implemented in NUANCE and is based on improvements to the Rein-Sehgal model originally

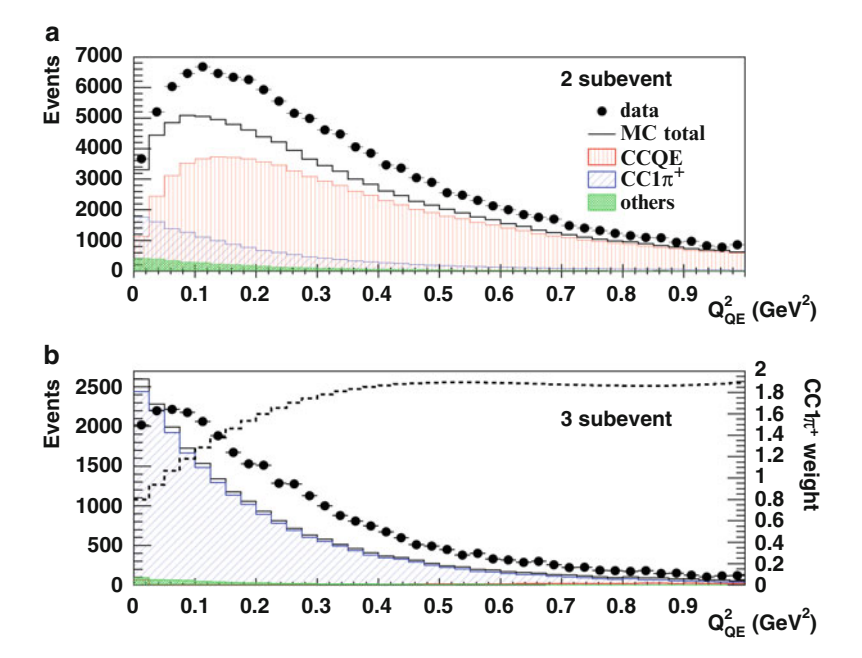


Fig. 7.19 Summary of the MiniBooNE $CC\pi^+$ analysis for the background measurement to the ν_{μ} CCQE sample. Shown is (a) the neutrino-mode CCQE sample and (b) the $CC\pi^+$ sample before the application of constraints and parameter fits. The *dashed line* in (b) shows the ratio of prediction to data in the $CC\pi^+$ sample, and its value is given by the right ordinate axis. This measurement is used to indirectly constrain the rate and kinematics of the $CC\pi^-$ contribution to the $\bar{\nu}_{\mu}$ CCQE sample. Figure taken from [4]

developed in [42–44]. This updated calculation includes muon mass terms and a modified vector form factor to yield better agreement with world pion production data [45]. Figure 7.20 shows this model also offers excellent agreement with the MiniBooNE $CC\pi^+$ data for $Q^2 \gtrsim 0.1 \, \text{GeV}^2$.

This model is used as a second constraint on the prediction for the contribution of $CC\pi^-$ events to the $\bar{\nu}_\mu$ CCQE sample. The level of agreement between this calculation and the indirect constraint based on the observed MiniBooNE $CC\pi^+$ data is shown in Fig. 7.21. Consistency between these two predictions for $CC\pi^-$ production suggests an uncertainty of 20% is sufficient for the $CC\pi^-$ background.

7.3 All Other Backgrounds

The analyses in Sects. 7.1 and 7.2 constrain the contribution of ν_{μ} CCQE and CC π^{\pm} interactions to the $\bar{\nu}_{\mu}$ CCQE sample. According to Table 6.2, the remaining channels account for \sim 6% of the analysis sample. About half of these interactions are from

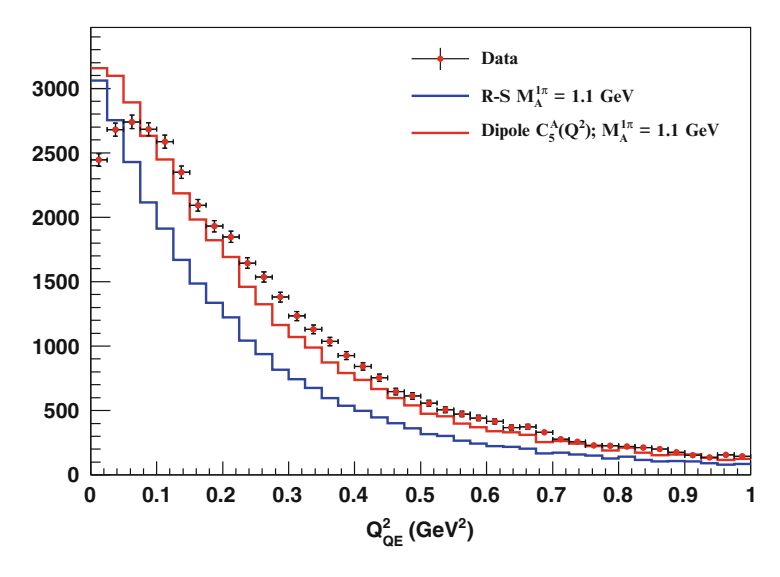


Fig. 7.20 Comparison of the nominal Rein-Sehgal model to a more modern model that also describes world pion-production data more accurately

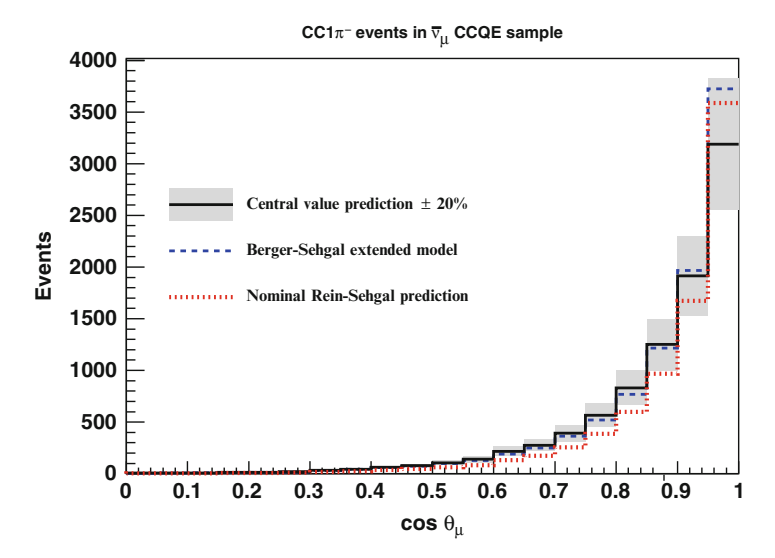


Fig. 7.21 Three calculations for the $CC\pi^-$ background contribution to the $\bar{\nu}_\mu$ CCQE sample as a function of $\cos\theta_\mu$. The "central value" distribution corresponds to the nominal Rein-Sehgal prediction for $CC\pi^-$ events in MiniBooNE constrained by the observed kinematics in the neutrino-mode ν_μ CC π^+ sample. This agrees well with a more recent calculation ("Berger-Sehgal extended model") that is based on an improved version of the Rein-Sehgal model. For comparison, the nominal Rein-Sehgal prediction for $CC\pi^-$ events is also shown. Distributions are normalized to flux

 ν_{μ} and $\bar{\nu}_{\mu}$ CC π^0 production, and following the normalization discrepancy found in the MiniBooNE ν_{μ} CC π^0 cross-section analysis [3], the contribution from both ν_{μ} and $\bar{\nu}_{\mu}$ CC π^0 events is increased by 60% of the prediction. The remaining half is dominated by $\bar{\nu}_{\mu}$ Cabibbo-suppressed quasi-elastic hyperon production, which ought to be closely related to the $\bar{\nu}_{\mu}$ CCQE results, but is experimentally poorly understood.

Two configurations of $\bar{\nu}_{\mu}$ CCQE cross sections are produced in this dissertation: incident on mineral oil (with atomic composition \sim CH₂) and incident on carbon only. Many measurements of ν_{μ} and $\bar{\nu}_{\mu}$ CCQE on free or quasi-free nucleons at a variety of energies have produced results consistent with the RFG model and $M_A \sim 1\,\mathrm{GeV}$ [46], and so the carbon-only configuration is attained by treating the $\bar{\nu}_{\mu}$ CCQE events on hydrogen as background. Its contribution is predicted with the RFG and $M_A = 1.026 \pm 0.021\,\mathrm{GeV}$ following the analysis of relevant global data in [47].

7.4 Background Constraint Summary

The largest backgrounds in the $\bar{\nu}_{\mu}$ CCQE sample are those from ν_{μ} and from the $\bar{\nu}_{\mu}$ CC π^- contributions. The dominant ν_{μ} interactions are from CCQE and CC π^+ channels, and their fundamental cross sections have been measured in the MiniBooNE data [1,4]. The implementation of these direct constraints is explained in Sect. 7.1.4. The ν_{μ} flux accepted into the antineutrino-mode data is constrained by the novel and unique measurements presented in Sect. 7.1, and per Sect. 7.1.6, the combined constraint on the ν_{μ} flux relative to the extrapolated and highly-uncertain prediction (described in Sect. 5.2.4) is 0.77 ± 0.10 . No additional error is taken on the ν_{μ} CCQE and CC π^+ interactions, as the ν_{μ} flux uncertainty is nearly fully correlated with the CCQE and CC π^+ cross section errors.

As discussed in Sect. 7.2, the $CC\pi^-$ interaction cross sections are only indirectly constrained through the measurement of the rate and kinematics of ν_μ $CC\pi^+$ events extrapolated to the $\bar{\nu}_\mu$ processes. Consistency between this prediction for the $CC\pi^-$ contribution to the $\bar{\nu}_\mu$ CCQE analysis sample with an external model for resonance events capable of describing world $CC\pi$ production data provides confidence in our description of $CC\pi^-$ events. Following these studies, a 20 % normalization uncertainty is assigned to the $CC\pi^-$ interactions.

Finally, the small contribution from ν_{μ} and $\bar{\nu}_{\mu}$ $CC\pi^{0}$ events are increased by 60% of the NUANCE-based prediction to reflect the MiniBooNE ν_{μ} $CC\pi^{0}$ results [3]. The uncertainty on interactions not induced by ν_{μ} and are non- $CC\pi^{-}$ interactions is 30% of their prediction.

A summary of the various backgrounds in the $\bar{\nu}_{\mu}$ CCQE sample, including their uncertainties and constraints, if any, is provided in Table 7.17.

Table 7.17 Summary of background constraints and uncertainties in the $\bar{\nu}_{\mu}$ CCQE sample

rance very summary or o			Sampre	
	Contribution to			Fractional
Interaction	$\bar{\nu}_{\mu}$ CCQE sample (%) Flux constraint	Flux constraint	Cross-section constraint uncertainty (%)	uncertainty (%)
All ν_{μ}	22	This chapter	[1,3,4]	13
$\bar{\nu}_{\mu}$ CCQE on hydrogen	17	[48]	[47]	2
$ar{ u}_{\mu}~{ m CC}\pi^-$	14	[48]	[4] (indirect)	20
Non-CCQE, non-CC π^{\pm}	9	This chapter (ν_{μ} processes) [3]	[3]	30
	o	and [48] $(\bar{\nu}_{\mu}$ processes) $(\nu_{\mu}$ CC π^{0} only)	$(\nu_{\rm m} \ {\rm CC}\pi^0 \ {\rm onlv})$	

subject to both categorical uncertainties. Interactions of $\bar{\nu}_{\mu}$ CCQE on hydrogen are only treated as a background in the extraction of $\bar{\nu}_{\mu}$ CCQE cross sections on carbon. Additional uncertainties on the $\bar{\nu}_{\mu}$ processes enter through the HARP π^- production data Notice there is a small overlap between the ν_{μ} and non-CCQE, non-CC π^{\pm} categories. Events belonging to both classes are and beamline simulations

References

- 1. A.A. Aguilar-Arevalo et al. [MiniBooNE Collaboration], Phys. Rev. D83, 052007 (2011)
- 2. A.A. Aguilar-Arevalo et al. [MiniBooNE Collaboration], Phys. Rev. D81, 013005 (2010)
- 3. A.A. Aguilar-Arevalo et al. [MiniBooNE Collaboration], Phys. Rev. D83, 052009 (2011)
- 4. A.A. Aguilar-Arevalo et al. [MiniBooNE Collaboration], Phys. Rev. D81, 092005 (2010)
- 5. A.A. Aguilar-Arevalo et al. [MiniBooNE Collaboration], Phys. Rev. Lett. 103, 081801 (2009)
- 6. A.A. Aguilar-Arevalo et al. [MiniBooNE Collaboration], Phys. Rev. **D82**, 092005 (2010)
- 7. A.A. Aguilar-Arevalo et al. [MiniBooNE Collaboration], Phys. Lett. **B664**, 41 (2008)
- 8. M.G. Catanesi et al. [HARP Collaboration], Eur. Phys. J. C52, 29 (2007)
- P. Adamson et al. [MINOS Collaboration], Study of muon neutrino disappearance using the Fermilab Main Injector neutrino beam. Phys. Rev. D77, 072002 (2008)
- 10. P. Astier et al. [NOMAD Collaboration], Search for $\nu_{\mu} \rightarrow \nu_{e}$ oscillations in the NOMAD experiment. Phys. Lett. **B570**, 19–31 (2003)
- P.-A. Amaudruza [T2K ND280 FGD Collaboration], The T2K fine-grained detectors. Nucl. Instrum. Methods A696, 1 (2012)
- D.S. Ayres et al. [NOvA Collaboration], The NOvA Technical Design Report. FERMILAB-DESIGN-2007-01 (2007)
- V. Barger et al. [LBNE Collaboration], Report of the US long baseline meutrino experiment study. arXiv:0705.4396 (2007)
- A. de Bellefon et al. MEMPHYS: a large water Čerenkov detector at Fréjus. arXiv:hep-ex/ 0607026 (2006)
- K. Nakamura, Hyper-Kamiokande a next generation water Cherenkov detector. Int. J. Mod. Phys. A 18, 4053 (2003)
- 16. P. Huber, T. Schwetz, Phys. Lett. **B669**, 294 (2008). arXiv:0805.2019
- 17. D.D. Stancil et al. [MINERvA Collaboration], Demonstration of communication using neutrinos. Mod. Phys. Lett. **A27**, 1250077 (2012)
- A.A. Aguilar-Arevalo et al. [MiniBooNE Collaboration], Measurement of the neutrino component of an anti-neutrino beam observed by a non-magnetized detector. Phys. Rev. D84, 072005 (2011). arxiv:1102.1964
- A.A. Aguilar-Arevalo et al. [MiniBooNE Collaboration], First measurement of the muon anti-neutrino double-differential charged current quasi-elastic cross section. Phys. Rev. D88, 032001 (2013)
- 20. A. Shinohara et al. Phys. Rev. A53, 130 (1996)
- 21. E.J. Maier, R.M. Edelstein, R.T. Siegel, Phys. Rev. 133, B663 (1964)
- 22. L.Ph. Roesch et al. Phys. Lett. **107B**, 31 (1981)
- 23. Yu.G. Budyashov et al. Sov. Phys. JETP **31**, 651 (1970)
- 24. M.E. Plett, S.E. Sobottka, Phys. Rev. C3, 1003 (1971)
- 25. B. Macdonald et al. Phys. Rev. 139, B1253 (1965)
- 26. G.H. Miller et al. Phys. Lett **41B**, 50 (1972)
- 27. A.A. Aguilar-Arevalo et al. [MiniBooNE Collaboration], Phys. Rev. D81, 013005 (2010)
- 28. A.A. Aguilar-Arevalo et al. [MiniBooNE Collaboration], Phys. Rev. D82, 092005 (2010)
- 29. J. Grange for the MiniBooNE Collaboration, AIP Conf. Proc. 1405, 83 (2011)
- 30. See http://root.cern.ch/root/html/TMinuit.html (1995)
- 31. B.P. Roe, Nucl. Instrum. Meth. A **570**, 159 (2007)
- 32. AA. Aguilar-Arevalo et al. [MiniBooNE Collaboration], Phys. Rev. Lett. 103, 061802 (2009)
- M. Martini et al. Neutrino and antineutrino quasielastic interactions with nuclei, Phys. Rev. C81, 045502 (2010)
- J. Nieves et al. Inclusive charged-current neutrino-nucleus reactions. Phys. Rev. C83,045501 (2011). arXiv:1102.2777
- J. Amaro et al. Meson-exchange currents and quasielastic antineutrino cross sections in the SuperScaling Approximation. arXiv:1112.2123
- 36. A. Meucci, C. Giusti, Phys. Rev. **D85**, 093002 (2012)

References 107

- 37. A. Bodek et al. Eur. Phys. J. C71, 1726 (2011)
- 38. M.S. Athar, S. Ahmad, S.K. Singh, Charged current antineutrino reactions from ¹²C at MiniBooNE energies. Phys. Rev. **D75**, 093003 (2007)
- 39. J.R. Sanford, C.L. Wang, Brookhaven National Laboratory Note 11299 (1967)
- 40. M.G. Cox et al. The generalized weighted mean of correlated values. Metrologia 43, S268 (2006)
- 41. J. Nowak, AIP Conf. Proc. 1189, 243 (2009)
- 42. Ch. Berger, L.M. Sehgal, Phys. Rev. **D76**, 113004 (2007)
- 43. K.S. Kuzmin, V.V. Lyubushkin, V.A. Naumov, Polarization of tau leptons produced in quasielastic neutrino-nucleon scattering. Mod. Phys. Lett. A19, 2919 (2004)
- 44. K.S. Kuzmin, V.V. Lyubushkin, V.A. Naumov, Extended Rein-Sehgal model for tau lepton production. Nucl. Phys. B (Proc. Suppl.) 139, 154 (2005)
- 45. K.M. Graczyk, J.T. Sobczyk, Phys. Rev. D77, 053001 (2008)
- 46. A. Bodek et al. J. Phys. Conf. Ser. 110, 082004 (2008)
- 47. V. Bernard et al. J. Phys. G28, R1 (2002)
- 48. D. Schmitz, A measurement of hadron production cross-sections for the simulation of accelerator neutrino beams and a search for muon neutrino to electron neutrino oscillations in the $\Delta m^2 \sim 1 \text{ eV}^2$ region. Ph.D. thesis, Columbia University, 2008

Chapter 8 $\bar{\nu}_{\mu}$ CCQE Cross-Section Measurement

Following the introduction to this measurement given in Chap. 6 and the opportunistic background measurements and constraints presented in Chap. 7, we now turn to the cross-section calculation and its various ingredients. This measurement is also described in [1].

8.1 Data Stability

Certainly the most important quantity to have confidence in is the data itself. A total of 10.09×10^{20} POT of antineutrino-mode data are used in this analysis. This corresponds to the full MiniBooNE antineutrino-mode data set through April 2012, excluding the brief period in 2006 when absorber blocks fell into the meson decay tunnel. Many stability checks have been performed on the CCQE sample over the years and they've typically shown consistency within 1%. Those most directly related to this analysis are presented here. For historical reasons, the data selection used in these stability checks differ slightly from that described in Sect. 6.2, however the two selection sets result in roughly the same purity and efficiency. To test for any effective time dependence in the distributions, perhaps due to a systematic change in the experimental setup, the data is separated chronologically into groups described in Table 8.1. The shape compatibility of the four distributions we will turn into cross sections, Q_{QE}^2 (Eq. (6.8)), E_{v}^{QE} (Eq. (6.7)) and the muon kinematic properties T_{μ} and $\cos\theta_{\mu}$ are assessed over different run periods are assessed through the Kolmogorov-Smirnoff (K-S) test [2] and are presented in Fig. 8.1.

Not independent from Fig. 8.1 but perhaps more accessible is the shape of the E_v^{QE} distribution shown for the same run periods on Fig. 8.2.

A direct test of the normalization of the primary analysis sample is presented in Fig. 8.3, where the events passing selection are given per POT for each period.

Label	Run dates	POT (×10 ²⁰)
"Jul07"	Jan. 2006 to Sep. 2008	2.205
"Sep09"	Sep. 2008 to Jun. 2009	1.477
"Mar10"	Aug. 2009 to Mar. 2010	0.798
"Oct10"	Mar. 2010 to Oct. 2010	1.160
"May11"	Oct. 2010 to May 2011	1.763
"Mar12"	May 2011 to Apr. 2012	2.688

Table 8.1 Summary of data groups input to the stability tests

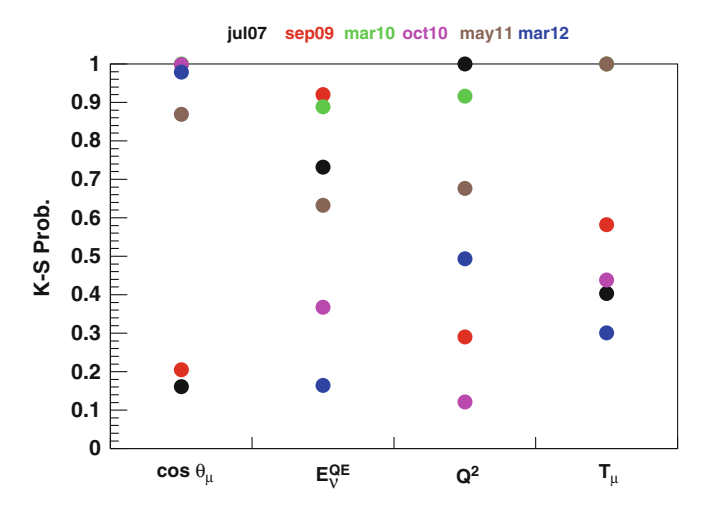


Fig. 8.1 Kolmogorov-Smirnoff test for different antineutrino run periods. Each data point is the result of the K-S test of that run against the sum of the other subsamples. The data are consistent with a uniform distribution between null and unity. Important to note is that E_{ν}^{QE} and Q_{QE}^2 are derived quantities from T_{μ} and $\cos\theta_{\mu}$, so these tests are not independent

8.2 $\bar{\nu}_{\mu}$ CCQE Simulation

Data extraction is mostly insensitive to assumptions on the signal processes, but it is important to qualify their event generation to better understand the final cross-section comparisons between data and simulation.

The RFG simulation of $\bar{\nu}_{\mu}$ CCQE interactions in this analysis assumes an axial mass for $\bar{\nu}_{\mu}$ CCQE events on protons bound in carbon atoms (hereafter referred to as " M_A^C ") of 1.35 GeV, and for events on free protons (" M_A^H ") of 1.02 GeV. Signal events involving bound nucleons also receive the mild Pauli blocking modification $\kappa=1.007$ (Sect. 4.4.1). These parameters are chosen because they adequately reproduce the shape of the data in the reconstructed quantities (Fig. 6.5) while maintaining consistency with the MiniBooNE ν_{μ} CCQE analysis [3] and the light-target CCQE data [4]. If not for a few issues in generating the MiniBooNE MC, this description of our signal assumptions would be sufficient.

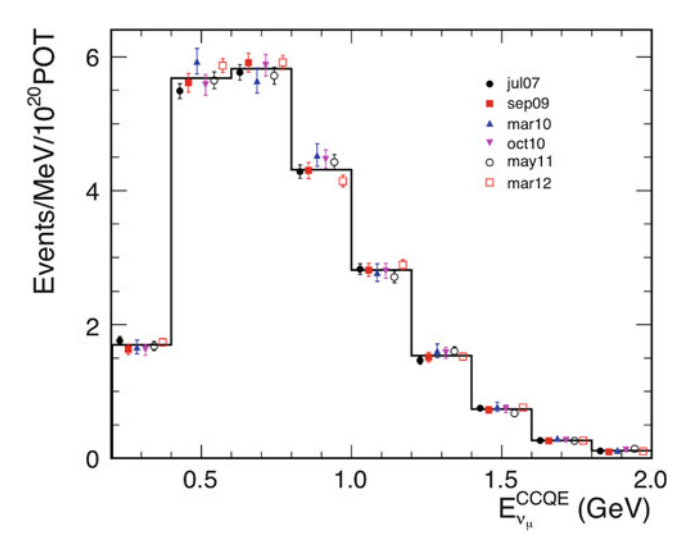


Fig. 8.2 Reconstructed antineutrino data for various run periods. Good agreement within statistical errors indicate stable running. Included here in "jul07" and not in the main analysis is the small absorber down sample

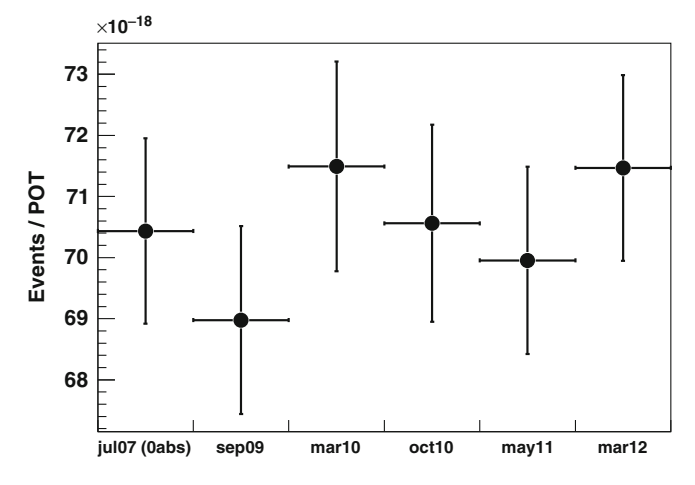


Fig. 8.3 Normalization stability over various run periods. Included uncertainties are statistics and a 2% error on delivered POT

The first issue originates in the reweighting scheme for finding $\kappa=1.007$. Following the 2008 ν_{μ} CCQE analysis [5], the MC files were generated with $M_A^C=1.23\,{\rm GeV}$ and $\kappa=1.022$. As κ is a lower bound on the available outgoing nucleon phase space, we cannot produce a lower value of κ compared to the generated value using traditional reweighting. In other words, events that do not exist cannot be recovered by reweighting.

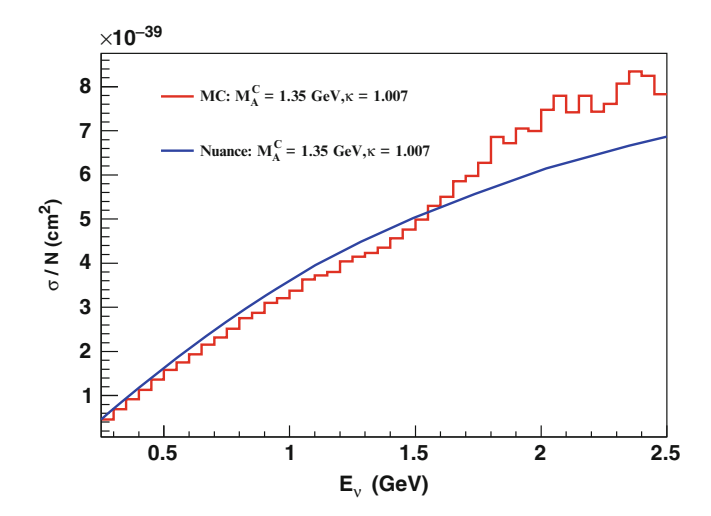


Fig. 8.4 Comparison between generator-level total cross section for bound signal events to the unfolded MC. The files input to the MC distribution were generated with $\kappa=1.022$, and the failed attempt to recover $\kappa=1.007$ through traditional reweighting is clear at lower energies, while the flux sampling issue dominates the discrepancy at high energy

For our simulation to reflect $\kappa=1.007$, we first calculate the absolute cross section per nucleon for signal events involving bound protons from the baseline MC. We exclude hydrogen events here because they are unaffected by κ . This cross section is compared to the NUANCE-generated rate for $M_A^C=1.35\,\mathrm{GeV}$ and $\kappa=1.007$ in Fig. 8.4. The deficit in MC due to lowering κ is clear at lower energies, while an independent problem shows itself above $E_{\nu}\sim1.5\,\mathrm{GeV}$. When the same baseline MC was generated, NUANCE was run in the logarithmic low precision flux sampling mode, meaning the flux spectrum was sampled increasingly sporadically at higher energies. As the $\bar{\nu}_{\mu}$ flux rapidly decreases with $E_{\nu}>1\,\mathrm{GeV}$ or so (Fig. 5.9), this level of sensitivity to the $\bar{\nu}_{\mu}$ flux shape is sufficient for the all non-cross section MiniBooNE analyses. In the present analysis, the $\bar{\nu}_{\mu}$ flux was sufficiently sampled for the bulk of the distribution but the high energy tail was not accurately explored by NUANCE. If not corrected, the details of the issue would lead to a too-low detection efficiency and a spuriously high cross section.

As κ was introduced to improve kinematic agreement with ν_{μ} CCQE data, it would be insufficient to recover it by reweighting MC to NUANCE based on the total cross section. Therefore we scale MC to the generator-level distribution in bins of the double-differential cross section in muon kinematics $\frac{d^2\sigma}{dT_{\mu}d\cos\theta_{\mu}}$, and the resultant weights are shown in Fig. 8.5.

As the double-differential cross section is flux-integrated, it is only mildly sensitive to the high-energy flux tail. A final set of weights in the absolute cross section is applied to MC to achieve generator-level agreement at the few-% level even at high energies.

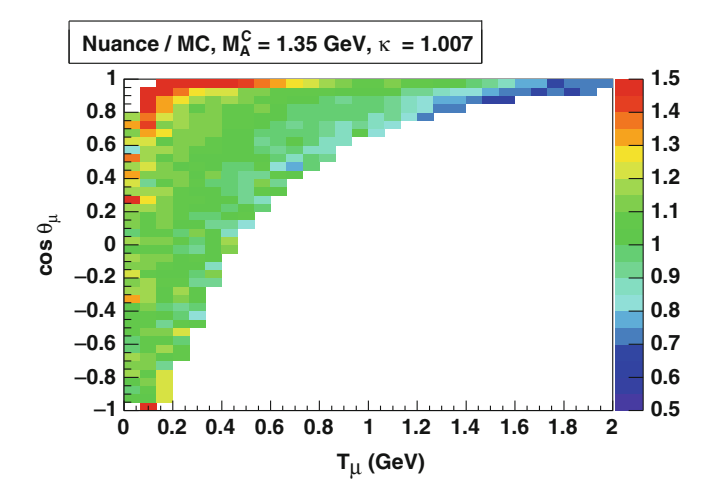


Fig. 8.5 Weights as a function of muon kinematics applied to MC to recover $\kappa = 1.007$. As expected, the weights are strongest in regions of forward-going, low-energy muons

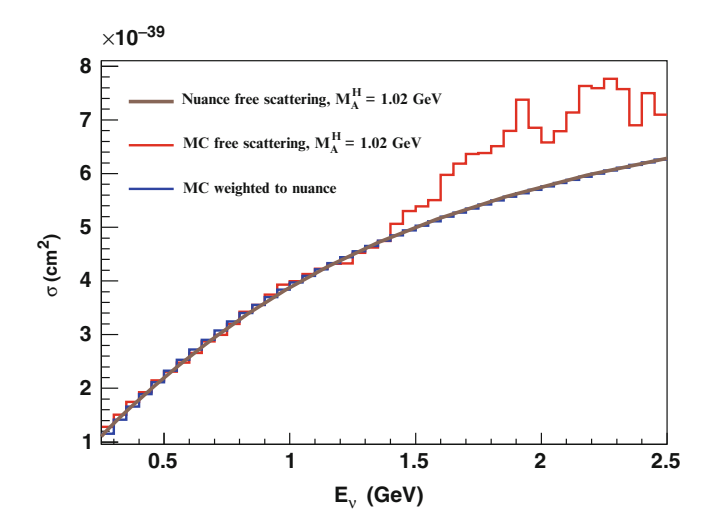
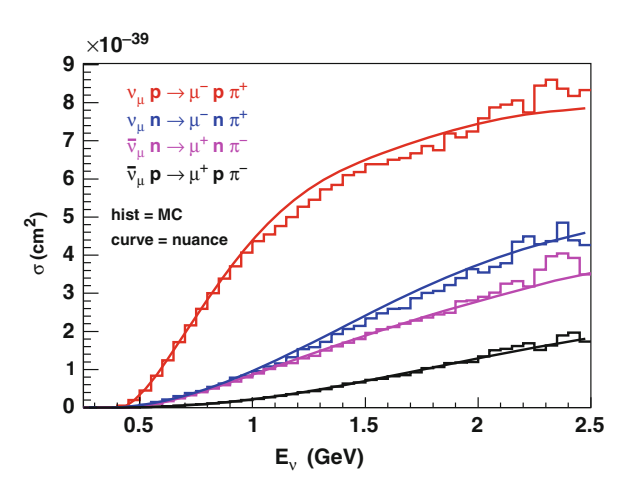


Fig. 8.6 Summary of the high energy rate correction for $\bar{\nu}_{\mu}$ CCQE interactions on hydrogen

As mentioned, the κ issue is irrelevant for signal scattering off hydrogen, but of course the high energy issue is present. Figure 8.6 shows MC before and after correcting for the flux sampling problem.

It is important to note that, with the exception of the high-energy issue affecting the efficiency calculation, these signal assumptions hardly affect our extracted cross sections. The normalization of the MC signal events does not enter the crosssection calculation, while sensitivity to the simulated true shape of signal events

Fig. 8.7 Comparison of NUANCE-generated single pion cross sections to the unfolded MC. Unlike in the CCQE interactions, the high energy flux sampling problem is small enough to ignore here



is quite small. It will be shown later that a conservatively large span of M_A^C and κ signal values lead to negligible differences on the final cross sections. However, this procedure of reweighting our simulation to the NUANCE cross sections with $\kappa=1.007$ was an important step to have a reliable efficiency calculation and be able to faithfully report the model used in data extraction and comparisons.

A final note on the high-energy flux sampling problem involves its effect on the $CC\pi$ interactions. Since the Q^2_{QE} -based correction (described in Sect. 7.2) to $CC\pi^+$ and $CC\pi^-$ events was measured in the neutrino-mode $CC\pi^+$ sample, the constraint could be sensitive to the details of the high-energy problem and its implementation into the antineutrino-mode analyses could be erroneous through the mildly different accepted ν_μ spectra between the two run configurations. However, Fig. 8.7 shows that the flux sampling problem has a much more mild effect on $CC\pi$ interactions compared to CCQE, presumably due to the different shape of the total cross section around the MiniBooNE energy range.

8.3 Cross-Section Calculation

The total cross section per nucleon in the *i*th bin is given by

$$\sigma\left(E_{\nu}\right)_{i} = \frac{\sum_{j} U_{ij} \left(d_{j} - b_{j}\right)}{\epsilon_{i} \Phi_{i} N},\tag{8.1}$$

where d_j (b_j) is the data (background) reconstructed in the jth bin, U_{ij} is the probability for an event of true quantity within bin i to be reconstructed in bin j, ϵ is the detection efficiency, Φ is the \bar{v}_μ flux corresponding to the delivered protons on target, and N is the number of nuclear targets in the volume considered. The differential expressions are similar: for Q_{OE}^2 we have

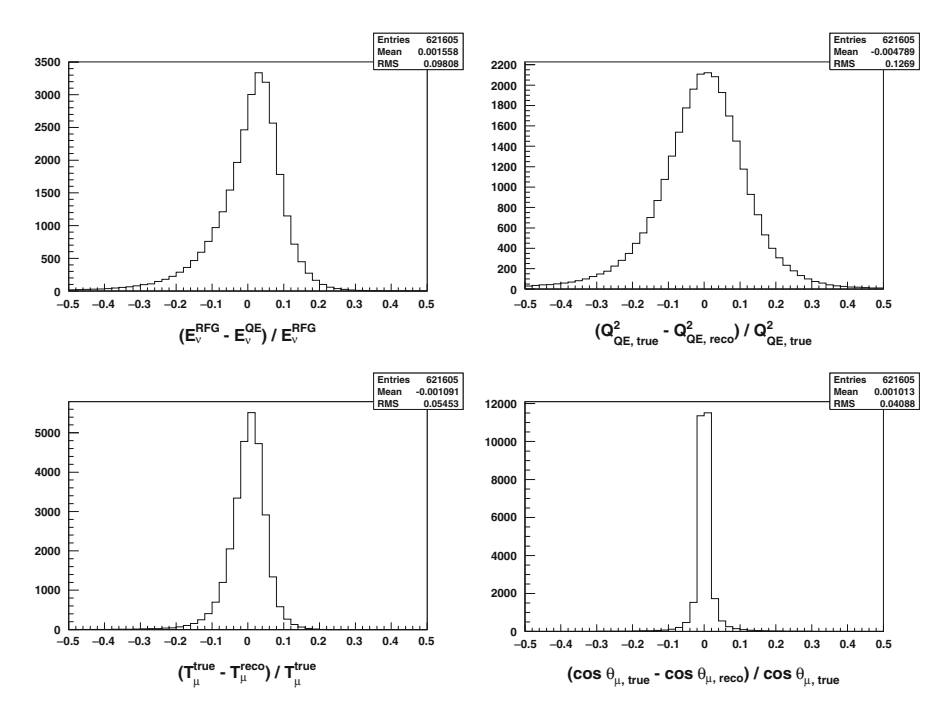


Fig. 8.8 Fractional differences between truth and reconstructed quantities in the four relevant variables. As in all distributions peaked near null, the average fractional difference in Q_{QE}^2 is higher than it would be otherwise

$$\frac{d\sigma}{dQ_{QE}^{2}}_{i} = \frac{\sum_{j} U_{ij} \left(d_{j} - b_{j} \right)}{\Delta Q_{QE}^{2} \epsilon_{i} \Phi N}, \tag{8.2}$$

where ΔQ_{QE}^2 is the width of the *i*th bin and Φ is now the integrated flux. The double-differential calculation is a trivial extension:

$$\frac{d^2\sigma}{dT_{\mu}d\left(\cos\theta_{\mu}\right)_{i}} = \frac{\sum_{j} U_{ij}\left(d_{j} - b_{j}\right)}{\Delta T_{\mu}\Delta\cos\theta_{\mu}\,\epsilon_{i}\,\Phi\,N}.$$
(8.3)

The following subsections expands on each of these quantities.

8.3.1 Unsmearing to True Quantities

All measurements are biased at some level by detectors and analysis tools. The unsmearing process removes this bias so that the underlying quantities may be reported. First we should understand the overall relationship between the quantities we are looking to connect. Figure 8.8 shows the fractional difference between the reconstructed and truth-level variables relevant to this analysis.

It is tempting to refer to the RMS values printed in Fig. 8.8 as the resolution of the MiniBooNE detector to these quantities, but this is not the case for Q_{QE}^2 and, in particular, for the neutrino energy. To avoid dependence on the nuclear model of the RFG, reconstructed Q_{QE}^2 is unsmeared to "true" Q_{QE}^2 , that is using the truth-level μ quantities in Eq. (6.8) instead of the generator-level squared four-momentum transfer. Of course this is not a perfect solution, as any theoretical calculation of the underlying Q^2 will have to first be translated into Q_{QE}^2 before a rigorous comparison with these data can be made. In contrast, reconstructed E_{ν}^{QE} is corrected to the generator-level neutrino energy, referred to here as E_{ν}^{RFG} . E_{ν}^{QE} and E_{ν}^{RFG} are entirely different quantities, and the RMS printed on Fig. 8.8 is simply the average fractional difference between the two. The choice of correcting the neutrino energy back to the generated value is made to be able to compare with historical data produced with the same assumptions.

It is partially for these reasons that the double-differential cross section $\frac{d^2\sigma}{dT_\mu d\cos\theta_\mu}$ is the main result of this work, as it does not rely on a physics model to connect the reconstructed and true quantities. Of course the other advantage is that no assumptions (as are implicit in Eqs. (6.7) and (6.8)) about the primary interaction need be made to reconstruct muon kinematics.

Following the other MiniBooNE cross-section analyses [3, 6–9], the primary method for unsmearing detector effects employs the Bayesian approach [10]. This method is biased by MC assumptions on the underlying distribution, but we will show this prejudice is small. An unbiased estimator will be used to cross-check the results (albeit in less compelling binning), and ultimately the bias is assessed by evaluating the results under a conservatively wide range of signal assumptions. Fortunately error due to this bias is negligible compared to flux and background uncertainties. Another motivation to use the Bayesian method is the aim to follow as closely as reasonable the analysis choices of the ν_{μ} CCQE cross section to better facilitate the combined analysis of Chap. 9.

If we refer to the underlying true data distribution as $\vec{\alpha}$ and to the same distribution under the influence of detector and reconstruction biases as $\vec{\beta}$, the two are connected by the unsmearing matrix U present in Eqs. (8.1)–(8.3) as simply:

$$\vec{\alpha} = \check{U}\,\vec{\beta} \tag{8.4}$$

Each entry U_{ij} represents the probability for an event drawn from the underlying distribution in bin i to be reconstructed in the jth bin. In a perfect detector, \check{U} would be the identity matrix. The reconstructed vector $\vec{\beta}$ is readily recognized as $\left(\vec{d}-\vec{b}\right)$ in the cross section formulae. To build \check{U} we first populate a matrix with signal MC events in the reconstructed vs. true variables, referred to here as \check{M} . The entries of \check{M} are simply connected to \check{U} by normalization factors

$$U_{ij} = \frac{M_{ij}}{\sum_{k} M_{kj}} \tag{8.5}$$

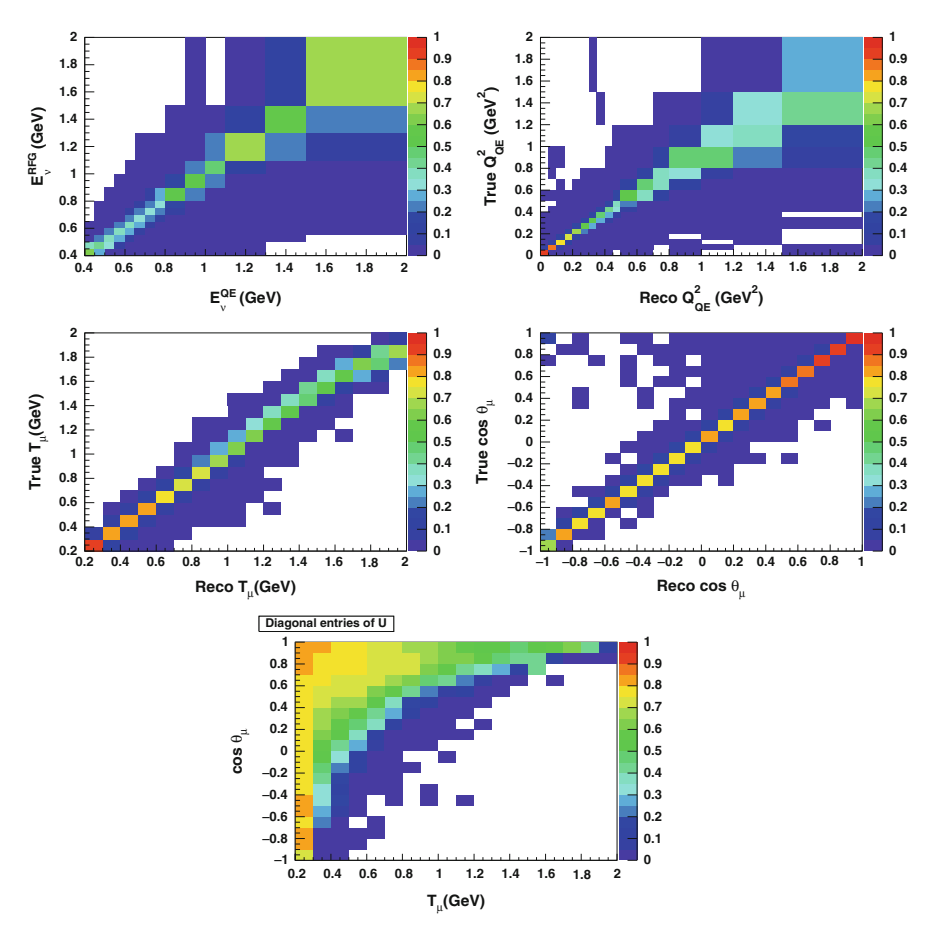


Fig. 8.9 The matrix \check{U} connecting the true and reconstructed quantities for the four variables of interest. For the two-dimensional distribution, in principle \check{U} is four dimensional and only its diagonal entries are shown here

This naturally conserves the number of reconstructed events, i.e. $\sum_i U_{ij} = 1$ for all j. The probability matrix \check{U} is shown in Fig. 8.9 for the four standard distributions in the binning chosen for this analysis, as well as the diagonal entries for muon kinematic plane.

In the application of this method to histograms whose domain may exclude part of the sample, underflow and overflow bins are included. A simple consistency check, passed for all distributions, is that this unsmearing procedure applied to reconstructed MC signal events exactly returns the generated distribution.

Figure 8.10 shows the effect of the \check{U} matrix to the vector $\vec{d} - \vec{b}$, where \vec{d} and \vec{b} are the reconstructed data and background, respectively. The distributions in the same figure represent the numerator in cross-section Eqs. (8.1)–(8.3).

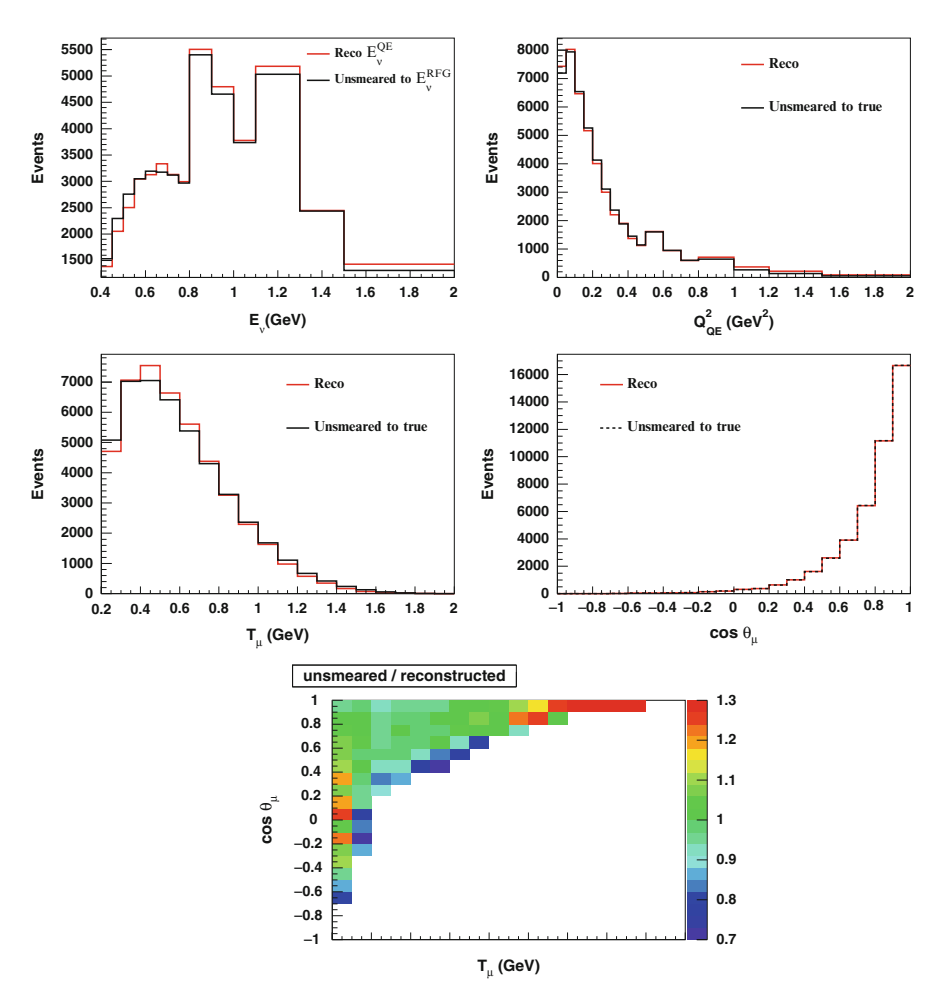


Fig. 8.10 Comparison of before and after the unsmearing procedure for signal events. The twodimensional ratio includes a requirement that there be at least 10 events in each bin of both the reconstructed and unsmeared distributions

The so-called "inversion method" of connecting the reconstructed to true distributions is unbiased by a priori assumptions about the underlying interactions. In this procedure the matrix (referred to as \check{R}) that describes unsmearing operates on the true distribution $\vec{\alpha}$:

$$\vec{\beta} = \check{R}\,\vec{\alpha} \tag{8.6}$$

A quick comparison with Eq. (8.4) shows $\check{R} = \check{U}^{-1}$. The matrix \check{R} is also formed with \check{M} , but this time by normalizing over the reconstructed index:

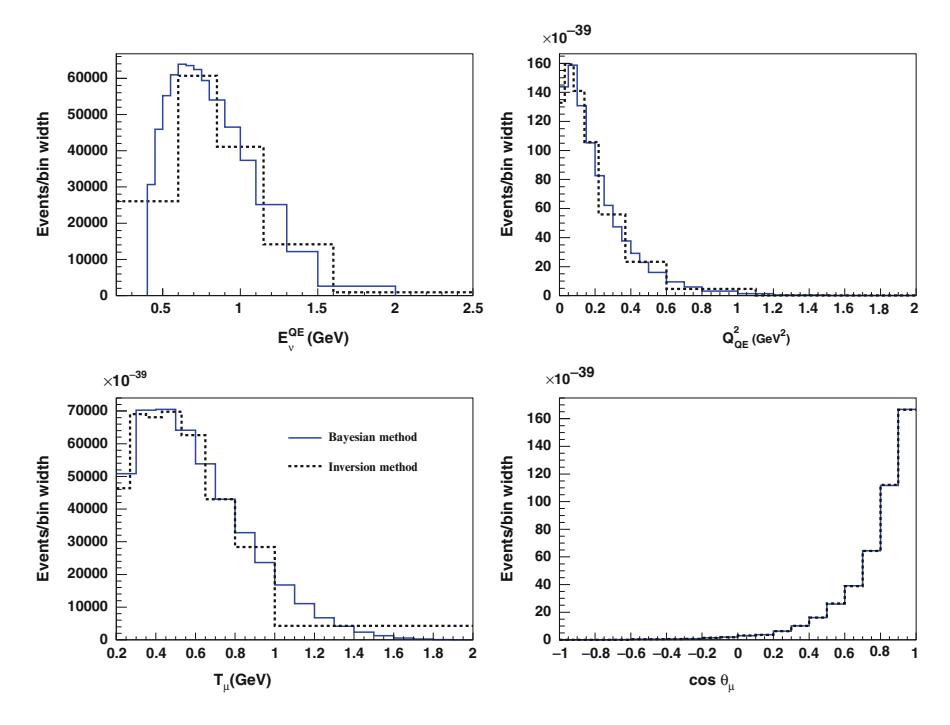


Fig. 8.11 Comparison of the two unsmearing methods studied in this section

$$R_{ij} = \frac{R_{ij}}{\sum_k M_{ik}} \tag{8.7}$$

Since \check{R} must be inverted in order to find the true distribution, the matrix inversion method of unsmearing is exceptionally unstable. In particular, too-fine binning gives rise to the "Gibb's phenomenon", where the calculated true distribution oscillates wildly bin-to-bin. Anecdotally, this can be avoided by choosing the binning such that on-diagonal elements of \check{R} are no lower than 0.8. This requirement constrains the bins to be quite modest. This is particularly true in the case of the neutrino energy, where the correlation between the E_{ν}^{QE} and E_{ν}^{RFG} variables is relatively weak (Fig. 8.8).

Figure 8.11 compares the results of the matrix inversion method to the Bayesian procedure described previously. The binning has been optimized such that the entries R_{ii} are close to 0.8, because binning finer than those shown might be subject to the Gibb's phenomenon. That the Bayesian method gives results consistent with the unbiased matrix inversion method gives a qualitative upper limit to its bias. However, since unsmearing is a shape-only procedure and the binning in the unbiased method is relatively conservative, this is not an especially powerful test.

More compelling evidence that the Bayesian method does not significantly bias the results is shown in Sect. 8.4, where the prejudice is evaluated to be negligible in the presence of other systematic uncertainties.

8.3.2 Efficiency Correction

To correct for the signal events lost due to sample selection, the detection efficiency is calculated and applied to data bin-by-bin in each distribution. Since the unsmearing procedure described previously has (up to some uncertainty) returned the observed data to the true distribution, efficiencies are measured as a function of the true variable. The efficiency is evaluated in a simulated sample of signal events in a spherical volume of radius 550 cm, the value of which is chosen to avoid a potential rate bias due to the iron optical barrier at 575 cm (this effect is visible in Fig. 6.2), while a negligible number of signal events (<0.2%) that pass selection criteria have a generated radius greater than 550 cm.

Figure 8.12 shows sequential efficiency for each analysis cut in the four standard variables, as well as the total efficiency for the two-dimensional distribution. The majority of the loss of events is caused by requirements on the kinematics of the muon, the simulation for which has been vetted most rigorously against cosmic ray muon data (Sect. 5.3.4).

8.3.3 Flux and Interaction Targets

As described in Sect. 5.2.4, the prediction for the absolute $\bar{\nu}_{\mu}$ flux in antineutrino mode is nearly model independent. Figure 8.13 shows the outgoing π^- phase space at the BNB target contributing to the present data set is well-constrained by the HARP data.

Combining the HARP production data with detailed Geant4 target, horn and beamline geometry gives the absolute $\bar{\nu}_{\mu}$ flux prediction shown in Fig. 8.14.

Since the total cross section and the flux are both functions of the neutrino energy, the flux histogram in Fig. 8.14 is rebinned to match that used in the analysis. In the case of the differential measurements, the integrated flux is used excluding the region E_{ν} < 100 MeV due to the interaction requirement of muon production.

The final element in the cross-section calculations is the number of nucleon targets for the signal. This involves the detector volume corresponding to that assumed by the efficiency correction in Sect. 8.3.2, the mineral oil density, the mass density of relevant protons per molecule, and Avogadro's number. This is calculated for all protons (bound protons only) by:

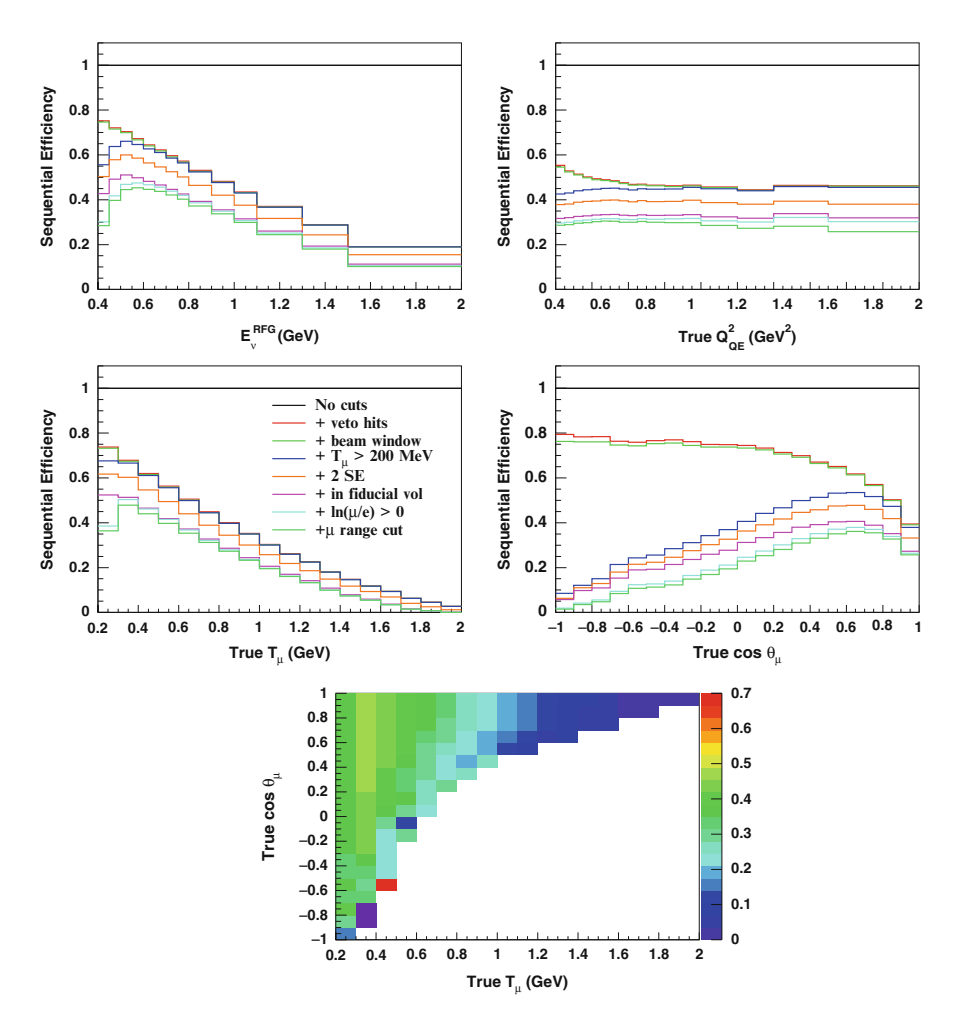


Fig. 8.12 Detection efficiency for each cut in the relevant distributions. Only the total efficiency is shown for two-dimensional muon kinematics

$$N = \frac{4}{3}\pi \left[550 \,\mathrm{cm}\right]^3 \times 0.845 \frac{\mathrm{g}}{\mathrm{cm}^3} \times 6.02214 \cdot 10^{23} \times \frac{6.0(8.06)}{14.06} = 1.5134 \,(2.0330) \times 10^{32}$$
(8.8)

The density of the oil is measured from a sample extracted from the detector, and the composition of the oil is determined to be C_nH_{2n+2} , $n \sim 30$.

Fig. 8.13 Predicted outgoing phase space for π^- before horn focusing. Only π^- 's focused by the horn and that subsequently lead to an interaction in the detector are shown. As printed on the figure, roughly 90 % of the flux is covered by the HARP π^- cross-section data

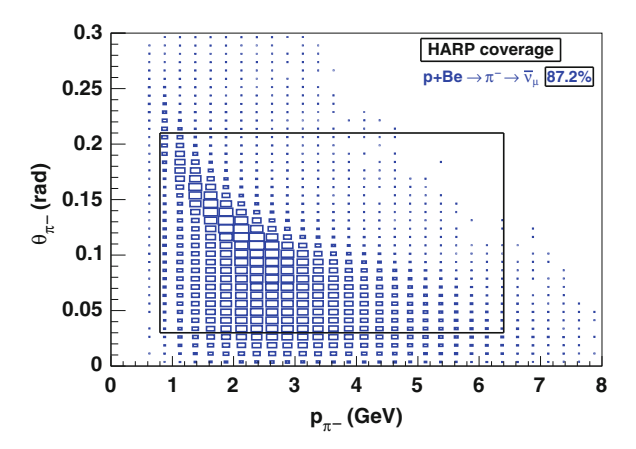
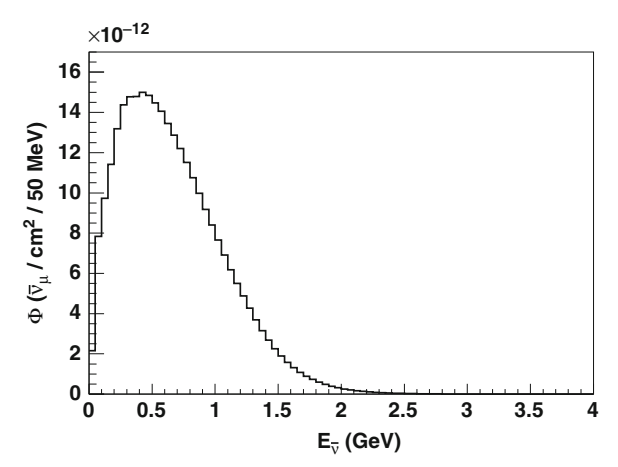


Fig. 8.14 Flux prediction for $\bar{\nu}_{\mu}$ in antineutrino mode for 10.1×10^{20} POT



8.3.4 Statistical Uncertainty

To avoid regions of statistics that would be incorrectly analyzed with a Gaussian treatment, at least 25 events are required to appear in each reconstructed bin $(\vec{d} - \vec{b})$. The statistical error in the *i*th bin is calculated by

Stat error_i =
$$\frac{\sqrt{T_i \times \frac{\text{data}}{\text{MC}}}}{S_i} \times \sigma_i$$
 (8.9)

where T_i and S_i are the predicted number of events in the total and signal samples respectively, "data" and "MC" are the respective normalizations and σ is the (total or differential) cross section in that bin. The data / MC ratio is included to correct for the observed statistics. It might be tempting to not include the normalization ratio

and instead use the number of data events for T_i , but then the statistical error itself would be subject to statistical fluctuations. As with all MiniBooNE cross-section measurements, the statistical error will prove to be negligible with the exception of the tails of the double-differential cross section.

8.4 Systematic Uncertainty

Broadly, systematic errors are evaluated by recalculating the cross sections under appropriate excursions from the assumptions input to the MC regarding parameters and processes that might affect the extraction of the $\bar{\nu}_{\mu}$ CCQE cross sections. The implementation of this idea varies among the systematic errors and the details are presented in this section. The differences between these alternate cross sections and the one described in the previous section are then used to form covariance matrices, and the on-diagonal elements of the quadrature addition of all error matrices sets the total uncertainty on the data. The formation of this covariance matrix is developed in Sect. 7.1.5 and is not repeated here.

8.4.1 Background Uncertainties

Uncertainty on the background is evaluated by the "unisim" method, where a single excursion from the central value prediction is sufficient to propagate uncertainty onto data. Appropriate to the description in Sect. 7.4, backgrounds are separated into three categories: ν_{μ} events from π^+ decay in the beam, $CC\pi^-$, and non-CCQE, non-CC π^\pm interactions. As reported in Table 6.2, these backgrounds comprise 17 %, 14 %, and 6 % of the sample, respectively. Note there is some overlap in the ν_{μ} and the non-CCQE, non-CC π^\pm categories. Section 7.4 summarizes the background constraints and assumed uncertainties on their contributions to the $\bar{\nu}_{\mu}$ CCQE sample.

With the uncertainties on the background interactions set, we re-calculate the cross sections from data with the various backgrounds one standard deviation from their nominal prediction:

$$\sigma (E_{\nu})_{i}^{\text{bkg err}} = \frac{\sum_{j} U_{ij} \left(d_{j} - \left[b_{j} \pm \delta b_{j} \right] \right)}{\epsilon_{i} \Phi_{i} N},$$

$$\frac{d\sigma}{dX_{i}}^{\text{bkg err}} = \frac{\sum_{j} U_{ij} \left(d_{j} - \left[b_{j} \pm \delta b_{j} \right] \right)}{\Delta X \epsilon_{i} \Phi N},$$

$$\frac{d^{2}\sigma}{dT_{\mu} d \left(\cos \theta_{\mu} \right)_{i}}^{\text{bkg err}} = \frac{\sum_{j} U_{ij} \left(d_{j} - \left[b_{j} \pm \delta b_{j} \right] \right)}{\Delta T_{\mu} \Delta \cos \theta_{\mu} \epsilon_{i} \Phi N},$$
(8.10)

where X is a single-differential cross sections and δb is the uncertainty on each background. Since the error matrix formed by these uncertainties involves squaring differences between these alternate calculations and the central value cross sections, it is irrelevant whether the uncertainty on the background is added or subtracted in Eq. (8.10). A separate error matrix is formed for each background by

$$EM_{ij}^{bkg} = \left(\sigma_i^{CV} - \sigma_i^{bkg}\right) \times \left(\sigma_j^{CV} - \sigma_j^{bkg}\right), \tag{8.11}$$

where σ refers to any of the cross section measurements. The total error in a given bin *i* for these error matrices is simply $\sqrt{\text{EM}_{ii}}$.

The gross deviation of the cross sections calculated in Eq. (8.10) compared to the central value is summarized in Sect. 8.4.3.

As mentioned in Sect. 8.4.2, uncertainties on processes affecting signal rates like flux and the optical model also affect background levels and so a small part of these errors are due to backgrounds.

8.4.2 Signal Errors

Uncertainties affecting signal rates are handled in subtly different ways, according to how the excursions from the central value are practically generated.

Flux, inter-medium pion interactions, and model dependence errors are evaluated by the MultisimMatrix package. It takes as input a covariance matrix for a set of parameters and generates a set of weights corresponding to individual throws against a Gaussian distribution for each parameter, according to its specified uncertainty, and is constrained by correlations. Each set of weights k are then used to calculate the range of cross sections due to the input covariance matrix:

$$\sigma (E_{\nu})_{i}^{k} = \frac{\sum_{j} U_{ij}^{k} \left(d_{j} - b_{j}^{k}\right)}{\left[\frac{N \operatorname{acc,k}}{N \operatorname{gen,CV}}\right]_{i} \Phi_{i} N},$$

$$\frac{d\sigma}{dX_{i}}^{k} = \frac{\sum_{j} U_{ij}^{k} \left(d_{j} - b_{j}^{k}\right)}{\left[\frac{N \operatorname{acc,k}}{N \operatorname{gen,CV}}\right]_{i} \Delta X \Phi N},$$

$$\frac{d^{2}\sigma}{dT_{\mu} d \left(\cos\theta_{\mu}\right)_{i}}^{k} = \frac{\sum_{j} U_{ij}^{k} \left(d_{j} - b_{j}^{k}\right)}{\left[\frac{N \operatorname{acc,k}}{N \operatorname{gen,CV}}\right]_{i} \Delta T_{\mu} \Delta \cos\theta_{\mu} \Phi N}.$$
(8.12)

The set of weights appear in three terms: the unsmearing matrix U_{ij}^k , the background prediction b_j^k and in an alternate efficiency calculation $\left[\frac{N^{\mathrm{acc,k}}}{N^{\mathrm{gen,CV}}}\right]_i$. The alternate unsmearing matrix incorporates shape uncertainties in the generated signal

distribution. Perhaps most intuitively, for example, this is where uncertainties on the flux spectrum will result in shape errors on the total cross section.

The final term $\frac{N^{\mathrm{acc},k}}{N^{\mathrm{gen,CV}}}$ incorporates uncertainties on the signal process due to the kth throw, if any. $N^{\mathrm{acc},k}$ refers to the number of signal events passing selection for the kth excursion from the central value, while $N^{\mathrm{gen,CV}}$ is the distribution of signal events before cuts for the central value prediction. It may be non-intuitive to account for flux uncertainties through the efficiency term, but it is trivial to see how a flux excursion from the nominal prediction would affect the calculated error on the cross section in an identical fashion if the normalization difference originated in the ϵ term rather than the Φ term. Note that, in principle, this could lead to a calculated efficiency greater than 1, but of course these factors are related to normalization uncertainties and not true detection rates. Since the errors discussed in this section are generated by reweighting the central value prediction, it is crucial that the denominator in this alternate efficiency calculation refer to the generated central value prediction, and not that from the kth generated distribution. If the weighted generated distribution were taken, the weights intended to be propagated as uncertainties onto the data would be suppressed.

This is also the method for measuring the cross-section uncertainty due to the model for light propagation in the detector (described in Sect. 5.3.2), where 35 possibly correlated parameters are varied within their uncertainty according to external measurements and calibration data. In this case, k in Eq. (8.12) refers to the kth optical model. Additionally, to remove the statistical error the optical models were generated with, for the neutrino energy and Q_{QE}^2 variables the ratio of each optical model to the central value prediction is smoothed to a fourth order polynomial. Such attempts at smoothing for the two-dimensional distribution would be untenable, so to minimize the intrinsic statistical error of the optical models, the size of each sample used is increased to a little more than twice that of the data statistics. As statistical error in this analysis is negligible, this mild overestimate negligibly affects the extracted cross section.

For the optical model and each systematic uncertainty evaluated with Multisim-Matrix, the error matrix is calculated by:

$$EM_{ij} = \frac{\sum_{k=1}^{N_k} \left(\sigma_i^{CV} - \sigma_i^k\right) \times \left(\sigma_j^{CV} - \sigma_j^k\right)}{N_k - 1},$$
(8.13)

where N_k refers to the number of variations from the central value used, and again σ refers to the various cross sections calculated. $N_k=100$ for uncertainties on the π^- flux, the $\bar{\nu}_\mu$ CCQE model dependence, processes entering the sample due to π charge exchange or absorption, and, in the case of calculating the carbon-only $\bar{\nu}_\mu$ CCQE cross sections, the $\bar{\nu}_\mu$ CCQE hydrogen background. $N_k=70$ for the optical model variations.

The flux errors due to π^- production at the target are taken from a spline fit to the HARP π^- double-differential cross-section uncertainties. All other flux uncertainties not directly related to secondary π^- production are referred to as beam

unisim errors, and the most important of these include reinteractions in the target and uncertainties due to magnetic focusing and are further described in Sect. 5.2.4. The uncertainties on the inter-medium pion interactions of charge exchange (absorption) are set at 50% (35%) based on comparisons between simulation and external data [11].

The model dependence of the unsmearing procedure is evaluated by forming variations of the unsmearing matrix \check{U} with conservative errors on the underlying model parameters $M_A^C=1.35\pm0.35\,\mathrm{GeV},\,M_A^H=1.02\pm0.35\,\mathrm{GeV},\,\mathrm{and}\,\kappa=1.007\pm0.007$. In this case, *only* the matrix \check{U} is varied in Eq. (8.12), as it is the only term sensitive to the underlying physics model. Finally, applicable only when the hydrogen CCQE component is treated as background, its rates are varied according to a global fit to the light-target data, where $M_A^H=1.020\pm0.014\,\mathrm{GeV}.$

The final systematic errors are related to uncertainties on the PMT discriminator threshold (labeled in figures and tables as "disc") and changes in rates due to charge-time correlation ("QT corr") effects. An independent MC sample is available for each uncertainty, and so the alternate cross sections extracted using these samples are entirely based on their distributions:

$$\sigma (E_{\nu})_{i}^{p} = \frac{\sum_{j} U_{ij}^{p} \left(d_{j} - b_{j}^{p} \right)}{\epsilon_{i}^{p} \Phi_{i} N},$$

$$\frac{d\sigma}{dX_{i}}^{p} = \frac{\sum_{j} U_{ij}^{p} \left(d_{j} - b_{j}^{p} \right)}{\epsilon_{i}^{p} \Delta X \Phi N},$$

$$\frac{d^{2}\sigma}{dT_{\mu} d \left(\cos \theta_{\mu} \right)_{i}}^{p} = \frac{\sum_{j} U_{ij}^{p} \left(d_{j} - b_{j}^{p} \right)}{\epsilon_{i}^{p} \Delta T_{\mu} \Delta \cos \theta_{\mu} \Phi N},$$
(8.14)

where p refers to each of the two distributions with alternate assumptions on the PMT behavior. Note that this is identical to Eq. (8.12) with the replacement of the MC central value generated distribution in the effective efficiency calculation by the same quantity in the independent samples. The error matrices associated with these detector uncertainties are calculated by:

$$EM_{ij}^{p} = \left(\sigma_{i}^{CV} - \sigma_{i}^{p}\right) \times \left(\sigma_{j}^{CV} - \sigma_{j}^{p}\right). \tag{8.15}$$

The various contributions to the total uncertainty for the $\bar{\nu}_{\mu}$ CCQE cross sections incident on mineral oil and on carbon only are summarized in Sects. 8.4.3 and 8.4.4.

8.4.3 Uncertainty Summary for \bar{v}_{μ} CCQE on Mineral Oil

The total error matrix is formed by simply adding together each error matrix calculated in the previous subsections. As the entries of the error matrix represent bin-by-bin variances and covariances, the linear addition of the entries is equivalent to addition in quadrature. Then, the total uncertainty in bin i is simply $\sqrt{EM_{ii}^{tot}}$. The overall effect and relative importance of each error can be evaluated with bin-by-bin fractional error $\left(\frac{\sqrt{EM_{ii}^{tot}}}{\sigma_i^{CV}}\right)$, where σ^{CV} is the central value cross section for each uncertainty. Figure 8.15 shows fractional errors for each source of uncertainty for the four one-dimensional distributions and their sum for the two-dimensional cross section. Figure 8.16 shows the same for those with large maximum uncertainties.

The overall uncertainty for each error source can be reported numerically with the total normalization error. This quantity is equivalent to the total uncertainty if the measurement were a single number (e.g., a distribution with a single bin). Using the sum rule for variances and covariances ($\sigma_{i+j}^2 = \sigma_i^2 + \sigma_j^2 + 2\rho_{ij}\sigma_i\sigma_j$, where σ [ρ] refers to a total error [correlation]), the total normalization error for a given uncertainty in terms of its error matrix is simply

Norm. error =
$$\frac{\sqrt{\sum_{ij} EM_{ij}}}{\sum_{i} \sigma_{i}^{CV}}$$
 (8.16)

These values are given in Table 8.2 for each uncertainty and each result. Due to the exclusion of some events whose value in the distribution may be excluded from the choices in binning, care must be taken in comparing normalization uncertainties across the different distributions. Events generated with $T_{\mu} < 0.2 \, {\rm GeV}$ and $T_{\mu} > 2 \, {\rm GeV}$ are not recovered through the efficiency calculation in the $\frac{d\sigma}{dT_{\mu}}$ and $\frac{d^2\sigma}{dT_{\mu}d\cos\theta_{\mu}}$ cross sections, while only events whose true energy would lie in $0.4 > E_{\nu}^{RFG} > 2 \, {\rm GeV}$ are included for the total cross section. For $\cos\theta_{\mu}$ the entire range of kinematics is included, while the same is almost true for Q_{QE}^2 , where the effective cut of $Q_{QE}^2 > 2 \, {\rm GeV}^2$ excludes very few events.

8.4.4 Uncertainty Summary for \bar{v}_{μ} CCQE on Carbon

Fractional uncertainty levels for the results treating the free scattering component of $\bar{\nu}_{\mu}$ CCQE interactions as background are given in Table 8.3 and Fig. 8.17. Figure 8.18 shows the full range of fractional uncertainty for those with some values greater than unity.

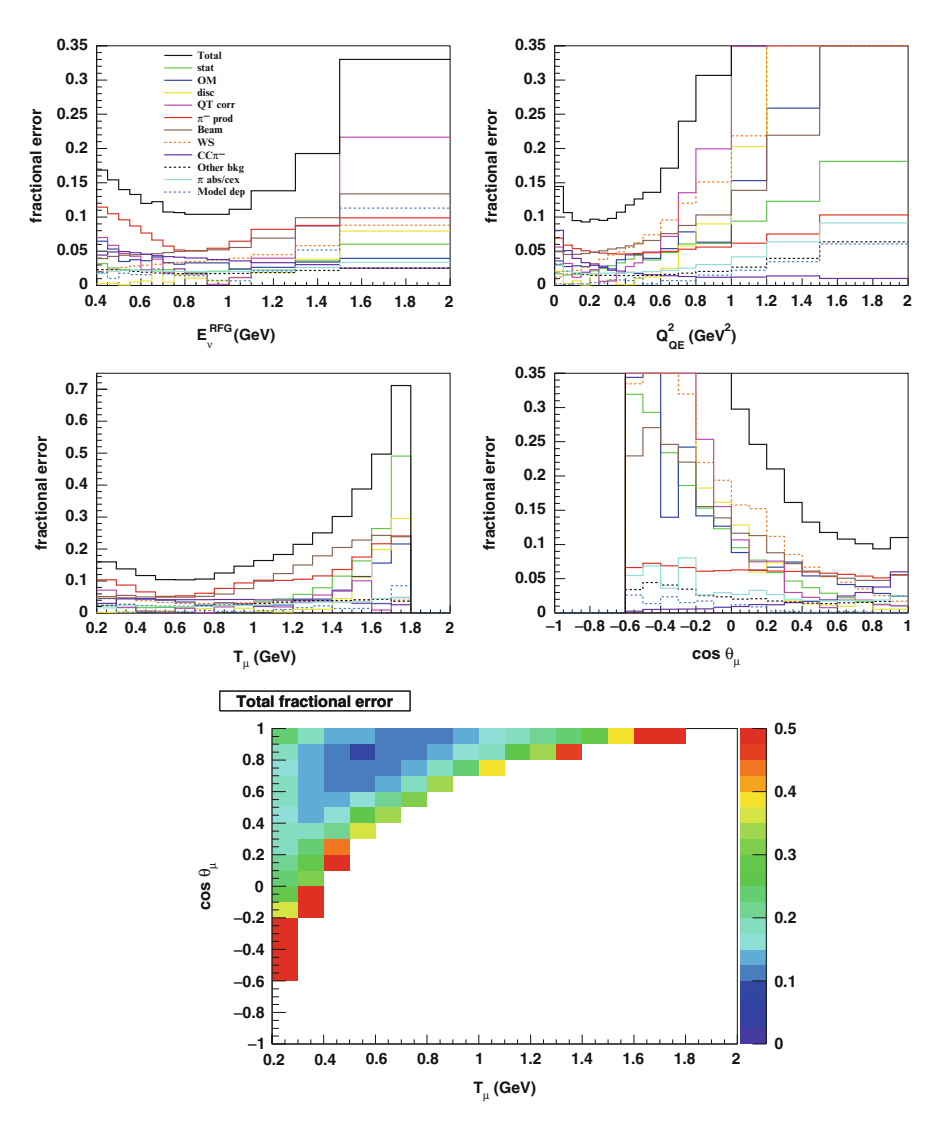


Fig. 8.15 Fractional uncertainty contributions to the total and differential cross sections including the hydrogen content as signal. The total uncertainty is the quadrature sum of the error sources shown

8.5 Results

Results for defining the analysis signal as either all $\bar{\nu}_{\mu}$ CCQE interactions or only those bound in carbon atoms are presented in this section. While the more inclusive measurement is a more precise and less model-dependent measurement, the assumption that the free scattering interaction is well-known is motivated

8.5 Results 129

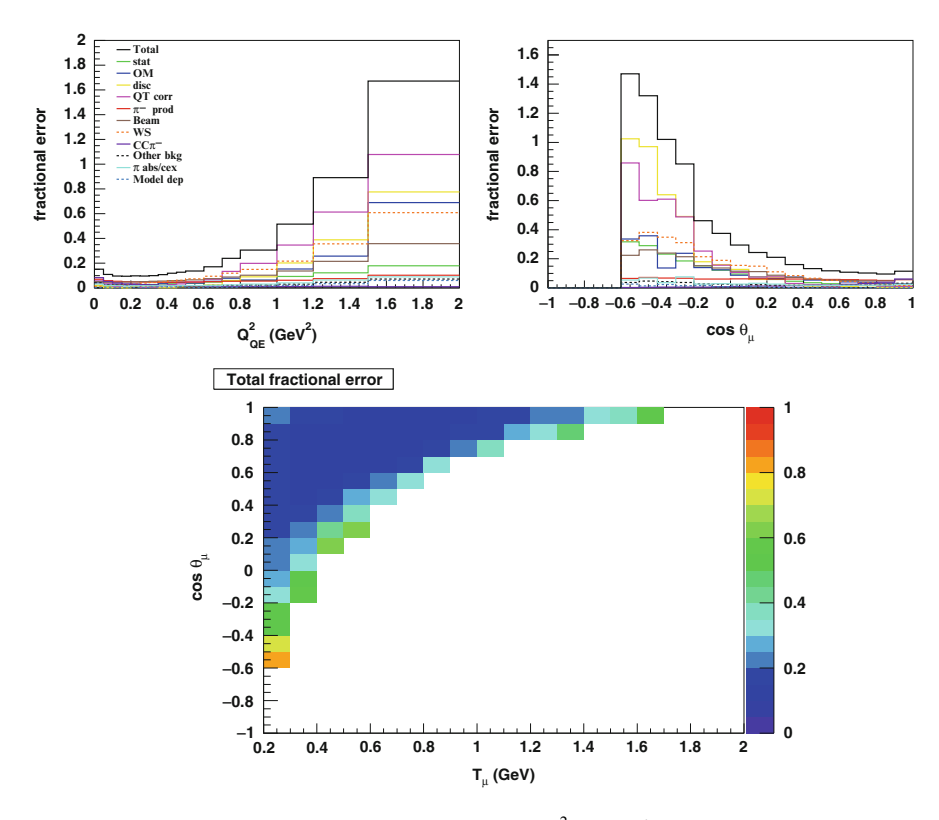


Fig. 8.16 The full range of fractional uncertainty for Q_{QE}^2 , $\cos \theta_{\mu}$ and the double-differential cross sections including the hydrogen content as signal

both by consistency among the previous light-target data sets and by theoretical calculations predicting enhancements only for bound nucleon targets.

8.5.1 Results Incident on Mineral Oil

Results including the hydrogen CCQE component are presented in Fig. 8.19.

The agreement between data and the RFG model under various assumptions in the double-differential cross section is shown in Fig. 8.20.

It is clear that the MC lies somewhat low from data in normalization, and the level of agreement in the shape can be evaluated by forming the shape-only error matrix. The covariance matrix can be used to separate the correlated normalization uncertainties from the total error, leaving information related to how much the shape of the observed data may vary within the systematic errors [12]. These uncertainties are identified by first defining a data vector V with entries corresponding to the observed

Uncertainty source	Normalization error (%)					
	E_{ν}^{RFG}	Q_{QE}^2	T_{μ}	$\cos \theta_{\mu}$	T_{μ} - cos θ_{μ}	
Statistics	1.1	0.7	1.0	0.7	0.8	
Optical model	2.8	3.1	2.9	3.8	3.8	
PMT discriminator thresh.	1.5	0.1	0.7	1.7	0.1	
PMT charge-time corr.	2.9	1.4	0.1	0.7	0.9	
π^- production	5.1	5.3	5.4	5.2	6.4	
Beam unisims	6.4	5.0	6.5	5.5	7.2	
All ν_{μ} background	4.4	3.1	3.6	4.6	3.5	
CCπ [−] background	3.8	4.3	4.0	4.4	4.0	
Non-CCQE, non-CC π^{\pm} background	2.6	2.5	2.6	2.7	2.6	
Unsmearing model dependence	1.7	0.0	0.2	0.2	0.8	
π charge exchange + absorption	2.3	2.1	2.3	2.2	2.3	
Total	11.7	10.2	11.1	11.4	12.9	

Table 8.2 Normalization errors for each cross section and each source of error for $\bar{\nu}_{\mu}$ CCQE events on mineral oil

Due to differences in cross-section shapes and relative regional sensitivity to each uncertainty, the normalization errors vary by a few percent across the distributions. The hydrogen content is included as signal here. T_{μ} - $\cos\theta_{\mu}$ refers to the double-differential cross section

Table 8.3 Normalization errors for each cross section and each source of error, treating $\bar{\nu}_{\mu}$ CCQE events on hydrogen as background

	Normalization error (%)						
Uncertainty source	E_{v}^{RFG}	Q_{QE}^2	T_{μ}	$\cos \theta_{\mu}$	T_{μ} - $\cos \theta_{\mu}$		
Statistics	1.4	0.9	1.3	1.0	1.2		
Optical model	3.9	4.1	4.6	5.0	4.2		
PMT discriminator thresh.	2.3	0.3	0.4	2.3	1.1		
PMT charge-time corr.	4.2	1.5	1.9	1.4	2.6		
π^- production	6.8	7.2	6.7	7.1	8.0		
Beam unisims	8.3	6.8	9.0	7.4	9.2		
All ν_{μ} background	5.8	4.1	6.2	5.4	6.8		
CCπ [−] background	5.1	5.8	6.7	5.9	7.4		
Non-CCQE, non-CC π^{\pm} background	3.4	3.3	4.8	3.6	5.5		
Unsmearing model dependence	2.4	0.0	1.4	0.2	2.2		
Hydrogen background	0.8	1.0	1.6	0.9	2.2		
π charge exchange + absorption	3.0	2.9	3.3	3.0	3.6		
Total	15.5	13.8	17.2	15.0	18.6		

Fractional uncertainties are generally higher compared to those reported in Table 8.2 due to the significantly lower purity of the sample

relative normalization of each bin: $V_i = \{D_1/D_T, D_2/D_T, \dots, D_n/D_T, D_T\}$. Notice this vector has dimension n+1, where n is the number of bins measured. The covariance matrix Q for this new vector V involves the Jacobian matrix of partial derivatives J and is given by:

8.5 Results 131

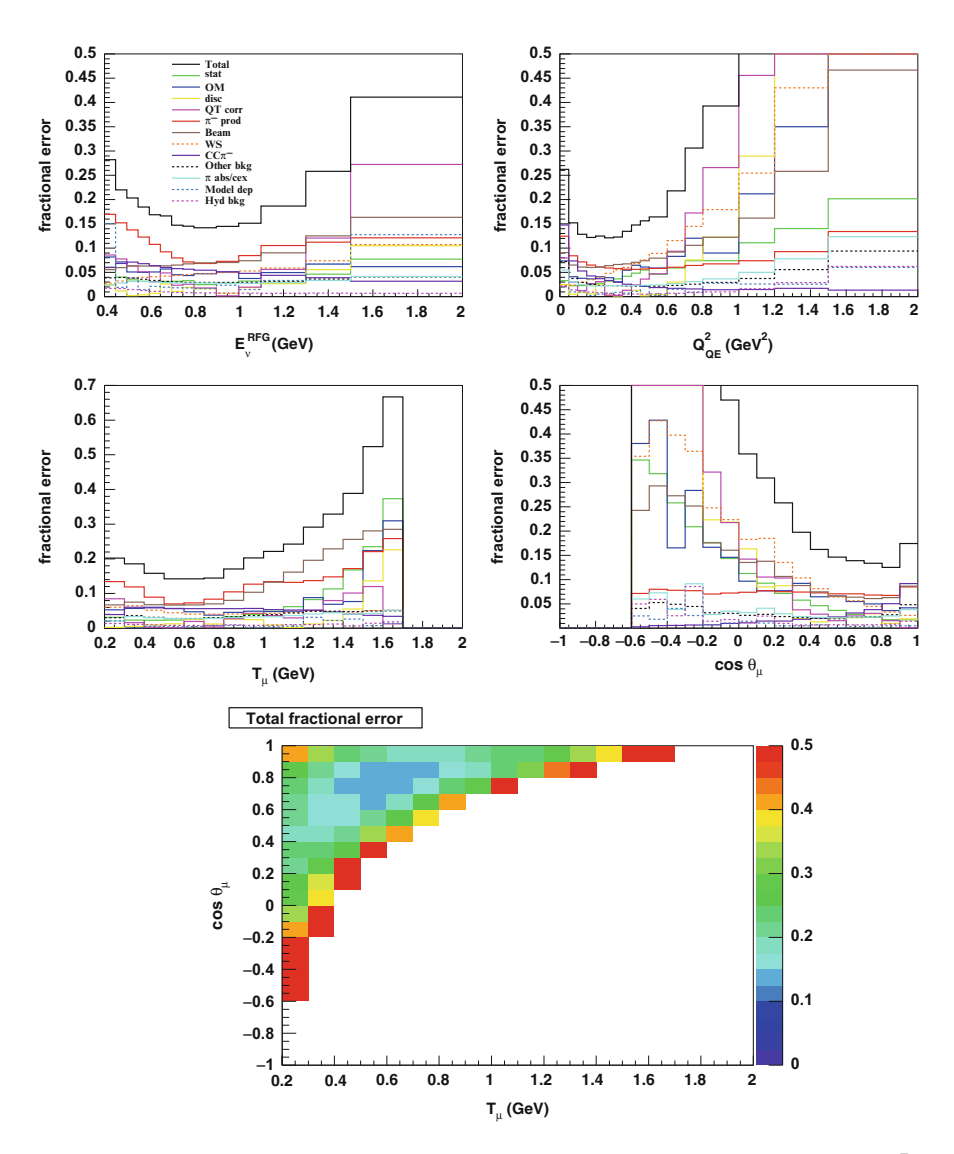


Fig. 8.17 Fractional uncertainty contributions to the total and differential cross sections taking $\bar{\nu}_{\mu}$ CCQE interaction on hydrogen as background. The total uncertainty is the quadrature sum of the error sources shown

$$Q_{kl} = \sum_{ij}^{n} J_{ki} M_{ij} J_{lj} = \sum_{ij}^{n} \frac{\partial V_k}{\partial D_i} M_{ij} \frac{\partial V_l}{\partial D_j} . \tag{8.17}$$

The diagonals of the matrix Q are related to the shape uncertainty in each kinematic bin. For entries $\{1, 2, \dots, n\}$,

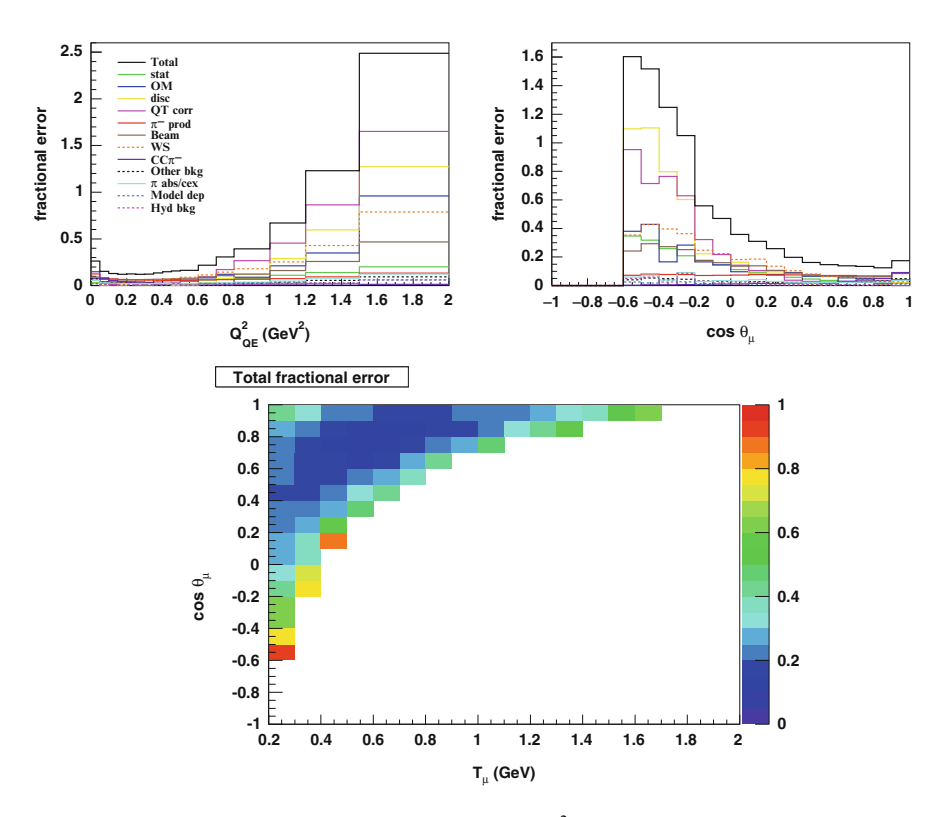


Fig. 8.18 The full range of fractional uncertainty for Q_{QE}^2 , $\cos \theta_{\mu}$ and the double-differential cross sections

$$Q_{kk} = \frac{1}{D_T^2} \left[M_{kk} - 2 \frac{D_k}{D_T} \sum_{i}^{n} M_{ik} + \frac{N_k^2}{N_T^2} \sum_{ij}^{n} M_{ij} \right]$$

$$= (\delta D_{k,\text{shape}})^2$$
(8.18)

The shape and total error of the cross sections is compared to MC normalized to data in Fig. 8.21. As values for M_A are typically extracted from the Q^2 distribution, it's helpful to at least calculate the compatibility between data and MC. Printed on the Q_{QE}^2 distribution is the χ^2 between MC and data using shape-only uncertainties.

8.5.2 Results Incident on Carbon

Results for all distributions treating the free scattering $\bar{\nu}_{\mu}$ CCQE component as background are shown in Fig. 8.22 and Fig. 8.23 presents a detailed view of the

8.5 Results 133

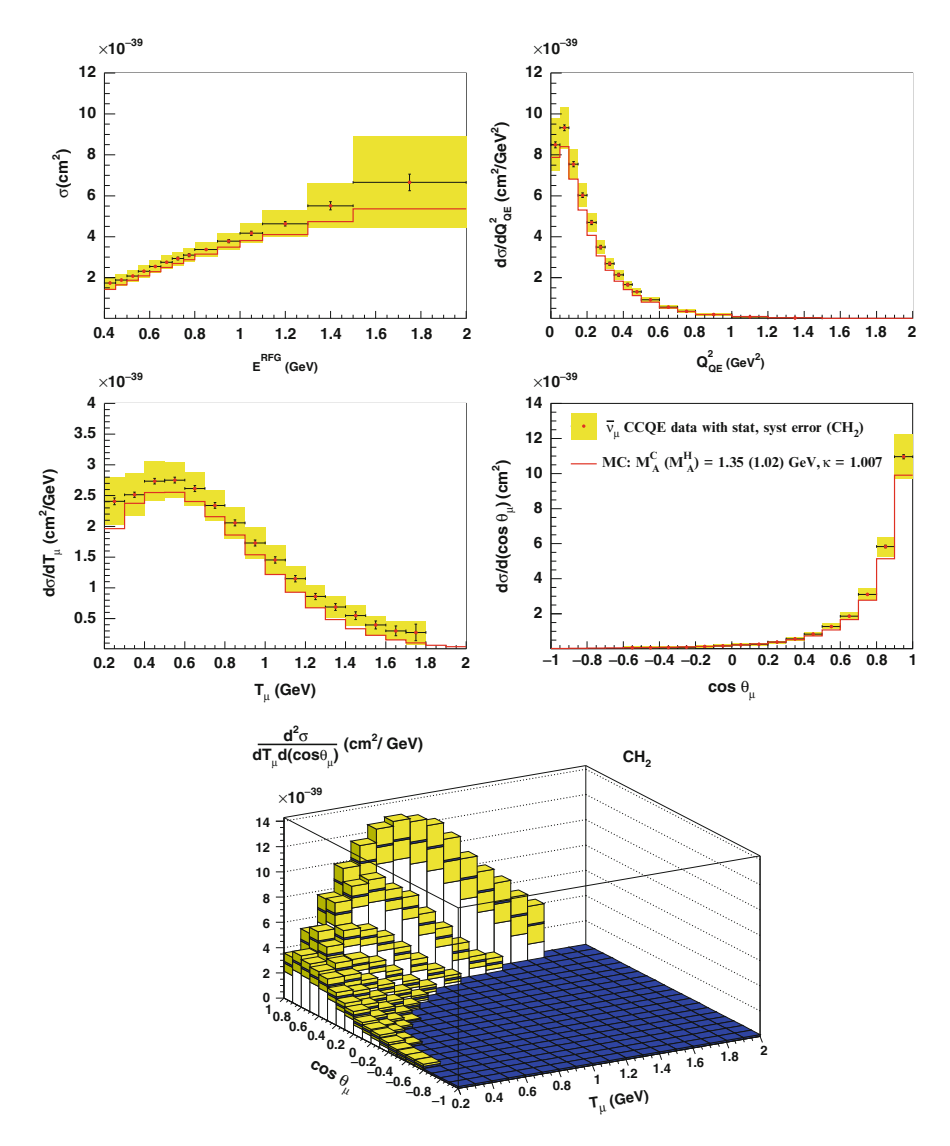


Fig. 8.19 Extracted $\bar{\nu}_{\mu}$ CCQE cross sections with total uncertainty compared to central value MC with the hydrogen component not subtracted

double-differential cross section with comparisons to the RFG and three external predictions [13–15].

Analogous to Fig. 8.21, Fig. 8.24 compares shape and total errors on data to relatively normalized MC.

As CCQE model parameters are typically extracted from the Q^2 distribution, it's interesting to see how these data compare to the historically-accepted values.

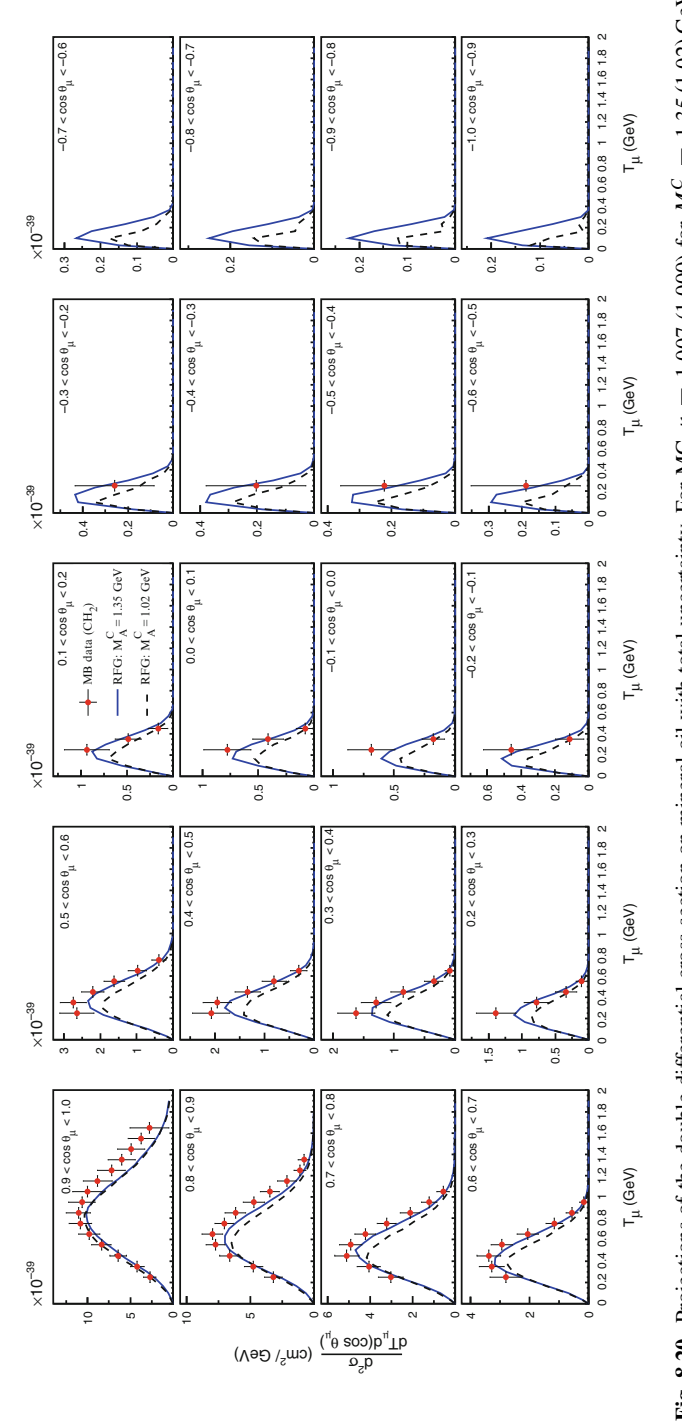


Fig. 8.20 Projections of the double-differential cross section on mineral oil with total uncertainty. For MC, $\kappa=1.007$ (1.000) for $M_A^C=1.35$ (1.02) GeV and in both cases $M_A^H=1.02$ GeV

8.5 Results 135

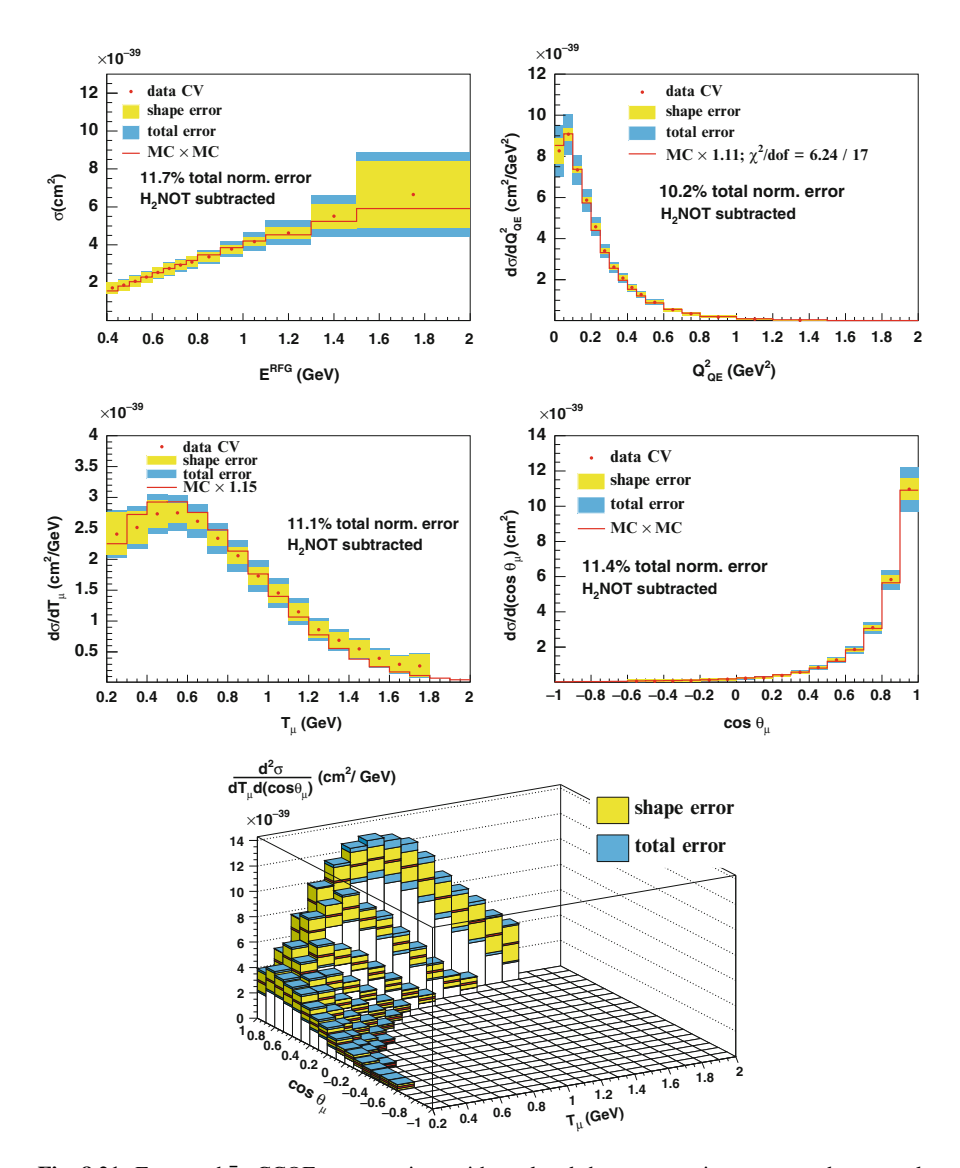


Fig. 8.21 Extracted $\bar{\nu}_{\mu}$ CCQE cross sections with total and shape uncertainty compared to central value MC with the hydrogen component *not* subtracted. For the differential cross sections, MC is scaled to the integrated cross section from data $(\int \frac{d\sigma}{dX} dX)$, while for the total cross section MC is scaled to data based on the discrepancy in the bin at the interaction peak $(0.65-0.7 \, \text{GeV})$

Figure 8.25 compares the shape of the RFG with various choices of M_A and κ to the data. To give a feel numerically for the shape compatibility of each distribution with the data, printed on the figure legend is the χ^2 for each parameter choice using

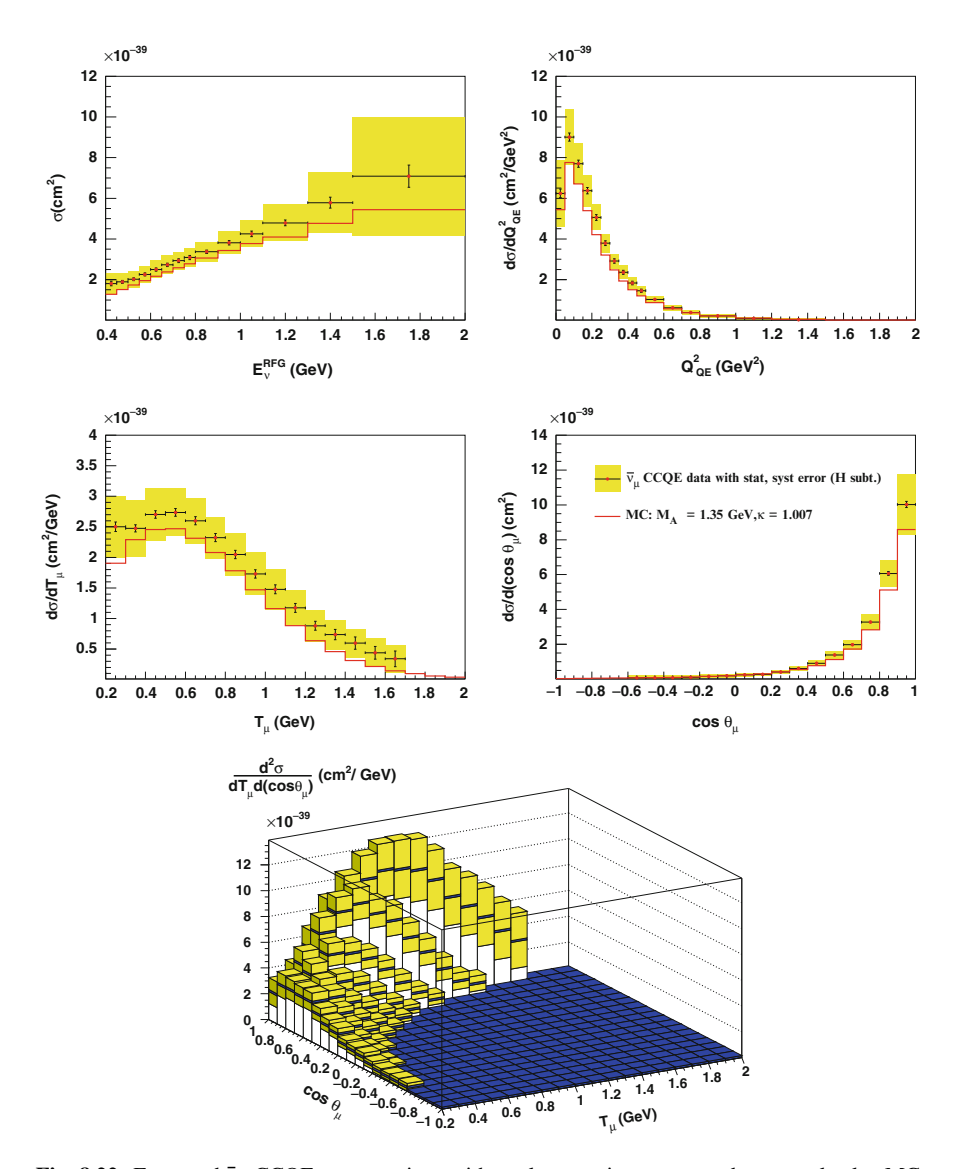


Fig. 8.22 Extracted $\bar{\nu}_{\mu}$ CCQE cross sections with total uncertainty compared to central value MC with the hydrogen component subtracted

the shape-only uncertainties. The χ^2 for the RFG with $M_A=1.35$ GeV, $\kappa=1.007$ is surprisingly low at just 3.7 for 17 degrees of freedom.

Along the same lines, one of the only recent experiments using nuclear targets to measure $M_A \sim 1 \, \text{GeV}$ is the NOMAD experiment. Much speculation revolving around the disparate energy regimes and detector types has been made in attempts to reconcile the discrepancy in ν_{μ} CCQE cross section between MiniBooNE and

8.5 Results 137

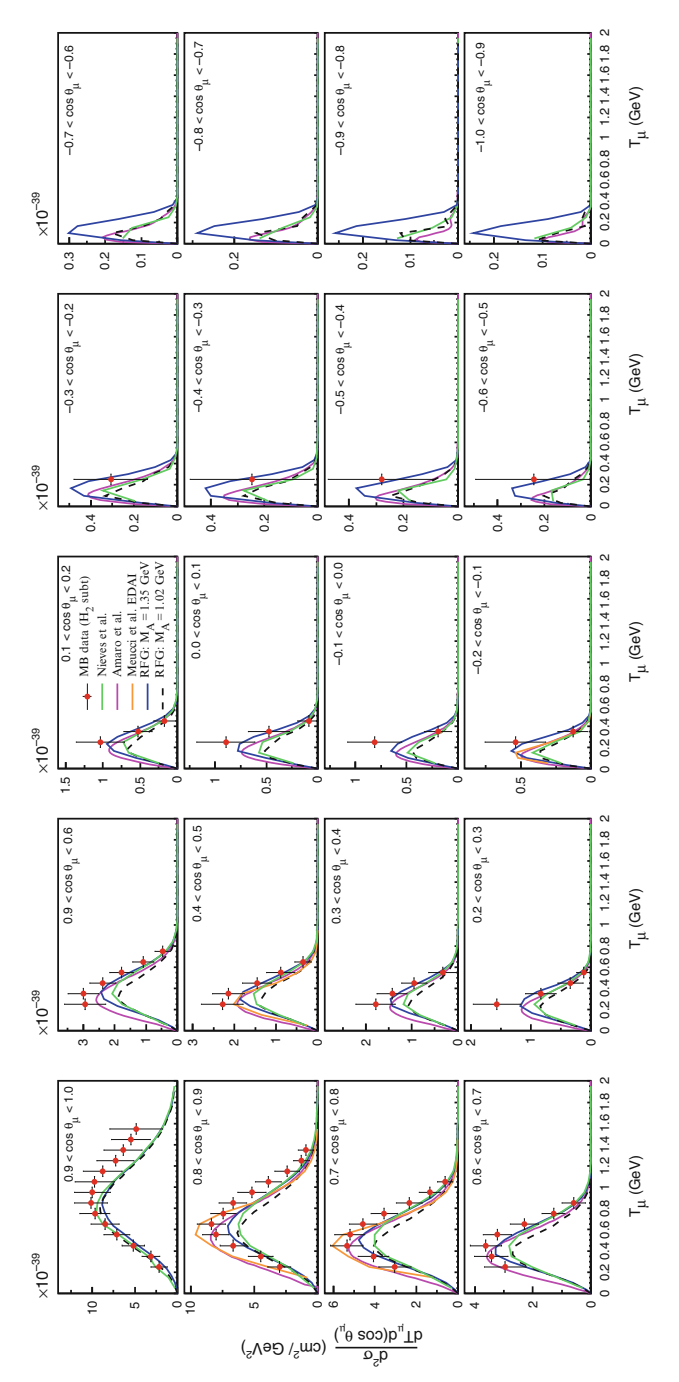


Fig. 8.23 Projections of the double-differential cross section on carbon with total uncertainty

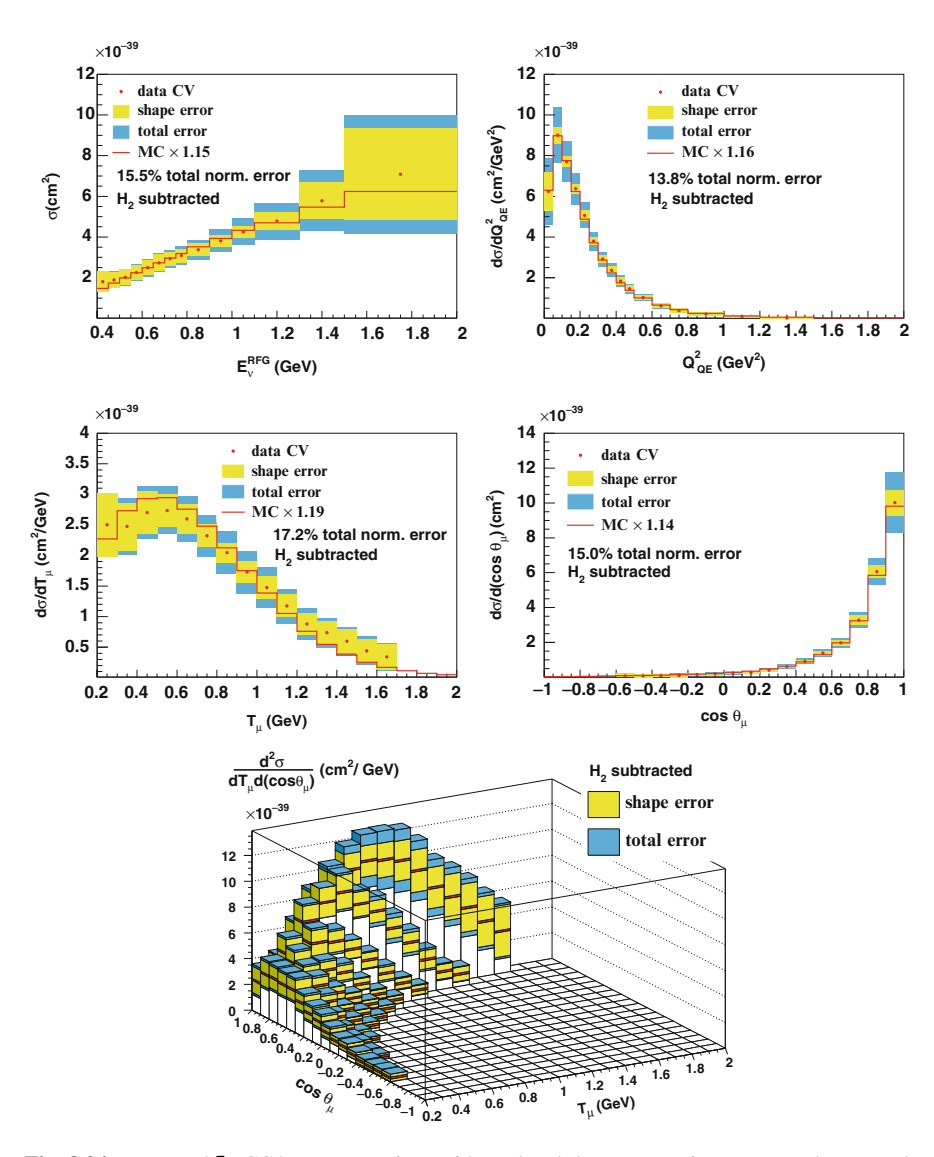


Fig. 8.24 Extracted $\bar{\nu}_{\mu}$ CCQE cross sections with total and shape uncertainty compared to central value MC with the hydrogen component subtracted. For the differential cross sections, MC is scaled to the integrated cross section from data $(\int \frac{d\sigma}{dX} dX)$, while for the total cross section MC is scaled to data based on the discrepancy in the bin at the interaction peak (0.65–0.7 GeV)

8.5 Results 139

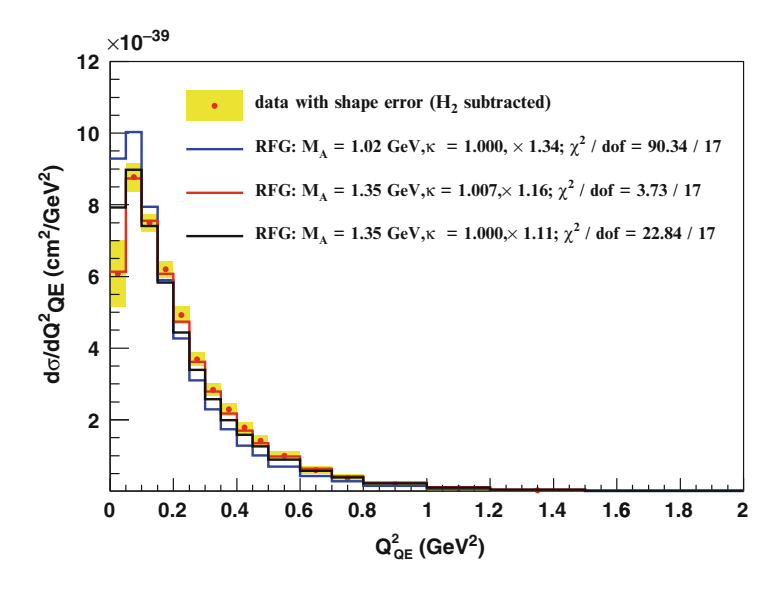


Fig. 8.25 Shape comparison for hydrogen-subtracted data and the RFG under various parameter choices. The shape of central value MC with $M_A=1.35\,\mathrm{GeV}$ and $\kappa=1.007$ agrees with data remarkably well. In particular, the mild change in κ (1.000 \rightarrow 1.007) determined from the ν_μ CCQE analysis seems to be preferred by the data. Also printed on the figure is the scale for each prediction to match the data in normalization

NOMAD [16], and Fig. 8.26 compares the ν_{μ} and $\bar{\nu}_{\mu}$ CCQE data sets from both experiments.

Figure 8.27 compares the total cross sections to the available theoretical predictions [13–15, 17–20], and Fig. 8.28 also includes the level of agreement between the same models and the ν_{μ} data.

It is clear that the RFG model with canonical assumptions does not adequately describe these data neither in shape nor in normalization. Consistent with other recent CCQE measurements on nuclear material [3, 21–23], a significant enhancement in the normalization that grows with decreasing muon scattering angle is observed compared to the expectation with $M_A=1$ GeV. As discussed in Sect. 4.4, these observations are consistent with the presence of an intra-nuclear mechanism of greater importance than previously expected, and contributions from such a source are tested in comparisons between various predictions and the data analyzed here in Figs. 8.23 and 8.27.

However, these data find tension with the NOMAD $\bar{\nu}_{\mu}$ CCQE results, which are described both in shape and normalization by $M_A \sim 1\,\text{GeV}$ [24]. This tension is also common to the ν_{μ} CCQE analyses from the two experiments. However, care should be taken in comparing model-dependent results among experiments with such different neutrino fluxes and detector technologies. A definitive unification of these apparently discrepant data sets will require the continued increase of both experimental and theoretical activity surrounding this topic. Fortunately, many

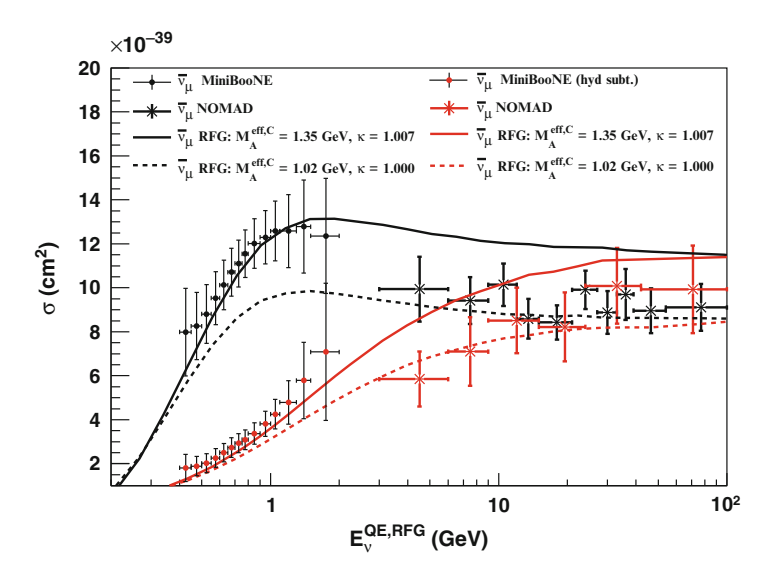


Fig. 8.26 Comparison between MiniBooNE and NOMAD ν_{μ} and $\bar{\nu}_{\mu}$ data, as well as some predictions from the RFG. Tension exists across both ν_{μ} and $\bar{\nu}_{\mu}$ data from the two experiments under the assumptions of CCQE with the RFG. NOMAD data from [32]

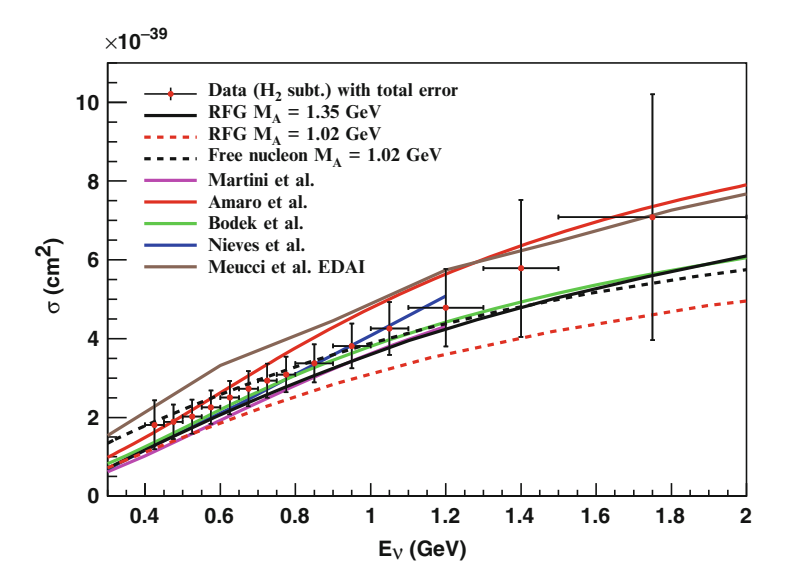


Fig. 8.27 Total cross section per nucleon for $\bar{\nu}_{\mu}$ CCQE data with the hydrogen content removed compared to various predictions

References 141

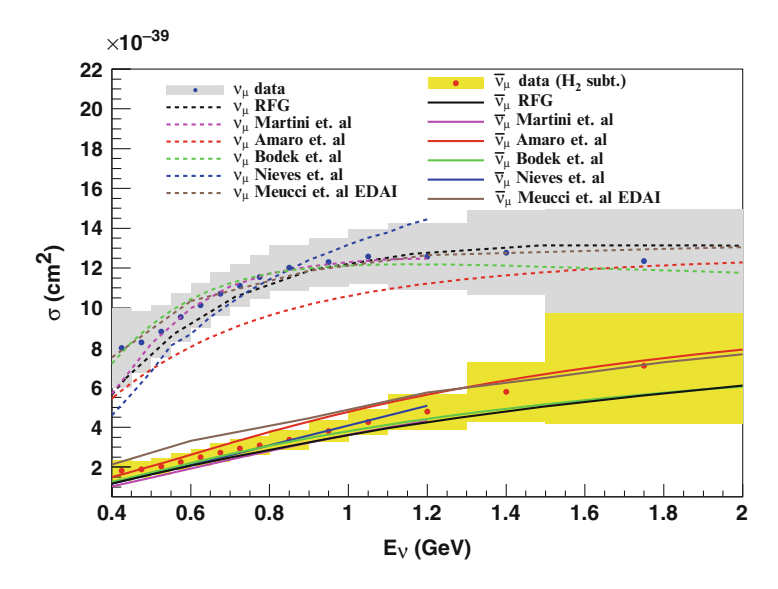


Fig. 8.28 Total cross section per nucleon for v_{μ} and \bar{v}_{μ} CCQE data compared to various predictions. The "RFG" distribution assumes $M_A=1.35\,\mathrm{GeV}$ and $\kappa=1.007$. Total uncertainty is shown with both MiniBooNE data sets

experiments at a variety of neutrino energies capable of making high-resolution, model-independent neutrino and antineutrino CCQE measurements with different detector technologies and nuclear media currently have data or will soon. These include MINER ν A [25], SciBooNE [26], MicroBooNE [27], ArgoNeuT [28], ICARUS [29] and the T2K [30] and NO ν A [31] near detectors.

References

- A.A. Aguilar-Arevalo et al. [MiniBooNE Collaboration], First measurement of the muon anti-neutrino double-differential charged current quasi-elastic cross section. Phys. Rev. D88, 032001 (2013)
- A. Kolmogorov, Sulla determinazione empirica di una legge di distribuzione. G. Inst. Ital. Attuari 4, 83 (1933); N.V. Smirnov, Tables for estimating the goodness of fit of empirical distributions. Ann. Math. Stat. 19, 279 (1948)
- 3. A.A. Aguilar-Arevalo et al. [MiniBooNE Collaboration], Phys. Rev. D81, 092005 (2010)
- 4. V. Bernard et al. J. Phys. G28, R1 (2002)
- A.A. Aguilar-Arevalo [MiniBooNE Collaboration], Measurement of muon neutrino quasielastic scattering on carbon. Phys. Rev. Lett. 100, 032301 (2008)
- 6. A.A. Aguilar-Arevalo et al. [MiniBooNE Collaboration], Phys. Rev. D83, 052007 (2011)
- A.A. Aguilar-Arevalo et al. [MiniBooNE Collaboration], Phys. Rev. D81, 013005 (2010)
- 8. A.A. Aguilar-Arevalo et al. [MiniBooNE Collaboration], Phys. Rev. **D83**, 052009 (2011)
- A.A. Aguilar-Arevalo et al. [MiniBooNE Collaboration], Measurement of the neutrino neutralcurrent elastic differential cross section. Phys. Rev. D82, 092005 (2010)

- 10. G. D'Agostini, Nucl. Instrum. Methods **A362**, 487 (1995)
- D. Ashery et al. Phys. Rev. C23, 2173 (1981); M.K. Jones et al. Phys. Rev. C48, 2800 (1993);
 R.D. Ransome et al. Phys. Rev. C45, R509 (1992)
- 12. T. Katori, Ph.D. thesis, Indiana University, 2008
- J. Nieves et al. Two particle-hole excitations in charged current quasielastic antineutrinonucleus scattering (2013). arXiv:1302.0703
- J. Amaro et al. Meson-exchange currents and quasielastic antineutrino cross sections in the SuperScaling Approximation (2011). arXiv:1112.2123
- 15. A. Meucci, C. Giusti, Phys. Rev. **D85**, 093002 (2012)
- 16. P. Astier et al. [NOMAD Collaboration], Search for $\nu_{\mu} \rightarrow \nu_{e}$ oscillations in the NOMAD experiment. Phys. Lett. **B570**, 19–31 (2003)
- M. Martini et al. Neutrino and antineutrino quasielastic interactions with nuclei. Phys. Rev. C81, 045502 (2010)
- J. Nieves et al. Inclusive charged-current neutrino-nucleus reactions. Phys. Rev. C83, 045501 (2011). arXiv:1102.2777
- J. Amaro et al. Relativistic analyses of quasielastic neutrino cross sections at MiniBooNE kinematics. Phys. Rev. D84, 033004 (2011). arXiv:1104.5446
- 20. A. Bodek et al. Eur. Phys. J. C71, 1726 (2011)
- 21. R. Gran et al., Phys. Rev. D74, 052002 (2006)
- 22. M. Dorman for the MINOS Collaboration, AIP Conf. Proc. 1189, 133 (2009)
- 23. S. Brice, MiniBooNE Note 257
- K.S. Kuzmin, V.V. Lyubushkin, V.A. Naumov, Eur. Phys. J. C 54, 517 (2008); V.V. Lyubushkin et al. [NOMAD Collaboration]. arXiv:0812.4543 [hep-ex]
- 25. D.D. Stancil et al. [MINERvA Collaboration], Demonstration of communication using neutrinos. Mod. Phys. Lett. **A27**, 1250077 (2012)
- 26. A.A. Aguilar-Arevalo et al. [SciBooNE Collaboration]. arXiv:0601022 [hep-ex]
- 27. M. Soderberg for the MicroBooNE Collaboration, AIP Conf. Proc. 1189, 83 (2009)
- 28. C. Anderson et al. [ArgoNeuT Collaboration], Phys. Rev. Lett. 108, 161802 (2012)
- 29. S. Amoruso et al. [ICARUS Collaboration], Eur. Phys. J. C33, 233 (2004)
- P.-A. Amaudruza [T2K ND280 FGD Collaboration], The T2K fine-grained detectors. Nucl. Instrum. Methods A696, 1 (2012)
- D.S. Ayres et al. [NOvA Collaboration], The NOvA Technical Design Report. FERMILAB-DESIGN-2007-01 (2007)
- 32. K.S. Kuzmin, V.V. Lyubushkin, V.A. Naumov, Eur. Phys. J. C 54, 517 (2008); V.V. Lyubushkin et al. [NOMAD Collaboration]. arXiv:0812.4543

Chapter 9

Combined ν_{μ} and $\bar{\nu}_{\mu}$ CCQE Measurements

With the high-statistics MiniBooNE ν_{μ} [1] and $\bar{\nu}_{\mu}$ (Chap. 8 and [2]) CCQE cross sections, an opportunity exists to extract even more information out of these data sets by exploiting correlated systematic uncertainties between the two measurements. Simple difference and ratio analyses between the two results will more stringently test the various models for CCQE-like interactions around 1 GeV. We begin with a brief discussion of how to use correlated information to reduce uncertainties in combined measurements.

9.1 Correlated Measurements

This treatment of systematic correlations follows [3]. Consider two arbitrary results x and y that are used to calculate some combined measurement q(x, y). As in any quantity, given the set of N measurements of the quantity q, its uncertainty σ_q is:

$$\sigma_q^2 = \frac{1}{N} \sum_{i}^{N} (q_i - \bar{q})^2, \qquad (9.1)$$

where \bar{q} is the CV measurement of q. We are interested in how the object q changes under variations in x and y, so we begin by examining how individual excursions x_i and y_i from their respective results (\bar{x}, \bar{y}) propagate onto q:

$$q_i = q\left(x_i, y_i\right) \tag{9.2}$$

$$= \sum_{n_1=0}^{\infty} \sum_{n_2=0}^{\infty} \frac{(x_i - \bar{x})^{n_1} (y_i - \bar{y})^{n_2}}{n_1! n_2!} \frac{\partial^{n_1+n_2}}{\partial x^{n_1} \partial y^{n_2}} q(\bar{x}, \bar{y})$$
(9.3)

[©] Springer International Publishing Switzerland 2015

J. Grange, First Measurement of the Muon Anti-Neutrino Charged

Current Quasielastic Double-Differential Cross Section, Springer Theses,

DOI 10.1007/978-3-319-09573-8_9

$$\approx q(\bar{x}, \bar{y}) + (x_i - \bar{x}) \frac{\partial}{\partial x} q(\bar{x}, \bar{y}) + (y_i - \bar{y}) \frac{\partial}{\partial y} q(\bar{x}, \bar{y}), \tag{9.4}$$

where disregarding the higher order terms in the last step assumes the deviations $(x_i - \bar{x})$ and $(y_i - \bar{y})$ to be small. Recognizing $q(\bar{x}, \bar{y}) = \bar{q}$ and substituting Eq. (9.4) into Eq. (9.1), we get:

$$\sigma_q^2 = \frac{1}{N} \sum_{i}^{N} \left[\frac{\partial q}{\partial x} (x_i - \bar{x}) + \frac{\partial q}{\partial y} (y_i - \bar{y}) \right]^2$$

$$= \left(\frac{\partial q}{\partial x} \right)^2 \frac{1}{N} \sum_{i}^{N} (x_i - \bar{x})^2 + \left(\frac{\partial q}{\partial y} \right)^2 \frac{1}{N} \sum_{i}^{N} (y_i - \bar{y})^2$$

$$+ 2 \frac{\partial q}{\partial x} \frac{\partial q}{\partial y} \frac{1}{N} \sum_{i}^{N} (x_i - \bar{x})(y_i - \bar{y}),$$

$$(9.6)$$

where the partial derivatives of q are still evaluated at the point (\bar{x}, \bar{y}) . The first two terms in Eq. (9.6) are readily recognized as the standard deviations σ_x and σ_y , while the last term gives information about the correlation between x and y. It is easy to see that if the measurements of x and y were independent of one another, the last term will approach zero as $N \to \infty$. It is convenient to define a correlation coefficient ρ_{xy} in terms of this information and the standard deviations of x and y:

$$\rho_{xy} = \frac{\sum_{i}^{N} (x_{i} - \bar{x})(y_{i} - \bar{y})}{\sqrt{\sum_{i}^{N} (x_{i} - \bar{x})^{2} \sum_{i}^{N} (y_{i} - \bar{y})^{2}}} = \frac{\frac{1}{N} \sum_{i}^{N} (x_{i} - \bar{x})(y_{i} - \bar{y})}{\sigma_{x} \sigma_{y}}.$$
 (9.7)

Notice that $\rho_{xy} \in \{-1, 1\}$. Then Eq. (9.6) becomes:

$$\sigma_q^2 = \left(\frac{\partial q}{\partial x}\right)^2 \sigma_x^2 + \left(\frac{\partial q}{\partial y}\right)^2 \sigma_y^2 + 2\frac{\partial q}{\partial x}\frac{\partial q}{\partial y}\rho_{xy}\sigma_x\sigma_y. \tag{9.8}$$

Depending on the sign of the product $\frac{\partial q}{\partial y} \frac{\partial q}{\partial y} \rho_{xy}$, the uncertainty on the measurement of q will either be increased or reduced by including the correlation information.

9.2 Combined ν_{μ} and $\bar{\nu}_{\mu}$ CCQE Measurements

Many systematic uncertainties of the MiniBooNE ν_{μ} and $\bar{\nu}_{\mu}$ CCQE cross-section results are related to the resolution of μ^- and μ^+ kinematics in the detector, and are therefore expected to affect the two measurements in a similar way.

Upon examination of Eq. (9.7), such an expectation would predict the correlation coefficient $\rho_{\nu\bar{\nu}}$ to be a positive quantity in most regions. Then, to form a combined measurement for the ν_{μ} and $\bar{\nu}_{\mu}$ CCQE cross sections that features greater precision by including the information about their correlation, the sign of $\frac{\partial q}{\partial \nu} \frac{\partial q}{\partial \bar{\nu}}$ ought to be negative. Two simple cases of this are difference $(\nu_{\mu} - \bar{\nu}_{\mu})$ and ratio $\left(\frac{\nu_{\mu}}{\bar{\nu}_{\mu}}\right)$ measurements of the cross sections in the various distributions, most importantly the double-differential cross section $\frac{d^2\sigma}{dT_{\mu}d\cos\theta_{\mu}}$.

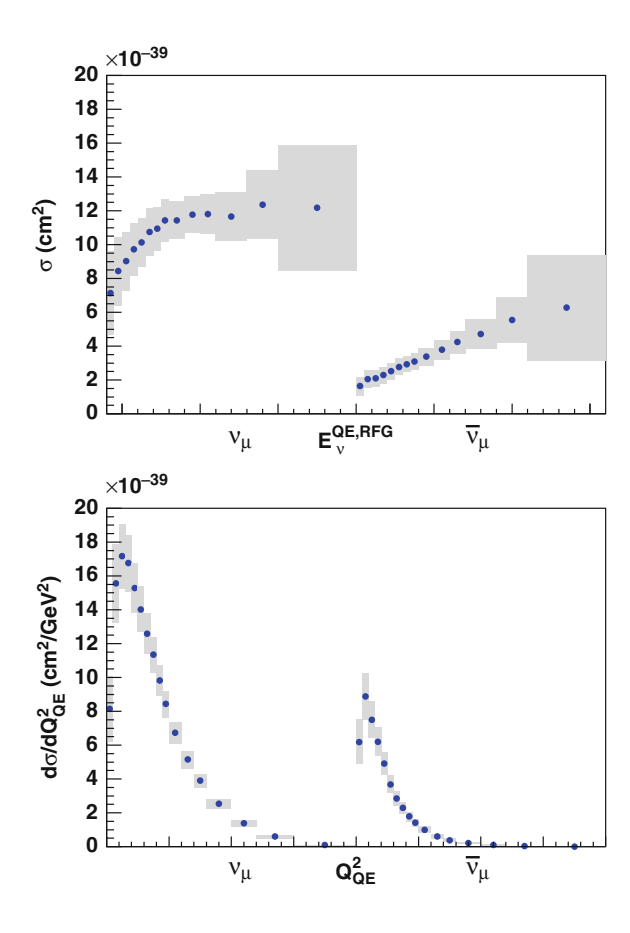
It is important to mention that this study is incomplete: while all systematic uncertainties inherent to the MiniBooNE instruments are included here, possible correlations between the π^+ and π^- production data from the HARP experiment (Sect. 5.2.4) are unknown. In this study, the correlation between the ν_{μ} and $\bar{\nu}_{\mu}$ parent π^+ and π^- primary production cross sections are assumed to be uncorrelated. As the uncertainties on these quantities significantly contribute to the ν_{μ} and $\bar{\nu}_{\mu}$ CCQE cross-section errors, it will be important to eventually include this information.

The goal of this study is to simply evaluate the level of correlation between each bin in the various ν_{μ} and $\bar{\nu}_{\mu}$ CCQE cross sections in order to use Eq. (9.7) to extract the most information possible from the MiniBooNE data sets. To more easily interpret the results of this study as measurements of nuclear effects in carbon, we use the $\bar{\nu}_{\mu}$ CCQE cross section configurations in which the hydrogen CCQE component is treated as background. We begin by forming the covariance matrix to be used in the calculation of an arbitrary combined measurement q in the same way as presented in Sect. 7.1.5: the various ν_{μ} and $\bar{\nu}_{\mu}$ CCQE cross sections and the systematic uncertainty histograms are combined into a single distribution, side-byside. Then, as in Eq. (7.26), a covariance matrix is formed that now includes the correlation information between each ν_{μ} and $\bar{\nu}_{\mu}$ CCQE bin.

The details of the calculated covariance matrix offer a few important consistency checks: the normalization uncertainty (Eq. (8.16)) of each systematic error when only considering the ν_{μ} or $\bar{\nu}_{\mu}$ region of the covariance matrix must be compared to the original normalization uncertainty findings, and the calculated cross sections from data must of course match the results of the original analyses. In this analysis, the relevant quantities match the original ν_{μ} and $\bar{\nu}_{\mu}$ CCQE results within a few percent of their value. Also important to note when cross-checking these results, mild statistical differences are expected between the obtained neutrino-mode ν_{μ} CCQE cross sections compared to those in [1] due to the inclusion of additional data. The analysis in [1] includes a total of 5.6×10^{20} POT, while we use the additional neutrino-mode data collected since then in this analysis for a total of 6.4×10^{20} POT. Figure 9.1 shows the resultant cross sections, along with the recovered total uncertainty from the diagonal entries of the covariance matrix.

The overall correlation coefficients between each bin in the ν_{μ} and $\bar{\nu}_{\mu}$ CCQE cross sections are evaluated through Eq. (9.7), where the term $\frac{1}{N}\sum_{i}^{N}(x_{i}-\bar{x})(y_{i}-\bar{y})$ can be recognized as a given entry in the covariance matrix between two arbitrary bins x and y. Figure 9.2 shows the overall correlation between each bin in the ν_{μ} and $\bar{\nu}_{\mu}$ CCQE total and single-differential cross sections. Recall correlations in the HARP data are not taken into account, so the correlations presented here are

Fig. 9.1 Recovered v_{μ} (left half of each distribution) and \bar{v}_{μ} (right half of each distribution) CCQE cross sections for the correlation analysis. Each bin in the $E_{v}^{QE,RFG}$ distribution (left) is $\in \{0.4, 2.0\}$ GeV and is identical to the bins delimited in Fig. 8.27, while the Q_{QE}^{2} distribution (right) is $\in \{0.0, 2.0\}$ GeV² and corresponds to the binning in Fig. 8.25



generally expected to be a mild underestimate. Also shown in the same figure is the total correlation between a given bin in the ν_{μ} and $\bar{\nu}_{\mu}$ CCQE double-differential cross sections.

Figure 9.2 shows the correlations between the ν_{μ} and $\bar{\nu}_{\mu}$ CCQE cross sections to be rather mild. This is mostly due to the presence of large ν_{μ} and CC π^- backgrounds unique to the $\bar{\nu}_{\mu}$ CCQE analysis. Figure 9.3 compares the coefficients $\rho_{\nu,\bar{\nu}}$ for the most important correlated systematic uncertainties.

From this correlation information, we will extract two quantities: the difference between the ν_{μ} ("A") and $\bar{\nu}_{\mu}$ ("B") CCQE measurements $q_{\rm diff}=A-B$ and their ratio $q_{\rm ratio}=\frac{A}{B}$. The application of Eq. (9.8) to $q_{\rm diff}$ is straightforward:

$$\sigma_{q_{\text{diff}}}^2 = \sigma_A^2 + \sigma_B^2 - 2\rho_{AB}\sigma_A\sigma_B, \tag{9.9}$$

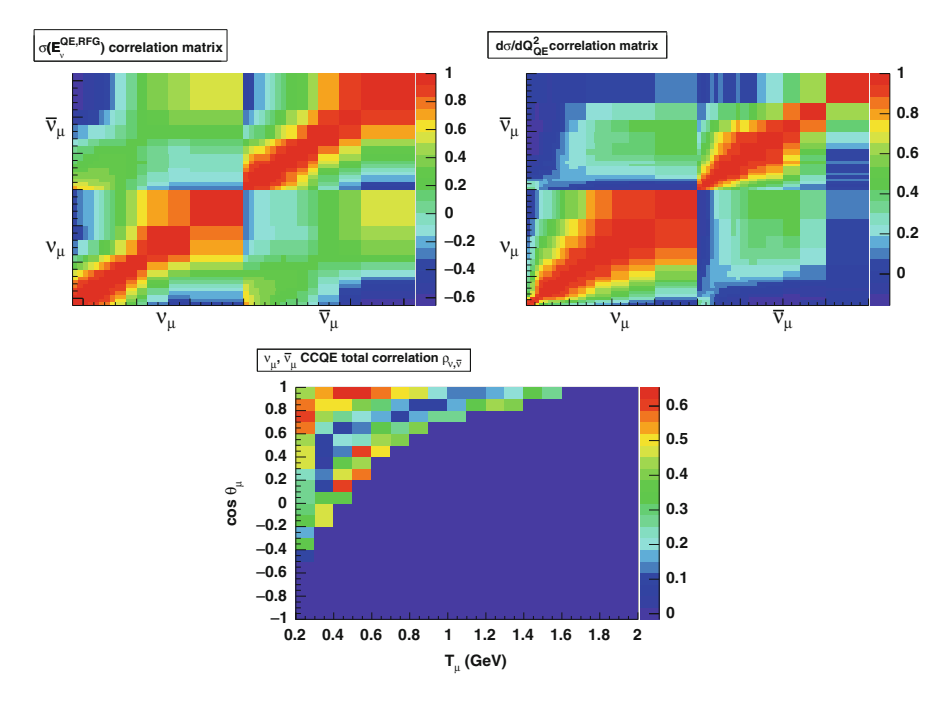


Fig. 9.2 Correlation matrices for the various ν_{μ} and $\bar{\nu}_{\mu}$ cross section results. To highlight the important information, only the $\rho_{\nu,\bar{\nu}}$ coefficients are shown for each bin in the $\frac{d^2\sigma}{dT_{\mu}d\cos\theta_{\mu}}$ distribution (bottom). The analogous entries correspond to the on-diagonal coefficients of the ν_{μ} - $\bar{\nu}_{\mu}$ off-diagonal blocks in the $\sigma(E_{\nu}^{QE,RFG})$ (top left) and $d\sigma/dQ_{QE}^2$ (top right) matrices

while the uncertainty for q_{ratio} :

$$\sigma_{q_{\text{ratio}}}^2 = \left(\frac{\sigma_A}{B}\right)^2 + \left(\frac{A\sigma_A}{B^2}\right)^2 - \frac{2A}{B^3}\rho_{AB}\sigma_A\sigma_B \tag{9.10}$$

can be written more coherently as a combination of fractional uncertainties:

$$\left(\frac{\sigma_{q_{\text{ratio}}}}{q_{\text{ratio}}}\right)^2 = \left(\frac{\sigma_A}{A}\right)^2 + \left(\frac{\sigma_B}{B}\right)^2 - 2\rho_{AB}\left(\frac{\sigma_A}{A}\right)\left(\frac{\sigma_B}{B}\right). \tag{9.11}$$

Notice Eqs. (9.9) and (9.11) are symmetric under $A \leftrightarrow B$. Using these expressions for the uncertainty and the level of correlation between each bin in the ν_{μ} and $\bar{\nu}_{\mu}$ CCQE cross section distributions, the combined measurements may be executed. Figure 9.4 shows the difference measurements, while Fig. 9.5 presents results from the ratio analysis.

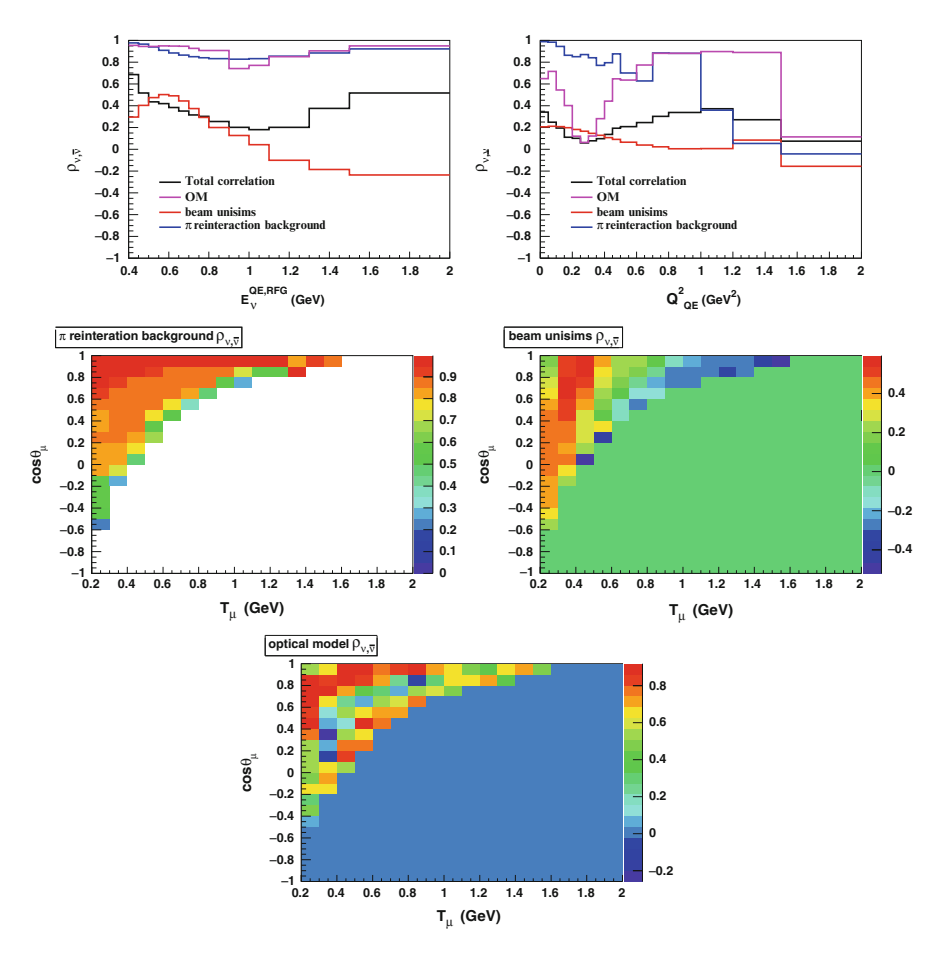


Fig. 9.3 Correlation coefficients by uncertainty type for the various distributions. As expected, the correlations are mostly positive between the ν_{μ} and $\bar{\nu}_{\mu}$ CCQE measurements

There is some independent information gleaned when comparing various predictions to the data across both the difference and the ratio measurements: the ratio $q_{\rm ratio}$ is sensitive only to the absolute normalization of the v_{μ} and \bar{v}_{μ} CCQE cross sections, while the difference $q_{\rm diff}$ is also sensitive to the relative normalization between the two cross sections. Up to the inclusion of the correlation of the HARP π^+ and π^- production data, these measurements represent the extraction of the most CCQE information possible with the MiniBooNE detector using only observations of the muon.

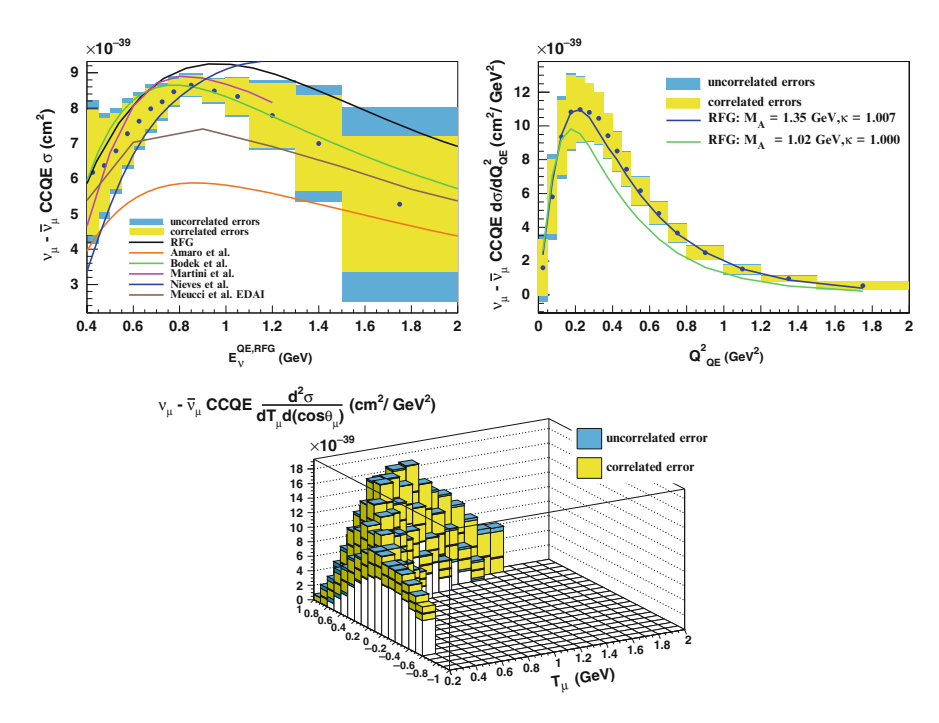


Fig. 9.4 Difference measurements of the ν_{μ} and $\bar{\nu}_{\mu}$ CCQE cross sections compared to various predictions. The "RFG" curve in the *top left figure* assumes $M_A=1.35\,\text{GeV}$ and $\kappa=1.007$. The "uncorrelated uncertainty", found by setting $\rho_{\nu,\bar{\nu}}=0$ in the uncertainty determination, is included to appreciate the level of sensitivity gained by using the correlation information

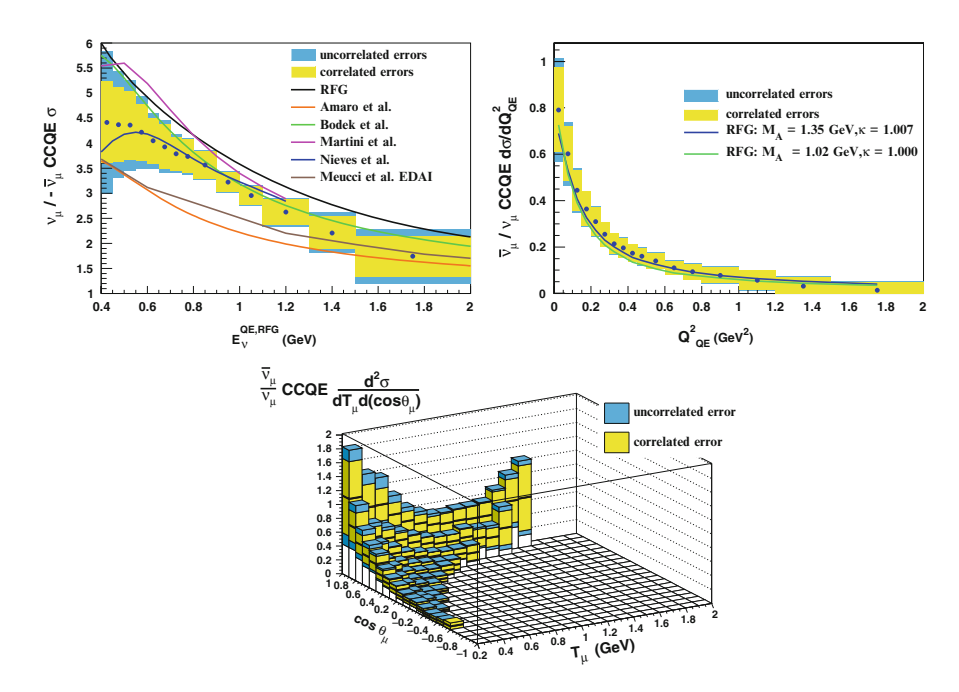


Fig. 9.5 Ratio measurements of the ν_{μ} and $\bar{\nu}_{\mu}$ CCQE cross sections compared to various predictions. The "RFG" curve in the *top left figure* assumes $M_A=1.35\,\text{GeV}$ and $\kappa=1.007$. The "uncorrelated uncertainty", found by setting $\rho_{\nu,\bar{\nu}}=0$ in the uncertainty determination, is included to appreciate the level of sensitivity gained by using the correlation information

References

- 1. A.A. Aguilar-Arevalo et al. [MiniBooNE Collaboration], Phys. Rev. D81, 092005 (2010)
- A.A. Aguilar-Arevalo et al. [MiniBooNE Collaboration], First measurement of the muon antineutrino double-differential charged current quasi-elastic cross section. Phys. Rev. D88, 032001 (2013)
- 3. J.R. Taylor, Error Analysis (University Science Books, Sausalito, 1997)

Chapter 10 Conclusion

This dissertation presents a variety of antineutrino CCQE cross sections, including the minimally model-dependent double-differential cross section. While the cross section configurations including the free scattering component of $\bar{\nu}_{\mu}$ CCQE interactions in the detector features the least model dependence and is the main result of this work, the results evoking an axial mass $M_A \sim 1\,\mathrm{GeV}$ to exclude the hydrogen component are also given to facilitate historical comparisons for neutrino and antineutrino interactions on carbon. This result is also used to test modern nuclear models that predict how a background arising from intra-nuclear correlations of greater size than expected might contribute to the analysis sample. These data are the first antineutrino cross-section results below 1 GeV, a crucial energy region for present and future neutrino oscillation experiments looking to measure CP violation.

To facilitate this measurement, novel and crucial evaluations of the ν_{μ} background to the $\bar{\nu}_{\mu}$ CCQE sample were developed and executed. In the absence of a magnetic field, the analyses described in Chap. 7 measure the ν_{μ} flux of the antineutrino mode beam with ~15% fractional uncertainty. These techniques could be used in current and future neutrino oscillation programs, particularly when modest charge identification is sufficient to meet the physics goals [1].

The combined measurements of the MiniBooNE ν_{μ} and $\bar{\nu}_{\mu}$ CCQE cross sections extract the most information of the CCQE processes possible with the MiniBooNE detector using only observations of the muon. While these measurements are entirely ignorant of hadronic activity, these analyses avoid model dependence typically associated with quantities such as momentum tracking thresholds and nucleon reinteractions used to identify CCQE interactions.

152 10 Conclusion

Reference

1. P. Huber, T. Schwetz, Phys. Lett. **B669**, 294 (2008). arXiv:0805.2019

Biographical Sketch

Joseph Grange received his bachelor's degree from the University of Puget Sound in 2006. His degrees from the University of Florida include a Master of Science in 2009 and a Doctor of Philosophy in 2013. This dissertation was selected as the winner of the Universities Research Association 2014 Outstanding Doctoral Thesis competition. It was selected above all other research dissertations connected with Fermilab and submitted in 2013.

He is presently a Research Associate with Argonne National Laboratory involved with the precision measurement of the anomalous magnetic moment of the muon.

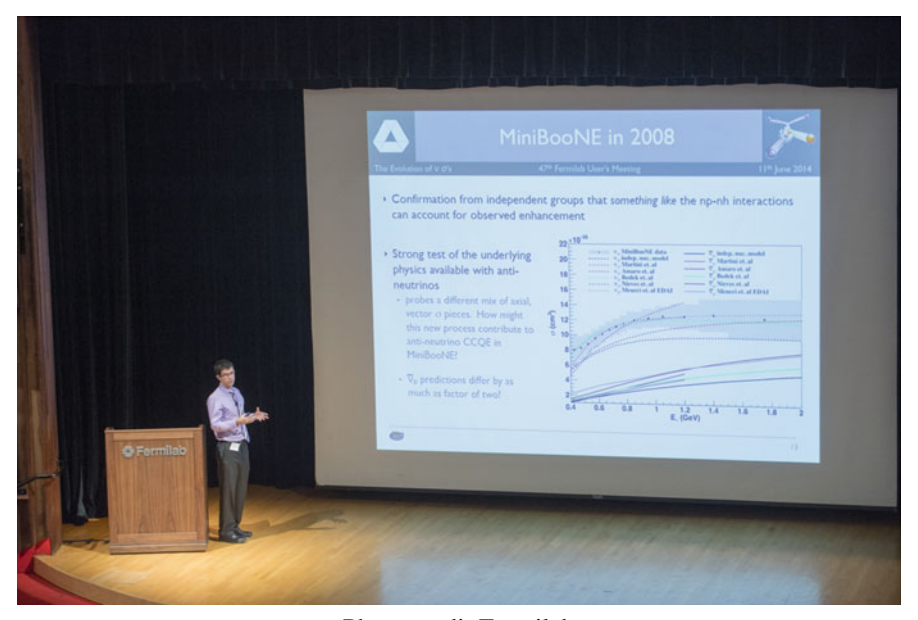


Photo credit Fermilab

[©] Springer International Publishing Switzerland 2015

¹⁵³